

Stony Brook University



OFFICIAL COPY

The official electronic file of this thesis or dissertation is maintained by the University Libraries on behalf of The Graduate School at Stony Brook University.

© All Rights Reserved by Author.

**Spectroscopic study of the dehydration and dehydroxylation of
phyllosilicate and zeolite minerals: Applications to laboratory study
and Martian exploration**

A Dissertation Presented

by

Congcong Che

to

The Graduate School

in Partial Fulfillment of the

Requirements

for the Degree of

Doctor of Philosophy

in

Geosciences

Stony Brook University

May 2012

Stony Brook University

The Graduate School

Congcong Che

We, the dissertation committee for the above candidate for the
Doctor of Philosophy degree, hereby recommend
acceptance of this dissertation.

**Timothy D. Glotch – Dissertation Advisor
Professor, Department of Geosciences**

**Scott M. McLennan – Chairperson of Defense
Professor, Department of Geosciences**

**Brian L. Phillips
Professor, Department of Geosciences**

**A. Deanne Rogers
Professor, Department of Geosciences**

**Bethany L. Ehlmann
Professor, Division of Geological and Planetary Sciences
California Institute of Technology**

This dissertation is accepted by the Graduate School

Charles Taber
Interim Dean of the Graduate School

Abstract of the Dissertation

**Spectroscopic study of the dehydration and dehydroxylation of
phyllosilicate and zeolite minerals: Applications to laboratory study
and Martian exploration**

by

Congcong Che

Doctor of Philosophy

in

Geosciences

Stony Brook University

2012

Phyllosilicates on Mars mapped by infrared spectroscopic techniques may have been affected by dehydration and/or dehydroxylation associated with volcanism or shock heating induced by meteor impact. The effects of heat-induced dehydration and/or dehydroxylation on the infrared spectra of 14 phyllosilicates from four structural groups (kaolinite, smectite, sepiolite-palygorskite, and chlorite) and 2 natural zeolites are reported in the 1st and 2nd parts of this dissertation. Pressed powders of size-separated phyllosilicate and natural zeolite samples were heated incrementally from 100 to 900 °C, cooled to room temperature, and measured using multiple spectroscopic techniques: mid-infrared (mid-IR) ($400\text{-}4000\text{ cm}^{-1}$) attenuated total reflectance (ATR), mid-to-far-IR reflectance ($50\text{-}1400\text{ cm}^{-1}$), mid-to-far-IR emission ($100\text{-}1400\text{ cm}^{-1}$), and near-infrared (NIR) reflectance ($1.2\text{-}2.5\text{ }\mu\text{m}$) spectroscopies. Correlated

thermogravimetric analysis (TGA), differential scanning calorimetry (DSC), and X-ray diffraction (XRD) data were also acquired in order to clarify the thermal transformation of each sample. The results indicate that (1) all phyllosilicates exhibit characteristic degradations in both NIR and mid-to-far-IR spectral properties between 400-800 °C, mainly attributable to the dehydroxylation and recrystallization processes as temperature increases. Spectral features of natural zeolites persist to higher temperatures compared to features of phyllosilicates during heating treatments. (2) The thermal behaviors of phyllosilicate infrared (IR) properties are greatly influenced by the compositions of the octahedral cations: changes in both the NIR and mid-to-far-IR spectra of phyllosilicates tend to occur at lower temperatures (300 to 400 °C) in the Fe³⁺-rich samples as compared to the Al³⁺-rich types (400-600 °C); Mg²⁺-trioctahedral phyllosilicates hectorite, saponite, and sepiolite all display major mid-to-far-IR spectral changes at 700 °C, corresponding to the formation of enstatite; phyllosilicates that have minor replacement of Mg²⁺ for Al³⁺ in octahedral positions (e.g. cheto-type montmorillonite and palygorskite) show an absorption band at ~920 cm⁻¹ that becomes strong at 900 °C. (3) Spectral results have provided suggestive evidence for the scenario that some phyllosilicates could lose all original spectral features in mid-to-far-IR region while maintaining their characteristic hydration bands in NIR region in the same temperature range.

Using the mid-IR emissivity and NIR spectra collected in the 2nd part, a detailed analysis of phyllosilicates in the ancient Nili Fossae region of Mars was conducted in the 3rd part of this dissertation. Analysis of remote sensing data including both thermal and near IR dataset suggests that thermally altered nontronite (400 °C) is likely present in the Nili Fossae region of Mars mixed with unaltered nontronite. The mixing of altered and unaltered phyllosilicates is the likely

cause for the apparent disconnect between previous VNIR and TIR observations of nontronite-bearing surfaces in Nili Fossae.

Dedication

To Mom and Dad, with love

Table of Contents

List of Figures.....	xiii
List of Tables.....	xix
Acknowledgements.....	xx
Chapter 1: Introduction.....	1
1.1. Samples and laboratory measurements.....	4
1.1.1 Samples.....	4
1.1.2 Laboratory techniques.....	7
1.1.2.1 TGA and DSC.....	7
1.1.2.2 XRD.....	7
1.1.2.3 IR spectroscopic measurements.....	8
1.2. Overview of Chapter 2.....	10
1.3. Overview of Chapter 3.....	12
1.4. Overview of Chapter 4.....	16
References.....	17
Chapter 2: Spectroscopic study of the dehydration and/or dehydroxylation of phyllosilicate and zeolite minerals.....	23

Abstract.....	23
2.1. Introduction.....	24
2.2. Background.....	29
2.2.1 Brief review of phyllosilicates and zeolite structures.....	29
2.2.2 Previous studies of dehydration and/or dehydroxylation of phyllosilicates and zeolites.....	31
2.2.3 The significance of this work.....	33
2.3. Methodology.....	34
2.3.1 Acquisition and preparation of sample.....	34
2.3.2 Thermogravimetric analysis.....	35
2.3.3 Acquisition of powder XRD patterns.....	39
2.3.4 Infrared spectroscopic measurements.....	39
2.4. Results and interpretations.....	40
2.4.1 Kaolinite-serpentine group.....	40
2.4.1.1 Attenuated total reflectance spectra.....	41
2.4.1.2 Specular reflectance spectra.....	41
2.4.1.3 Thermogravimetric and X-ray diffraction analysis.....	42
2.4.2 Smectite group.....	44
2.4.2.1 Montmorillonite.....	44
2.4.2.1.1 Attenuated total reflectance spectra.....	44
2.4.2.1.2 Specular reflectance spectra.....	48
2.4.2.1.3 Thermogravimetric and X-ray diffraction analysis.....	51
2.4.2.2 Saponite.....	54
2.4.2.2.1 Attenuated total reflectance spectra.....	54
2.4.2.2.2 Specular reflectance spectra.....	54

2.4.2.2.3 Thermogravimetric and X-ray diffraction analysis.....	55
2.4.2.3 Beidellite.....	57
2.4.2.3.1 Attenuated total reflectance spectra.....	57
2.4.2.3.2 Specular reflectance spectra.....	60
2.4.2.3.3 Thermogravimetric and X-ray diffraction analysis.....	62
2.4.2.4 Hectorite.....	64
2.4.2.4.1 Attenuated total reflectance spectra.....	64
2.4.2.4.2 Specular reflectance spectra.....	64
2.4.2.4.3 Thermogravimetric and X-ray diffraction analysis.....	65
2.4.2.5 Nontronite.....	67
2.4.2.5.1 Attenuated total reflectance spectra.....	67
2.4.2.5.2 Specular reflectance spectra.....	69
2.4.2.5.3 Thermogravimetric and X-ray diffraction analysis.....	69
2.4.3 Chlorite group.....	72
2.4.3.1 Attenuated total reflectance spectra.....	72
2.4.3.2 Specular reflectance spectra.....	72
2.4.3.3 Thermogravimetric and X-ray diffraction analysis.....	73
2.4.4 Sepiolite-palygorskite group.....	75
2.4.4.1 Attenuated total reflectance spectra.....	75
2.4.4.2 Specular reflectance spectra.....	78
2.4.4.3 Thermogravimetric and X-ray diffraction analysis.....	80
2.4.5 Zeolite group.....	82
2.4.5.1 Attenuated total reflectance spectra.....	82
2.4.5.2 Specular reflectance spectra.....	84
2.4.5.3 Thermogravimetric and X-ray diffraction analysis.....	84

2.5. Discussion.....	87
2.5.1 Effect of adsorbed H ₂ O.....	87
2.5.2 Effect of octahedral cations.....	87
2.6. Summary and conclusions.....	88
Appendix.....	90
Acknowledgments.....	92
References.....	92

Chapter 3: The effect of high temperatures on the mid-to-far-infrared emission and near-infrared reflectance spectra of phyllosilicates and natural zeolites:

Implications for Martian exploration.....	106
Abstract.....	106
3.1. Introduction.....	107
3.2. Methods.....	111
3.2.1 Sample description, preparation, and characterization.....	111
3.2.2 Differential scanning calorimetry measurements (DSC).....	114
3.2.3 Infrared spectroscopic measurements.....	114
3.2.3.1 NIR diffuse reflectance spectra.....	115
3.2.3.2 Emissivity spectra.....	115
3.3. Results.....	116

3.3.1 Differential thermal investigation: DSC.....	116
3.3.2 Mid-to-far-IR emissivity spectra.....	118
3.3.2.1 Kaolinite group.....	119
3.3.2.2 Smectite group.....	121
3.3.2.3 Sepiolite-palygorskite group.....	129
3.3.2.4 Chlorite group.....	131
3.3.2.5 Zeolite group.....	131
3.3.2.6 Other observations.....	134
3.3.3 NIR diffuse reflectance spectra.....	134
3.3.3.1 Kaolinite group.....	135
3.3.3.2 Smectite group.....	137
3.3.3.3 Sepiolite-palygorskite group.....	145
3.3.3.4 Chlorite group.....	147
3.3.3.5 Zeolite group.....	147
3.3.3.6 Other observations.....	150
3.4. Discussion.....	151
3.4.1 Effects of thermal behaviors of phyllosilicates and natural zeolites.....	151
3.4.2 Effects of octahedral cations.....	158
3.4.3 Inconsistency between spectral behaviors in the mid-to-far-IR and NIR regions and geologic implications.....	160
3.5. Summary and conclusions.....	161
Acknowledgments.....	163
References.....	163

Chapter 4: Characterizing thermally altered nontronites in Nili Fossae, Mars using thermal and near IR spectroscopy	172
4.1 Introduction.....	172
4.2 Data and methods.....	177
4.3 Results.....	181
4.4 Discussion.....	197
4.5 Conclusion.....	198
References.....	199
References	204

List of Figures

Chapter 1

- Figure 1.1:** Near IR reflectance and mid-to-far-IR emissivity spectra of sepiolite heated for 24 hours to 100 °C, 300 °C, 700 °C, and 900 °C.....14
- Figure 1.2:** Near IR reflectance and mid-to-far-IR emissivity spectra of nontronite heated for 24 hours to 100 °C, 300 °C, 400 °C, 600 °C, and 900 °C.....15

Chapter 2

- Figure 2.1:** Mid-IR ATR spectra, mid-to-far-IR specular reflectance spectra, TGA plot, and X-ray diffraction profiles of kaolinite (KGa-1b) calcined at various temperatures.....43

Figure 2.2: Mid-IR ATR spectra of “Cheto” montmorillonite (SAz-1), montmorillonite (Otay) (SCa-3), Texas montmorillonite (STx-1), and (d) Na-montmorillonite (Wyoming) (SWy-2) calcined at various temperatures.....	47
Figure 2.3: Mid-to-far-IR specular reflectance spectra of montmorillonites SAz-1, SCa-3, STx-1, SWy- 2) calcined at various temperatures.....	50
Figure 2.4: TGA plots and X-ray diffraction profiles of montmorillonites SAz-1, SCa-3, STx-1, SWy-2.....	53
Figure 2.5: Mid-IR ATR spectra, mid-to-far-IR specular reflectance spectra, TGA plot, and X-ray diffraction profiles of saponite (SapCa-2) calcined at various temperatures.....	56
Figure 2.6: Mid-IR ATR spectra of beidellite (SBCa-1) and mica-montmorillonite (Syn-1) calcined at various temperatures.....	59
Figure 2.7: Mid-to-far-IR specular reflectance spectra of beidellite (SBCa-1) and mica-montmorillonite (Syn-1) calcined at various temperatures.....	61
Figure 2.8: TGA plots and X-ray diffraction profiles of SBCa-1 beidellite and Syn-1 mica-montmorillonite.....	63
Figure 2.9: Mid-IR ATR spectra, mid-to-far-IR specular reflectance spectra, TGA plot, and X-ray diffraction profiles of hectorite (SHCa-1) calcined at various temperatures.....	66
Figure 2.10: Mid-IR ATR spectra of nontronite (NAu-1) and nontronite (NAu-2) calcined at various temperatures.....	68
Figure 2.11: Mid-to-far-IR specular reflectance spectra of nontronite (NAu-1) and nontronite (NAu-2) calcined at various temperatures.....	70
Figure 2.12: TGA plots and X-ray diffraction profiles of NAu-1 nontronite and NAu-2 nontronite.....	71

Figure 2.13: Mid-IR ATR spectra, mid-to-far-IR specular reflectance spectra, TGA plot, and X-ray diffraction profiles of clinochlore calcined at various temperatures.....	74
Figure 2.14: Mid-IR ATR spectra of palygorskite (PFl-1) and sepiolite (SepSp-1) calcined at various temperatures.....	77
Figure 2.15: Mid-to-far-IR specular reflectance spectra of palygorskite (PFl-1) and sepiolite (SepSp-1) calcined at various temperatures.....	79
Figure 2.16: TGA plots and X-ray diffraction profiles PFl-1 palygorskite and SepSp-1 sepiolite.....	81
Figure 2.17: Mid-IR ATR spectra of clinoptilolite (27031) and mordenite (27133) calcined at various temperatures.....	83
Figure 2.18: Mid-to-far-IR specular reflectance spectra of clinoptilolite (27031) and mordenite (27133) calcined at various temperatures.....	85
Figure 2.19: TGA plots and X-ray diffraction profiles (offset) of 27031 clinoptilolite and 27133 mordenite.....	86
Figure 2.20: Diagram of vibration modes in phyllosilicates discussed in this study.....	91

Chapter 3

Figure 3.1: DSC curves of 14 phyllosilicates and 2 natural zeolites.....	117
Figure 3.2: Mid-to-far-IR emissivity spectra of kaolinite (KGa-1b) calcined at various temperatures.....	120
Figure 3.3: Mid-to-far-IR emissivity spectra of montmorillonites SAz-1, SCa-3, STx-1 and SWy-2 calcined at various temperatures.....	122
Figure 3.4: Mid-to-far-IR emissivity spectra of nontronite (NAu-1) and nontronite (NAu-2) calcined at various temperatures.....	124
Figure 3.5: Mid-to-far-IR emissivity spectra of Saponite (SapCa-2) calcined at various temperatures.....	125
Figure 3.6: Mid-to-far-IR emissivity spectra of Hectorite (SHCa-1) calcined at various temperatures.....	126
Figure 3.7: Mid-to-far-IR emissivity spectra of Beidellite (SBCa-1) and Mica-montmorillonite (Syn-1) calcined at various temperatures.....	128
Figure 3.8: Mid-to-far-IR emissivity spectra of Palygorskite (PFI-1) and Sepiolite (SepSp-1) calcined at various temperatures.....	130
Figure 3.9: Mid-to-far-IR emissivity spectra of Clinocllore calcined at various temperatures.....	132
Figure 3.10: Mid-to-far-IR emissivity spectra of Clinoptilolite (27031) and Mordenite (27133) calcined at various temperatures.....	133
Figure 3.11: NIR diffuse reflectance spectra of kaolinite (KGa-1b) calcined at various temperatures.....	136
Figure 3.12: NIR diffuse reflectance spectra of montmorillonites SAz-1, SCa-3, STx-1 and SWy-2 calcined at various temperatures.....	138

Figure 3.13: NIR diffuse reflectance spectra of nontronite (NAu-1) and nontronite (NAu-2) calcined at various temperatures.....	140
Figure 3.14: NIR diffuse reflectance spectra of Saponite (SapCa-2) calcined at various temperatures.....	141
Figure 3.15: NIR diffuse reflectance spectra of Hectorite (SHCa-1) calcined at various temperatures.....	142
Figure 3.16: NIR diffuse reflectance spectra of Beidellite (SBCa-1) and Mica-montmorillonite (Syn-1) calcined at various temperatures.....	144
Figure 3.17: NIR diffuse reflectance spectra of Palygorskite (PFI-1) and Sepiolite (SepSp-1) calcined at various temperatures.....	146
Figure 3.18: NIR diffuse reflectance spectra of Clinochlore calcined at various temperatures.....	148
Figure 3.19: NIR diffuse reflectance spectra of Clinoptilolite (27031) and Mordenite (27133) calcined at various temperatures.....	149

Chapter 4

Figure 4.1: Laboratory emissivity spectral results of hectorite, saponite, and their heating products	175
--	------------

Figure 4.2: Near IR reflectance and mid-to-far-IR emissivity spectra of nontronite heated for 24 hours to 100 °C, 300 °C, 400 °C, 600 °C, and 900 °C.....	176
Figure 4.3: Context image of the Nili Fossae region showing positions of TES and CRISM data discussed below and shown in Figures 4.4, 4.5, and 4.10.....	183
Figure 4.4: Measured surface and modeled TES spectra occurring on and off the nontronite deposit identified by OMEGA and CRISM.....	184
Figure 4.5: Ratios of TES spectra occurring on and off deposits identified in Nili Fossae as nontronite-bearing by CRISM.....	186
Figure 4.6: Regional-scale map of the 450 cm ⁻¹ index in the Nili Fossae region.....	188
Figure 4.7: Target and recovered spectra of Martian atmospheric components	191
Figure 4.8: Spectral shapes recovered from FATT method using TES ST1 (basalt), TES ST2 (basaltic andesite), and Martian average surface dust	192
Figure 4.9: a) FATT-derived spectra of thermally altered nontronite and pure nontronite. b) Linear deconvolution of our FATT-derived spectrum.....	193
Figure 4.10: a) Ratio of 1.4 and 1.9 μm indices from CRISM image FRT0000BEC0. b) CRISM I/F spectra shown for each of the regions of interest.....	196

Lists of Tables

Chapter 1

Table 1.1: Summary of phyllosilicates and zeolites for this study.....	6
---	----------

Chapter 2

Table 2.1: Summary of phyllosilicates and zeolites for this study.....	36
Table 2.2: Summary of major elemental composition.....	37
Table 2.3: Summary of structural composition.....	38
Table 2.4: Fundamental vibration modes discussed in this study.....	90

Chapter 3

Table 3.1: Summary of phyllosilicates and zeolites for this study.....	112
Table 3.2: Summary of major elemental composition.....	113

Chapter 4

Table 4.1: Spectral library used in the deconvolution of TES data and FATT-derived spectrum	179
Table 4.2: Modeled mineral abundances of TES spectra occurring on and off a “nontronite” deposit identified by OMEGA and CRISM.....	185
Table 4.3: Mineral group abundances associated with the thermally altered nontronite FATT-derived spectrum.....	194

Acknowledgments

My first thanks go to my advisor, Tim Glotch. Tim has been an amazing advisor over the past few years. He has been extremely patient during this dissertation work. He always gave valuable insights for my work. His scientific enthusiasm has been always encouraging. More importantly, he taught me how to think like a scientist. I own a great deal to Tim's guidance, advice, and encouragement at all times. I wish him and his family the best.

I'd like thank my committee members: Scott McLennan, Brian Phillips, Deanne Rogers, and Bethany Ehlmann. Their time and detailed reviews for this work are greatly appreciated. A special thanks to Bethany for flying from California for my defense.

I am also thankful for the people in our research group. I consider myself fortunate to work with these wonderful people who have been always supportive and understanding. Thank you: Heidi Jsensen, Jessy Arnold, Lonia Friedlander, Eli Sklute, Matt Ferrari, Craig Hardgrove, Lauren Beavon, Brian Hahn, and Suniti Karunatilake.

I gratefully acknowledge the support and assistance given by faculty, staff, and fellow students from Department of Geosciences (Stony Brook University). In particular, thanks to Diane Isgro, Loretta Budd, Owen Evans, and Yvonne Barbour, for much appreciated help and many smiles. And thanks to Yuyan Zhao, Hui Long, for being my all-around friends.

In additional, I must thank several collaborators. I am indebted to David Bish, Joseph Michalski, and Wenqian Xu for their discussion and assistance in manuscript preparation, especially at the early stage of my research.

And finally, I'd like to thank my family and friends. My father and my mother give me endless love and support. My friends are always there to help out in times of stress. And my husband Xiaomeng Ban, you truly deserve thanks for your love, encouragement, and patience throughout my PhD study.

This work was supported by Mars Fundamental Research Program NNX08AN62G.

Chapter 1: Introduction

Data from the Mars Express Observatoire pour la Minéralogie, l'Eau, les Glaces, et l'Activité (MEx/OMEGA) and Compact Reconnaissance Imaging Spectrometer for Mars (MRO/CRISM) visible and near infrared imaging spectrometers have shown phyllosilicates to be present on the Martian surface [Poulet *et al.*, 2005; Bibring *et al.*, 2006; Loizeau *et al.*, 2007; Mangold *et al.*, 2007]. The identification of phyllosilicates is based on the detection of $\sim 1.4 \mu\text{m}$ (the first overtone of the O-H stretching modes), $\sim 1.9 \mu\text{m}$ (H-O-H band) and $\sim 2.15\text{-}2.4 \mu\text{m}$ (metal-OH bands) features. Phyllosilicates are detected in a number of contexts on Mars, primarily associated with heavily cratered Noachian terrains [e.g., Poulet *et al.*, 2005; Bibring *et al.*, 2006; Mangold *et al.*, 2007; Michalski and Noe Dobrea, 2007].

It has been suggested that at least some phyllosilicates on Mars were likely formed from long-lived hydrothermal systems initiated by impact processes [e.g., Schwenger and Kring, 2009], while others have suggested that pre-existing phyllosilicates were excavated by repeated impact events [Fairén *et al.*, 2010]. Abramov and Kring [2005] modeled an impact-induced hydrothermal system on Mars and the results indicated that temperatures as high as $1200 \text{ }^\circ\text{C}$ could last for thousands of years in the region of the impact. Fairén *et al.*, [2010] calculated the temperature increases in a transient crater resulting from an impact, and their model showed that temperatures can reach close to $1000 \text{ }^\circ\text{C}$ in a certain area around the point of impact. In the laboratory, $400\text{-}500 \text{ }^\circ\text{C}$ is sufficient for phyllosilicates to lose their interlayer H_2O and most

phyllosilicates can be completely dehydroxylated at 900 °C [e.g., *Guggenheim and Koster van Groos*, 2001]. These previous conclusions lead us to propose that phyllosilicates on Mars may have been affected by impact processes, with an emphasis on post-shock heating, and that dehydrated and/or dehydroxylated phyllosilicates may be present on the Martian surface.

Further, the process of phyllosilicate dehydration or dehydroxylation may also help explain the apparent disconnect between visible and near-IR (VNIR) and thermal IR (TIR) observations of phyllosilicates on Mars. Data from the MEx/OMEGA (0.4-5 µm, 0.3-2 km/pixel) and MRO/CRISM (0.4-3.9 µm, 18 m/pixel) VNIR imaging spectrometers have provided unambiguous evidence for the widespread presence of phyllosilicates [e.g., *Poulet et al.*, 2005; *Bibring et al.*, 2006; *Loizeau et al.*, 2007; *Mangold et al.*, 2007], while global detection of phyllosilicates in the Mars Global Surveyor (MGS) Thermal Emission Spectrometer (TES) data (6-50 µm, ~3 x 8km/pixel) has remained unclear because it is difficult to distinguish phyllosilicates and amorphous silica-rich phases (e.g., glass or amorphous weathering products) in the truncated spectral range of TES [e.g., *Bandfield*, 2002; *Ruff*, 2003; *Michalski et al.*, 2005; *Michalski et al.*, 2006; *Ruff and Christensen*, 2007]. However, it may be possible to identify these minerals at local scales if they are present in significant abundances. The phyllosilicate deposits in Nili Fossae detected by OMEGA exhibited different spectral features from surrounding regions in Thermal Emission Imaging System (THEMIS, 6-15 µm, 100m/pixel) images [*McDowell and Hamilton*, 2007a, 2007b]. The THEMIS phyllosilicate index of *Viviano and Moersch* [2011] also indicated that THEMIS may be able to provide more reliable phyllosilicate abundance than TES because of its higher spatial resolution. The bright and dark terrains around Mawrth Vallis show distinct spectral character in TES data, in which the dark

terrain is consistent with TES Surface Type 1 (ST1, basalt, *Bandfield et al.*, 2000) while the bright terrain is clearly different. In the Mawrth Vallis phyllosilicate deposits, TES spectra show evidence for significant abundances of poorly crystalline silica that may be actual opaline silica or a spectroscopic substitution for poorly crystalline phyllosilicates [*Michalski and Fergason*, 2009]. Also in the Nili Fossae region, recent work by *Michalski et al.* [2010] shows that it is possible to identify phyllosilicate deposits from their long-wavelength spectral features. TES data consistently show a spectral absorption located near 450 cm^{-1} within the same surfaces where OMEGA and CRISM show phyllosilicate occurrences around Nili Fossae. While the presence of these features is consistent with the occurrence of Fe^{2+} -bearing phyllosilicates and/or poorly crystalline Fe/Mg-rich clays, the overall TES spectrum of these surfaces lacks other diagnostic bands normally associated with phyllosilicates: Si-O stretching features in the $900\text{--}1100\text{ cm}^{-1}$ region. In summary, TES TIR and OMEGA/CRISM VNIR spectra give different perspectives on phyllosilicate mineralogy, crystallinity, and abundance on Mars. Among the potential reasons for this disconnect is the possibility that phyllosilicates on Mars have been modified by the effects of dehydration and/or dehydroxylation. Such effects modify the mineral structures in such a way that their spectroscopic signatures appear different from various wavelength-perspectives. Laboratory spectral studies of dehydrated or dehydroxylated phyllosilicates are essential to characterize how high temperatures affect NIR and TIR spectra in different ways.

The study described in this dissertation contributes to the laboratory IR spectral studies of dehydrated or dehydroxylated phyllosilicates and the search for thermally altered phyllosilicates on Mars. As part of the work described in Chapter 2, I collected mid-IR attenuated total

reflectance (ATR) spectra, mid-to-far-IR specular reflectance spectra, powder x-ray diffraction (XRD) data, and thermogravimetric analysis (TGA) data of 14 phyllosilicates and 2 natural zeolites as they were dehydrated or dehydroxylated due to exposure to heat. The main objective of Chapter 2 is to improve upon previous IR spectral studies of thermally altered phyllosilicates [e.g., *Bruckenthal and Singer, 1987; Milliken and Mustard, 2005; Gavin and Chevrier, 2010*]. As part of the work described in Chapter 3, I acquired mid-to-far-IR emissivity spectra, NIR diffuse reflectant spectra, and differential scanning calorimetry measurements (DSC) data of the same suite of samples from Chapter 2. The goal of chapter 3 is to establish both mid-to-far-IR emissivity and NIR reflectance spectral libraries for identification of dehydrated or dehydroxylated phyllosilicates on Mars. As part of the work described in Chapter 4, I applied spectral results of Chapter 3 to phyllosilicate-bearing sediments on Mars, in order to search for the presence of dehydrated or dehydroxylated phyllosilicates on the Martian surface. Brief summary of samples, laboratory techniques, and the major findings for each chapter are provided below.

1.1 Samples and laboratory measurements

1.1.1 Samples

Fourteen phyllosilicate and 2 zeolite samples were selected for the laboratory part of this dissertation (**Table 1.1**). Most phyllosilicates selected have been identified or tentatively identified on Mars based on OMEGA and CRISM data [e.g., *Poulet et al., 2005; Ehlmann et al., 2009; Bishop et al., 2011*]. Two natural zeolite minerals were also analyzed because zeolite is another important class of minerals that are present on Mars in a hydrated state [e.g., *Ehlmann et*

al., 2009] and zeolites minerals have chemical compositions similar to phyllosilicates. Phyllosilicates have the typical layer structures and zeolites have a rigid three-dimensional structure [e.g., *Farmer*, 1974; *Bailey*, 1980; *Barrer*, 1978]. Therefore, analysis of zeolite samples can help provide insights for how the crystal structures affect spectral changes of minerals upon heating. Phyllosilicates selected for this study can be divided into four groups according to their structural type: the kaolinite-serpentine group, smectite group, chlorite group, and sepiolite-palygorskite group. I studied phyllosilicates from four structural groups, so that differences in spectral behaviors among groups can be investigated. In the smectite group, I analyzed four montmorillonites and two nontronites, to study if the minor chemical composition differences could influence on the spectral changes of phyllosilicates with heating. All samples were prepared to <2 μm size fraction and heated under normal atmospheric conditions at 100, 200, 300, 400, 500, 600, 700, 800, and 900 $^{\circ}\text{C}$. The heating duration for each temperature was 24 hours.

Table 1.1 Summary of phyllosilicates and zeolites for this study*

Structural Group	Mineral	Sample Number	Source	Size Fraction
Smectite group				
	“Cheto” montmorillonite	SAz-1	CMS	<2 μm
	Texas montmorillonite	STx-1	CMS	<2 μm
	Na-montmorillonite (Wyoming)	SWy-2	CMS	<2 μm
	Montmorillonite (Otay)	SCa-3	CMS	<2 μm
	Mica-montmorillonite	Syn-1	CMS	<2 μm
	Beidellite	SBCa-1	CMS	<2 μm
	Hectorite	SHCa-1	CMS	<2 μm
	Saponite	SapCa-2	CMS	<2 μm
	Nontronite	NAu-1	CMS	<2 μm
	Nontronite	NAu-2	CMS	<2 μm
Kaolinite-serpentine group				
	Kaolinite	KGa-1b	CMS	<2 μm
Sepiolite-palygorskite group				
	Sepiolite	SepSp-1	CMS	<2 μm
	Palygorskite (Attapulgite)	PFI-1	CMS	<2 μm
Chlorite group				
	Clinochlore	Clinochlore	Mineral Unlimited	<2 μm
Zeolite group				
	Mordenite	27133	Mineral Research	<2 μm
	Clinoptilolite	27031	Mineral Research	<2 μm

* Table adopted from Che *et al.* 2011

1.1.2 Laboratory techniques

In this dissertation, I performed a variety of IR spectroscopic measurements on the thermally altered phyllosilicates and natural zeolites, in order to characterize the changes in the mid-to-far-IR and NIR spectra of the samples when they were exposure to increasingly higher temperatures. Correlated TGA, DSC, and X-ray diffraction (XRD) data were also acquired in order to clarify the thermal transformation of each sample.

1.1.2.1 TGA and DSC

TGA is the most direct tool to observe the temperature dependence of mineral mass. DSC can be used to study the thermal reactions (e.g. endothermic and exothermic reactions) of phyllosilicates and natural zeolites during dehydration and/or dehydroxylation processes. In this study, the temperature ranges of thermal activities such as dehydration, dehydroxylation, collapse of samples' layer structure, and recrystallization were clarified using TGA and DSC measurements.

1.1.2.2 XRD

XRD is the most common technique used to study crystal structure of minerals. Powder XRD patterns were acquired for all phyllosilicates and zeolites and their heated products in order to confirm their mineralogy and to observe the crystal structural changes of phyllosilicates and zeolites upon heating. In this dissertation, I correlated changes in the mid-to-far-IR and NIR

spectral ranges with structural changes in the phyllosilicate natural zeolites minerals due to dehydration and dehydroxylation.

1.1.2.3 IR spectroscopic measurements

Mid-IR ATR

An ATR spectrum is acquired as the beam of IR radiation passes through an ATR element (which has high refractive index) in contact with sample. When IR source radiation enters the ATR element, a total internal reflection occurs and an evanescent wave is formed at the boundary between the ATR element and sample. The sampling surface is pressed into intimate optical contact with the top surface of the ATR crystal and the resulting evanescent wave penetrates only a few microns into the sample. Because of ATR's easy sample preparation and effectiveness with small grain size, ATR has been considered a potential *in situ* IR technique for future planetary explorations [Chemtob and Glotch, 2007]. In this study, the changes in the H₂O and OH contents of samples were observed by examination of the H₂O bending (~1630 cm⁻¹) and/or OH stretching (~3600 cm⁻¹) bands displayed in ATR spectra.

Mid-to-far-IR specular reflectance

Specular reflectance peaks are generally referred to as “reststrahlen” features. These occur because the absorption coefficient of a vibrational band is so high that a mirror-like opacity is induced, resulting in strong reflectance from the smooth surface of the samples [Salisbury, 1993]. “Reststrahlen bands” appear at very strong molecular vibration regions, such as Si-O vibration

[e.g., *Madejov a'*, 2003]. In this study, the spectral changes associated with SiO₄ vibrations (~1000 cm⁻¹ and ~500 cm⁻¹) were investigated using specular reflectance spectral results of thermally altered samples.

NIR diffuse reflectance

The NIR reflectance spectra (1.2 - 2.5 μm) were collected for all samples and their heated products. The NIR is very useful for characterization of the dehydration and dehydroxylation of hydrous minerals, because it is in this region that the minerals have spectral bands due to overtones and combinations of OH and H₂O vibrations. In general, the overtone of the OH stretching modes occurs in the 1.4 μm region, combination modes of H₂O molecules produce the absorptions in the 1.9 μm region, and spectral features near 2.2-2.4 μm regions are due to a combination of the OH stretching and M-OH bending modes [e.g., *Gaffey et al.*, 1993; *Bishop et al.*, 1994].

Mid-to-far-IR emissivity

Emissivity spectra were acquired by switching off the Globar IR source and measuring the radiation from the heated samples directly. A blackbody heated to 70 °C and 100 °C was used to calibrate the emissivity spectra in the manner of *Ruff et al.* [1997]. The mid-to-far-IR emissivity spectral library (available at <http://aram.ess.sunysb.edu/tglotch/spectra.html>) of dehydrated and/or dehydroxylated phyllosilicates and natural zeolites was created using the end result of emissivity measurements. This dissertation is based on a hypothesis that dehydrated and/or dehydroxylated phyllosilicates due to impact heating may remain on Mars. NIR spectra cannot identify these possible dehydrated and/or dehydroxylated phases because phyllosilicates show

almost no spectral feature in near-IR region after they have been heated to high temperatures [e.g., *Milliken and Mustard*, 2005; *Gavin and Chevrier*, 2010]. Therefore it is very important to understand the effects of temperature on the mid-IR emissivity spectra of phyllosilicates. I anticipate this spectral library will be used in future Mars data analysis studies which will make use of TES, THEMIS, and Miniature Thermal Emission Spectrometer (Mini-TES), so that these data may be more correctly interpreted.

1.2. Overview of Chapter 2

Although the dehydration and dehydroxylation of several phyllosilicates and natural zeolites have been studied extensively using primarily TGA [e.g. *Guggenheim and Koster van Groos*, 2001], XRD [e.g. *Harris et al.*, 1992; *Aceman et al.*, 1997], and nuclear magnetic resonance (NMR) spectroscopy [e.g. *Frost and Barron*, 1984; *Fitzgerald et al.*, 1989, 1996; *Sanchez-Soto et al.*, 1993], and to a lesser extent using VNIR spectroscopy [e.g., *Bruckenthal and Singer*, 1987; *Milliken and Mustard*, 2005], there is no substantive work thoroughly describing the mid-to-far-IR spectral changes of these minerals upon heating. This study documents the effects of heating on 16 phyllosilicates and zeolite minerals based on ATR, IR reflectance, TGA, and powder XRD measurements. The XRD and TGA measurements were utilized to complement IR spectroscopy. Heat treatment produces distinct changes in the infrared spectral features ($\sim 100\text{-}4000\text{ cm}^{-1}$) of phyllosilicates and zeolites. These changes are associated with dehydration and/or

dehydroxylation processes, determined primarily by the specific crystal structures and affected by their octahedral and extraframework cation compositions:

(1) For phyllosilicate samples, the OH stretching ($\sim 3600\text{ cm}^{-1}$), OH bending ($\sim 590\text{-}950\text{ cm}^{-1}$), and/or H₂O bending ($\sim 1630\text{ cm}^{-1}$) bands all become very weak or completely disappear upon heating to temperatures $>500\text{ }^{\circ}\text{C}$. The spectral changes associated with SiO₄ vibrations ($\sim 1000\text{ cm}^{-1}$ and $\sim 500\text{ cm}^{-1}$) show large variations depending on the compositions and structures of phyllosilicates. Spectral features of kaolinite change significantly at $\sim 400\text{ }^{\circ}\text{C}$ and the new bands are relatively stable until $900\text{ }^{\circ}\text{C}$. Most smectite samples display two distinct spectral changes with increased temperature. Clinocllore also exhibited dual changes in spectral features on heating, likely due to the presence of two different types of hydroxyl groups. The modulated tetrahedral sheets of palygorskite/sepiolite minerals showed more complex spectral changes on heating than other phyllosilicates included in this study. Compared to the phyllosilicates, the spectral features of two natural zeolites, clinoptilolite and mordenite, are less affected by thermal treatments. Even after heating to $900\text{ }^{\circ}\text{C}$, the IR spectral features do not show significant differences from those of unheated zeolites. These spectral results are consistent with the fact that the three-dimensionally rigid crystal structure of zeolite is stabler than the layer structure of phyllosilicates.

(2) The composition of octahedral sites showed a great influence on spectral behaviors of phyllosilicates: IR spectra of Al³⁺ rich smectites are stabler than those of Fe³⁺ rich smectites; spectral behaviors of Mg²⁺ rich phyllosilicates are distinctly affected by the formation of new crystal phases around $700\text{ }^{\circ}\text{C}$; phyllosilicates with a small amount of Mg²⁺ on their octahedral sites all showed new spectral band at $\sim 900\text{ cm}^{-1}$ upon heating to $700\text{ }^{\circ}\text{C}$ or higher temperatures.

1.3. Overview of Chapter 3

The reflectance spectral results from Chapter 2 can be used to approximate emissivity spectra using Kirchhoff's Law ($E=1-R$). However, Kirchhoff's Law only holds true when the surface is a Lambertian scatterer [e.g., *Salisbury et al.*, 1994], so laboratory mid-to-far-IR reflectance spectra may have limitations when applied to analysis of data from the non-Lambertian Martian surface. Therefore in Chapter 3, in order to complement mid-to-far-IR studies of dehydrated and/or dehydroxylated phyllosilicates and zeolites and establish both mid-to-far-IR emissivity and NIR reflectance spectral libraries for identification of dehydrated or dehydroxylated phyllosilicates on Mars, I reported NIR diffuse reflectance and mid-to-far-IR emissivity spectra of 14 phyllosilicates and 2 natural zeolites at various temperatures. DSC measurements were also performed on each sample in order to clarify their thermal activities. The main findings are:

(1) Spectral features in both the NIR and mid-to-far-IR regions of phyllosilicates and natural zeolites are significantly affected by heating. The spectral behavior of each sample is unique and thermal behaviors of phyllosilicates and zeolites showed a great influence on the IR spectra upon heating. In general, the effect of dehydration on the IR properties of all phyllosilicates and zeolites in this study is very small. The major spectral changes to phyllosilicate spectra are associated with dehydroxylation reactions, collapse of layer structures,

and/or recrystallization to new phases. The two natural zeolites studied here showed minor spectral changes, corresponding to deformation of the zeolite structure at ~700-900 °C.

(2) The composition of octahedral sites strongly influences the spectral behaviors of phyllosilicates: IR spectra of Al³⁺-rich smectites are more stable than those of Fe³⁺-rich smectites; stability of Al³⁺-rich smectites decreases as the Al³⁺ abundance decreases; spectral behaviors of Mg²⁺-rich phyllosilicates are distinctly affected by the formation of new crystalline phases near 700 °C; phyllosilicates with a small amount of Mg²⁺ in their octahedral sites all displayed a new spectral band at ~920 cm⁻¹ upon heating to 700 °C or higher temperatures.

(3) Results from Chapter 3 have shown that some phyllosilicates can lose all original spectral features in the TIR region while maintaining the characteristic hydration bands in NIR region in the same temperature range (**Figure 1.1, 1.2**).

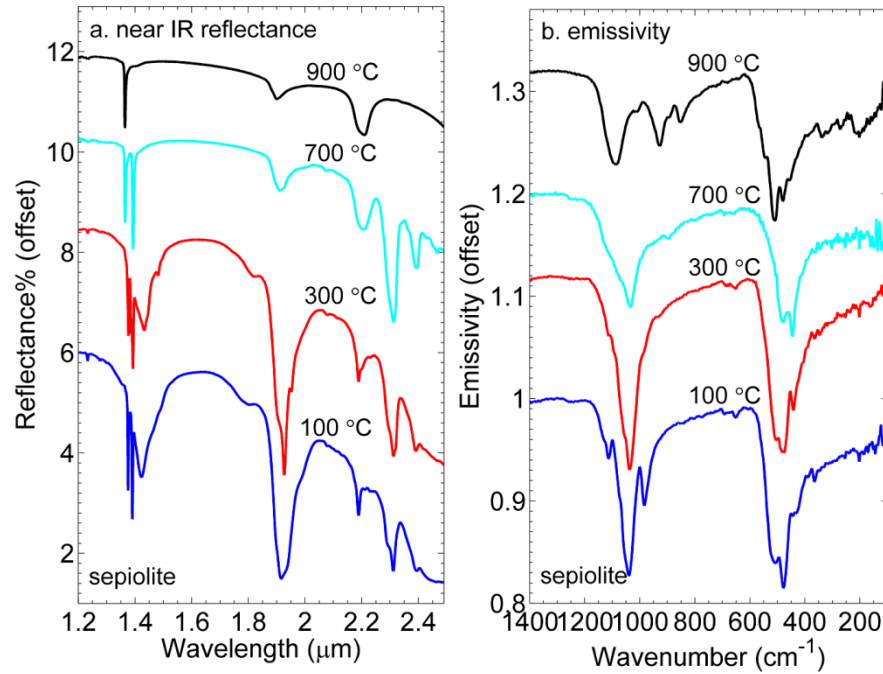


Figure 1.1 (a) Near IR reflectance and (b) emissivity spectra of sepiolite heated for 24 hours to 100 °C, 300 °C, 700 °C, and 900 °C. At 900 °C, sepiolite still maintains diagnostic spectral bands of phyllosilicates (1.9, 2.2 μm), while its thermal IR spectrum at temperature of 900 ° is already dominated by spectral bands of enstatite.

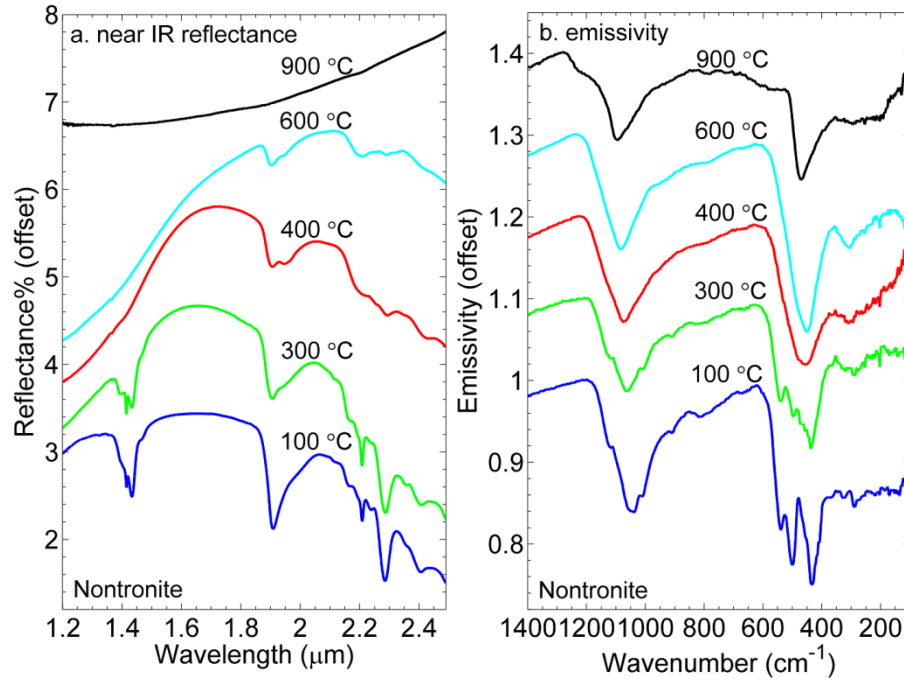


Figure 1.2 (a) Near IR reflectance and (b) emissivity spectra of nontronite heated for 24 hours to 100 °C, 300 °C, 400 °C, 600 °C, and 900 °C. At 300 °C, the spectral features in the range 400-600 cm⁻¹ display significant change, while no obvious changes are observed for nontronite's NIR spectral features. At 400 °C, the triplet spectral feature in the Si-O bending region is replaced by one single absorption centered at ~450 cm⁻¹, while nontronite sample keeps weak 1.9, 2.3, and 2.4 μm spectral bands in NIR region.

1.4. Overview of Chapter 4

In Chapter 4 I contribute to the search for thermally altered nontronite in the Nili Fossae region, Mars using thermal and near IR spectroscopic methods along with spectra collected from Chapter 3.

Interpretation of both OMEGA and CRISM spectra shows that Nili Fossae contains one of the most significant phyllosilicate exposures on Mars, and that phyllosilicates detected in this region are predominantly Fe/Mg-rich smectite minerals [e.g., *Poulet et al.*, 2005; *Mangold et al.*, 2007; *Ehlmann et al.*, 2009; *Michalski et al.*, 2010]. *Michalski et al.* [2010] analyzed the nontronite deposits in the Nili Fossae area using data from both OMEGA and the TES. The VNIR spectrum of the area displays an Fe-OH feature at 2.28 μm and associated hydration bands (1.4 and 1.9 μm), suggesting the presence of nontronite or a nontronite-like Fe-rich smectite mineral. However, thermal IR (TIR) spectra from TES consistently exhibit an absorption near 450 cm^{-1} , that does not match any particular Fe-rich smectite. I collected laboratory spectra (Chapter 3) of heated nontronite and found that the doublet or triplet spectral feature in the Si-O bending region disappears at 400 $^{\circ}\text{C}$ and is replaced by a single absorption at $\sim 450 \text{ cm}^{-1}$ while the nontronite sample keeps weak 1.9, 2.29, and 2.4 μm spectral bands in the VNIR region (**Figure 1.2**). This leads me to suggest that the nontronite deposits in the Nili Fossae region may be wholly or partly composed of nontronite heated to temperatures around 400 $^{\circ}\text{C}$.

In Chapter 4, I used a variety of spectroscopic methods, covering NIR to MIR wavelengths to search for thermally altered nontronite in the Nili Fossae region. These include (1) local-scale linear deconvolution of TES data using a spectral library that includes dehydrated and dehydroxylated nontronite, (2) use of spectral ratios of TES data to determine the long-

wavelength spectral character of nontronite-bearing deposits, (3) local-scale spectral index mapping of dehydrated and dehydroxylated nontronite features, based on the unique TIR spectral properties of this sample, (4) factor analysis and target transformation (FATT) analyses of TES data, to determine the independently variable spectral components in regions of interest, and (5) spectral index mapping and detailed spectral analysis of CRISM data. The results have shown that thermally altered nontronite (400 °C) is likely present in the Nili Fossae region of Mars. Nontronite in the Nili Fossae region is not present as a pure phase, suggesting that it was partially affected by post-depositional thermal alteration. The mixing of altered and unaltered phyllosilicates is the likely cause for the apparent disconnect between previous VNIR and TIR observations of nontronite-bearing surfaces in Nili Fossae. The presence of thermally altered nontronite may also help understand the potential effects of post-depositional thermal alteration on Martian sediments as a key component of understanding past Martian habitability and biosignature preservation.

References

- Abramov, O., and D. A. Kring (2005), Impact-induced hydrothermal activity on early Mars, *J. Geophys. Res.*, *110*, E12S09, doi:10.1029/2005JE002453.
- Aceman, S., N. Lahav, and S. Yariv (1997), XRD study of the dehydration and rehydration of Al-pillared smectites differing in source of charge, *J. Therm. Anal.*, *50*, 241--256.

Bailey, S. W. (1980), Structures of layer silicates, In *Crystal Structures of Clay Minerals and Their X-ray Identification*, edited by G. W. Brindley and G. Brown, pp. 1-124, Mineral. Soc., London.

Bandfield, J. L. (2002), Global minerals distributions on Mars, *J. Geophys. Res.*, 107(E6), 5042, doi:10.1029/2001JE001510.

Bandfield, J. L., V. E. Hamilton, P. R. Christensen (2000), A global view of Martian surface compositions from MGS-TES, *Science*, 287, 1626-1630.

Barrer, R. M. (1978), Zeolite frameworks, cations and water molecules, In *Zeolites and Clay Minerals as Sorbents and Molecular Sieves*, pp. 32-102, Academic Press, London.

Bibring, J. -P., Y. Langevin, J. F. Mustard, F. Poulet, R. Arvidson, A. Gendrin, B. Gondet, N. Mangold, P. Pinet, F. Forget, and the OMEGA team (2006), Global mineralogical and aqueous Mars history derived from OMEGA/Mars Express data, *Science*, 312, 400-404.

Bishop, J. L., W. P. Gates, H. D. Makarewicz, N. K. McKeown, and T. Hiroi (2011), Reflectance spectroscopy of beidellites and their importance for Mars, , *Clays Clay Miner.*, 59, 378-399.

Bishop, J. L., C. M. Pieters, J. O. Edwards (1994). Infrared spectroscopic analyses on the nature of water in montmorillonite. *Clays Clay Miner.* 42, 701-715.

Bruckenthal, E. A., and R. B. Singer (1987), Spectral effects of dehydration on phyllosilicates, *Proc. Lunar Planet. Sci. Conf. 18th*, 135.

Chemtob, S. M., and T. D. Glotch (2007), Linear deconvolution of attenuated total reflectance infrared spectra of fine-grained mineral mixtures, *Lunar Planet. Sci.*, 38th, abstract 1097.

Ehlmann, B. L., J. F. Mustard, G. A. Swayze, R. N. Clark, J. L. Bishop, F. Poulet, D. J. Des Marais, L. H. Roach, R. E. Milliken, J. J. Wray, O. Barnouin-Jha, and S. L. Murchie (2009), Identification of hydrated silicate minerals on Mars using MRO-CRISM: Geologic context near Nili Fossae and implications for aqueous alteration, *J. Geophys. Res.*, *114*, E00D08, doi:10.1029/2009JE003339.

Fairén, A. G. et al. (2010), Noachian and more recent phyllosilicates in impact craters on Mars, *Proceedings of the National Academy of Sciences*, *107*, 12095-12100, doi:10.1073/pnas.1002889107.

Farmer, V. C. (1974), The layer silicates, In *The Infrared Spectra of Minerals*, edited by V. C. Farmer, pp. 331-363, Mineral. Soc., London.

Fitzgerald, J. J., S. F. Dec, and A. I. Hamza (1989), Observation of 5-coordinated Al in pyrophyllite dehydroxylate by solid-state ^{27}Al NMR spectroscopy at 14 T, *Am. Mineral.*, *74*, 1405-1408.

Fitzgerald, J. J., A. I. Hamza, S. F. Dec, and C. E. Bronnimann (1996), Solid-state ^{27}Al and ^{29}Si NMR and ^1H CRAMPS studies of the thermal transformations of the 2:1 phyllosilicate pyrophyllite, *J. Phys. Chem.*, *100*, 17351-17360.

Frost, R. L., and P. F. Barron (1984), Solid-state silicon-29 and aluminum-27 nuclear magnetic resonance investigation of the dehydroxylation of pyrophyllite, *J. Phys. Chem.*, *88*, 6206-6209.

Gaffey, S. J., L. A. McFadden, D. Nash, C. M. Pieters (1993), Ultraviolet, Visible, and Near-infrared Reflectance Spectroscopy: Laboratory spectra of Geologic Materials, In: Pieters, C. M.,

Englert, P. A. J. (Eds.), *Remote Geochemical Analysis: Elemental and Mineralogical Composition*. Cambridge University Press, Cambridge, pp. 43-78.

Gavin, P., V. Chevrier (2010), Thermal alteration of nontronite and montmorillonite: Implications for the martian surface, *Icarus*, 208, 721-734, doi:10.1016/j.icarus.2010.02.027.

Guggenheim, S. and A. F. Koster van Groos (2001), Baseline studies of the clay minerals society source clays: Thermal analysis, *Clays Clay Miner.*, 49, 433-443.

Harris, W. G., K. A. Hollien, S. R. Bates, and W. A. Acree (1992), Dehydration of hydroxyl-interlayered vermiculite as a function of time and temperature, *Clay. Clay Min.*, 40, 335-340.

Loizeau, D., N. Mangold, F. Poulet, J. -P. Bibring, A. Gendrin, V. Ansan, C. Gomez, B. Gondet, Y. Langevin, P. Masson, and G. Neukum (2007), Phyllosilicates in the Mawrth Vallis region of Mars, *J. Geophys. Res.*, 112, E08S08, doi:10.1029/2006JE002877.

Madejov *a'*, J. (2003), FTIR techniques in clay mineral studies, *Vib. Spectrosc.*, 31, 1-10.

Mangold, N., et al. (2007), Mineralogy of the Nili Fossae region with OMEGA/Mars Express data; 2. Aqueous alteration of the crust, *J. Geophys. Res.*, 112, E08S04, doi:10.1029/2006JE002835.

McDowell, M. L., and V. E. Hamilton (2007a), Phyllosilicate detection and uncertainty from thermal infrared data in the vicinity of the Nili Fossae, *Lunar Planet. Sci.*, XXXVIII, abstract 1872.

McDowell, M. L., and V. E. Hamilton (2007b), Examination of phyllosilicate-bearing materials in the vicinity of the Nili Fossae using thermal infrared data, *Seventh Intl. Conf. Mars*, abstract 3095.

Michalski, J. R., and R. L. Fergason (2009), Composition and thermal inertia of the Mawrth Vallis region of Mars and THEMIS data, *Icarus*, *199*, 25-48, doi: 10.1016/j.icarus.2008.08.016.

Michalski, J. R., and E. Z. Noe Dobrea (2007), Evidence for a sedimentary origin of clay minerals in the Mawrth Vallis region, Mars, *Geology*, *35*, 951-954.

Michalski, J. R., F. Poulet, J. -P. Bibring, and N. Mangold (2010), Analysis of phyllosilicate deposits in Nili Fossae region of Mars: Comparison of TES and OMEGA data, *Icarus*, doi:10.1016/j.icarus.2009.09.006.

Michalski, J. R., M. D. Kraft, T. G. Sharp, L. B. Williams, and P. R. Christensen (2005), Mineralogical constraints on the high-silica martian surface component observed by TES, *Icarus*, *174*, 161-177.

Michalski, J. R., M. D. Kraft, T. G. Sharp, L. B. Williams, and P. R. Christensen (2006), Emission spectroscopy of clay minerals and evidence for poorly crystalline aluminosilicates on Mars from Thermal Emission Spectrometer data, *J. Geophys. Res.*, *111*, E03004, doi:10.1029/2005JE002438.

Milliken, R. E., and J. F. Mustard (2005), Quantifying absolute water content of minerals using near-infrared reflectance spectroscopy, *J. Geophys. Res.*, *110*, E12001, doi:10.1029/2005JE002534.

Poulet, F., J. -P. Bibring, J. F. Mustard, A. Gendrin, N. Mangold, Y. Langevin, R. E. Arvidson, B. Gondet, and the OMEGA team (2005), Phyllosilicates on Mars and implications for early martian climate, *Nature*, *438*, 623-627.

Ruff, S. W. (2003), Basaltic andesite or weathered basalt: A new assessment, *Sixth Intl. Conf. Mars*, abstract 3258.

Ruff, S. W., and P. R. Christensen (2007), Basaltic andesite, altered basalt, and a TES-based search for smectite clay minerals on Mars, *Geophys. Res. Lett.*, *34*, L10204, doi:10.1029/2007GL029602.

Ruff, S. W., P. R. Christensen, P. W. Barbera, D. L. Anderson (1997), Quantitative thermal emission spectroscopy of minerals: A technique for measurement and calibration. *J. Geophys. Res.* *102*, 14899-14913.

Salisbury, J. W. (1993), Mid-infrared spectroscopy: laboratory data, In *Remote Geochemical Analysis: Elemental and Mineralogical Composition*, edited by C. M. Pieters and P. A. J. Englert, pp. 79-98, Cambridge Univ. Press, New York.

Salisbury, F. B., A. Wald, D. M. D'Aria (1994), Thermal-infrared remote sensing and Kirchhoff's law 1. Laboratory measurements. *J. Geophys. Res.* *99* (B6), 11897-11911.

Sanchez-Soto, P. J., I. Sobrados, J. Sanz, and J. L. Perez-Rodriguez (1993), ^{29}Si and ^{27}Al magic-angle-spinning nuclear magnetic resonance study of the thermal transformations of pyrophyllite, *J. Am. Ceram. Soc.*, *76*, 3024-3028.

Schwenzer, S. P., and D. A. Kring (2009), Impact-generated hydrothermal systems capable of forming phyllosilicates on Noachian Mars, *Geology*, *37*, 1091-1094.

Viviano, C. E., J. E. Moersch (2011), Using THEMIS to address discrepancies between OMEGA/CRISM and TES detections of phyllosilicates. *Lunar Planet. Sci. XLII*, 2251 (abstract).

Chapter 2: Spectroscopic study of the dehydration and/or dehydroxylation of phyllosilicate and zeolite minerals

This chapter is a reformatted version of a paper by the same name published in Journal of Geophysical Research-Planets in 2011 by Congcong Che, Timothy D. Glotch, David L. Bish, Joseph R. Michalski, and Wenqian Xu. All laboratory measurements were performed by Congcong Che.

Che, C., T. D. Glotch, D. L. Bish, J. R. Michalski, and W. Xu (2011), Spectroscopic study of the dehydration and dehydroxylation of phyllosilicate and zeolite minerals, J. Geophys. Res., 116, E05007, doi:10.1029/2010JE003740.

Abstract Phyllosilicates on Mars mapped by infrared spectroscopic techniques could have been affected by dehydration and/or dehydroxylation associated with chemical weathering in hyper-arid conditions, volcanism or shock heating associated with meteor impact. The effects of heat-induced dehydration and/or dehydroxylation on the infrared spectra of fourteen phyllosilicates from four structural groups (kaolinite, smectite, sepiolite-palygorskite, and chlorite) and two natural zeolites are reported here. Pressed powders of size-separated phyllosilicate and natural zeolite samples were heated incrementally from 100 to 900 °C, cooled to room temperature, and measured using multiple spectroscopic techniques: mid-infrared (400-4000 cm⁻¹) attenuated total reflectance (ATR), mid-infrared reflectance (400-1400 cm⁻¹), and far-infrared reflectance (50-600 cm⁻¹) spectroscopies. Correlated thermogravimetric analysis (TGA) and X-ray diffraction (XRD) data were also acquired in order to clarify the thermal

transformation of each sample. For phyllosilicate samples, the OH stretching ($\sim 3600\text{ cm}^{-1}$), OH bending ($\sim 590\text{-}950\text{ cm}^{-1}$), and/or H₂O bending ($\sim 1630\text{ cm}^{-1}$) bands all become very weak or completely disappear upon heating to temperatures $>500\text{ }^{\circ}\text{C}$. The spectral changes associated with SiO₄ vibrations ($\sim 1000\text{ cm}^{-1}$ and $\sim 500\text{ cm}^{-1}$) show large variations depending on the compositions and structures of phyllosilicates. The thermal behavior of phyllosilicate IR spectra is also affected by the type of octahedral cations. For example, spectral features of Al³⁺-rich smectites are more stable than those of Fe³⁺-rich smectites. The high-temperature ($>800\text{ }^{\circ}\text{C}$) spectral changes of trioctahedral Mg²⁺-rich phyllosilicates such as hectorite, saponite, and sepiolite result primarily from crystallization of enstatite. Phyllosilicates with moderate Mg²⁺ concentration (e.g., palygorskite, clinochlore) and dioctahedral montmorillonites (e.g., SAz-1 and SCa-3) with partial Mg²⁺-for-Al³⁺ substitution all have new spectral feature developed at $\sim 900\text{ cm}^{-1}$ upon heating to $800\text{ }^{\circ}\text{C}$. Compared with phyllosilicates, spectral features of two natural zeolites, clinoptilolite and mordenite, are less affected by thermal treatments. Even after heating to $900\text{ }^{\circ}\text{C}$, the IR spectral features attributed to Si (Al)-O stretching and bending vibration modes do not show significant differences from those of unheated zeolites.

2.1. Introduction

Data from the Mars Express Observatoire pour la Minéralogie, l'Eau, les Glaces, et l'Activité (MEx/OMEGA) and Compact Reconnaissance Imaging Spectrometer for Mars (MRO/CRISM) visible and near infrared imaging spectrometers have shown phyllosilicates to be present on the Martian surface [Poulet *et al.*, 2005; Bibring *et al.*, 2006; Loizeau *et al.*, 2007; Mangold *et al.*, 2007]. The identification of phyllosilicates is based on the detection of $\sim 1.4\text{ }\mu\text{m}$ (the first

overtone of the O-H stretching modes), $\sim 1.9 \mu\text{m}$ (H-O-H band) and $\sim 2.15\text{-}2.4 \mu\text{m}$ (metal-OH bands) features. Phyllosilicates are detected in a number of contexts on Mars, primarily associated with ancient, layered terrain, deep clay deposits exposed in canyon walls or exhumed by impact craters, or remobilized units in the highlands corresponding to intracrater fans and deltas [Poulet *et al.*, 2005; Bibring *et al.*, 2006; Poulet *et al.*, 2007; Mustard *et al.*, 2008; Murchie *et al.*, 2009].

However, analysis of mid-IR region ($5\text{-}50 \mu\text{m}$) covered by Thermal Emission Spectrometer (TES) has not unambiguously detected phyllosilicates on the surface of Mars. The TES Surface Type 2 (ST2) was initially interpreted as a basaltic andesite [Bandfield *et al.*, 2000]. Later, Wyatt and McSween [2002] showed that weathered basaltic composition including clays could also produce an acceptable model fit. Still there is no definitive evidence in TES data showing that clay minerals dominate any particular geographic region of Mars or are globally distributed because it is difficult to distinguish phyllosilicates from other high silica phases in TES data at global scale [Bandfield, 2002; Ruff, 2003; Michalski *et al.*, 2005; Michalski *et al.*, 2006; Ruff and Christensen, 2007]. Recent studies show it can be possible to identify phyllosilicates at local scales: thermal emission spectra can be used to delineate phyllosilicate deposits from their long-wavelength spectra features [Ruff and Christensen, 2007; Michalski *et al.*, 2010]. However, in general TES spectra of the same deposits where OMEGA and CRISM delineate phyllosilicate occurrences do not show unambiguous evidence for these minerals. One reason for this disconnect could be that Martian phyllosilicates could have structures modified by postdepositional processes which would affect near infrared and thermal infrared spectral properties in different ways.

Phyllosilicates detected on the surface of Mars have been primarily dated as early-to-mid Noachian in age [Bibring *et al.*, 2005; Poulet *et al.*, 2005; Mustard *et al.*, 2007], which suggests phyllosilicates on Mars may have been altered by multiple processes (e.g. chemical weathering in hyper-arid conditions, volcanism or shock heating associated with meteor impact). Impact events may be one of the most important processes that affected phyllosilicates. It is possible that the phyllosilicates were repeatedly subjected to high temperatures resulting from impact processes and continuous exposure to high temperatures is likely to lead to the dehydration and/or dehydroxylation of phyllosilicates. Both their structural properties and spectral features could have been modified significantly by high temperature and pressure induced by impact shocking. Previous studies showed suggestive evidence of dehydrated and/or dehydroxylated phyllosilicates on Mars.

Mawrth Vallis has been studied by several authors because this region is potentially significant for understanding the different climatic and geologic environments of ancient Mars [Poulet *et al.*, 2005; Michalski and Noe Dobrea., 2007; Loizeau *et al.*, 2007; Bishop *et al.*, 2008a; Bishop *et al.*, 2009; Farrand *et al.*, 2009; Michalski and Fergason, 2009]. The distribution of phyllosilicates detected near Mawrth Vallis corresponds to the light-toned deposits in the surrounding Noachian plains [Loizeau *et al.*, 2007]. However, Loizeau *et al.* [2007] noticed a lack of phyllosilicates on a few bright outcrops near Mawrth Vallis. For example, they did not find any evidence showing the presence of phyllosilicates on a bright outcrop which was located on the west of Mawrth Vallis. Processes of dehydration and/or dehydroxylation were among the reasons they hypothesized to explain this observation. Michalski and Noe Dobrea [2007] also pointed out that all the phyllosilicates identified near Mawrth Vallis are associated with light-tone bedrock, but not all light-toned bedrock contains

phyllosilicates. *Milliken et al.* [2007] calculated and produced a hydration map for Mawrth Vallis region by examining the strength of the $\sim 3 \mu\text{m}$ absorption of OMEGA data. The estimated water content of the bright outcrop without phyllosilicate detection as described by *Loizeau et al.* [2007]'s work is significantly less than that of the bright outcrops mantled by phyllosilicates, but still higher than surrounding terrains with similar albedo values. This result is consistent with the possibility that the outcrop on the west of Mawrth Vallis is covered by dehydrated and/or dehydroxylated phyllosilicates.

A recent study by *Gavin and Chevrier* [2010] showed that near-infrared spectral features from the ejecta of Toro crater are more consistent with those of thermally treated nontronite. *Fairen et al.* [2010] calculated the maximum temperature increases in a transient crater and their model showed that temperatures can reach as high as $1000 \text{ }^\circ\text{C}$ in certain areas. Not only do meteoric impacts induce flash heating of the target, but they also deposit a significant amount of energy into the planetary surface that could lead to longer term heating of the target rocks. In the impact-induced hydrothermal systems modeled by *Abramov and Kring* [2005], they calculated that temperature as high as $1200 \text{ }^\circ\text{C}$ can last for tens of thousands of years. In the laboratory, temperatures as low as $500\text{-}700 \text{ }^\circ\text{C}$ are sufficient to cause the complete dehydration and/or dehydroxylation of most phyllosilicates within 24 hours [e.g. *Guggenheim and Koster van Groos*, 2001]. Examinations of meteorites by several authors suggested that shock heating plays a major role in the modification of phyllosilicates [*Ohnishi and Tomeoka*, 2002; *Tonui et al.*, 2003; *Tomeoka et al.*, 2007]. Relatively little work has been done to systematically analyze the effects of shock on phyllosilicates, though previous authors demonstrated that phyllosilicates (serpentine, nontronite) do in fact lose volatiles due to shock pressures and shock heating [*Boslough et al.* 1980; *Lange and Ahrens*, 1982]. In addition, serpentines that have not lost their

OH during shock appear to be more susceptible to dehydroxylation post-shock than their unshocked counterparts, as a result of increased disorder in their structures [Tyburcz and Ahrens, 1988]. Recent work on near infrared (NIR) spectroscopy of a shocked sample of nontronite revealed few spectral changes as a function of impactor velocity [Gavin and Chevrier, 2008], but this work did not provide details on the interpreted shock pressures or the amount of volatile loss. All of the previous work shows, however, that volatile loss in phyllosilicates occurs as a result of shock pressure. The combined effects of shock heating and shock pressure are difficult to analyze together in the laboratory. However, these effects can be analyzed independently, and the effects of heat-induced dehydration and/or dehydroxylation are analyzed here.

The objective of this study is to characterize the mid-to-far-IR spectral features of phyllosilicates from four groups (smectite, kaolinite, chlorite, and sepiolite-palygorskite) that have been heated to increasingly higher temperatures in order to gain insights into the crystal structures of phyllosilicates at different temperatures and to enable future identification of these types of minerals on Mars. A subsequent paper will examine the effect of dehydration and/or dehydroxylation on visible and near-IR (VNIR) reflectance spectra.

In addition to phyllosilicates, we also analyzed the spectral features of two natural zeolite minerals as a part of this study. Zeolites may be another important class of minerals that are present on the surface of Mars in a hydrated state [Bish *et al.*, 2003]. Ruff [2004] has provided some evidence of zeolites in martian surface dust using TES data and using CRISM near-infrared spectral data, Ehlmann *et al.* [2009] identified zeolites in craters west of Nili Fossae. Zeolites have chemical compositions similar to phyllosilicates and they are common hydrous alteration products of basaltic rocks. Therefore study of both phyllosilicates and zeolites can provide a

more comprehensive spectral feature library for dehydrated and/or dehydroxylated aluminosilicate minerals.

2.2 Background

2.2.1 Brief review of phyllosilicates and zeolite structures

The crystal structures of phyllosilicate minerals are well known and only basic information will be provided here in order to provide context for the spectroscopy results [*Farmer, 1974; Bailey, 1980; Moore and Reynolds Jr., 1989a*].

There are many kinds of phyllosilicates due to the possible structural and chemical variations within this mineral family, but most have the typical layer structures composed of two different kinds of sheets: tetrahedral sheets (T) and octahedral sheets. The dominant cation (normally Si^{4+} , Al^{3+} , or Fe^{3+}) in the tetrahedral sheet(s) is tetrahedrally coordinated to four oxygen anions and the corner-linked tetrahedra extend infinitely in two dimensions. Individual tetrahedral sheets have a composition of T_2O_5 , but the Si/O ratio varies from 0.3 to 0.4 as Si^{4+} cations are replaced by Al^{3+} or Fe^{3+} to various extents. The octahedral sheet can be described as a sheet of edge-linked octahedra, extending infinitely in the same two dimensions as the tetrahedral sheets. The octahedral cations are typically Al^{3+} , Mg^{2+} , Fe^{3+} , or Fe^{2+} , but most other transition elements (except Sc) and Li can occur in some minerals. Cations in the octahedral sheet are octahedrally coordinated to oxygens and hydroxyls. The tetrahedral sheets and octahedral sheet are linked

together by shared apical oxygens to form the layer structures. Unlike the tetrahedra, not all of octahedral sites must be filled by cations. The smallest structural unit contains three octahedra and the number of cations can vary between two and three, to meet the general requirement of a total positive charge of six for these three sites. For example, there could be 3 Mg^{2+} ions or 2 Al^{3+} ions in the octahedral sites. When three ions are present, the structure is called trioctahedral, and if only two of the three sites are occupied, it is called dioctahedral.

Phyllosilicates selected for this study can be divided into four groups according to their structural type: the kaolinite-serpentine group, smectite group, chlorite group, and sepiolite-palygorskite group. The kaolinite-serpentine group minerals are characterized by uncharged 1:1 (one octahedral sheet is linked to one tetrahedral sheet) layers, and they contain no cations or H_2O molecules in their interlayers. Minerals of the smectite group are all 2:1 (one octahedral sheet is linked to two tetrahedral sheets, one on each side) layers and they have interlayer cations to balance a negative charge on the 2:1 layers. They also typically contain H_2O molecules in their interlayer region. Both dioctahedral and trioctahedral smectite minerals are discussed here. Members of the chlorite group also have a negatively charged 2:1 layer structure, but they have positively charged $(\text{R}^{2+}, \text{R}^{3+})_3(\text{OH})_6$ octahedral sheets in the interlayers instead of large cations and H_2O molecules. Sepiolite and palygorskite (also known as attapulgite) also contain 2:1 layers in their structural units but they are different from other phyllosilicates. Sepiolite and palygorskite have similar ribbon-like morphologies and their octahedral and tetrahedral sheets are divided into ribbons by inversion, although the tetrahedral sheets are still linked. The alternating channels between ribbon strips are occupied by H_2O molecules and exchangeable cations.

Zeolites are microporous aluminosilicates and their structures have been summarized by *Breck* [1974a], *Barrer* [1978, 1982], *Newsam* [1986], and *Armbruster and Gunter* [2001]. Zeolites are composed of $(\text{SiO}_4)^{4-}$ and $(\text{AlO}_4)^{5-}$ tetrahedra that share oxygen atoms, and they have chemical compositions similar to phyllosilicates. However, compared with phyllosilicates characterized by layer structures, zeolites have a three-dimensionally linked crystal structure. The $(\text{SiO}_4)^{4-}$ and $(\text{AlO}_4)^{5-}$ tetrahedra are linked together to form a framework consisting of interconnected tunnels and cages. Ions of suitable size such as K^+ , Ca^{2+} , and Na^+ can enter into the extraframework sites in zeolites, and H_2O molecules can also exist inside the porous structures.

2.2.2 Previous studies of dehydration and/or dehydroxylation of phyllosilicates and zeolites

Many techniques have been used to analyze the dehydration and/or dehydroxylation behaviors of phyllosilicates in the past. Infrared (IR) spectroscopy, thermogravimetric analysis (TGA), X-ray diffraction (XRD) analysis, and nuclear magnetic resonance (NMR) spectroscopy are the most important of them.

TGA is the most direct tool to observe the temperature dependence of mineral mass. XRD is the most common technique used to study changes in crystal structure when a mineral is heated or exposed to different atmospheres [e.g. *Harris et al.*, 1992; *Aceman et al.*, 1997; *Sarikaya et al.*, 2000], and NMR spectroscopy can help to follow the changes in the coordination environments of H, Si, Al, and interlayer cations within phyllosilicates and zeolites caused by thermal treatment [e.g. *Frost and Barron*, 1984; *Fitzgerald et al.*, 1989, 1996; *Sanchez-Soto et al.*, 1993; *Carroll et al.*, 2005; *Roch et al.*, 1998; *Drachman et al.*, 1997; *Sanz et al.*, 1988; *Lambert et al.*, 1989; *Rocha and Klinowski*, 1990; *Slade and Davies*, 1991; *Massiot et al.*, 1995;

Rocha, 1999; *McManus et al.*, 2001; *He et al.*, 2003]. Of these, TGA and XRD analysis were utilized in this study to complement IR spectroscopy, and NMR will be used in the extension of this present work.

Grim and Kulbicki [1961] published IR transmission spectra of about forty montmorillonite-group samples after heating to 1400 °C. *Bruckenthal and Singer* [1987] suggested that dehydrated phyllosilicates may exist on Mars and several asteroids due to the anhydrous nature of the extraterrestrial environment. They reported the NIR reflectance (~0.5-4.5 µm) spectra of hydrated 1:1 and 2:1 layer phyllosilicates (including serpentine, talc, Ca-montmorillonite, and saponite) and their heating products (120, 160, 200, 250, 300, 400, 600, and 750 °C), in order to provide information for future spectroscopic observations of other planets. *Villieras et al.* [1994] used transmission infrared spectroscopy (400-4000 cm⁻¹) to study the thermal modifications of chlorite. Further infrared spectroscopic studies of dehydrated and/or dehydroxylated phyllosilicates developed gradually over the past ten years. *Kloprogge et al.* [1999; 2000; 2005] published a series of reports about emission (400-4000 cm⁻¹) analysis of dehydroxylated phyllosilicates including smectite group, kaolinite group, and chlorite group minerals. However, their technique was considered a transmission measurement according to the different definitions of radiance and emissivity [*Michalski et al.*, 2006]. *Milliken and Mustard* [2005] acquired reflectance spectra (1.3-5.0 µm) of five hydrated materials (including montmorillonite and clinoptilolite) at different temperatures in order to quantify the H₂O content of hydrated minerals. *Gavin and Chevrier* [2010] thermally treated nontronite and montmorillonite and used NIR (1.0-2.5 µm) reflectance spectra to characterize the structural changes occurring on heating. They showed that high-temperature (above 1000 °C) heating causes all NIR spectral features to disappear.

Most studies of the dehydration of natural zeolites have been based on thermogravimetric analysis (TGA), differential thermal analysis (DTA), and XRD measurements. The extraframework cation compositions [Bish, 1988], the energetics of the H₂O in the zeolite channels [Bish and Carey, 2001], the Si/Al ratio of a zeolite, and the ionic potential [Cruciani, 2006] all affect the thermal behavior of natural zeolites significantly. Relatively fewer results have been reported on the infrared spectroscopy of dehydrated natural zeolites. *Rodriguez-Fuentes et al.* [1998]'s work suggested that the IR spectral features (400-1700 cm⁻¹) of clinoptilolite and heulandite samples were most affected by their exchangeable cation composition and the history of thermal treatment. The dehydration processes of naturally occurring zeolites (including stilbite and mesolite) were investigated by *in situ* FTIR spectroscopy (400-8000 cm⁻¹) by *Prasad et al.* [2005, 2007], who reported the IR absorbance spectra of dehydrated natural zeolites.

2.2.3 The significance of this work

Although the dehydration and/or dehydroxylation behaviors of phyllosilicates and zeolites have been studied extensively in the past, there is no substantive work thoroughly describing the mid-to-far-IR spectral reflectance changes of these minerals upon heating. In the introduction section, we hypothesized that dehydrated and/or dehydroxylated phyllosilicates due to impact heating may remain on Mars. NIR spectra cannot identify these possible dehydrated and/or dehydroxylated phases because phyllosilicates show almost no spectral feature in near-IR region after they have been heated to high temperatures [Milliken and Mustard, 2005; Gavin and

Chevrier, 2010; Che et al., 2010]. Therefore it is very important to understand the effects of temperature on the mid-IR spectra of phyllosilicates.

In this study, we (1) report how the mid-IR ATR and mid-to- far-IR specular reflectance spectra of phyllosilicates and zeolites change with exposure to increasingly higher temperatures, All spectra presented in this manuscript will be made available online at "<http://aram.ess.sunysb.edu/tglotch/spectra.html>"; (2) discuss differences in spectral behaviors within and among groups of smectites, sepiolite-palygorskite, kaolinite, chlorites, and zeolites; (3) provide a reference database for future search of the possible existence of dehydrated and/or dehydroxylated phyllosilicates resulting from impact-induced high temperatures on the surface of Mars.

2.3 Methodology

2.3.1 Acquisition and preparation of samples

Fourteen phyllosilicate and two zeolite samples were selected for this study (**Table 2.1**). All samples were purchased from the Clay Minerals Society (CMS) Source Clays repository unless otherwise stated. In addition, two zeolite minerals, mordenite and clinoptilolite, were selected for analysis of their dehydration behavior. Chemical and structure compositions for these samples are summarized in **Table 2.2** and **Table 2.3**.

To facilitate precise characterization of our samples, a particle size separation method introduced by *Moore and Reynolds Jr.* [1989b] was performed on the phyllosilicates and zeolites in order to remove impurities that occur mostly in the $>2\ \mu\text{m}$ size fraction [*Moore and Reynolds Jr.*, 1989b]. As such, all samples described in this study were prepared to $<2\ \mu\text{m}$ size fractions prior to heat treatments. The phyllosilicates and zeolites were then heated under normal atmospheric conditions at 100, 200, 300, 400, 500, 600, 700, 800, and 900 °C. The heating duration for each temperature was 24 hours. All heated products were stored in a desiccator before spectral measurements.

2.3.2 Thermogravimetric analysis

Detailed thermal analysis results for most CMS Source Clay samples have been reported as a part the baseline studies of the source clays [*Guggenheim and Koster van Groos*, 2001]. We performed thermogravimetric analysis on all phyllosilicates and zeolites in order to provide a reference for the IR study of dehydration and dehydroxylation processes. However, it should be pointed out that TGA cannot be compared directly with the IR and XRD results of heated samples because the heating treatment of samples for TGA and other measurements were different. A Netzsch Simultaneous TG-DTA/DSC Apparatus Model STA 449C was used to measure TGA data for all size-separated samples, measuring from 20 °C to 1000 °C at a heating rate of $10\ \text{°C}\cdot\text{min}^{-1}$. An N_2 purge gas system was used to protect samples from atmospheric gases (H_2O and CO_2).

Table 2.1 Summary of phyllosilicates and zeolites for this study

Structural Group	Mineral	Sample Number	Source	Size Fraction
Kaolinite-serpentine group				
	kaolinite	KGa-1b	CMS	<2 μm
Smectite group				
	montmorillonite (“cheto”)	SAz-1	CMS	<2 μm
	montmorillonite (“Otay”)	SCa-3	CMS	<2 μm
	Ca-montmorillonite	STx-1	CMS	<2 μm
	Na-montmorillonite	SWy-2	CMS	<2 μm
	saponite	SapCa-2	CMS	<2 μm
	beidellite	SBCa-1	CMS	<2 μm
	mica-montmorillonite	Syn-1	CMS	<2 μm
	hectorite	SHCa-1	CMS	<2 μm
	nontronite	NAu-1	CMS	<2 μm
	nontronite	NAu-2	CMS	<2 μm
Chlorite group				
	clinochlore	Clinochlore	Mineral Unlimited	<2 μm
Sepiolite-palygorskite group				
	palygorskite (attapulgite)	PFI-1	CMS	<2 μm
	sepiolite	SepSp-1	CMS	<2 μm
Zeolite group				
	mordenite	27133	Mineral Research	<2 μm
	clinoptilolite	27031	Mineral Research	<2 μm

Table 2.2 Summary of major elemental composition

Sample number	SiO ₂	Al ₂ O ₃	Fe ₂ O ₃	FeO	TiO ₂	MgO	CaO	Na ₂ O	K ₂ O	P ₂ O ₅	OH/H ₂ O ¹
SAz-1 ²	51.36	17.20	1.54	n.a.	0.22	5.80	2.71	0.05	0.16	0.01	20.96
STx-1 ²	63.36	16.17	1.09	n.a.	0.24	3.43	1.57	0.28	0.06	0.01	13.78
SWy-2 ²	56.08	20.12	3.99	n.a.	0.08	2.68	1.08	1.34	0.18	0	14.45
SCa-3 ³	55.78	12.47	1.53	n.a.	n.a.	8.55	0.04	2.84	n.a.	n.a.	18.78
Syn-1 ²	47.70	36.75	0.11	n.a.	0.03	0.17	0.05	0.08	0	0	14.91
SBCa-1 ⁴	51.03	30.71	2.34	0.11	0.57	1.03	1.11	<0.01	0.79	0.12	12.17
SHCa-1 ²	46.11	0.85	0.32	n.a.	0.04	19.77	13.84	1.33	0.14	0	17.60
NAu-1 ⁵	41.55	6.59	29.07	n.a.	0.02	0.15	2.89	0.02	0.01	n.a.	19.70
NAu-2 ⁵	49.52	2.74	33.36	n.a.	0.02	0.23	2.06	0.12	0.01	n.a.	11.94
SapCa-2 ⁶	53.33	4.60	1.19	n.a.	0.09	24.49	1.30	1.19	0.19	n.a.	13.63
KGa-1b ⁷	43.98	38.22	0.20	n.a.	1.62	0.06	0.03	0.03	0.02	n.a.	15.84
SepSp-1 ⁸	55.00	1.40	0.40	0.02	0.04	22.38	1.07	<0.15	0.20	<0.05	19.29
PFI-1 ²	54.33	10.02	3.37	n.a.	0.43	9.52	1.70	0.05	0.78	0.83	18.97
Clinochlore ⁹	26.38	29.24	1.64	5.05	n.a.	25.36	n.a.	n.a.	n.a.	n.a.	12.34
27133 ¹⁰	67.06	15.51	n.a.	n.a.	n.a.	0.37	3.10	3.92	0.51	n.a.	12.58
27031 ¹¹	61.94	11.97	2.12	n.a.	0.23	1.61	0.91	4.02	1.54	n.a.	15.55

¹ OH/H₂O takes as total weight loss on ignition (after heating sample to 1000 °C);

² Mermur & Faz Cano [2001];

³ Van olphen & Fripiat [1979];

⁴ Unofficially reported by CMS: <http://www.clays.org/SOURCE%20CLAYS/SCdata.html>;

⁵ Keeling et al. [2000];

⁶ Post [1984];

⁷ Pruett & Webb [1993];

⁸ USGS Digital Spectral Library: <http://speclab.cr.usgs.gov/spectral.lib04/DESCRIPT/sepiolite.SepSp-1.html>;

⁹ Ballet et al. [1985];

¹⁰ <http://www.handbookofmineralogy.org/pdfs/mordenite.pdf>;

¹¹ Bish [1984]; n.a.=not analysed

Table 2.3 Summary of structural composition

Sample ID	Structural composition	Reference
SAz-1	$(Ca_{.39} Na_{.36} K_{.02})[Al_{2.71} Mg_{1.11} Fe(III)_{.12} Mn_{.01} Ti_{.03}][Si_{8.00}]O_{20}(OH)_4$	a
STx-1	$(Ca_{.27} Na_{.04} K_{.01})[Al_{2.41} Fe(III)_{.09} Mn_{tr} Mg_{.71} Ti_{.03}][Si_{8.00}]O_{20}(OH)_4$	a
SWy-2	$(Ca_{.12} Na_{.32} K_{.05})[Al_{3.01} Fe(III)_{.41} Mn_{.01} Mg_{.54} Ti_{.02}][Si_{7.98} Al_{.02}]O_{20}(OH)_4$	a
SCa-3	$(Mg_{.45} Ca_{.15} Na_{.26} K_{.01})[Al_{2.55} Fe(III)_{.12} Mn_{tr} Mg_{1.31} Ti_{.02}][Si_{7.81} Al_{.19}]O_{20}(OH)_4$	a
Syn-1	$(Mg_{.06} Ca_{.04} Na_{.12} K_{tr})[Al_{3.99} Fe(III)_{tr} Mn_{tr} Ti_{tr}][Si_{6.50} Al_{1.50}]O_{20}(OH)_4$	a
SBCa-1	$(Mg_{.3} Ca_{.16} K_{.15})[Al_{3.82} Fe(III)_{.18} Mn_{tr} Ti_{.06}][Si_{6.80} Al_{1.20}]O_{20}(OH)_4$	a
SHCa-1	$(Mg_{.56} Na_{.42} K_{.05})[Mg_{4.60} Li_{1.39} Mn_{tr} Ti_{.01}][Si_{7.75} Al_{1.17} Fe(III)_{.05}]O_{20}(OH)_4$	a
NAu-1	$(M^{+1.05})[Si_{6.98} Al_{1.02}][Al_{0.29} Fe_{3.68} Mg_{0.04}]O_{20}(OH)_4$	b
NAu-2	$(M^{+0.72})[Si_{7.55} Al_{0.45}][Fe_{3.83} Mg_{0.05}]O_{20}(OH)_4$	b
SapCa-2	$(Ca_{1.14} Na_{.79} K_{.07})[Mg_{5.98} Mn_{.01} Ti_{tr}][Si_{7.19} Al_{.74} Fe(III)_{.07}]O_{20}(OH)_4$	a
KGa-1b	$(Mg_{.02} Ca_{.01} Na_{.01} K_{.01})[Al_{3.86} Fe(III)_{.02} Mn_{tr} Ti_{.11}][Si_{3.83} Al_{.17}]O_{10}(OH)_8$	a
SepSp-1	$(K_{.01})[Mg_{5.54} Al_{.35} Mn_{.02} Fe(II)_{.04} Fe(III)_{.14}][Si_{7.90} Al_{.1}]O_{20}(OH)_4$	a
PFI-1	$(Mg_{.33} Ca_{.62} Na_{.04} K_{.13})[Al_{1.50} Fe(III)_{.52} Fe(II)_{.01} Mn_{.01} Mg_{1.91} Ti_{.06}][Si_{7.88} Al_{.22}]O_{20}(OH)_4$	a
Clinochlore	$[Si_{3.00} Al_{1.00}]\{Al_{0.96} Fe(II)_{0.48} Fe(III)_{0.14} Mg_{4.30}\}O_{10}(OH)_8$	c
27133	$(Na_{1.11} Ca_{0.48} K_{0.10} Mg_{0.08})Al_{2.16} Si_{9.80} O_{24} \cdot 5.86H_2O$	d
27031	$(Na_{1.80} Ca_{0.23} K_{0.45} Mg_{0.55} Ti_{0.04})Al_{3.25} Si_{14.28} O_{36} \cdot 11.07H_2O$	e

a. Unofficially reported by CMS: <http://www.clays.org/SOURCE%20CLAYS/SCdata.html>;

b. Keeling et al. [2000];

c. Ballet et al. [1985];

d. <http://www.handbookofmineralogy.org/pdfs/mordenite.pdf>;

e. Bish [1984].

2.3.3 Acquisition of powder XRD patterns

Powder XRD patterns were acquired for all phyllosilicates and zeolites and their heated products in order to confirm their mineralogy and to observe the crystal structural changes of phyllosilicates and zeolites upon heating. XRD data were measured using a Thermo ARL Scintag PAD-X automated powder diffractometer with Cu- $K\alpha$ radiation, collecting from 5° to $40^\circ 2\theta$ at a 0.6 degree/minute. Samples for XRD analysis were prepared using the smear-mount method with ground sample powders (<http://pubs.usgs.gov/of/2001/of01-041/html/docs/methods/xsslide.htm>).

2.3.4 Infrared spectroscopic measurements

Infrared specular reflectance and attenuated total reflectance (ATR) spectra were acquired at Stony Brook University in the Vibrational Spectroscopy Laboratory (VSL) using a Nicolet 6700 FTIR spectrometer.

Specular reflectance spectra. Specular reflectance peaks are generally referred to as “reststrahlen” features. These occur because the absorption coefficient of a vibrational band is so high that a mirror-like opacity is induced, resulting in strong reflectance from the smooth surface of the samples [Salisbury, 1993]. Mid-infrared ($400\text{-}1400\text{ cm}^{-1}$) and far-infrared specular reflectance ($100\text{-}600\text{ cm}^{-1}$) spectra were collected for all phyllosilicates and zeolites and their heated products. A gold-coated first surface mirror was used for the reflectance standard. Each sample was pressed in a Carver Hydraulic Press to create a pellet, 13mm in diameter and about 3mm in thickness. Spectra from $400\text{-}1400\text{ cm}^{-1}$ were acquired using a KBr beamsplitter and a thermoelectrically-cooled deuterated L-alanine doped tryglycine sulfate (DLATGS) detector with

a KBr window. For each sample, 256 scans in the mid-IR spectral range were recorded with a resolution of 4 cm^{-1} . Spectra from $100\text{-}600\text{ cm}^{-1}$ were acquired using a Thermo Fisher Solid Substrate beamsplitter and a DLaTGS detector with a polyethylene window. A total of 2048 scans and 4 cm^{-1} resolution were used for the far-IR spectral range. All specular reflectance measurements were collected using a Baseline FT-30 accessory with incidence and reflectance angles of 30° . A purge gas system was used to remove CO_2 and water vapor from the spectrometer.

Attenuated total reflectance. ATR measurements in the mid-IR ($400\text{-}4000\text{ cm}^{-1}$) range were acquired a Nicolet 6700 FTIR spectrometer equipped with a Smart Orbit single bounce ATR accessory with a type II A diamond ATR element which has high refractive index. When IR source radiation enters the ATR element, a total internal reflection occurs and an evanescent wave is formed at the boundary between ATR element and sample. ATR spectra were acquired from unprepared samples rather than pressed pellets because no sample preparation is needed for ATR measurement. The sampling surface is pressed into intimate optical contact with the top surface of ATR crystal and the resulting evanescent wave penetrates only a few microns into the sample. ATR standard was a spectrum with no sample on the ATR element. The resultant spectrum has the similar peak positions to an equivalent absorbance IR spectrum. Because of ATR's easy sample preparation and effectiveness with small grain size, ATR has been considered a potential *in situ* IR technique for future planetary explorations [Chemtob and Glotch, 2007].

2.4 Results and interpretations

2.4.1 Kaolinite-serpentine group

2.4.1.1 Attenuated total reflectance spectra

The ATR spectra of thermally treated KGa-1b kaolinite samples are shown in **Figure 2.1a**. OH-stretching vibration bands were observed at ~ 3620 , 3650 , 3660 , and 3680 cm^{-1} [Farmer, 1974] for samples heated from 100 - $400\text{ }^{\circ}\text{C}$. Dehydroxylation was evidenced by a decrease in intensities of OH-stretching vibration bands at $400\text{ }^{\circ}\text{C}$ and the disappearance of these bands at $500\text{ }^{\circ}\text{C}$. Corresponding to the changes in the 3650 cm^{-1} band, the OH-deformation bands at ~ 910 and $\sim 930\text{ cm}^{-1}$ [Madejova' and Komadel, 2001] became weaker at $400\text{ }^{\circ}\text{C}$ and disappeared at $500\text{ }^{\circ}\text{C}$. The characteristic Si-O stretching vibration bands around 1100 , 1020 , and 990 cm^{-1} [Madejova' and Komadel, 2001] disappeared at $500\text{ }^{\circ}\text{C}$ and a new peak at $\sim 1050\text{ cm}^{-1}$ formed after the dehydroxylation process was complete. Characteristic Si-O-Si bending vibrations occurring near 400 - 550 cm^{-1} [Bishop et al., 2008b] began to change significantly at $400\text{ }^{\circ}\text{C}$ and completely disappeared when the sample was heated to $500\text{ }^{\circ}\text{C}$. The relatively weak spectral features near 640 - 800 cm^{-1} were assigned to Si-O bands [Madejova' and Komadel, 2001], which also changed distinctly upon heating to $400\text{ }^{\circ}\text{C}$.

2.4.1.2 Specular reflectance spectra

The effects of dehydroxylation on the KGa-1b kaolinite reflectance spectra (**Figures 2.1b**) were similar to those exhibited in ATR spectra. In both cases, the original spectral features of KGa-1b kaolinite were lost at $400\text{ }^{\circ}\text{C}$, and spectral features from dehydroxylated KGa-1b kaolinite were relatively stable from $500\text{ }^{\circ}\text{C}$ to $900\text{ }^{\circ}\text{C}$. Spectral features in the specular reflectance data belonging to the original sample all disappeared at $400\text{ }^{\circ}\text{C}$, but the $400\text{ }^{\circ}\text{C}$ ATR spectrum of KGa-1b kaolinite retained decreased original spectral feature at $\sim 525\text{ cm}^{-1}$.

Upon heating to 400 °C, the SiO₄ stretching vibrations occurring at ~1010, ~1060, and ~1130 cm⁻¹ [Bishop *et al.*, 2008b] disappeared and were replaced by a new band around 1100 cm⁻¹. This new feature continued to shift toward higher wavenumbers upon heating (1076 cm⁻¹ at 400 °C and 1109 cm⁻¹ at 900 °C). Other significant changes in the mid-IR region (>400 cm⁻¹) included the disappearance of the OH deformation vibration bands at ~938 cm⁻¹ and 908 cm⁻¹ [Bishop *et al.*, 2008b] and Si-O bending vibration bands in the range 400-560 cm⁻¹ [Bishop *et al.*, 2008b] at 400 °C. A new spectral feature appeared in the Si-O bending region at 400 °C and this new peak gradually shifted to higher wavenumbers (440 cm⁻¹ at 400 °C and 460 cm⁻¹ at 900 °C) upon heating. In the far-IR region (<400 cm⁻¹), reflectance peaks occurring at 190, 271, and 345 cm⁻¹ were assigned to mixed vibrations which included the Si-O network, octahedral cations, and hydroxyl groups [Farmer, 1974]. As with some spectral features described in the mid-IR region, the bands disappeared at 400 °C and no new peaks formed at higher temperatures.

2.4.1.3 Thermogravimetric and X-ray diffraction analysis

TGA and XRD revealed similar behavior to IR spectroscopy for the dehydroxylation process in kaolinite. TGA data for kaolinite (**Figure 2.1c**) showed only one significant weight loss from 400 °C to 600 °C, associated with the loss of hydroxyl groups. The XRD pattern of kaolinite (Figure 1c) at 500 °C showed that the 001 peak disappeared, indicating that the layer structure of kaolinite has been destroyed by 500 °C. TGA data for this corresponding temperature range showed a 15 wt% loss due to evolution of H₂O from OH groups.

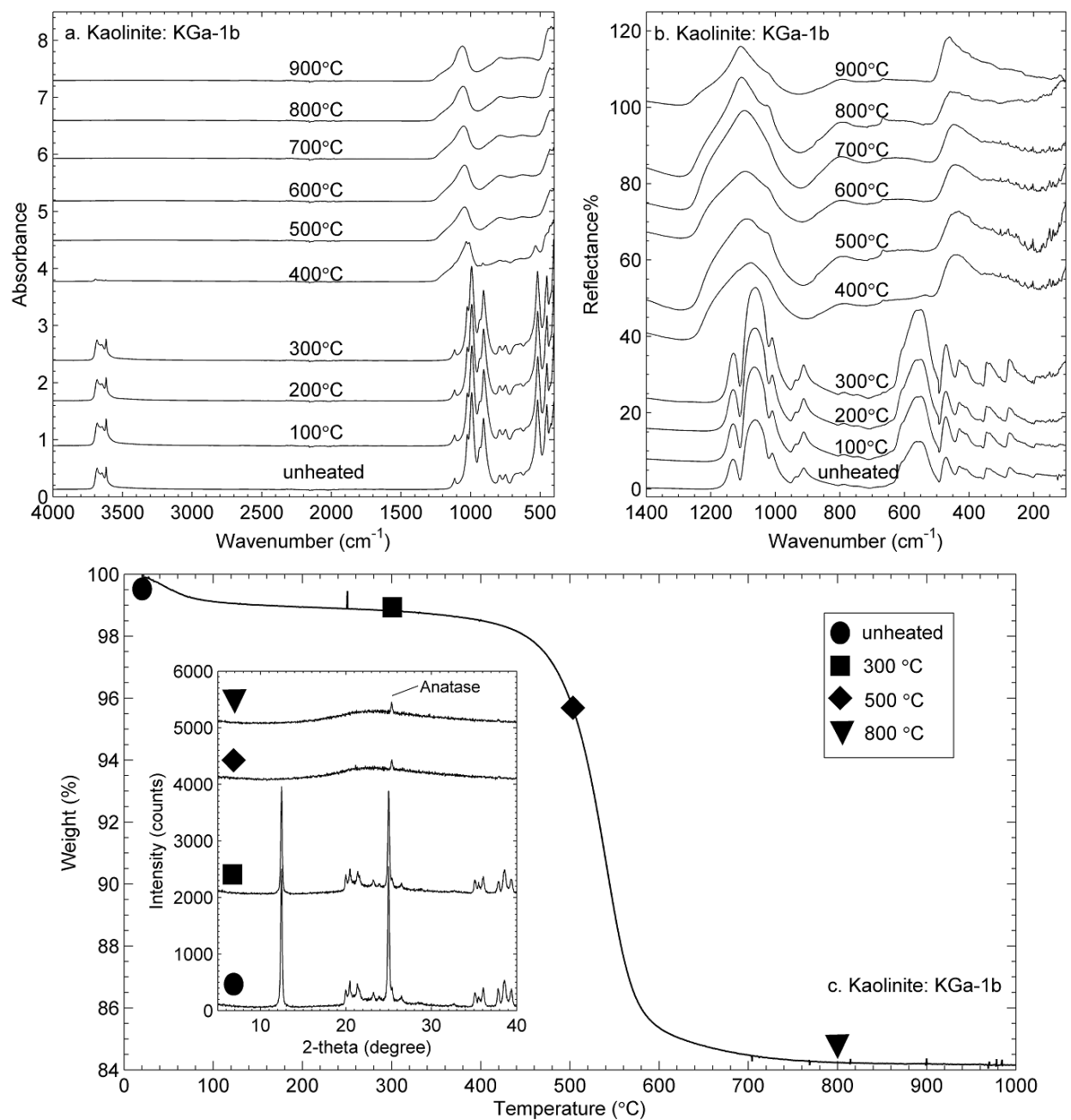


FIG. 2.1 (a) 400-4000 cm^{-1} ATR spectra of kaolinite (KGa-1b) calcined at various temperatures. (b) 100-1500 cm^{-1} specular reflectance spectra of kaolinite (KGa-1b) calcined at various temperatures. Linear vertical offset is applied to the spectra for clarity. (c) TGA plots and X-ray diffraction profiles (offset) of KGa-1b kaolinite.

2.4.2 Smectite group

2.4.2.1 Montmorillonite

Four montmorillonite samples of various origins and compositions are discussed in this section. A fifth sample, Syn-1 mica-montmorillonite is discussed later. Although Syn-1 is listed by the Clay Minerals Society as a synthetic mica-montmorillonite, previous study [Kloprogge *et al.*, 1999a] indicates that both its chemical composition and spectral features are close to those for beidellite. Therefore, data for Syn-1 will be discussed with the beidellite sample SBCa-1.

2.4.2.1.1 Attenuated total reflectance spectra

SAz-1 "Cheto" montmorillonite Dehydroxylation of SAz-1 montmorillonite, evidenced by disappearance of its Al-Al-OH deformation band (912 cm^{-1}), Al-Mg-OH deformation band (837 cm^{-1}), and OH stretching bands (3610 cm^{-1} , 3398 cm^{-1}) [Madejov *a'* and Komadel, 2001], occurred at $500\text{ }^{\circ}\text{C}$ (**Figure 2.2a**). The $500\text{ }^{\circ}\text{C}$ spectrum of SAz-1 retained a weak 1631 cm^{-1} H-O-H bending band but this feature disappeared in the $600\text{ }^{\circ}\text{C}$ spectrum. Over the same temperature range the 509 cm^{-1} Al-O-Si deformation band [Madejov *a'* and Komadel, 2001] disappeared. Beginning at a temperature of $500\text{ }^{\circ}\text{C}$, the Si-O stretching band at 972 cm^{-1} became broad and was eventually replaced by two bands at 922 cm^{-1} and 1059 cm^{-1} above $700\text{ }^{\circ}\text{C}$.

Another Si-O stretching band (longitudinal mode) at $\sim 1126 \text{ cm}^{-1}$ [Madejov a' and Komadel, 2001] was relatively stable but it disappeared at $800 \text{ }^\circ\text{C}$. An additional new strong feature began to develop at $\sim 780 \text{ cm}^{-1}$ when SAz-1 montmorillonite was heated to $800 \text{ }^\circ\text{C}$.

SCa-3 Montmorillonite (Otay) The SCa-3 montmorillonite showed similar spectral behavior to SAz-1 montmorillonite (**Figure 2.2b**). The OH-stretching bands ($\sim 3610 \text{ cm}^{-1}$ and $\sim 3398 \text{ cm}^{-1}$) disappeared at $600 \text{ }^\circ\text{C}$ and the H-O-H bending band ($\sim 1630 \text{ cm}^{-1}$) disappeared at $700 \text{ }^\circ\text{C}$. The Al-Al-OH deformation band, Al-Mg-OH deformation band, and Al-O-Si deformation band ($\sim 910 \text{ cm}^{-1}$, $\sim 830 \text{ cm}^{-1}$, and $\sim 505 \text{ cm}^{-1}$, respectively) disappeared at $500 \text{ }^\circ\text{C}$. The Si-O stretching band ($\sim 970 \text{ cm}^{-1}$) broadened and was replaced by two bands ($\sim 1050 \text{ cm}^{-1}$ and $\sim 920 \text{ cm}^{-1}$) at $700 \text{ }^\circ\text{C}$. The Si-O stretching band (longitudinal mode) gradually shifted to higher wavenumbers ($\sim 1109 \text{ cm}^{-1}$ at room temperature to $\sim 1138 \text{ cm}^{-1}$ at $700 \text{ }^\circ\text{C}$) and it disappeared at $800 \text{ }^\circ\text{C}$. Finally, a new spectral feature at $\sim 780 \text{ cm}^{-1}$ formed at $800 \text{ }^\circ\text{C}$.

STx-1 Texas Montmorillonite Most OH groups were removed from the STx-1 structure by $500 \text{ }^\circ\text{C}$, evidenced by disappearance of the Al-Mg-OH deformation ($\sim 842 \text{ cm}^{-1}$), Al-Al-OH deformation ($\sim 914 \text{ cm}^{-1}$), and OH stretching (3624 cm^{-1} and 3340 cm^{-1}) bands (**Figure 2.2c**). The 515 cm^{-1} Al-O-Si deformation band disappeared at $500 \text{ }^\circ\text{C}$, and a new band at $\sim 567 \text{ cm}^{-1}$ began to develop at $600 \text{ }^\circ\text{C}$ and disappeared at $800 \text{ }^\circ\text{C}$. The Si-O stretching band experienced a distinct shift toward higher frequencies at $500 \text{ }^\circ\text{C}$ heating ($\sim 993 \text{ cm}^{-1}$ at room temperature, $\sim 1074 \text{ cm}^{-1}$ at $900 \text{ }^\circ\text{C}$) and the weak Si-O stretching (longitudinal mode) band at $\sim 1126 \text{ cm}^{-1}$ disappeared after $800 \text{ }^\circ\text{C}$ heating. The spectral feature at $\sim 792 \text{ cm}^{-1}$ was assigned to Si-O stretching of cristobalite [Madejov a' and Komadel, 2001] and it showed no changes on heating.

SWy-2 Na-Montmorillonite (Wyoming) The OH-stretching ($\sim 3624\text{ cm}^{-1}$, $\sim 3390\text{ cm}^{-1}$), Al-Al-OH deformation ($\sim 914\text{ cm}^{-1}$), and Al-Fe-OH deformation ($\sim 881\text{ cm}^{-1}$) bands disappeared at $600\text{ }^{\circ}\text{C}$, indicating the loss of OH groups (**Figure 2.2d**). Upon heating to $800\text{ }^{\circ}\text{C}$, the 989 cm^{-1} Si-O stretching band of SWy-2 montmorillonite shifted to higher frequencies, to $\sim 1065\text{ cm}^{-1}$ at $900\text{ }^{\circ}\text{C}$. The 1117 cm^{-1} Si-O stretching (longitudinal mode) band became weaker with an increase in temperature and it disappeared above $800\text{ }^{\circ}\text{C}$. The 513 cm^{-1} Al-O-Si deformation band disappeared at $600\text{ }^{\circ}\text{C}$ and a new peak at $\sim 561\text{ cm}^{-1}$ began to grow at this temperature. This new peak disappeared at $800\text{ }^{\circ}\text{C}$. The 777 cm^{-1} and 796 cm^{-1} bands were assigned to Si-O stretching modes of quartz admixture [*Madejov a' and Komadel, 2001*], and were not affected by the heating treatment.

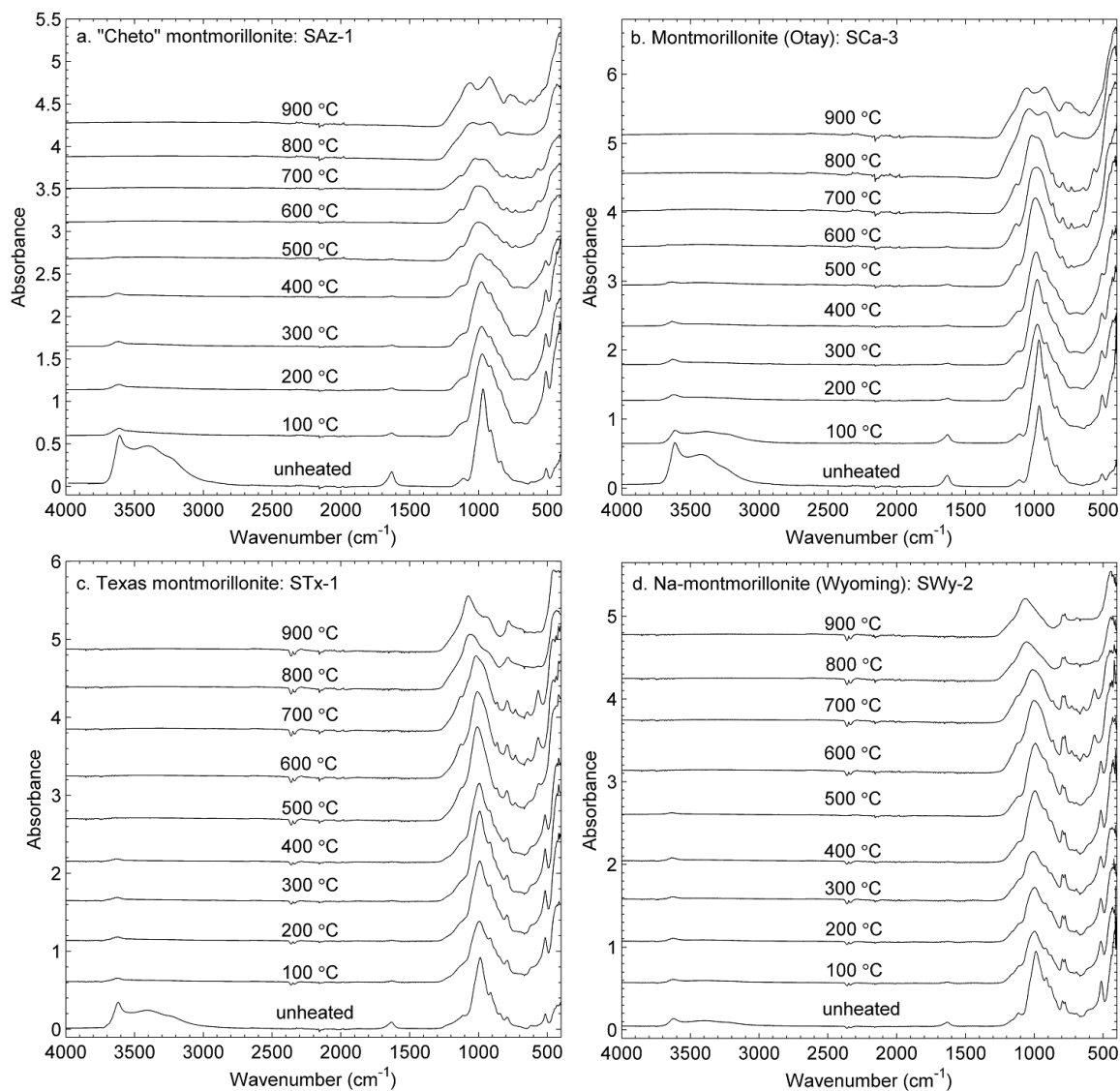


FIG. 2.2 400-4000 cm^{-1} ATR spectra of (a) “Cheto” montmorillonite (SAz-1), (b) montmorillonite (Otay) (SCa-3), (c) Texas montmorillonite (STx-1), and (d) Na-montmorillonite (Wyoming) (SWy-2) calcined at various temperatures. Linear vertical offset is applied to the spectra for clarity.

2.4.2.1.2 Specular reflectance spectra

SAz-1 "Cheto" montmorillonite and SCa-3 Montmorillonite (Otay) SAz-1 and SCa-3 montmorillonites had similar reflectance spectral behaviors when they were heated (**Figure 2.3a, 2.3b**), and three stages of spectral change were observed. There was no distinct spectral change from 100 °C to 400 °C, although the spectra showed minor increases in intensity and high-frequency shifting of the Si-O stretching (longitudinal mode) band (1117 cm⁻¹ to 1140 cm⁻¹ for SAz-1, 1114 cm⁻¹ to 1138 cm⁻¹ for SCa-3). From 500 °C to 700 °C, the Si-O stretching region was dominated by two broad peaks (~1153 cm⁻¹ and ~1061 cm⁻¹ for SAz-1, ~1149 cm⁻¹ and ~1057 cm⁻¹ for SCa-3). The Si-O bending region showed more significant changes than the Si-O stretching region over this temperature range. The original doublet feature at ~500 cm⁻¹ was completely lost and was replaced by a strong band with complex shoulder spectral features (~486 cm⁻¹ for SAz-1, ~487 cm⁻¹ for SCa-3). The original 327 cm⁻¹ spectral feature in the far-IR region disappeared and a new peak formed at ~302 cm⁻¹ for both SAz-1 and SCa-3 samples. After heating to 800 °C and 900 °C, multiple spectral features for SAz-1 and SCa-3 combined to form a single strong peak for both Si-O stretching and bending regions. A new strong band (~933 cm⁻¹ for SAz-1, ~927 cm⁻¹ for SCa-3) also developed in this temperature range.

STx-1 Texas Montmorillonite The reflectance spectra of STx-1 montmorillonite and its heating products are displayed in **Figure 2.3c**. The 500 °C heat treatment produced significant spectral changes. The doublet feature at ~500 cm⁻¹ caused by Si-O bending modes and the ~330 cm⁻¹ peak in the far-IR region disappeared. Two bands at ~1100 cm⁻¹ due to Si-O stretching vibrations shifted away from each other, and new spectral features caused by heating were observed at ~565 cm⁻¹, ~484 cm⁻¹, and 302 cm⁻¹. Upon heating to 800 °C, all new spectral features formed at

lower temperatures disappeared, and two strong reflectance bands at $\sim 1105\text{ cm}^{-1}$ and $\sim 470\text{ cm}^{-1}$ dominated the mid-IR and far-IR regions of the STx-1 montmorillonite spectra.

SWy-2 Na-Montmorillonite (Wyoming) In the case of the Swy-2 montmorillonite, two spectral features associated with Si-O stretching around 1070 cm^{-1} and 1130 cm^{-1} broadened and shifted away from each other at $600\text{ }^{\circ}\text{C}$ and they were replaced by a band near 1107 cm^{-1} (**Figure 2.3d**) at $800\text{ }^{\circ}\text{C}$. A new shoulder feature near 1130 cm^{-1} formed at $200\text{ }^{\circ}\text{C}$ and disappeared at $500\text{ }^{\circ}\text{C}$. New reflectance peaks at $\sim 568\text{ cm}^{-1}$ and $\sim 484\text{ cm}^{-1}$ appeared at $600\text{ }^{\circ}\text{C}$ and the Al-O-Si deformation ($\sim 534\text{ cm}^{-1}$) and Si-O-Si deformation (474 cm^{-1}) bands disappeared completely at this temperature. However, these new peaks disappeared at $800\text{ }^{\circ}\text{C}$ and a new strong reflectance band appeared at $\sim 462\text{ cm}^{-1}$. Distinct spectral changes also occur at $600\text{ }^{\circ}\text{C}$ and $800\text{ }^{\circ}\text{C}$ in the far-IR region ($<400\text{ cm}^{-1}$), evidenced by disappearance of the original 335 cm^{-1} feature and formation of a new 302 cm^{-1} band at $600\text{ }^{\circ}\text{C}$. All of these spectral features disappeared at $800\text{ }^{\circ}\text{C}$. Spectral features at 775 cm^{-1} , 795 cm^{-1} , 393 cm^{-1} , and 366 cm^{-1} are related to quartz admixture [*Madejov a' and Komadel, 2001*] and they persisted through the dehydration and dehydroxylation of SWy-2 montmorillonite.

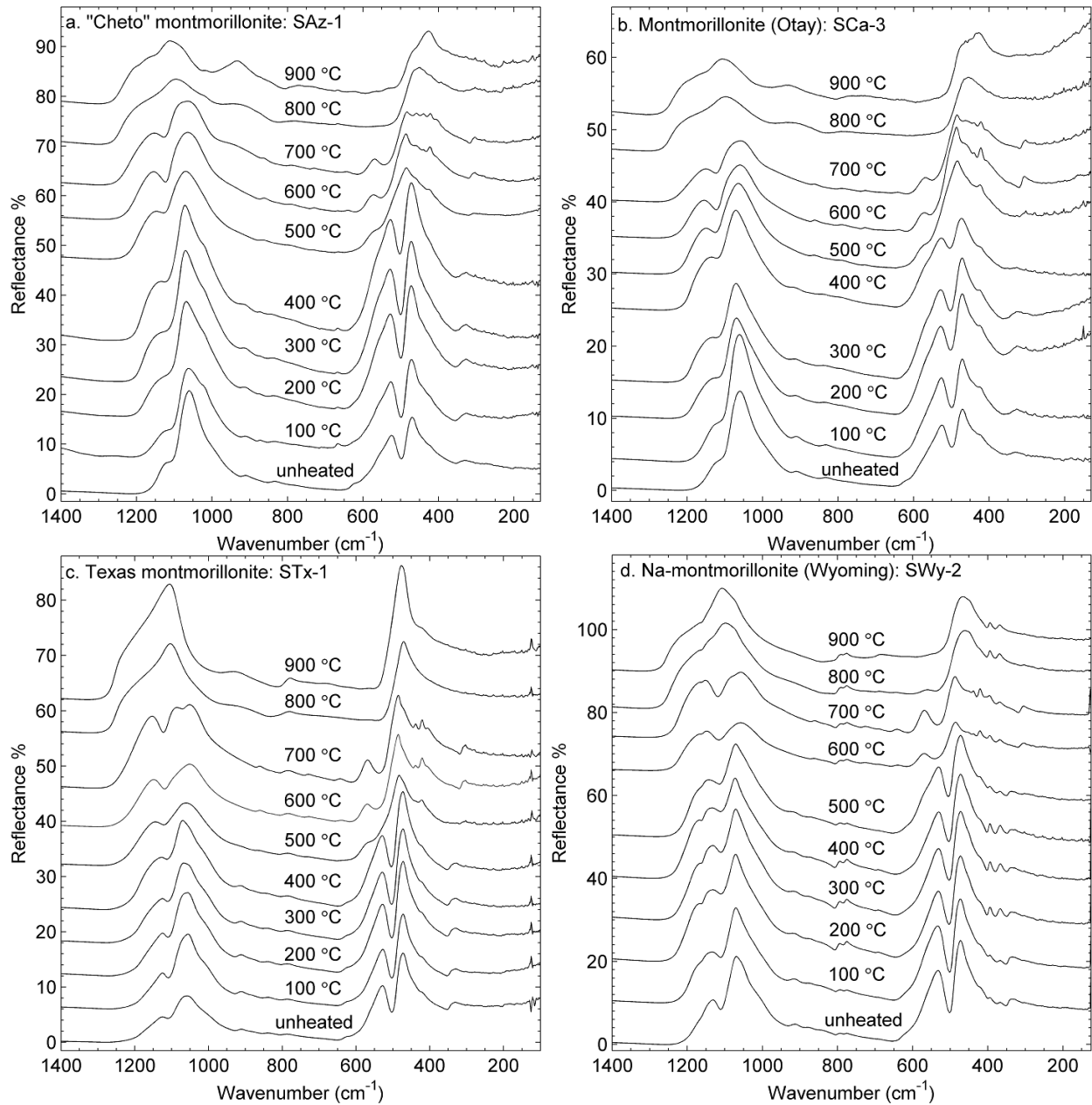


FIG. 2.3 (a) 130-1400 cm^{-1} specular reflectance spectra of “Cheto” montmorillonite (SAz-1) calcined at various temperatures. (b) 130-1400 cm^{-1} specular reflectance spectra of montmorillonite (Otay) (SCa-3) calcined at various temperatures. (c) 100-1400 cm^{-1} specular reflectance spectra of Texas montmorillonite (STx-1) calcined at various temperatures. (d) 125-1400 cm^{-1} specular reflectance spectra of montmorillonite (Wyoming) (SWy-2) calcined at various temperatures. Linear vertical offset is applied to the spectra for clarity.

2.4.2.1.3 Thermogravimetric and X-ray diffraction analysis

SAz-1 “Cheto” montmorillonite and SCa-3 montmorillonite (Otay) have similar thermal behaviors, related to their identical structures and similar chemical compositions [*Grim and Kulbicki*, 1961]. Two distinct changes in the TGA curves (**Figures 2.4a, 2.4b**) were observed for both montmorillonites, consistent with the fact that they contain both molecular H₂O and hydroxyl groups in their structures. The dehydration processes, as evidenced by abrupt weight losses at ~100-200 °C, indicate that both samples began to lose H₂O rapidly from the beginning of heat treatment. Both montmorillonites began to lose their structural OH groups gradually from 600 to 700 °C. XRD data showed that these two montmorillonites retained their original 001 reflection positions at 300 °C, and the TGA results indicated that most of their interlayer H₂O molecules were lost by 200 °C. The reason may be related to the details of our experimental process for both phyllosilicates and zeolites as heated samples were not protected from rehydration during XRD measurements [e.g. *Gavin and Chevrier*, 2010]. The XRD results showed that these two montmorillonites were capable of reabsorbing H₂O from the air after heating to 300 °C. The d-spacing of the 001 reflections decreased at 500 °C showing structural collapse, and at 800 °C the 001 reflections disappeared, indicating that the layer structures of SAz-1 and SCa-3 montmorillonites had been destroyed.

STx-1 montmorillonite (**Figure 2.4c**) has a lower overall content (~14%) of OH and H₂O (Table 2.2) in its structure than SAz-1 (~21%) and SCa-3 (~19%), due primarily to differences in

exchangeable-cation composition. The STx-1 montmorillonite dehydroxylated more rapidly at higher temperatures (~700 °C) than the other two montmorillonites (~650 °C). Otherwise, the dehydration and dehydroxylation processes of STx-1 montmorillonite manifested in TGA and XRD results (Figure 2.4c) are similar to those of SAz-1 and SCa-3 montmorillonites.

SWy-2 montmorillonite is the most stable among the four montmorillonites examined here. The 001 reflection of SWy-2 remained as a weak peak at 800 °C (**Figure 2.4d**), indicating that dehydroxylation at this point was incomplete.

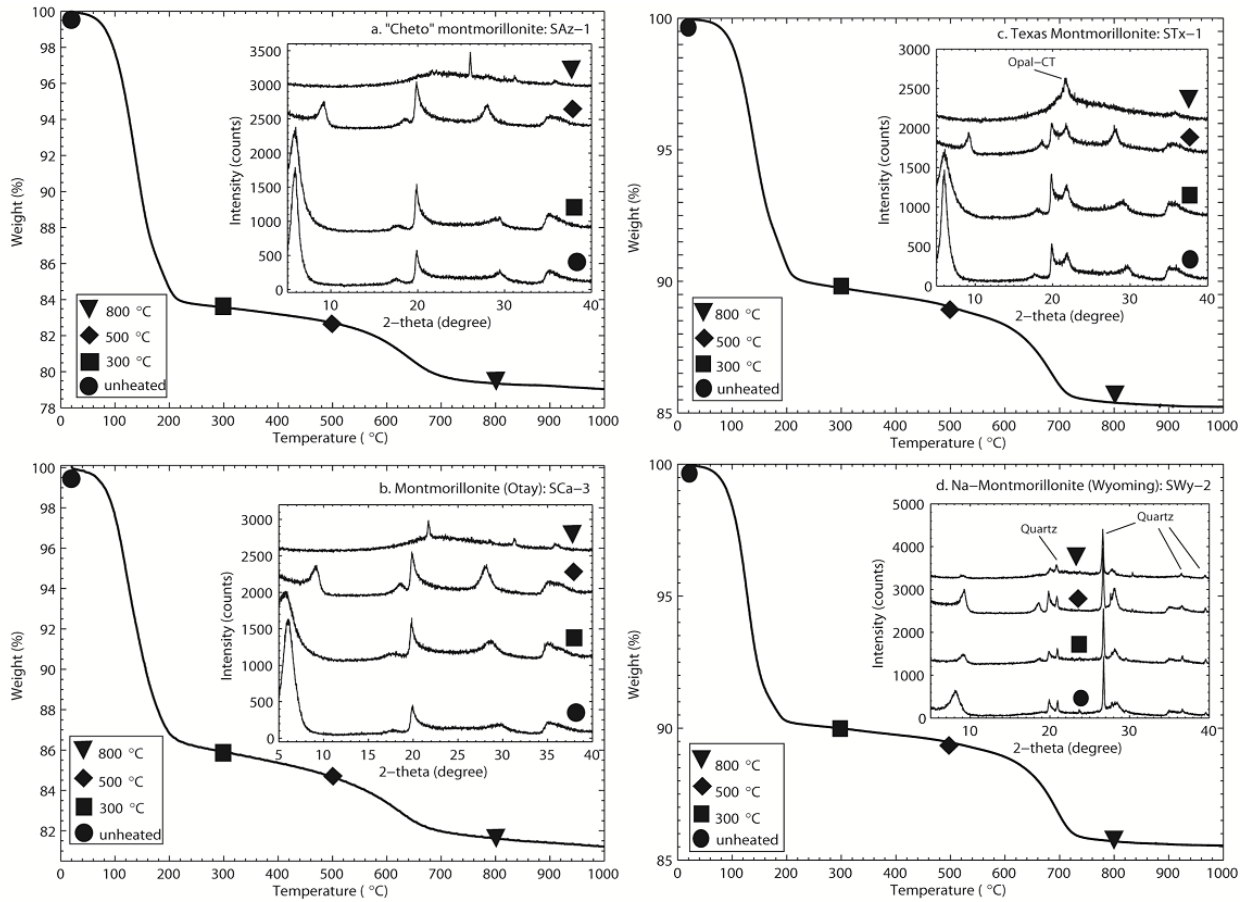


FIG. 2.4 TGA plots and X-ray diffraction profiles (offset) of (a) SAz-1 “Cheto” montmorillonite, (b) SCA-3 montmorillonite (Otay), (c) STx-1 Texas montmorillonite and (d) SWy-2 Na-montmorillonite (Wyoming).

2.4.2.2 Saponite (SapCa-2)

2.4.2.2.1 Attenuated total reflectance spectra

The spectral features at $\sim 3678\text{ cm}^{-1}$, $\sim 3625\text{ cm}^{-1}$, and $\sim 3410\text{ cm}^{-1}$ were assigned to Mg-O-H stretching, Al-O-H stretching, and H-O-H stretching modes, respectively [Van der Marel *et al.*, 1976]. The Al-O-H stretching and H-O-H stretching bands disappeared at $200\text{ }^{\circ}\text{C}$ but the Mg-O-H stretching feature persisted to $700\text{ }^{\circ}\text{C}$ (**Figure 2.5a**), indicating that most of the OH groups in the saponite structure were lost around $700\text{ }^{\circ}\text{C}$. Correspondingly, the Mg-OH libration band at $\sim 650\text{ cm}^{-1}$ [Van der Marel *et al.*, 1976] was observed only to $700\text{ }^{\circ}\text{C}$. The H₂O bending band near 1630 cm^{-1} disappeared at $600\text{ }^{\circ}\text{C}$. No distinct change occurred for Si-O stretching bands ($\sim 1080\text{ cm}^{-1}$ and $\sim 950\text{ cm}^{-1}$) until $700\text{ }^{\circ}\text{C}$. Upon heating to $800\text{ }^{\circ}\text{C}$, the original Si-O stretching bands disappeared and were replaced by multiple spectral features between $850\text{-}1200\text{ cm}^{-1}$, and similar changes were seen between 600 cm^{-1} and 750 cm^{-1} at this temperature.

2.4.2.2.2 Specular reflectance spectra

Similar to the ATR spectra for SapCa-2 saponite, the reflectance spectra did not show any distinct change until $700\text{ }^{\circ}\text{C}$ (**Figure 2.5b**), although the intensity of the weak Si-O stretching band at $\sim 1115\text{ cm}^{-1}$ increased gradually with temperature. The $800\text{ }^{\circ}\text{C}$ and $900\text{ }^{\circ}\text{C}$ reflectance spectra of saponite exhibited completely different features from those at $700\text{ }^{\circ}\text{C}$. Spectral ranges from 800 cm^{-1} to 1200 cm^{-1} and from 200 cm^{-1} to 600 cm^{-1} were both dominated by complex multiple bands at $800\text{ }^{\circ}\text{C}$ and $900\text{ }^{\circ}\text{C}$.

2.4.2.2.3 Thermogravimetric and X-ray diffraction analysis

TGA data (**Figure 2.5c**) for SapCa-2 saponite showed that most interlayer H₂O molecules were lost below 150 °C, whereupon saponite remained relatively stable until 800 °C. From 800 °C to 850 °C, a significant weight loss was observed, associated with dehydroxylation of saponite. XRD data (**Figure 2.5c**) show that the layer structure of saponite was not affected distinctly until ~500 °C. Above this temperature, a new well-crystallized phase was formed at 800 °C, just before the onset of the dehydroxylation process as evidenced by TGA data. This high-temperature phase of saponite has been determined by previous studies and confirmed in this study [e.g. *Kulbicki*, 1959] to be enstatite (MgSiO₃), which accounts for the nature of the high-temperature spectral data.

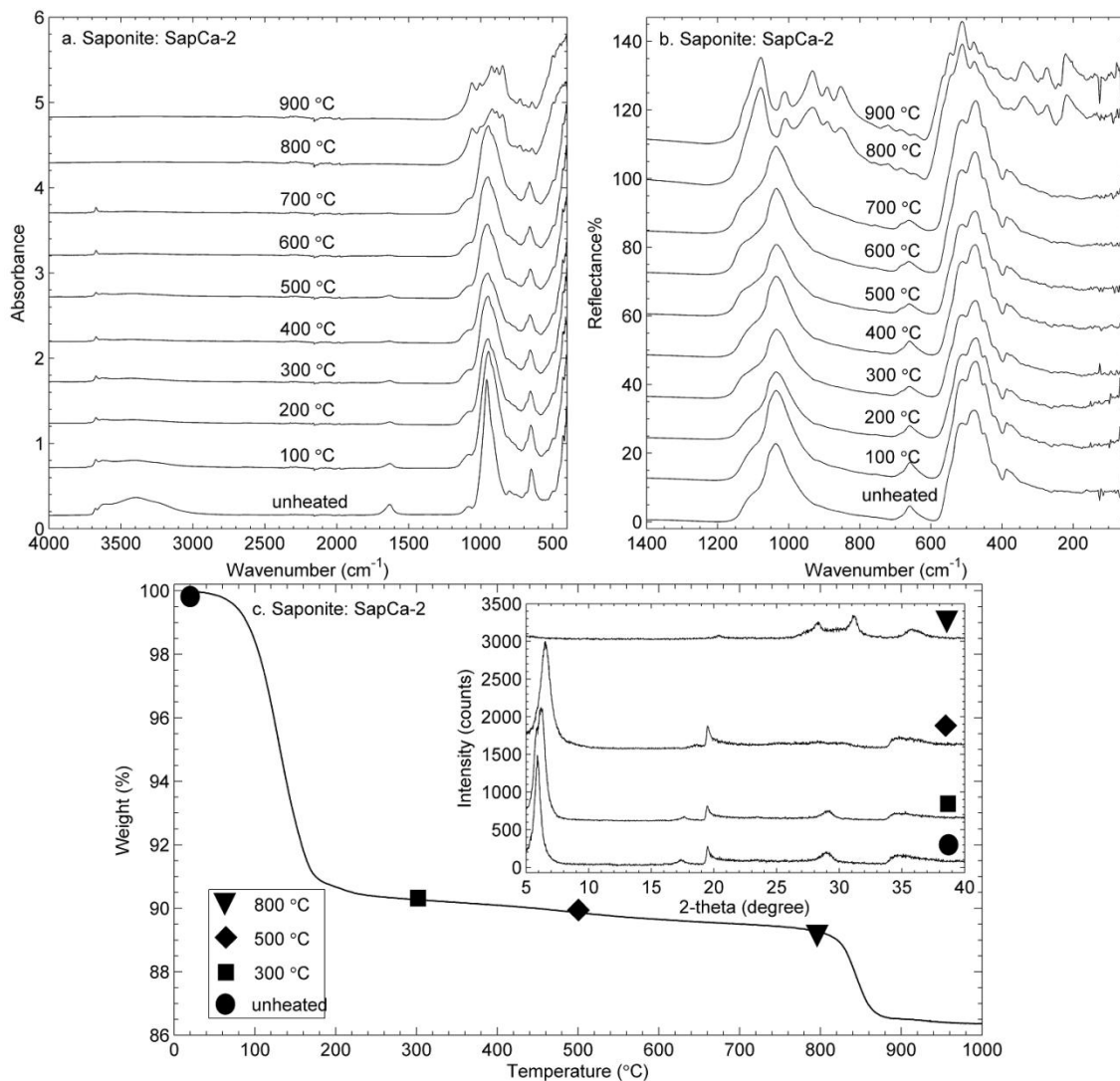


FIG. 2.5 (a) 400-4000 cm^{-1} ATR spectra of saponite (SapCa-2) calcined at various temperatures. (b) 50-1400 cm^{-1} specular reflectance spectra of saponite (SapCa-2) calcined at various temperatures. Linear vertical offset is applied to the spectra for clarity. (c) TGA plots and X-ray diffraction profiles (offset) of SapCa-2 saponite.

2.4.2.3 Beidellite

2.4.2.3.1 Attenuated total reflectance spectra

SBCa-1 beidellite Dehydroxylation of SBCa-1 beidellite resulted in the disappearance of its OH-stretching bands ($\sim 3697\text{ cm}^{-1}$, $\sim 3610\text{ cm}^{-1}$, and $\sim 3400\text{ cm}^{-1}$) and the Al-O-H libration band ($\sim 906\text{ cm}^{-1}$) at $\sim 500\text{ }^{\circ}\text{C}$ (**Figure 2.6a**). The 1090 cm^{-1} Si-O stretching (longitudinal mode) [Kloprogge *et al.*, 1998] band gradually became weaker as temperature increased. The 980 cm^{-1} Si-O stretching band was stable until $800\text{ }^{\circ}\text{C}$ and was replaced by a new spectral feature ($\sim 1024\text{ cm}^{-1}$) at $900\text{ }^{\circ}\text{C}$. The 519 cm^{-1} Al-O-Si bending band began to shift gradually toward higher wavenumbers ($\sim 524\text{ cm}^{-1}$ at $400\text{ }^{\circ}\text{C}$ and $\sim 553\text{ cm}^{-1}$ at $800\text{ }^{\circ}\text{C}$) after heating to $400\text{ }^{\circ}\text{C}$ and it was replaced by a weak band at $\sim 547\text{ cm}^{-1}$ at $900\text{ }^{\circ}\text{C}$.

Syn-1 mica-montmorillonite The dehydroxylation of Syn-1 montmorillonite was essentially complete around $600\text{ }^{\circ}\text{C}$, as evidenced by the disappearance of the OH-stretching band at $\sim 3629\text{ cm}^{-1}$ in the $600\text{ }^{\circ}\text{C}$ ATR spectrum (**Figure 2.6b**). The 1635 cm^{-1} H₂O bending feature Syn-1 montmorillonite disappeared at $400\text{ }^{\circ}\text{C}$. The 920 cm^{-1} Al-Al-OH deformation band decreased in intensity at $400\text{ }^{\circ}\text{C}$ and disappeared after $700\text{ }^{\circ}\text{C}$ heating. The Si-O stretching band at $\sim 976\text{ cm}^{-1}$

disappeared at 400 °C and was replaced by a broader band around 1018 cm⁻¹, which remained until 900 °C. The 518 cm⁻¹ feature associated with Si-O-Al bending mode decreased in intensity at 400 °C and this weaker band shifted to 562 cm⁻¹ at temperatures >400 °C. Syn-1 montmorillonite has ammonium in its interlayer [Kloprogge *et al.*, 1999a] and several spectral changes related to ammonium were observed on heating. Features in the 3300-2800 cm⁻¹ and near 1433 cm⁻¹ were assigned to stretching and deformation vibrations of NH₄⁺, respectively [Madejova' and Komadel, 2001]. The ammonium was lost at temperatures above 500 °C based on the disappearance of these spectral bands.

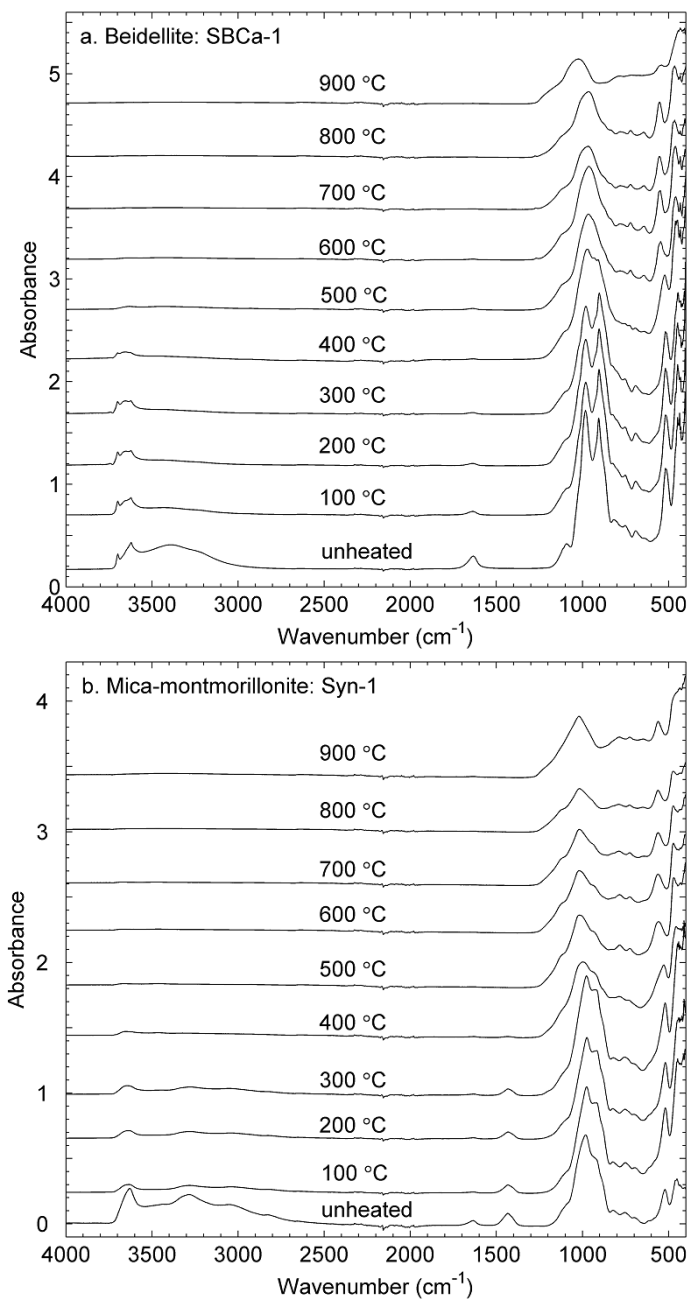


FIG. 2.6 (a) 400-4000 cm⁻¹ ATR spectra of beidellite (SBCa-1) calcined at various temperatures. (b) 400-4000 cm⁻¹ ATR spectra of mica-montmorillonite (Syn-1) calcined at various temperatures. Linear vertical offset is applied to the spectra for clarity.

2.4.2.3.2 Specular reflectance spectra

SBCa-1 beidellite Significant spectral changes in SBCa-1 beidellite began at 400 °C (**Figure 2.7a**). The 1125 cm⁻¹ and 1057 cm⁻¹ Si-O stretching bands began to shift away from each other (1134 cm⁻¹ and 1045 cm⁻¹ at 400 °C), the 1015 cm⁻¹ Si-O stretching shoulder band disappeared, the 910 cm⁻¹ Al-O-H libration band disappeared; the 550 cm⁻¹ Si-O-Al bending band [Kloprogge *et al.*, 1998] shifted to higher wavenumbers (shifting to 567 cm⁻¹ at 500 °C), and weak bands in the range 100 cm⁻¹ to 400 cm⁻¹ were all lost after 400 °C heating. A new spectral feature near 300 cm⁻¹ formed at 500 °C. Then all spectral features, including both the original features and new bands developed at lower temperatures, were completely lost at 900 °C. The 900 °C reflectance spectrum of SBCa-1 beidellite was dominated by four spectral features at ~1097 cm⁻¹, ~796 cm⁻¹, 553 cm⁻¹, and 462 cm⁻¹.

Syn-1 mica-montmorillonite The Si-O stretching bands at ~1122 cm⁻¹ and ~1053 cm⁻¹ continued to shift away from each other (1142 cm⁻¹ and 1045 cm⁻¹ at 800 °C) as temperature increased and at 900 °C they were replaced by a broad band centered near 1097 cm⁻¹ (**Figure 2.7b**). The weak Al-O-H libration band (~918 cm⁻¹) was lost after 400 °C heating. The 545 cm⁻¹ Si-O-Al bending band shifted to 570 cm⁻¹ after 500 °C and remained stable to 900 °C. The Si-O bending bands at ~480 cm⁻¹ and ~420 cm⁻¹ shifted slightly away from each other (484 cm⁻¹ and 406 cm⁻¹ at 900 °C) with increasingly higher temperatures and they existed in the 900 °C spectrum as features with comparable intensities.

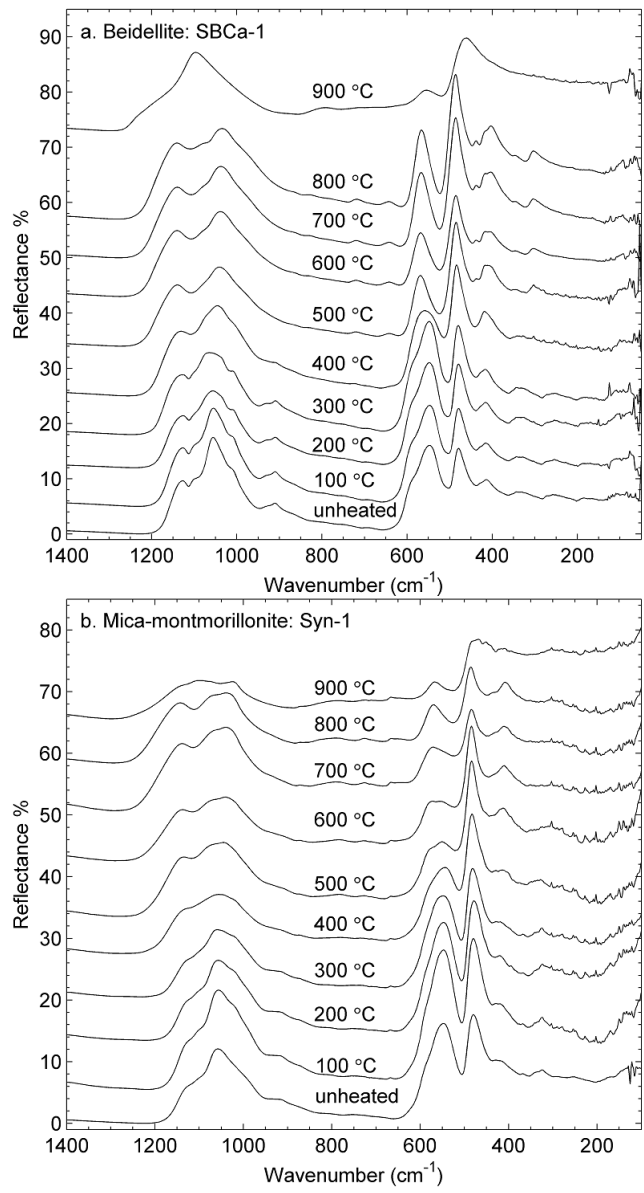


FIG. 2.7 (a) 50-1400 cm^{-1} specular reflectance spectra of beidellite (SBCa-1) calcined at various temperatures. (b) 100-1400 cm^{-1} specular reflectance spectra of mica-montmorillonite (Syn-1) calcined at various temperatures. Linear vertical offset is applied to the spectra for clarity.

2.4.2.3.3 Thermogravimetric and X-ray diffraction analysis

SBCa-1 beidellite and Syn-1 mica-montmorillonite both have high Al contents and comparable concentrations of OH and H₂O in their structures (**Table 2.2**). SBCa-1 exhibited two significant weight losses at ~150 °C and ~450-550 °C (**Figure 2.8a**), but XRD data indicated that its layer structure was stable to at least 800 °C. This conflict suggests that dehydration and dehydroxylation did not destroy the crystal structure by this temperature, and beidellite did not transform to an amorphous phase as montmorillonites did at 800 °C. Syn-1 mica-montmorillonite experienced the first weight loss in its TGA curve (**Figure 2.8b**) from room temperature to ~150 °C and the second significant weight loss occurred between 400 °C and 650 °C. The structure of Syn-1 mica-montmorillonite was also intact to 800 °C based on XRD data.

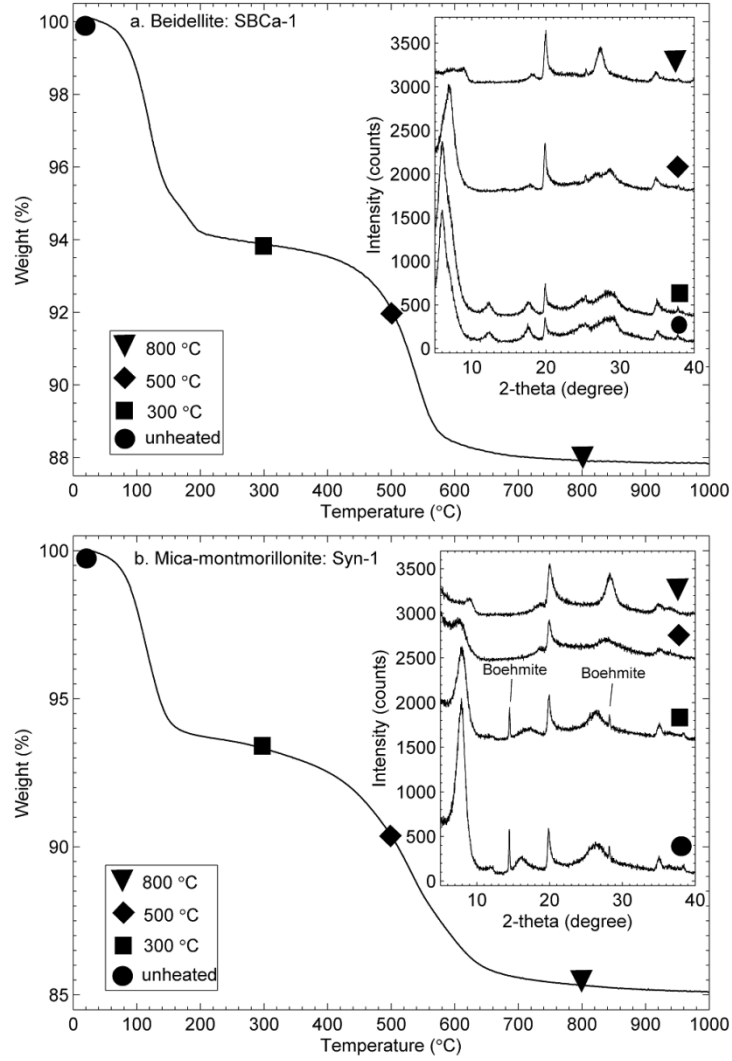


FIG. 2.8 TGA plots and X-ray diffraction profiles (offset) of (a) SBcA-1 beidellite and (b) Syn-1 mica-montmorillonite.

2.4.2.4 Hectorite (SHCa-1)

2.4.2.4.1 Attenuated total reflectance spectra

Heating to 600 °C resulted in disappearance of the H-O-H bending band at $\sim 1624\text{ cm}^{-1}$ and OH-stretching bands at $3400\text{-}3680\text{ cm}^{-1}$ (**Figure 2.9a**). The single Si-O stretching band at $\sim 960\text{ cm}^{-1}$ broadened at 400 °C and split into multiple spectral peaks after 500 °C heating. Beginning at 600 °C, significant change was observed for the Si-O stretching region and a series of new bands ($\sim 850\text{-}1060\text{ cm}^{-1}$) formed over this temperature range remained until 900 °C. The $\sim 650\text{ cm}^{-1}$ and $\sim 700\text{ cm}^{-1}$ spectral features were assigned to Mg-OH deformation of SHCa-1 hectorite and the in-plane CO_3^{2-} bending mode of calcite (existing as a contaminant in the hectorite sample), respectively [*Kloprogge et al.*, 2000a]. They both disappeared in the 600 °C spectrum and were replaced by two small bands at $\sim 670\text{ cm}^{-1}$ and $\sim 630\text{ cm}^{-1}$ after 600 °C heating.

2.4.2.4.2 Specular reflectance spectra

Specular reflectance results for SHCa-1 hectorite showed that distinct changes due to heating took place around 500 °C (**Figures 2.9b**). Upon heating to 500 °C, the 1047 cm^{-1} Si-O stretching band and the 476 cm^{-1} Si-O bending band both split into multiple bands between $900\text{-}1070\text{ cm}^{-1}$ and $400\text{-}500\text{ cm}^{-1}$ and a series of new spectral features formed in the far-IR region between $200\text{-}350\text{ cm}^{-1}$.

2.4.2.4.3 Thermogravimetric and X-ray diffraction analysis

Dehydration and dehydroxylation processes for SHCa-1 hectorite begin at ~150 °C and from ~650 °C to ~800 °C, respectively (**Figure 2.9c**). However, a unique weight loss around 770 °C may be caused by dolomite decarbonation [*Guggenheim and Van groos, 2001*]. XRD data show calcite in hectorite even after acid treatment, and the presence of calcite and dolomite may contribute to weight-loss events observed by TGA. Compared with the untreated sample, the 500 °C XRD pattern of hectorite showed collapse of original layer structure and formation of a new phase. The 800 °C XRD pattern of hectorite was consistent with well-ordered enstatite. The transformation from hectorite to enstatite at high temperatures has been summarized previously [e.g. *Green et al., 1970; Kloprogge et al., 2000a*].

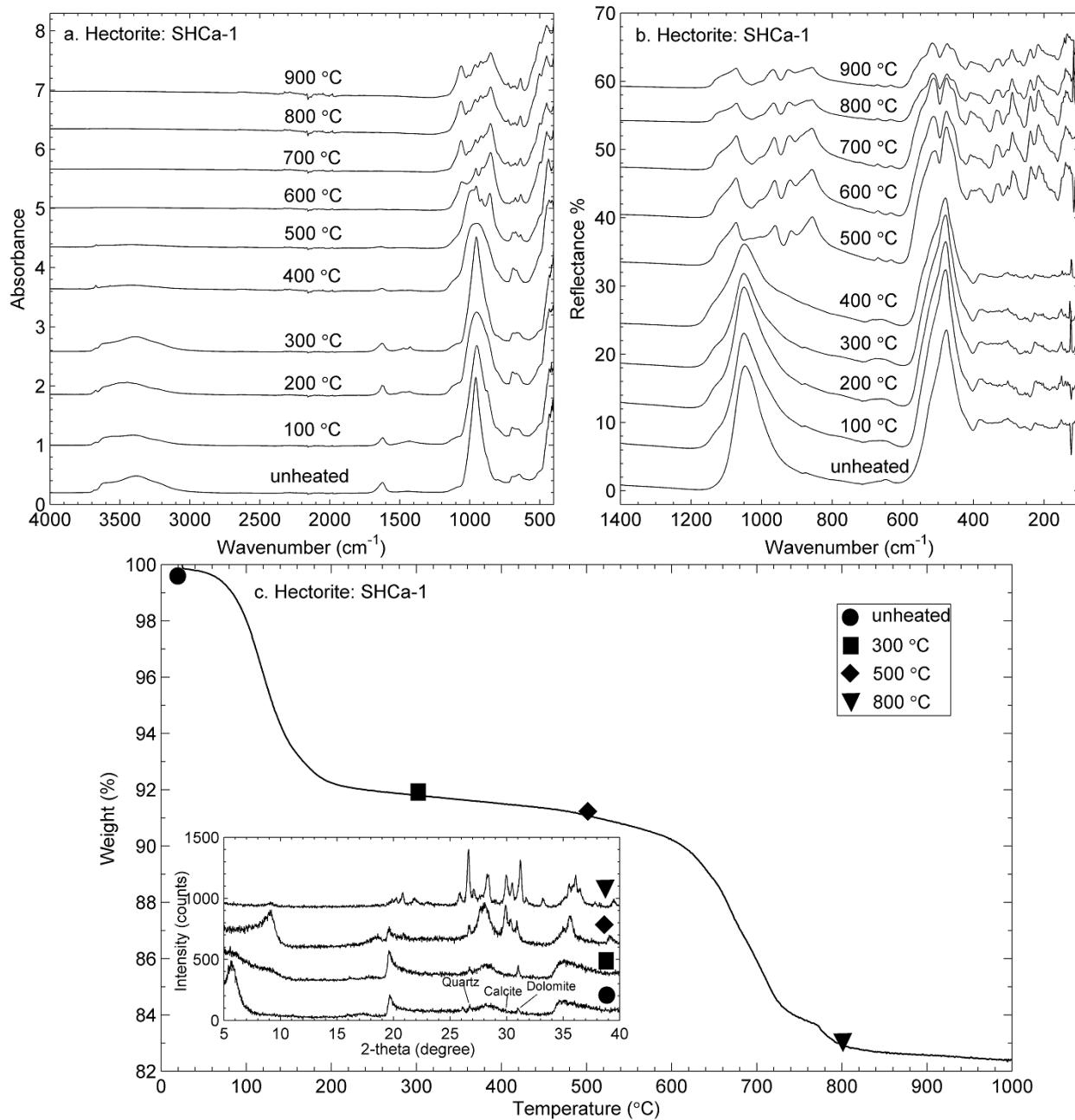


FIG. 2.9 (a) 400-4000 cm^{-1} ATR spectra of hectorite (SHCa-1) calcined at various temperatures. (b) 100-1400 cm^{-1} specular reflectance spectra of hectorite (SHCa-1) calcined at various temperatures. Linear vertical offset is applied to the spectra for clarity. (c) TGA plots and X-ray diffraction profiles (offset) of SHCa-1 hectorite.

2.4.2.5 Nontronite(NAu-1 and NAu-2)

2.4.2.5.1 Attenuated total reflectance spectra

NAu-1 and NAu-2 nontronites are both high-Fe dioctahedral smectites. The major chemical difference between them is a higher Al content in NAu-1 nontronite [Keeling *et al.*, 2000].

The first distinct ATR spectral change in NAu-1 nontronite occurred at 400 °C (**Figure 2.10a**). Most spectral features related to OH groups [Frost *et al.*, 2000, 2002], including the Fe-Fe-OH stretching band ($\sim 3560\text{ cm}^{-1}$), OH stretching of H₂O ($\sim 3400\text{ cm}^{-1}$), Al-Fe-OH deformation band ($\sim 908\text{ cm}^{-1}$), Fe-Fe-OH deformation band ($\sim 808\text{ cm}^{-1}$), and the Mg-Fe-OH deformation band ($\sim 742\text{ cm}^{-1}$), disappeared upon heating to 400 °C. The 484 cm^{-1} Si-O-Fe bending band also disappeared at 400 °C. The 1630 cm^{-1} H₂O bending band became weak at 400 °C and was lost at 500 °C. A new spectral feature at $\sim 790\text{ cm}^{-1}$ developed at 500 °C and remained until 900 °C. The Si-O stretching band near 1000 cm^{-1} showed a gradual shift to higher wavenumbers (975 cm^{-1} at room temperature and 1053 cm^{-1} after heating to 900 °C) as temperature increased. In addition, absorption features at $\sim 3695\text{ cm}^{-1}$ and $\sim 3620\text{ cm}^{-1}$ were related to kaolinite, which existed in the NAu-1 sample as a contaminant [Keeling *et al.*, 2000], and both bands disappeared at 400 °C.

NAu-2 nontronite exhibited spectral behavior upon heating similar to NAu-1 nontronite although the spectra had slightly different band positions (**Figure 2.10b**). Most of the original spectral features of NAu-2 nontronite disappeared at 400 °C or 500 °C; the Si-O stretching band around 1000 cm^{-1} continued to shift toward higher wavenumbers during the heat treatment and new spectral features developed in the range 500 cm^{-1} to 800 cm^{-1} upon heating to 600 °C. Based on the spectral results, there is no kaolinite in the NAu-2 nontronite.

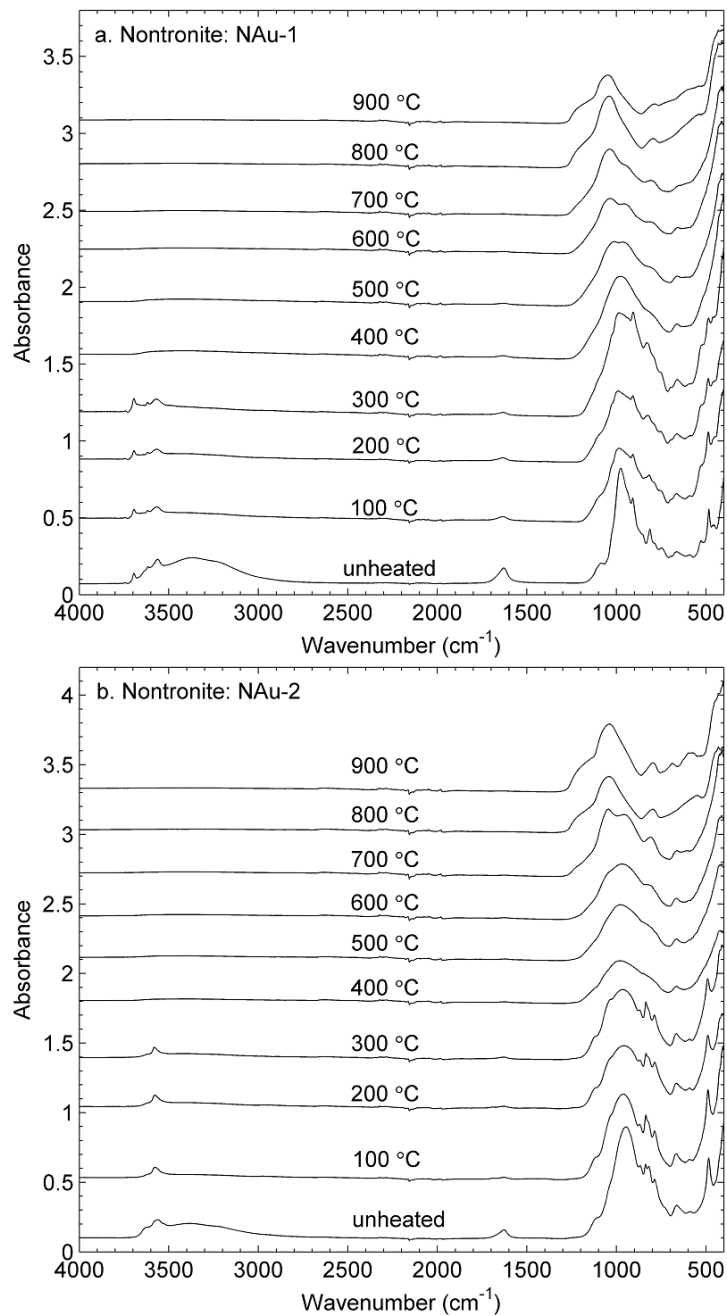


FIG. 2.10 (a) 400-4000 cm⁻¹ ATR spectra of nontronite (NAu-1) calcined at various temperatures. (b) 400-4000 cm⁻¹ ATR spectra of nontronite (NAu-2) calcined at various temperatures. Linear vertical offset is applied to the spectra for clarity.

2.4.2.5.2 Specular reflectance spectra

Two distinct spectral changes took place around 300-400 °C and 700-800 °C for both nontronite samples (**Figures 2.11a, 2.11b**) as they were heated. The spectral features in the 200-400 cm⁻¹ region related to mixed vibrations of the Si-O network [Farmer, 1974] and bands around 850 cm⁻¹ associated with OH deformation modes [Frost *et al.*, 2000, 2002] were all lost after 400 °C heating. Multiple Si-O bending bands near 500 cm⁻¹ disappeared and a new band formed (~460 cm⁻¹ for NAu-1 nontronite, ~470 cm⁻¹ for NAu-2 nontronite). The Si-O stretching bands of NAu-1 and NAu-2 nontronites near 1050 cm⁻¹ displayed changes similar to each other at 400 °C by combining and forming one single band. After 800 °C, these new bands in the Si-O stretching and bending regions both shifted slightly to higher frequencies and new spectral features developed in the range 600-800 cm⁻¹. In addition, a weak spectral band in the far-IR region (<400 cm⁻¹) around 310 cm⁻¹ appeared for both NAu-1 and NAu-2 nontronites at 400 °C and it remained until 900 °C.

2.4.2.5.3 Thermogravimetric and X-ray diffraction analysis

TGA data for nontronite samples NAu-1 and NAu-2 showed their first distinct weight loss below ~200 °C and the loss occurred from ~400 °C to ~600 °C (**Figures 2.12a, 2.12b**). XRD data for the nontronites indicated that their layer structures were destroyed by 800 °C. Simultaneously, new features appeared in the XRD patterns (~35°, 2θ) for both NAu-1 and NAu-2 nontronites, indicating crystallization of new phases (e.g., hematite, *Gavin and Chevrier*, 2010).

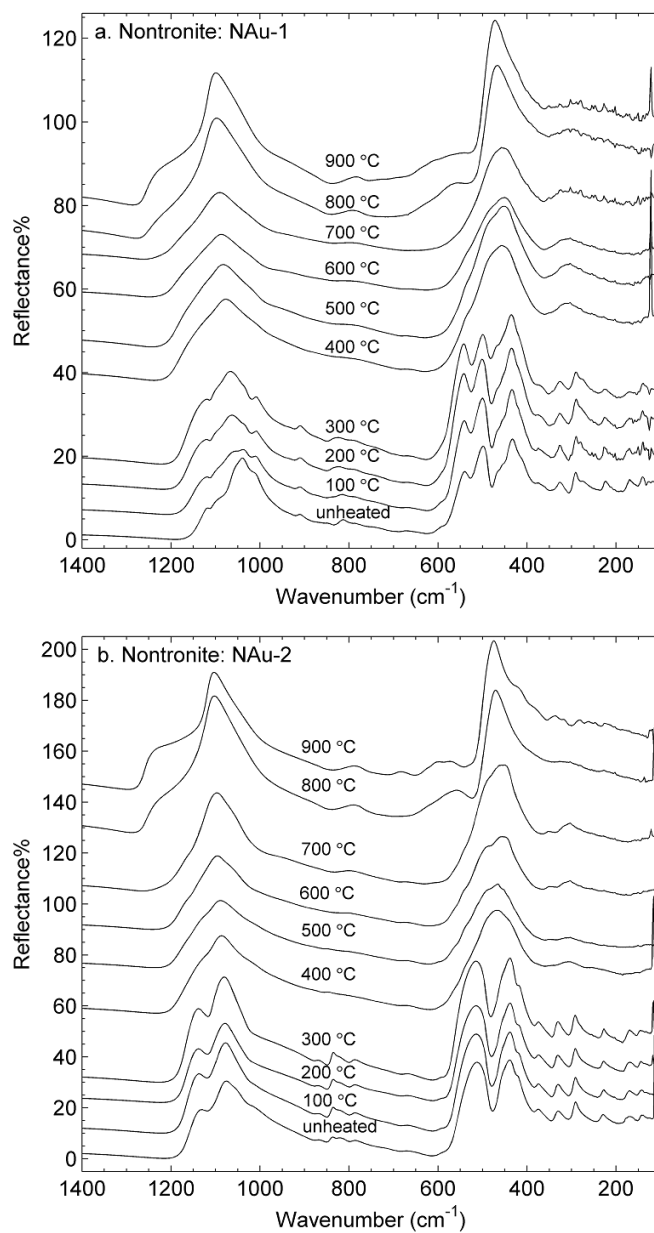


FIG. 2.11 (a) 100-1400 cm⁻¹ specular reflectance spectra of nontronite (NAu-1) calcined at various temperatures. (b) 100-1400 cm⁻¹ specular reflectance spectra of nontronite (NAu-2) calcined at various temperatures. Linear vertical offset is applied to the spectra for clarity.

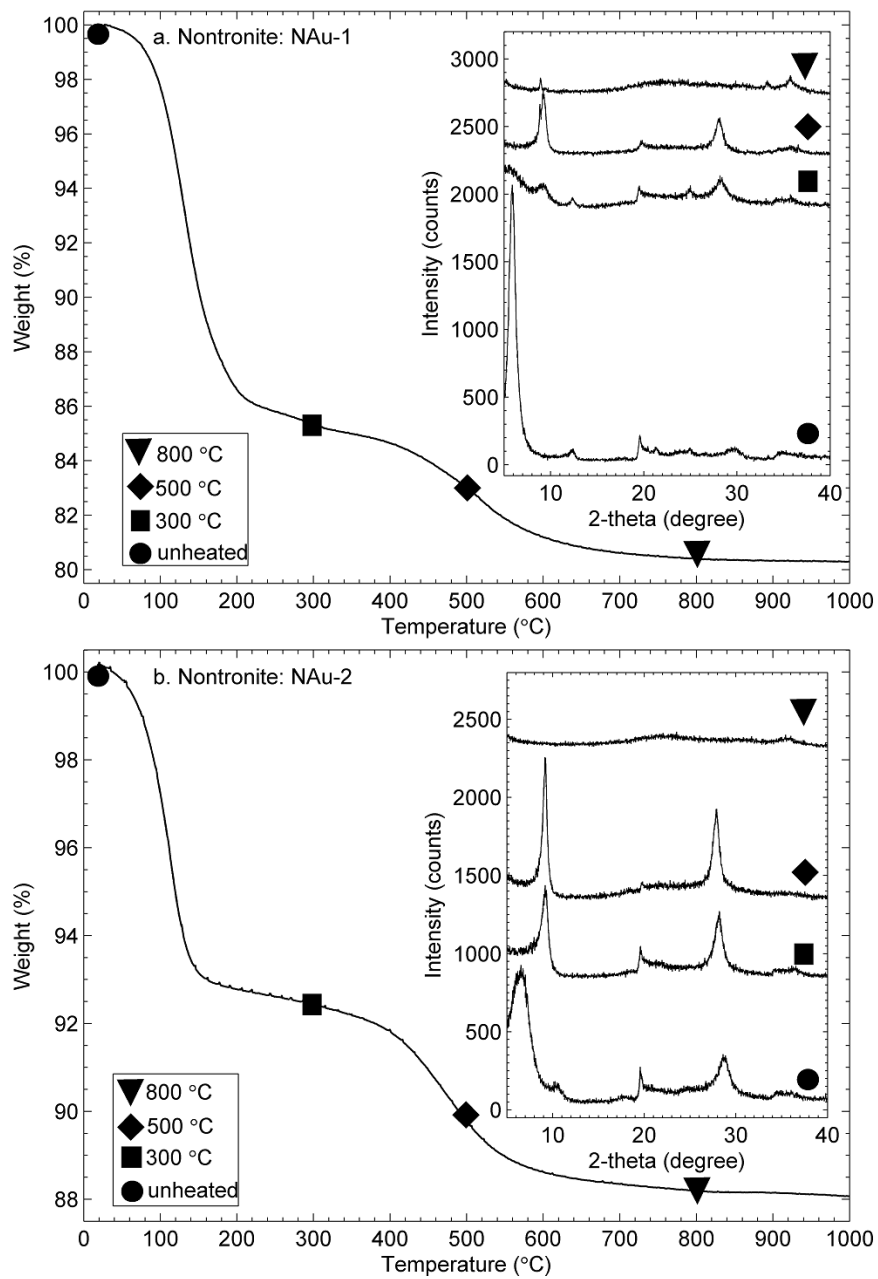


FIG. 2.12 TGA plots and X-ray diffraction profiles (offset) of (a) NAu-1 nontronite and (b) NAu-2 nontronite.

2.4.3 Chlorite group

2.4.3.1 Attenuated total reflectance spectra

Upon heating to 500 °C, OH-stretching bands ($\sim 3678\text{ cm}^{-1}$, $\sim 3535\text{ cm}^{-1}$, $\sim 3373\text{ cm}^{-1}$) disappeared (**Figure 2.13a**), but OH libration bands near $600\text{--}800\text{ cm}^{-1}$ [Farmer, 1974] remained as broad and weak features at 500 °C and were absent in the 800 °C ATR spectrum. The 943 cm^{-1} Si-O stretching band became very broad at 500 °C and shifts to lower wavenumbers at temperatures $>700\text{ °C}$. The Si-O bending vibration bands at $\sim 400\text{ cm}^{-1}$ also changed distinctly when clinochlore was heated to 500 °C.

2.4.3.2 Specular reflectance spectra

The Si-O stretching bands near $950\text{--}1100\text{ cm}^{-1}$ disappeared at 500 °C and a new broad band at $\sim 1084\text{ cm}^{-1}$ formed (**Figure 2.13b**). The multiple Si-O bending bands near $400\text{--}550\text{ cm}^{-1}$ combined together to form a single band around 475 cm^{-1} after heating to 500 °C. Bands at $650\text{--}800\text{ cm}^{-1}$ which were due to OH librations and a strong reflectance feature around 380 cm^{-1} all became very weak upon heating to 500 °C. After 800 °C heating, all spectral features formed at lower temperatures disappeared, and spectra of 800 and 900 °C clinochlore were dominated by a peak at $\sim 900\text{ cm}^{-1}$ and complex multiple peaks near $200\text{--}450\text{ cm}^{-1}$.

2.4.3.3 Thermogravimetric and X-ray diffraction analysis

The TGA curve for clinochlore showed a weight loss from ~550 °C to 800 °C, immediately followed by a second, more-abrupt weight loss from ~800 °C to 900 °C (**Figure 2.13c**). Previous studies [e.g., *Villieras et al.*, 1994] concluded that the first TGA weight loss was due to the dehydroxylation of the interlayer “brucite” sheets, and the loss of OH groups from the 2:1 layers produced the second weight loss. Changes in the XRD patterns as a function of heating were consistent with TGA results. The 001 reflection increased in intensity at 500 °C and the other 00*l* reflections generally decreased in intensity. Clinochlore lost its original structure at 700 °C and at 900 °C the sample transformed to new phases [e.g., olivine and spinel, *Brindley and Ali*, 1950].

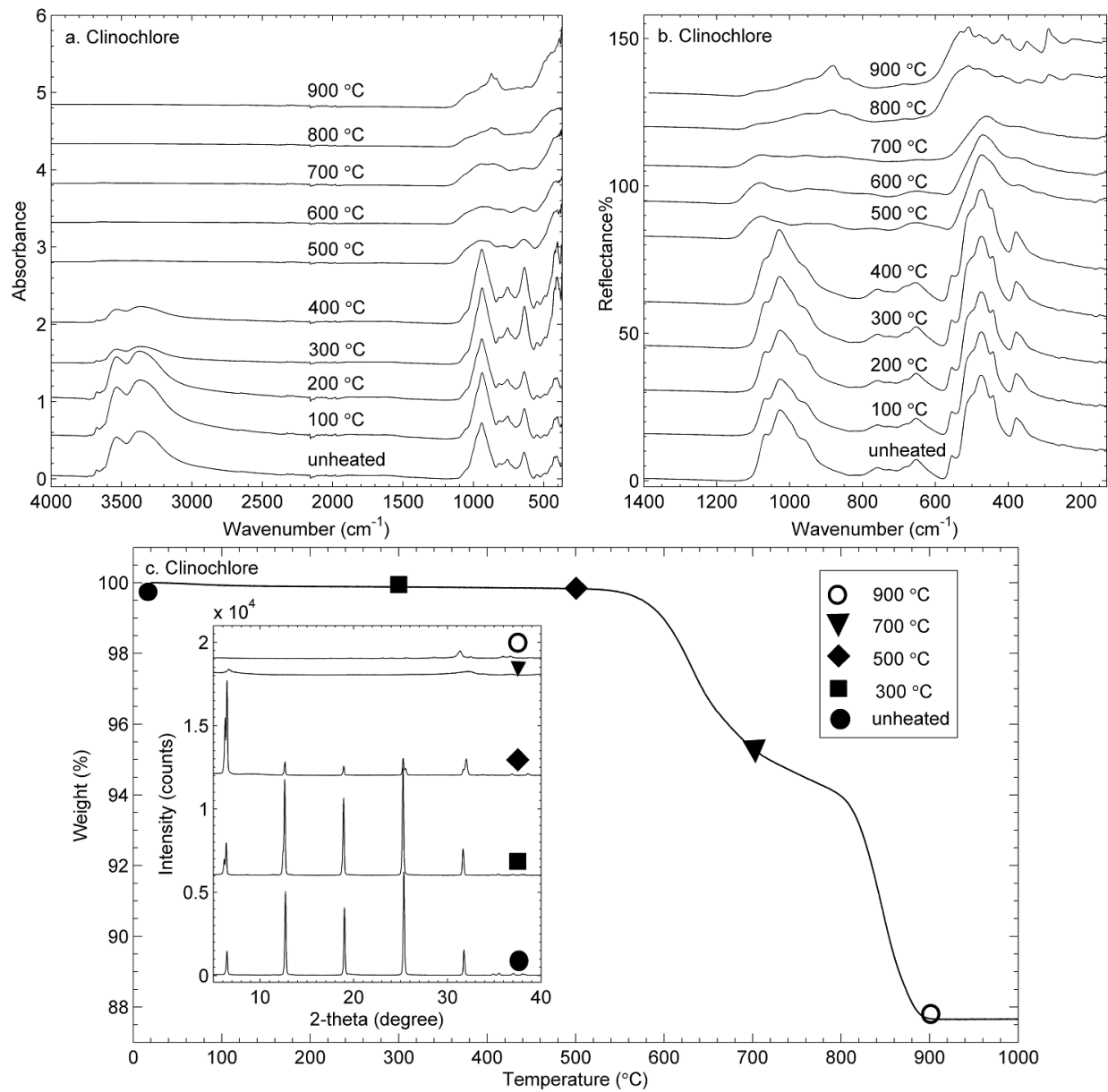


FIG. 2.13 (a) 370-4000 cm^{-1} ATR spectra of clinochlore calcined at various temperatures. (b) 130-1400 cm^{-1} specular reflectance spectra of clinochlore calcined at various temperatures. Linear vertical offset is applied to the spectra for clarity. (c) TGA plots and X-ray diffraction profiles (offset) clinochlore.

2.4.4 Sepiolite-palygorskite group

2.4.4.1 Attenuated total reflectance spectra

In the case of palygorskite (PFI-1), the disappearance of the structural OH-stretching bands at 3539 cm^{-1} and 3616 cm^{-1} and the 912 cm^{-1} Al-Al-OH deformation band [Madejov *a'* and Komadel, 2001] at $400\text{ }^{\circ}\text{C}$ indicates that most of the hydroxyl groups have been removed from the palygorskite structure (**Figure 2.14a**). The H_2O bending band around $\sim 1650\text{ cm}^{-1}$ shifted to $\sim 1620\text{ cm}^{-1}$ at $100\text{ }^{\circ}\text{C}$ and then maintained its position until $600\text{ }^{\circ}\text{C}$. However, the 1620 cm^{-1} feature was very weak above $400\text{ }^{\circ}\text{C}$. The Si-O stretching band at 976 cm^{-1} shifted to 1018 cm^{-1} above $400\text{ }^{\circ}\text{C}$ and was at $\sim 1051\text{ cm}^{-1}$ at $900\text{ }^{\circ}\text{C}$. The peak around 800 cm^{-1} was assigned to the Si-O stretching band of quartz [Madejov *a'* and Komadel, 2001] and existed throughout the heating process. In addition, two spectral features existed only in certain temperature ranges: the $\sim 870\text{ cm}^{-1}$ absorption band was present from $400\text{ }^{\circ}\text{C}$ to $600\text{ }^{\circ}\text{C}$ and the $\sim 940\text{ cm}^{-1}$ band appeared after palygorskite is heated to $800\text{ }^{\circ}\text{C}$.

The spectral changes of sepiolite (SepSp-1) due to heating can be divided into four steps (**Figure 2.14b**): (1) no significant change was observed until $200\text{ }^{\circ}\text{C}$; (2) at $300\text{ }^{\circ}\text{C}$, the H_2O bending band at $\sim 1660\text{ cm}^{-1}$ and Si-O stretching band around 1210 cm^{-1} disappeared and another Si-O stretching band at $\sim 972\text{ cm}^{-1}$ shifted towards lower frequency ($\sim 940\text{ cm}^{-1}$); (3) at $400\text{ }^{\circ}\text{C}$, two peaks around 3620 cm^{-1} and 3560 cm^{-1} attributed to OH stretching disappeared,

along with the 1620 cm^{-1} H_2O bending band. Correspondingly, the spectral features around 1000 cm^{-1} which were due to Si-O stretching vibrations became distinctly different from original spectral features; (4) The OH deformation and translation bands throughout the $600\text{-}800\text{ cm}^{-1}$ region [Frost *et al.*, 2001] disappeared at $800\text{ }^\circ\text{C}$, consistent with the disappearance of the 3690 cm^{-1} OH-stretching band at the same temperature. The Si-O stretching bands around 1000 cm^{-1} changed significantly after $800\text{ }^\circ\text{C}$ heating and were replaced by multiple spectral features over the rang $900\text{-}1200\text{ cm}^{-1}$.

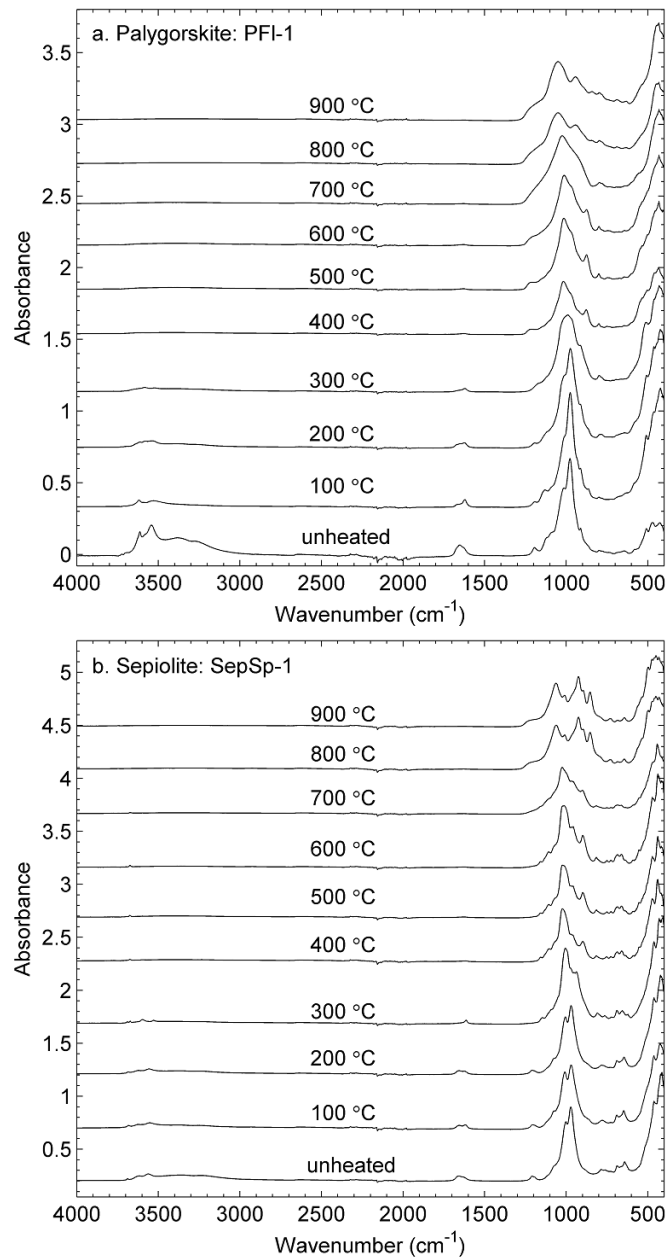


FIG. 2.14 (a) 400-4000 cm⁻¹ ATR spectra of palygorskite (PFI-1) calcined at various temperatures. (b) 400-4000 cm⁻¹ ATR spectra of sepiolite (SepSp-1) calcined at various temperatures. Linear vertical offset is applied to the spectra for clarity.

2.4.4.2 Specular reflectance spectra

For PFI-1 palygorskite, the Si-O stretching bands at $\sim 1130\text{ cm}^{-1}$, $\sim 1040\text{ cm}^{-1}$, and $\sim 987\text{ cm}^{-1}$ combined at $400\text{ }^{\circ}\text{C}$ to form a new feature centered at $\sim 1053\text{ cm}^{-1}$. This new band began to shift toward high wavenumbers and ended near 1107 cm^{-1} at $900\text{ }^{\circ}\text{C}$ (**Figure 2.15a**). The weak 910 cm^{-1} OH-deformation band disappeared at $400\text{ }^{\circ}\text{C}$. A new spectral band was formed at $\sim 870\text{ cm}^{-1}$ upon heating to $400\text{ }^{\circ}\text{C}$ and disappeared at $700\text{ }^{\circ}\text{C}$. Beginning at $300\text{ }^{\circ}\text{C}$, PFI-1 palygorskite began to lose its Si-O bending bands near $\sim 400\text{-}550\text{ cm}^{-1}$, and this spectral range was dominated by a single peak at $\sim 460\text{ cm}^{-1}$ up to $800\text{ }^{\circ}\text{C}$.

In the case of SepSp-1 sepiolite, with increasing temperature, significant spectral changes in the Si-O stretching region around 1000 cm^{-1} and in the Si-O bending region near $\sim 500\text{ cm}^{-1}$ took place at $\sim 300\text{ }^{\circ}\text{C}$, and then again around $800\text{ }^{\circ}\text{C}$ (**Figure 2.15b**). The OH-deformation band at $\sim 970\text{ cm}^{-1}$ became very weak after $300\text{ }^{\circ}\text{C}$ heating and disappeared at $800\text{ }^{\circ}\text{C}$. The OH translation bands in the $600\text{-}700\text{ cm}^{-1}$ range also disappeared at $800\text{ }^{\circ}\text{C}$. The spectral features for SepSp-1 sepiolite observed after heating to $800\text{ }^{\circ}\text{C}$, were completely different from those observed at lower temperatures. The spectra were no longer dominated by bands in two major spectral regions due to Si-O stretching (centered at $\sim 1050\text{ cm}^{-1}$) and Si-O bending (near $\sim 400\text{-}550\text{ cm}^{-1}$) and instead contained multiple bands near $\sim 800\text{-}1200\text{ cm}^{-1}$, a number of bands $\sim 500\text{ cm}^{-1}$, and several minor spectral features in the $200\text{-}400\text{ cm}^{-1}$ range.

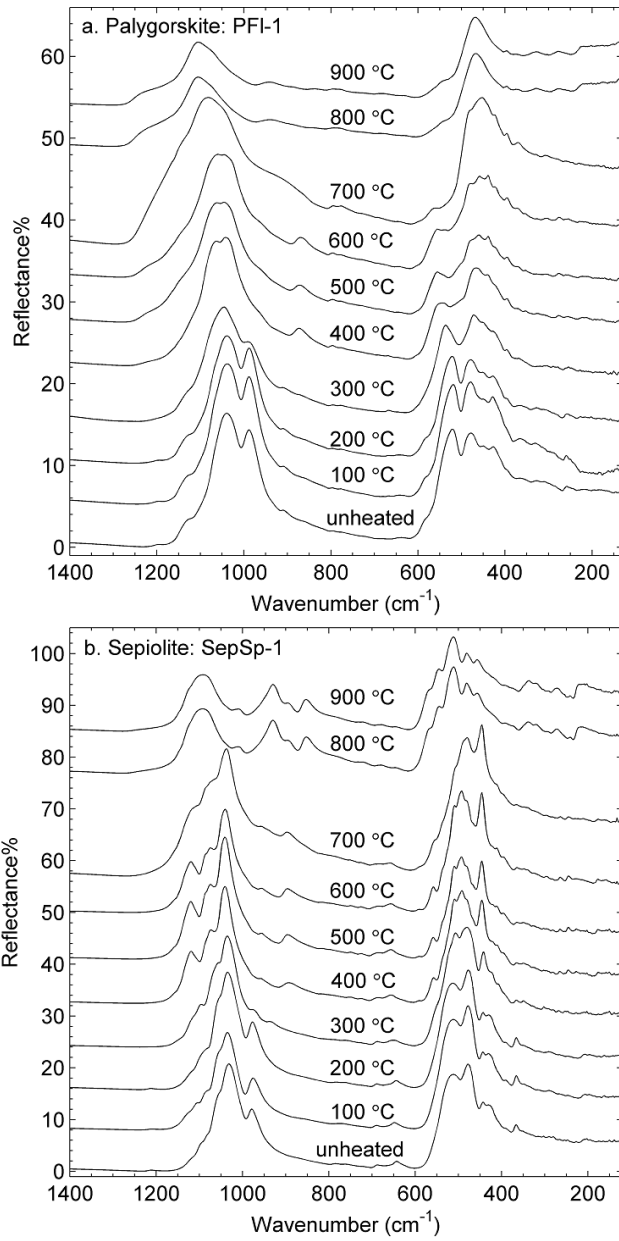


FIG. 2.15 (a) 130-1500 cm^{-1} specular reflectance spectra of palygorskite (PFI-1) calcined at various temperatures. (b) 120-1400 cm^{-1} specular reflectance spectra of sepiolite (SepSp-1) calcined at various temperatures. Linear vertical offset is applied to the spectra for clarity.

2.4.4.3 Thermogravimetric and X-ray diffraction analysis

Both PFI-1 palygorskite and SepSp-1 sepiolite exhibited complex dehydration and dehydroxylation processes in their TGA curves (**Figures 2.16a, 2.16b**). Palygorskite lost weight in multiple steps, below ~150 °C, from ~150 °C to ~280 °C, and from ~280 °C to 500 °C. Sepiolite showed even more complex weight loss behavior than palygorskite, with four overlapping events at ~150 °C, from 150 °C to 350 °C, from 350 °C to 550 °C, and from 550 °C to 850 °C. The high temperature phases of palygorskite and sepiolite have been described in many previous studies [e.g. *Kulbicki et al.*, 1959], which showed that both palygorskite and sepiolite transform to enstatite upon heating to 800 °C or elevated temperatures. In this study, the formation of enstatite was apparent in the XRD pattern of sepiolite heated to 800 °C because main reflections of enstatite (610) (31°, 2 θ) and (420) (28°, 2 θ) were recorded, while no clear evidence in the 800 °C XRD pattern of palygorskite showed the development of enstatite structure.

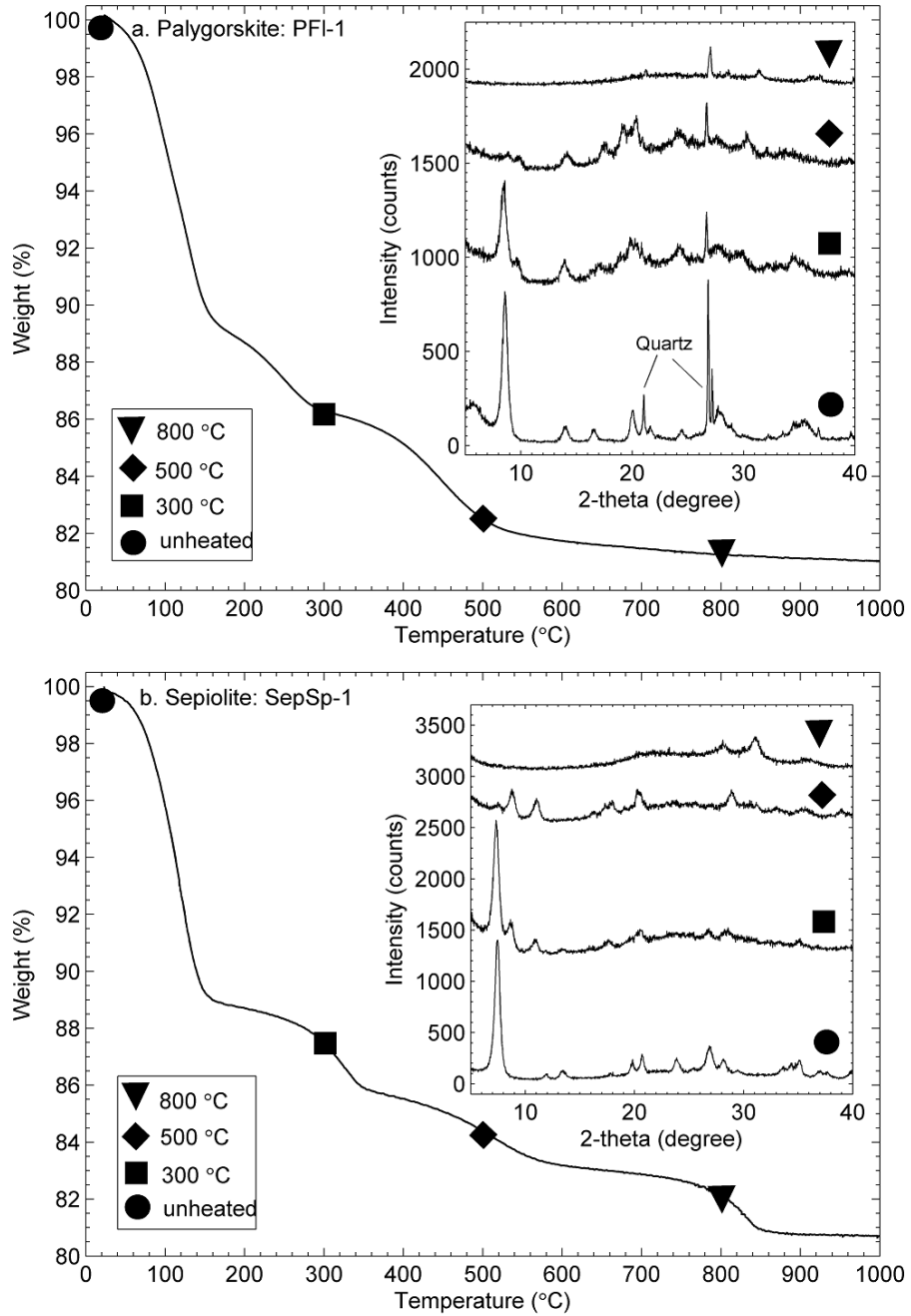


FIG. 2.16 TGA plots and X-ray diffraction profiles (offset) of (a) PFI-1 palygorskite and (b) SepSp-1 sepiolite.

2.4.5 Zeolite group

2.4.5.1 Attenuated total reflectance spectra

The infrared spectra of zeolites were summarized by *Breck* [1974b]. 27031 clinoptilolite lost its H₂O bending ($\sim 1630\text{ cm}^{-1}$) feature at 800 °C (**Figure 2.17a**). The spectral feature at $\sim 1000\text{ cm}^{-1}$ due to tetrahedron asymmetric stretching mode showed no obvious change upon heating, although the band became weaker and broader at 800 °C. The 790 cm^{-1} peak was assigned to the stretching modes involving mainly the tetrahedral atoms and remained until 900 °C. The bands at $\sim 500\text{-}650\text{ cm}^{-1}$ related to the double rings in the framework structures and the internal tetrahedral symmetric stretching bands over the range $\sim 650\text{-}720\text{ cm}^{-1}$ all disappeared at 800 °C.

The spectral behavior of 27133 mordenite (**Figure 2.17b**) was similar to that of 27031 clinoptilolite upon heating. However, the OH-stretching bands near 3400 cm^{-1} and the H₂O bending band at $\sim 1630\text{ cm}^{-1}$ persisted to 800 °C, although they were very weak at higher temperatures.

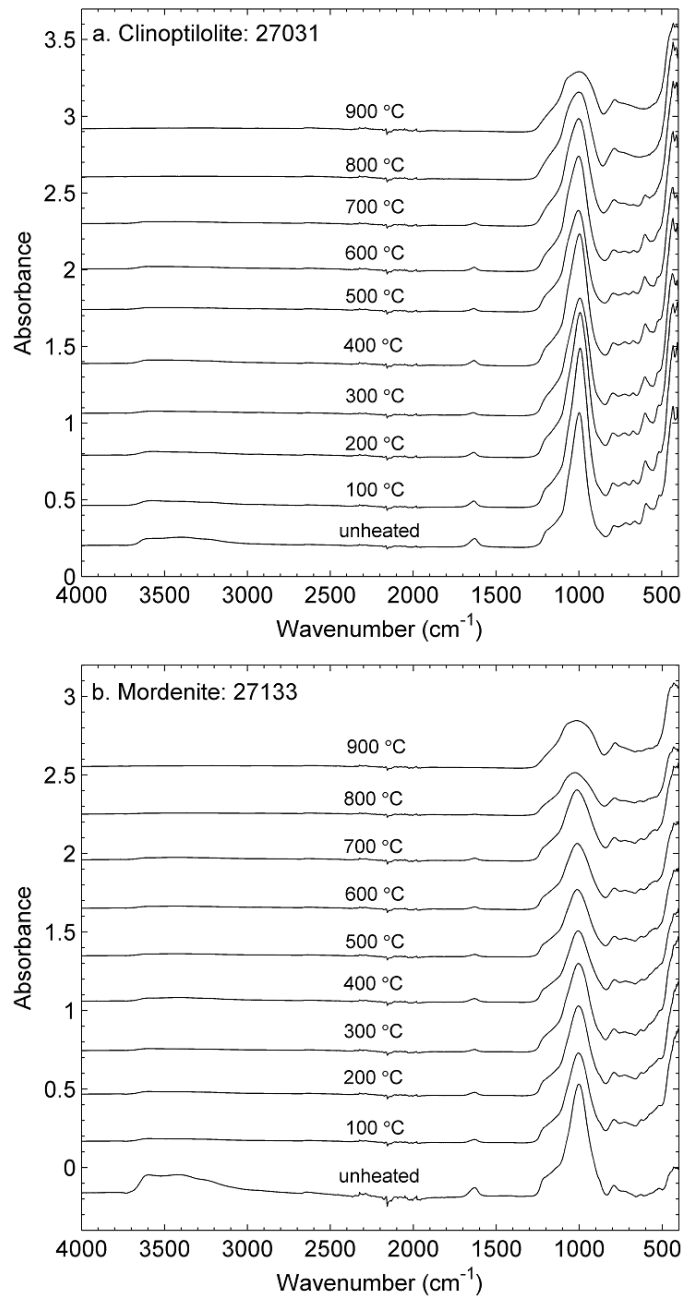


FIG. 2.17 (a) 400-4000 cm⁻¹ ATR spectra of clinoptilolite (27031) calcined at various temperatures. (b) 400-4000 cm⁻¹ ATR spectra of mordenite (27133) calcined at various temperatures. Linear vertical offset is applied to the spectra for clarity.

2.4.5.2 Specular reflectance spectra

The tetrahedral stretching band ($\sim 1086\text{ cm}^{-1}$) of clinoptilolite showed no change until $700\text{ }^{\circ}\text{C}$, and it shifted slightly to higher wavenumbers ($\sim 1100\text{ cm}^{-1}$) at $800\text{ }^{\circ}\text{C}$ (**Figure 2.18a**). Also a weak shoulder band at $\sim 1200\text{ cm}^{-1}$ developed at $800\text{ }^{\circ}\text{C}$. The weak band at $\sim 780\text{ cm}^{-1}$ associated with symmetric stretching of external linkages persisted to $900\text{ }^{\circ}\text{C}$. The $\sim 600\text{ cm}^{-1}$ double-ring band disappeared at $800\text{ }^{\circ}\text{C}$. The Si (Al)-O bending band at $\sim 470\text{ cm}^{-1}$ remained to $900\text{ }^{\circ}\text{C}$. The weak shoulder band at $\sim 378\text{ cm}^{-1}$, related to the motion of the tetrahedral rings which form the pore openings in the zeolites [Breck, 1974b] disappeared at $700\text{ }^{\circ}\text{C}$.

The two adjacent tetrahedron stretching bands around 1050 cm^{-1} (**Figures 2.18b**) combined at $500\text{ }^{\circ}\text{C}$ and this new band shifted to 1100 cm^{-1} at $700\text{ }^{\circ}\text{C}$. Two weak spectral features at ~ 550 and $\sim 625\text{ cm}^{-1}$ appeared upon heating to $700\text{ }^{\circ}\text{C}$ and disappeared at $900\text{ }^{\circ}\text{C}$. Other than these, the 1250 cm^{-1} Si (Al)-O stretching band, the 770 cm^{-1} stretching band of external linkages, and the 470 cm^{-1} Si (Al)-O bending band remained to $900\text{ }^{\circ}\text{C}$. No spectral features were observed in the far-IR range for mordenite.

2.4.5.3 Thermogravimetric and X-ray diffraction analysis

TGA data for clinoptilolite and mordenite show a slow and continuous loss in weight throughout the heat treatments (**Figures 2.19a, 2.19b**), showing that these two natural zeolites release H_2O from their rigid cage structures gradually upon heating. The XRD results show that the mordenite structure is not affected significantly by $800\text{ }^{\circ}\text{C}$ heating whereas clinoptilolite transformed to an amorphous phase at $800\text{ }^{\circ}\text{C}$.

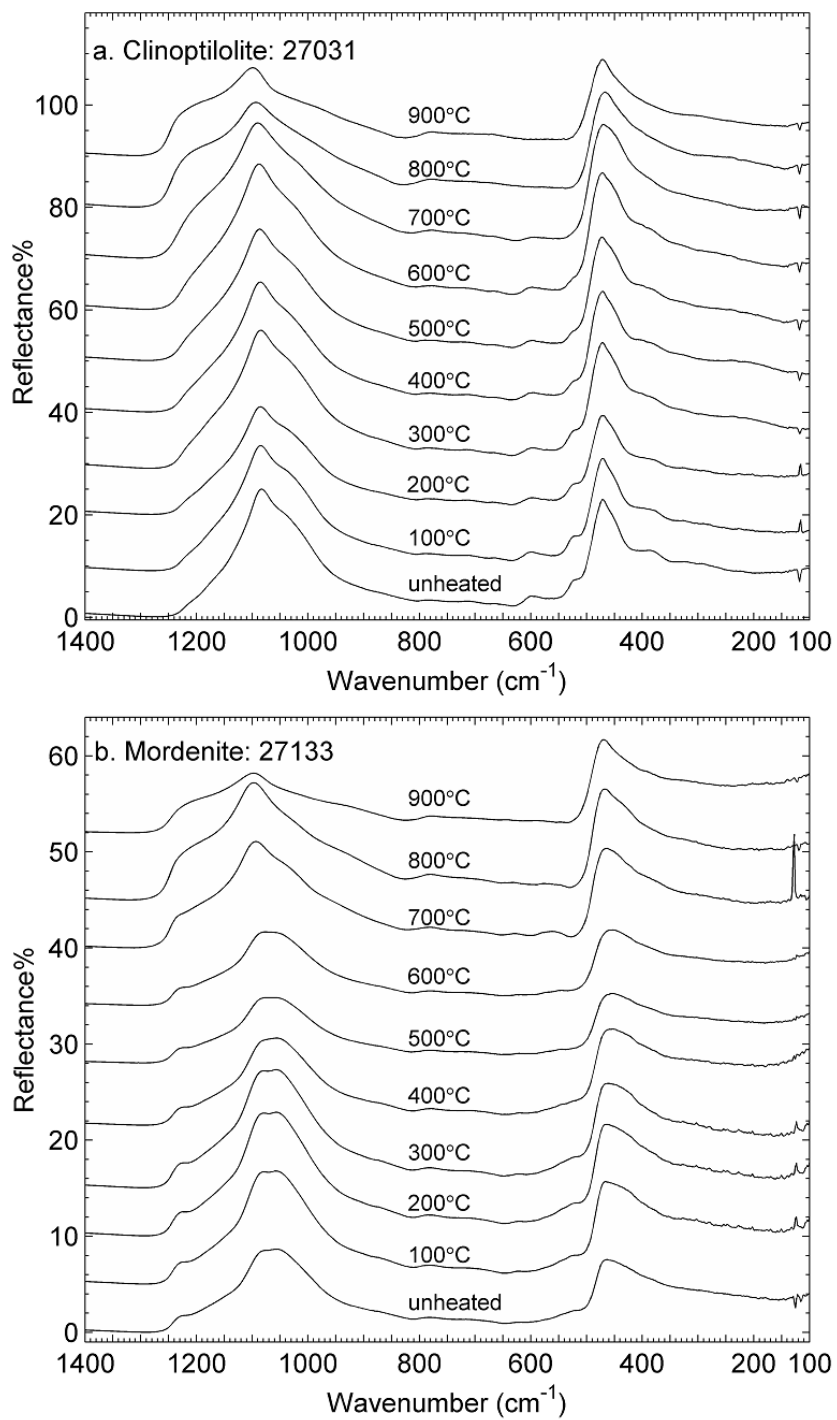


FIG. 2.18 (a) 100-1400 cm⁻¹ specular reflectance spectra of clinoptilolite (27031) calcined at various temperatures. (b) 100-1400 cm⁻¹ specular reflectance spectra of mordenite (27133) calcined at various temperatures. Linear vertical offset is applied to the spectra for clarity.

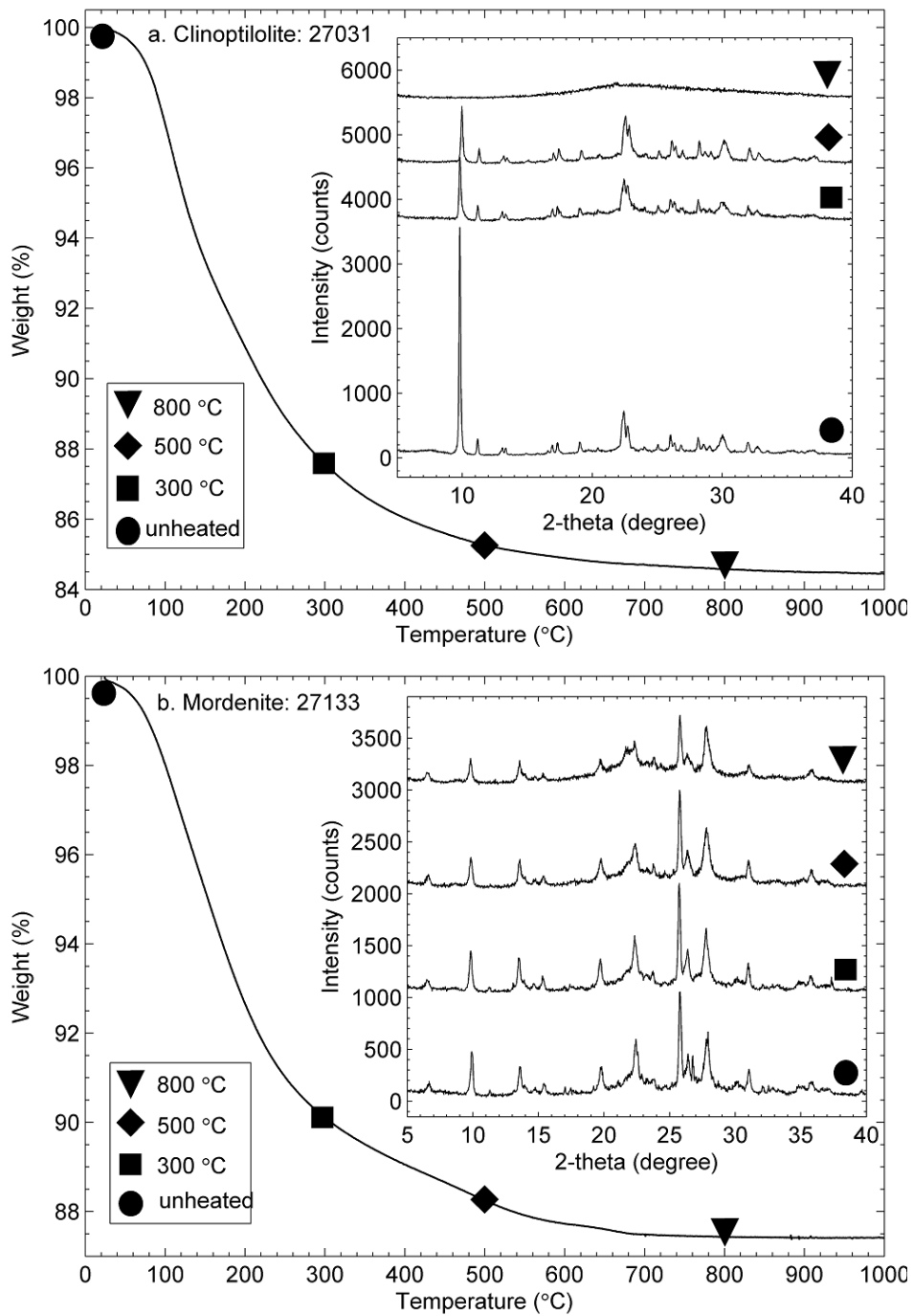


FIG. 2.19 TGA plots and X-ray diffraction profiles (offset) of (a) 27031 clinoptilolite and (b) 27133 mordenite.

2.5 Discussion

2.5.1 Effect of adsorbed H₂O

For most phyllosilicates analyzed here, TGA result showed that H₂O loss occurred at a low temperature (<200-300 °C), while ATR spectra revealed a much higher temperature (>400-500 °C) for the disappearance of the ~1630 cm⁻¹ H₂O bending band. For example, the H₂O molecules of SCa-3 montmorillonite were lost by 200 °C based on its TGA result (**Figure 2.4b**) whereas the H-O-H bending band of this montmorillonite was observed from its ATR spectrum up to 500 °C (**Figure 2.2b**). This conflict is very likely due to the re-adsorption of water onto the sample because, during ATR measurements, the sample was exposed to open air for 5 minutes and phyllosilicates have extremely high specific surface area [e.g. *Dogan et al.*, 2006]. Therefore the evolution of the ~1630 cm⁻¹ hydration band in ATR spectrum shows the change of the specific surface area due to heating treatment rather than the dehydration processes of phyllosilicates.

2.5.2 Effect of octahedral cations

The concentration of Al³⁺ or Fe³⁺ in dioctahedral smectites may affect their spectral behaviors on heating. Syn-1 mica-montmorillonite and SBCa-1 beidellite contain the highest concentrations of Al³⁺ (Al/Si=0.77, 0.6, respectively) in octahedral sites, and their IR spectra, particularly the multiple bands in the Si-O bending regions, did not show significant change until 800 °C. The montmorillonite series includes four samples in this study: SWy-2 (Al/Si=0.36), STx-1 (Al/Si=0.25), SAz-1 (Al/Si=0.33), and SCa-3 (Al/Si=0.22). The first distinct spectral change upon heating occurred around 600 °C for SWy-2, whereas the spectra of the three other montmorillonites changed significantly around 500 °C. NAu-1 and NAu-2 nontronites are both

Fe³⁺-rich smectites, and they lost their original spectral features completely at 400 °C. According to the above observations, Al-rich smectites may have greater thermal stability and maintain their spectral features to higher temperatures than Fe-rich smectites, which was also shown by previous investigators *Gavin and Chevrier* [2010].

Mg-rich phyllosilicates tend to transform to an enstatite phase at ~800 °C [e.g. *Kulbicki et al.*, 1959]. The 800 °C IR spectral features of the trioctahedral phyllosilicates hectorite, saponite, and sepiolite were completely different from the original spectral features that were dominated by Si-O stretching and Si-O bending bands, indicating the formation of a new phase, likely an enstatite structure. It was also observed that high-Mg phyllosilicates clinochlore (Mg/Si=0.96) and palygorskite (Mg/Si=0.18), moderate-Mg smectites SAz-1 (Mg/Si=0.11) and SCa-3 (Mg/Si=0.15) montmorillonites, and even low-Mg STx-1 (Mg/Si=0.09) montmorillonite all developed new IR spectral features around 900 cm⁻¹ when heated to 800 °C. No similar new spectral features were observed for SWy-2 (Mg/Si=0.07) montmorillonite at 800 °C.

2.6 Summary and conclusions

This study documents the effects of heating phyllosilicates and zeolite minerals based on ATR, IR reflectance, TGA, and powder XRD measurements. Heat treatment produces distinct changes in the infrared spectral features (~100-4000 cm⁻¹) of phyllosilicates and zeolites. These changes are associated with dehydration and/or dehydroxylation processes, determined primarily by the specific crystal structures and affected by their octahedral and extraframework cation compositions:

(1) For phyllosilicate samples, the OH stretching ($\sim 3600\text{ cm}^{-1}$), OH bending ($\sim 590\text{-}950\text{ cm}^{-1}$), and/or H₂O bending ($\sim 1630\text{ cm}^{-1}$) bands all become very weak or completely disappear upon heating to temperatures $>500\text{ }^{\circ}\text{C}$. The spectral changes associated with SiO₄ vibrations ($\sim 1000\text{ cm}^{-1}$ and $\sim 500\text{ cm}^{-1}$) show large variations depending on the compositions and structures of phyllosilicates. Spectral features of kaolinite change significantly at $\sim 400\text{ }^{\circ}\text{C}$ and the new bands are relatively stable until $900\text{ }^{\circ}\text{C}$. Most smectite samples display two distinct spectral changes with increased temperature, which may be related to their dehydration and dehydroxylation processes respectively. Clinocllore also exhibited dual changes in spectral features on heating, likely due to the presence of two different types of hydroxyl groups. The modulated tetrahedral sheets of palygorskite/sepiolite minerals showed more complex spectral changes on heating than other phyllosilicates included in this study. Compared to the phyllosilicates, the spectral features of two natural zeolites, clinoptilolite and mordenite, are less affected by thermal treatments. Even after heating to $900\text{ }^{\circ}\text{C}$, the IR spectral features do not show significant differences from those of unheated zeolites. These spectral results are consistent with the fact that the three-dimensionally rigid crystal structure of zeolite is stabler than the layer structure of phyllosilicates.

(2) The composition of octahedral sites showed a great influence on spectral behaviors of phyllosilicates: IR spectra of Al³⁺-rich smectites are stabler than those of Fe³⁺-rich smectites; spectral behaviors of Mg²⁺-rich phyllosilicates are distinctly affected by the formation of new crystal phases around $700\text{ }^{\circ}\text{C}$; phyllosilicates with a small amount of Mg²⁺ on their octahedral sites all showed new spectral band at $\sim 900\text{ cm}^{-1}$ upon heating to $700\text{ }^{\circ}\text{C}$ or higher temperatures.

Appendix Fundamental vibration modes in phyllosilicates discussed in this study

Spectral features in the mid-to-far-IR region discussed in this study are dominated by fundamental molecular vibration bands and are a particularly important indicator of mineralogy and chemical composition for the major rock-forming minerals [e.g., *Salisbury*, 1993]. Spectral features of phyllosilicates in this region and their interpretations have been studied comprehensively by numerous authors [e.g., *Farmer*, 1974; *Van der Marel and Beutelspacher*, 1976; *Kloprogge et al.*, 1998; *Frost and Kloprogge*, 2000; *Madajová and Komadel*, 2001; *Bishop et al.*, 2008b]. In general, absorption bands near 1200-1000 cm^{-1} are due to Si-O stretching motions in the tetrahedral sheets, spectral features near 550-400 cm^{-1} are associated with Si-O bending vibrations modes, and spectral bands observed in the 950-590 cm^{-1} range are related to M-OH or M-M-OH vibration modes in octahedral sheets. The following **Figure 2.20** and **Table 2.4** outline the fundamental vibration modes in phyllosilicates discussed in this study.

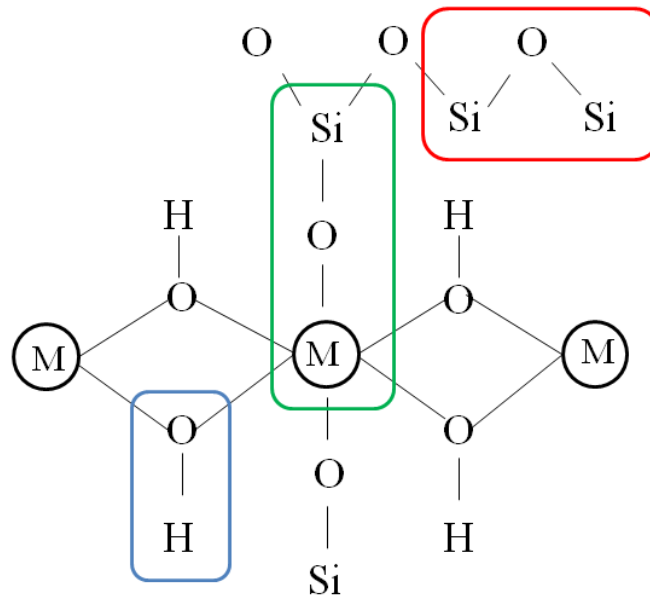
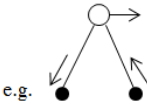
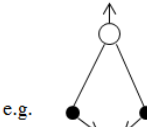
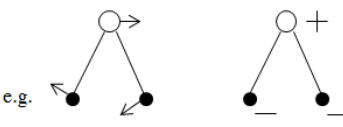
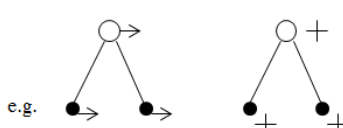


Figure 2.20 Diagram of vibration modes in phyllosilicates discussed in this study. The octahedral cations (typically Al^{3+} , Mg^{2+} , Fe^{3+} , or Fe^{2+}) are labeled as “M” in the figure. In the blue part, the OH stretching, the MMO-H bending, the MO-H translation and the MO-H libration vibration modes are discussed in this study. In the green part, the Si-O stretching and the Si-O-M bending vibration modes are discussed. In the red part, the Si-O stretching and the Si-O-Si (or Si-O) bending vibration modes are discussed (phyllosilicate structure derived from *Farmer 1974* and *Bishop et al.*, 2008b; spectral feature assignments cited from *Farmer, 1974*, *Frost et al.*, 2001, *Michalski et al.*, 2005; *Bishop et al.*, 2008b).

Table 2.4 Fundamental vibration modes discussed in this study*

Stretching vibrations	
Bending vibrations	
Libration vibrations	
Translation vibrations	

* Cited from *Farmer 1974*

Acknowledgments. This manuscript was greatly improved by the careful work of Editor Robert Carlson, and thorough reviews from Patricia Gavin and an anonymous reviewer, for which we are very grateful. We are also grateful for support from Mars Fundamental Research Program NNX08AN62G.

References

Abramov, O., and D. A. Kring (2005), Impact-induced hydrothermal activity on early Mars, *J. Geophys. Res.*, *110*, E12S09, doi:10.1029/2005JE002453.

Aceman, S., N. Lahav, and S. Yariv (1997), XRD study of the dehydration and rehydration of Al-pillared smectites differing in source of charge, *J. Therm. Anal.*, *50*, 241--256.

Armbruster, T. and Gunter, M. E. (2001), Crystal structure of natural zeolites. In D. L. Bish and D. W. Ming, Eds., *Natural zeolites: Occurrence, properties, application*. Reviews in *Mineralogy and Geochemistry*, *45*, 1-57. Mineralogical Society of America and Geochemical Society, Washington, U. S. A.

Bailey, S. W. (1980), Structures of layer silicates, In *Crystal Structures of Clay Minerals and Their X-ray Identification*, edited by G. W. Brindley and G. Brown, pp. 1-124, Mineral. Soc., London.

Ballet, O., J.M.D. Coey, and K. J. Burke (1985), Magnetic properties of sheet silicates; 2:1:1 layer minerals, *Phys. Chem. Minerals*, *12*, 370-378.

Bandfield, J. L., V. E. Hamilton, P. R. Christensen (2000), A global view of Martian surface compositions from MGS-TES, *Science*, *287*, 1626--1630.

Bandfield, J. L. (2002), Global minerals distributions on Mars, *J. Geophys. Res.*,107(E6), 5042, doi:10.1029/2001JE001510.

Barrer, R. M. (1978), Zeolite frameworks, cations and water molecules, In *Zeolites and Clay Minerals as Sorbents and Molecular Sieves*, pp. 32-102, Academic Press, London.

Barrer, R. M. (1982), Occurrence, classification and some properties of zeolites, In *Hydrothermal Chemistry of Zeolites*, pp. 1-42, Academic Press, London.

Bibring, J. -P., Y. Langevin, A. Gendrin, B. Gondet, F. Poulet, M. Berthé A. Soufflot, R. Arvidson, N. Mangold, J. Mustard, P. Drossart, and the OMEGA team (2005), Mars surface diversity as revealed by the OMEGA/Mars Express observations, *Science*,307, 1576--1581

Bibring, J. -P., Y. Langevin, J. F. Mustard, F. Poulet, R. Arvidson, A. Gendrin, B. Gondet, N. Mangold, P. Pinet, F. Forget, and the OMEGA team (2006), Global mineralogical and aqueous Mars history derived from OMEGA/Mars Express data, *Science*,312, 400--404.

Bish, D. L. (1984), Effects of exchangeable cation composition on the thermal expansion/contraction of clinoptilolite, *Clays and Clay Minerals*, 32 (6), 444-452.

Bish, D. L. (1988), Effects of composition on the dehydration behavior of clinoptilolite and heulandite, in *Occurrence, Properties and Utilization of Natural Zeolites*, D. Kallo and H.S. Sherry, eds., pp565, Akadémiai Kiadó Budapest.

Bish, D. L. and J.W. Carey (2001), Thermal properties of natural zeolites, in *Natural Zeolites: occurrence, properties, applications*, D.L. Bish and D.W. Ming, eds., pp403, Mineralogical Society of America, Washington.

Bish, D. L., J. W. Carey, D. T. Vaniman, and S. J. Chipera (2003), Stability of hydrous minerals on the martian surface, *Icarus*,*164*, 96-103.

Bishop, J. L., E. Z. Noe Dobrea, N. K. McKeown, M. Parente, B. L. Ehlmann, J. R. Michalski, R. E. Milliken, F. Poulet, G. A. Swayze, J. F. Mustard, S. L. Murchie, and J. -P. Bibring (2008a), Phyllosilicate diversity and past aqueous activity revealed at Mawrth Vallis, Mars, *Science*,*321*, 830-833.

Bishop, J. L., M. D. Lane, M. D. Dyar, and A. J. Brown (2008b), Reflectance and emission spectroscopy study of four groups of phyllosilicates: smectites, kaolinite-serpentines, chlorites and micas, *Clay Minerals*,*43*, 35-54.

Bishop, J. L., N. K. McKeown, D. J. DesMarais, E. Z. Noe Dobrea, M. Parente, F. Seelos, S. L. Murchie, and J. F. Mustard (2009), The ancient phyllosilicates at Mawrth Vallis and what they can tell us about possible habitable environments on early Mars, *Lunar Planet. Sci.*,*40th*, abstract 2239.

Boslough, M. B., R. J. Weldon, and T. J. Ahrens (1980), Impact-induced water loss from serpentine, nontronite and kernite, *Proc. Lunar Planet. Sci. Conf. 11th*, 2145-2158.

Breck, D. W. (1974a), Structure of zeolites, In *Zeolite Molecular Sieves: Structure, Chemistry, and Use*, pp. 29-185, John Wiley and Sons, London.

Breck, D. W. (1974b), Chemical properties and reactions of zeolites, In *Zeolite Molecular Sieves: Structure, Chemistry, and Use*, pp. 441-528, John Wiley and Sons, London.

Brindley, G. W., S. Z. Ali (1950), X-ray study of thermal transformations in some magnesian chlorite minerals. *Acta Cryst.* *3*, 25-30.

Bruckenthal, E. A., and R. B. Singer (1987), Spectral effects of dehydration on phyllosilicates, *Proc. Lunar Planet. Sci. Conf. 18th*, 135.

Carroll, D. L., T. F. Kemp, T. J. Bastow, and M. E. Smith (2005), Solid-state NMR characterisation of the thermal transformation of a Hungarian white illite, *Solid State Nucl. Magn. Reson.*, 28, 31-43.

Che, C. and T. D. Glotch (2010), The effect of high temperatures on the emission and VNIR reflectance spectra of phyllosilicates and zeolites, *Lunar Planet. Sci.*, 41st, abstract 1513.

Chemtob, S. M., and T. D. Glotch (2007), Linear deconvolution of attenuated total reflectance infrared spectra of fine-grained mineral mixtures, *Lunar Planet. Sci.*, 38th, abstract 1097.

Cruciani, G. (2006), Zeolites upon heating: Factors governing their thermal stability and structural changes, *Journal of Physics and Chemistry of Solids*, 67, 1973-1994.

Dogan, A. U., M. Dogan, M. Onal, Y. Sarikaya, A. Aburub and D. E. Wurster (2006), Baseline studies of the Clay Minerals Society source clays: specific surface area by the Brunauer Emmett Teller (BET) method, *Clays and Clay Minerals*, 54, 62-66.

Drachman, S. R., G. E. Roch, and M. E. Smith (1997), Solid state NMR characterisation of the thermal transformation of Fuller's Earth, *Solid State Nucl. Magn. Reson.*, 9, 257-267.

Ehlmann, B. L., J. F. Mustard, G. A. Swayze, R. N. Clark, J. L. Bishop, F. Poulet, D. J. Des Marais, L. H. Roach, R. E. Milliken, J. J. Wray, O. Barnouin-Jha, and S. L. Murchie (2009), Identification of hydrated silicate minerals on Mars using MRO-CRISM: Geologic context near Nili Fossae and implications for aqueous alteration, *J. Geophys. Res.*, 114, E00D08, doi:10.1029/2009JE003339.

Fairén, A. G. et al. (2010), Noachian and more recent phyllosilicates in impact craters on Mars, *Proceedings of the National Academy of Sciences*, *107*, 12095-12100, doi:10.1073/pnas.1002889107.

Farmer, V. C. (1974), The layer silicates, In *The Infrared Spectra of Minerals*, edited by V. C. Farmer, pp. 331-363, Mineral. Soc., London.

Farrand, W. H., T. D. Glotch, J. W. Rice Jr, J. A. Hurowitz, and G. A. Swayze (2009), Discovery of jarosite within the Mawrth Vallis region of Mars: Implications for the geologic history of the region, *Icarus*, *204*, 478-488, doi: 10.1016/j.icarus.2009.07.014.

Fitzgerald, J. J., S. F. Dec, and A. I. Hamza (1989), Observation of 5-coordinated Al in pyrophyllite dehydroxylate by solid-state ^{27}Al NMR spectroscopy at 14 T, *Am. Mineral.*, *74*, 1405-1408.

Fitzgerald, J. J., A. I. Hamza, S. F. Dec, and C. E. Bronnimann (1996), Solid-state ^{27}Al and ^{29}Si NMR and ^1H CRAMPS studies of the thermal transformations of the 2:1 phyllosilicate pyrophyllite, *J. Phys. Chem.*, *100*, 17351-17360.

Frost, R. L., and P. F. Barron (1984), Solid-state silicon-29 and aluminum-27 nuclear magnetic resonance investigation of the dehydroxylation of pyrophyllite, *J. Phys. Chem.*, *88*, 6206-6209.

Frost, R. L., J. T. Kloprogge (2000), Vibrational spectroscopy of ferruginous smectite and nontronite, *Spectrochimica Acta Part A*, *56*, 2177-2189.

Frost, R. L., J. T. Kloprogge, D. Zhe (2002), The Garfield and Uley nontronites-an infrared spectroscopic comparison, *Spectrochimica Acta Part A*, *58*, 1881-1894.

Frost, R. L., O. B. Locos, H. Ruan, J. T. Kloprogge (2001), Near-infrared and mid-infrared spectroscopic study of sepiolites and palygorskites, *Vib. Spectrosc.*,27, 1-13.

Gavin, P., V. Chevrier, and K. Ninagawa (2008), Effect of impact and heating on the spectral properties of clays on Mars, *Lunar Planet. Sci.*,39th, abstract 2033.

Gavin, P., V. Chevrier (2010), Thermal alteration of nontronite and montmorillonite: Implications for the martian surface, *Icarus*, 208, 721-734, doi:10.1016/j.icarus.2010.02.027.

Green, J. M., K. J. D. Mackenzie, and J. H. Sharp (1970), Thermal reactions of synthetic hectorite, *Clays Clay Miner.*,18, 339-346.

Grim, R. E., and G. Kulbicki (1961), Montmorillonite: high temperature reactions and classification, *Ameri. Mineral.*,46, 1329-1369.

Guggenheim, S. and A. F. Koster van Groos (2001), Baseline studies of the clay minerals society source clays: Thermal analysis, *Clays Clay Miner.*,49, 433-443.

Harris, W. G., K. A. Hollien, S. R. Bates, and W. A. Acree (1992), Dehydration of hydroxyl-interlayered vermiculite as a function of time and temperature, *Clay. Clay Min.*,40, 335-340.

He, H. P., J. G. Guo, J. X. Zhu, and C. Hu (2003), ²⁹Si and ²⁷Al MAS NMR study of the thermal transformations of kaolinite from North China, *Clay Min.*,38, 551-559.

Keeling, J. L., M. D. Raven, and W. P. Gates (2000), Geology and characterization of two hydrothermal nontronites from weathered metamorphic rocks at the Uley graphite mine, South Australia, *Clay. Clay Min.*,48, 537-548.

Kloprogge, J. T., S. Komarneni, K. Yanagisawa, R. L. Frost, R. Fry (1998), Infrared study of some synthetic and natural beidellites, *J. Mater. Sci. Lett.*,*17*, 1853-1855.

Kloprogge, J. T., R. L. Frost, and L. Hickey (1999a), Infrared absorption and emission study of synthetic mica-montmorillonite in comparison to rectorite, beidellite and paragonite, *J. Mater. Sci. Lett.*,*18*, 1921-1923.

Kloprogge, J. T., R. Fry, and R. L. Frost (1999b), An infrared emission spectroscopic study of the thermal transformation mechanisms in Al₁₃-pillared clay catalysts with and without tetrahedral substitutions, *J. Catal.*,*184*, 157-171.

Kloprogge, J. T., R. L. Frost, and L. Hickey (2000a), Infrared emission spectroscopic study of the dehydroxylation of some hectorites, *Thermochim. Acta*,*345*, 145-156.

Kloprogge, J. T., and R. L. Frost (2000b), The effect of synthesis temperature on the FT-Raman and FT-IR spectra of saponites, *Vib. Spectrosc.*,*23*, 119-127.

Kloprogge, J. T., and R. L. Frost (2005), Infrared emission spectroscopy of clay minerals: In *The application of vibrational spectroscopy to clay minerals and layered double hydroxides*, CMS Workshop Lectures, Vol. 13, J. Theo Kloprogge ed., The Clay Mineral Society, Aurora, CO, 99-124.

Kulbicki, G. (1959), High temperature phases in sepiolite, attapulgite and saponite, *The American Mineralogist*, *44*, 752-764.

Lambert, J. F., W. S. Millman, and J. J. Fripiat (1989), Revisiting kaolinite dehydroxylation: A ²⁹Si and ²⁷Al MAS NMR study, *J. Am. Chem. Soc.*,*111*, 3517-3522.

Lange, M. A., and T. J. Ahrens (1982), Impact induced dehydration of serpentine and the evolution of planetary atmosphere. *Proc. 13th Lunar Planet. Sci. Conf.*, A451-A456.

Loizeau, D., N. Mangold, F. Poulet, J. -P. Bibring, A. Gendrin, V. Ansan, C. Gomez, B. Gondet, Y. Langevin, P. Masson, and G. Neukum (2007), Phyllosilicates in the Mawrth Vallis region of Mars, *J. Geophys. Res.*, 112, E08S08, doi:10.1029/2006JE002877.

Madejov *a'*, J., and P. Komadel (2001), Baseline studies of the clay minerals society source clays: Infrared methods, *Clay. Clay Min.*, 49, 410-432.

Mangold, N., et al. (2007), Mineralogy of the Nili Fossae region with OMEGA/Mars Express data; 2. Aqueous alteration of the crust, *J. Geophys. Res.*, 112, E08S04, doi:10.1029/2006JE002835.

Massiot, D., P. Dion, J. F. Alcover, and F. Bergaya (1995), ²⁷Al and ²⁹Si MAS NMR study of kaolinite thermal decomposition by controlled rate thermal analysis, *J. Am. Ceram. Soc.*, 78, 2940-2944.

McManus, J., S. E. Ashbrook, K. J. D. MacKenzie, and S. Wimperis (2001), ²⁷Al multiple-quantum MAS and ²⁷Al{¹H} CPMAS NMR study of amorphous aluminosilicates, *J. Non-Cryst. Solids*, 282, 278-290.

Mermut, A. R., and A. Faz Cano (2001), Baseline studies of the clay minerals society source clays: Chemical analyses of major elements, *Clay. Clay Min.*, 49, 381-386.

Michalski, J. R., and R. L. Fergason (2009), Composition and thermal inertia of the Mawrth Vallis region of Mars and THEMIS data, *Icarus*, 199, 25-48, doi: 10.1016/j.icarus.2008.08.016.

Michalski, J. R., and E. Z. Noe Dobrea (2007), Evidence for a sedimentary origin of clay minerals in the Mawrth Vallis region, Mars, *Geology*,*35*, 951-954.

Michalski, J. R., M. D. Kraft, T. G. Sharp, L. B. Williams, and P. R. Christensen (2005), Mineralogical constraints on the high-silica martian surface component observed by TES, *Icarus*,*174*, 161-177.

Michalski, J. R., M. D. Kraft, T. G. Sharp, L. B. Williams, and P. R. Christensen (2006), Emission spectroscopy of clay minerals and evidence for poorly crystalline aluminosilicates on Mars from Thermal Emission Spectrometer data, *J. Geophys. Res.*,*111*, E03004, doi:10.1029/2005JE002438.

Michalski, J. R., F. Poulet, J. -P. Bibring, and N. Mangold (2010), Analysis of phyllosilicate deposits in Nili Fossae region of Mars: Comparison of TES and OMEGA data, *Icarus*, doi:10.1016/j.icarus.2009.09.006.

Milliken, R. E., and J. F. Mustard (2005), Quantifying absolute water content of minerals using near-infrared reflectance spectroscopy, *J. Geophys. Res.*,*110*, E12001, doi:10.1029/2005JE002534.

Milliken, R. E., J. F. Mustard, F. Poulet, D. Jouglet, J.-P Bibring, B. Gondet, and Y. Langevin (2007), Hydration state of the Martian surface as seen by Mars Express OMEGA: 2. H₂O content of the surface, *J. Geophys. Res.*, 112, E08S07, doi:10.1029/2006JE002853.

Moore, D. M. and R. C. Reynolds Jr. (1989a), Structure and properties of clay minerals, In *X-Ray Diffraction and the Identification and Analysis of Clay Minerals*, pp. 102-178, Oxford University Press, Oxford.

Moore, D. M. and R. C. Reynolds Jr. (1989b), *X-Ray Diffraction and the Identification and Analysis of Clay Minerals*, pp. 187-190, Oxford University Press, Oxford.

Murchie, S. L., et al. (2009), Compact Reconnaissance Imaging Spectrometer for Mars investigation and data set from the Mars Reconnaissance Orbiter's primary science phase, *J. Geophys. Res.*, *114*, E00D07, doi: 10.1029/2009JE003344.

Mustard, J. F., S. L. Murchie, B. L. Ehlmann, S. M. Pelkey, L. A. Roach, F. Seelos, F. Poulet, J. -P. Bibring, N. Mangold, J. A. Grant, R. E. Milliken and the CRISM team (2007), CRISM-OMEGA observations of phyllosilicate-olivine stratigraphy in Nili Fossae, Mars, *Lunar Planet. Sci.*, *38th*, abstract 2071.

Mustard, J. F., S. L. Murchie, S. M. Pelkey, B. L. Ehlmann, R. E. Milliken, J. A. Grant, J.-P. Bibring, F. Poulet, J. L. Bishop, E. Z. Noe Dobrea, L. H. Roach, F. P. Seelos, R. E. Arvidson, S. Wiseman, R. Green, C. Hash, D. Humm, E. Malaret, J. A. McGovern, Y. Langevin, T. Martin, P. McGuire, R. Morris, M. S. Robinson, T. Roush, M. Smith, G. Swayze, H. Taylor, and M. Wolf (2008), Hydrated silicate minerals on Mars observed by the Mars Reconnaissance Orbiter CRISM instrument, *Nature*, *454*, 305-309, doi:10.1038/nature07097.

Newsam, J. M. (1986), The zeolite cage structure, *Science*, *231*, 1093--1099.

Ohnishi, I., and K. Tomeoka (2002), Dark inclusions in the Mokoia CV3 chondrite: Evidence for aqueous alteration and subsequent thermal and shock metamorphism, *Met. Planet.Sci.*, *37*, 1843--1856.

Post, J. L. (1984), Saponite from near Ballarat, California, *Clay. Clay Min.*, *32*, 147--153.

Poulet, F., J. -P. Bibring, J. F. Mustard, A. Gendrin, N. Mangold, Y. Langevin, R. E. Arvidson, B. Gondet, and the OMEGA team (2005), Phyllosilicates on Mars and implications for early martian climate, *Nature*, 438, 623--627.

Poulet, F., C. Gomez, J.-P. Bibring, Y. Langevin, B. Gondet, P. Pinet, G. Belluci, and J. Mustard (2007), Martian surface mineralogy from Observatoire pour la Minéralogie, l'Eau, les Glaces et l'Activité on board the Mars Express spacecraft (OMEGA/MEx): Global mineral maps, *J. Geophys. Res.*, 112, E08S02, doi:10.1029/2006JE002840.

Prasad, P. S. R., K. S. Prasad, and S. R. Murthy (2005), Dehydration of natural stilbite: An *in situ* FTIR study, *American Mineralogist*, 90, 1630-1640.

Prasad, P. S. R., and K. S. Prasad (2007), Dehydration and rehydration of mesolite: An *in situ* FTIR study, *Microporous and Mesoporous Materials*, 100, 287-294.

Pruett, R. J., and H. L. Webb (1993), Sampling and analysis of KGa-1b well-crystallized kaolin source clay, *Clay. Clay Min.*, 41, 514--519.

Roch, G. E., M. E. Smith, and S. R. Drachman (1998), Solid state NMR characterization of the thermal transformation of an illite-rich clay, *Clays Clay Min.*, 46, 694-704.

Rocha, J. (1999), Single- and triple-quantum ^{27}Al MAS NMR study of the thermal transformation of kaolinite, *J. Phys. Chem. B*, 103, 9801-9804.

Rocha, J., and J. Klinowski (1990), ^{29}Si and ^{27}Al magic-angle-spinning NMR studies of the thermal transformation of kaolinite, *Phys. Chem. Mineral.*, 17, 179-186.

Rodriguez-Fuentes, G., A. R. Ruiz-Salvador, M. Mir, O. Picazo, G. Quintana, and M. Delgado (1998), Thermal and cation influence on IR vibrations of modified natural clinoptilolite, *Microporous and Mesoporous Materials*, 20, 269-281.

Rogers, A. D., and P. R. Christensen (2007), Surface mineralogy of Martian low-albedo regions from MGS-TES data: Implications for upper crustal evolution and surface alteration, *J. Geophys. Res.*, 112, E01003, doi:10.1029/2006JE002727.

Ruff, S. W. (2003), Basaltic andesite or weathered basalt: A new assessment, *Sixth Intl. Conf. Mars*, abstract 3258.

Ruff, S. W. (2004), Spectral evidence for zeolite in the dust on Mars, *Icarus*, 168, 131-143, doi:10.1016/j.icarus.2003.11.003.

Ruff, S. W., and P. R. Christensen (2007), Basaltic andesite, altered basalt, and a TES-based search for smectite clay minerals on Mars, *Geophys. Res. Lett.*, 34, L10204, doi:10.1029/2007GL029602.

Salisbury, J. W. (1993), Mid-infrared spectroscopy: laboratory data, In *Remote Geochemical Analysis: Elemental and Mineralogical Composition*, edited by C. M. Pieters and P. A. J. Englert, pp. 79-98, Cambridge Univ. Press, New York.

Sanchez-Soto, P. J., I. Sobrados, J. Sanz, and J. L. Perez-Rodriguez (1993), ^{29}Si and ^{27}Al magic-angle-spinning nuclear magnetic resonance study of the thermal transformations of pyrophyllite, *J. Am. Ceram. Soc.*, 76, 3024-3028.

Sanz, J., A. Madani, J. M. Serratosa, J. S. Moya, and S. Aza (1988), ^{27}Al and ^{29}Si magic-angle spinning nuclear magnetic resonance study of the kaolinite-mullite transformation, *J. Am. Ceram. Soc.*, *71*, C418-C421.

Sarikaya, Y., M. Onal, B. Baran, and T. Alemdaroglu (2000), The effect of thermal treatment on some of the physiochemical properties of a bentonite, *Clay. Clay Min.*, *48*, 557-562.

Slade, R. C. T., and T. W. Davies (1991), Evolution of structural changes during flash calcination of kaolinite: A ^{29}Si and ^{27}Al nuclear magnetic resonance spectroscopy study, *J. Mater. Chem.*, *1*, 361-364.

Tomioka, N., K. Tomeoka, K. Nakamura-Messenger, and T. Sekine (2007), Heating effects of the matrix of experimentally shocked Murchison CM chondrite: Comparison with micrometeorites, *Met. Planet. Sci.*, *42*, 19-30.

Tonui, E. K., M. E. Zolensky, M. E. Lipschutz, M. S. Wang, and T. Nakamura (2003), Yamato 86029: Aqueously altered and thermally metamorphosed CI-like chondrite with unusual textures, *Met. Planet. Sci.*, *38*, 269-292.

Tyburczy, J. A., and T. J. Ahrens (1988), Dehydration kinetics of shocked serpentine, *Proc. Lunar Planet. Sci. Conf. 18th*, 435-441.

Van der Marel, H. W., and H. Beutelspacher (1976), in: *Atlas of infrared spectroscopy of clay minerals and their admixtures*, Elsevier, Amsterdam, pp191.

Van Olphen, H., and J. J. Fripiat (1979), *Data Handbook for Clay Materials and other Non-Metallic Minerals*, Pergamon, Oxford.

Villieras, F., J. Yvon, J. M. Cases, P. De Donato, F. Lhote, and R. Baeza (1994), Development of microporosity in clinocllore upon heating, *Clays and Clay Minerals*, 42 (6), 679-688.

Wyatt, M. B., and H. Y. McSween Jr (2002), Spectral evidence for weathered basalt as an alternative to andesite in the northern lowlands of Mars, *Nature*, 417, 263—266.

Chapter 3: The effect of high temperatures on the mid-to-far-infrared emission and near-infrared reflectance spectra of phyllosilicates and natural zeolites: Implications for Martian exploration

This part is a reformatted version of a paper by the same name published in Icarus in 2012 by Congcong Che and Timothy D. Glotch. All laboratory measurements were performed by Congcong Che.

Che, C., and T. D. Glotch (2011), The effect of high temperatures on the mid-to-far-infrared emission and near-infrared reflectance spectra of phyllosilicates and natural zeolites: Implications for Martian exploration, Icarus, 218, 585-601.

Abstract

Most phyllosilicates on Mars appear to be associated with ancient terrains. As such, they may have experienced shock heating produced by impacts and could have been significantly altered or melted. We characterized the effects of high temperatures on the mid-to-far-infrared (mid-to-far-IR) emission ($100\text{-}1400\text{ cm}^{-1}$; $7.1\text{-}100\text{ }\mu\text{m}$) and near-infrared (NIR) reflectance ($1.2\text{-}2.5\text{ }\mu\text{m}$) spectra of phyllosilicates by measuring experimentally calcined ($100\text{-}900\text{ }^{\circ}\text{C}$) phyllosilicates and also two zeolites. Correlated differential scanning calorimetry (DSC) measurements were also performed on each sample to provide insight into the thermal activities of the phyllosilicates and natural zeolites. Our results indicate that all phyllosilicates exhibit characteristic degradations in both NIR and mid-to-far-IR spectral properties between $400\text{-}800\text{ }^{\circ}\text{C}$, mainly attributable to the

dehydroxylation and recrystallization processes as temperature increases. Spectral features of natural zeolites persist to higher temperatures compared to features of phyllosilicates during heating treatments. The thermal behaviors of phyllosilicate infrared (IR) properties are greatly influenced by the compositions of the octahedral cations: (1) changes in both the NIR and mid-to-far-IR spectra of phyllosilicates tend to occur at lower temperatures (300 to 400 °C) in the Fe³⁺-rich samples as compared to the Al³⁺-rich types (400-600 °C); (2) Mg²⁺-trioctahedral phyllosilicates hectorite, saponite, and sepiolite all display major mid-to-far-IR spectral changes at 700 °C, corresponding to the formation of enstatite; (3) phyllosilicates that have minor replacement of Mg²⁺ for Al³⁺ in octahedral positions (e.g. cheto-type montmorillonite and palygorskite) show an absorption band at ~920 cm⁻¹ that becomes strong at 900 °C. Inconsistency between spectral behaviors in the mid-to-far-IR and NIR regions is also discussed for phyllosilicates. Results from this study have provided suggestive evidence for the scenario that some phyllosilicates could lose all original spectral features in mid-to-far-IR region while maintaining their characteristic hydration bands in NIR region in the same temperature range.

Keywords: Mars; Mineralogy; Spectroscopy

3.1. Introduction

Phyllosilicates detected on the surface of Mars are primarily associated with heavily cratered Noachian terrains (e.g., Poulet *et al.* 2005; Bibring *et al.* 2006; Mangold *et al.* 2007; Michalski

and Noe Dobrea 2007). It has been suggested that at least some phyllosilicates on Mars were likely formed from long-lived hydrothermal systems initiated by impact processes (e.g., Schwenger and Kring 2009), while others have suggested that pre-existing phyllosilicates were excavated by repeated impact events (Fairén *et al.* 2010). Abramov and Kring (2005) modeled an impact-induced hydrothermal system on Mars and the results indicated that temperatures as high as 1200 °C could last for thousands of years in the region of the impact. Fairén *et al.* (2010) calculated the temperature increases in a transient crater resulting from an impact, and their model showed that temperatures can reach close to 1000 °C in a certain area around the point of impact. In the laboratory, 400-500 °C is sufficient for phyllosilicates to lose their interlayer H₂O and most phyllosilicates can be completely dehydroxylated at 900 °C (e.g., Che *et al.* 2011). These previous conclusions lead us to propose that phyllosilicates on Mars may have been affected by impact processes, with an emphasis on post-shock heating, and that dehydrated and/or dehydroxylated phyllosilicates may be present on the Martian surface.

The process of phyllosilicate dehydration or dehydroxylation may also help explain the apparent disconnect between visible and near-IR (VNIR) and thermal IR (TIR) observations of phyllosilicates on Mars. Data from the Mars Express Observatoire pour la Minéralogie, l'Eau, les Glaces, et l'Activité (MEx/OMEGA) (0.4-5 µm, 0.3-2 km/pixel) and Compact Reconnaissance Imaging Spectrometer for Mars (MRO/CRISM) (0.4-3.9 µm, 18 m/pixel) VNIR imaging spectrometers have provided unambiguous evidence for the widespread presence of phyllosilicates (e.g., Poulet *et al.* 2005; Bibring *et al.* 2006; Loizeau *et al.* 2007; Mangold *et al.* 2007), while global detection of phyllosilicates in the Mars Global Surveyor (MGS) Thermal Emission Spectrometer (TES) data (6-50 µm, ~3 x 8km/pixel) has remained unclear because it is difficult to distinguish phyllosilicates and amorphous silica-rich phases (e.g., glass or amorphous

weathering products) in the truncated spectral range of TES (e.g., Bandfield 2002; Ruff 2003; Michalski *et al.* 2005; Michalski *et al.* 2006; Ruff and Christensen 2007). However, it may be possible to identify these minerals at local scales. The phyllosilicate deposits in Nili Fossae detected by OMEGA exhibited different spectral features from surrounding regions in Thermal Emission Imaging System (THEMIS, 6-15 μm , 100m/pixel) images (McDowell and Hamilton 2007a, 2007b). The THEMIS phyllosilicate index of Viviano and Moersch(2011) also indicated that THEMIS may be able to provide more reliable phyllosilicate abundance than TES because of its higher spatial resolution. The bright and dark terrains around Mawrth Vallis show distinct spectral character in TES data, in which the dark terrain is consistent with TES Surface Type 1 (ST1, Bandfield *et al.* 2000) while the bright terrain is clearly different. In the Mawrth Vallis phyllosilicate deposits, TES spectra show evidence for significant abundances of poorly crystalline silica that may be actual opaline silica or a spectroscopic substitution for poorly crystalline phyllosilicates (Michalski and Fergason 2009). Also in the Nili Fossae region, recent work by Michalski *et al.* (2010) shows that it is possible to identify phyllosilicate deposits from their long-wavelength spectral features. TES data consistently show a spectral absorption located near 450 cm^{-1} within the same surfaces where OMEGA and CRISM show phyllosilicate occurrences around Nili Fossae. While the presence of these features is consistent with the occurrence of Fe^{2+} -bearing phyllosilicates and/or poorly crystalline Fe/Mg-rich clays, the overall TES spectrum of these surfaces lacks other diagnostic bands normally associated with phyllosilicates: Si-O stretching features in the $900\text{-}1100\text{ cm}^{-1}$ region. In summary, TES TIR and OMEGA/CRISM VNIR spectra give different perspectives on phyllosilicate mineralogy, crystallinity, and abundance on Mars. Among the potential reasons for this disconnect is the possibility that phyllosilicates on Mars have been modified by the effects of dehydration and/or

dehydroxylation. Such effects modify the mineral structures in such a way that their spectroscopic signatures appear different from various wavelength-perspectives. Laboratory spectral studies of dehydrated or dehydroxylated phyllosilicates are essential to characterize how high temperatures affect NIR and TIR spectra in different ways.

The effects of high temperatures on VNIR reflectance spectra of several types of phyllosilicates (including montmorillonites and nontronites) were studied previously (e.g., Milliken and Mustard 2005; Fairén *et al.* 2010; Gavin and Chevrier 2010). In general, these laboratory studies showed that VNIR spectra of phyllosilicates change distinctly as temperature increases and become mostly featureless because of the dehydroxylation process at temperatures above 700 °C. However, there is no substantive work that thoroughly describes the mid-to-far-IR emissivity spectra of dehydrated and/or dehydroxylated phyllosilicates. A detailed study was carried out on the attenuated total reflectance (ATR) and mid-to-far-IR specular reflectance of dehydrated and/or dehydroxylated phyllosilicates by Che *et al.* (2011). The reflectance spectra can be used to approximate emissivity spectra using Kirchhoff's Law ($E=1-R$). However, Kirchhoff's Law only holds true when the surface is a Lambertian scatterer (e.g., Salisbury *et al.* 1994), so laboratory mid-to-far-IR reflectance spectra may have limitations when applied to analysis of data from the non-Lambertian Martian surface. In this study we present the mid-to-far-IR emissivity and NIR reflectance spectra of dehydrated and/or dehydroxylated phyllosilicates (from the same suite of samples as in Che *et al.* 2011). These samples come from four structural groups: kaolinite, smectite, chlorite, and palygorskite-sepiolite. In addition to phyllosilicates, two natural zeolite samples were included in this study. Zeolites are also important hydrous minerals identified on Mars (e.g., Ruff 2004; Ehlmann *et al.* 2009) and they have similar chemical compositions to phyllosilicates. Analysis of zeolite samples can help

provide a more comprehensive database for characterizing how the mid-to-far-IR emissivity and NIR reflectance spectra of aluminosilicates change upon heating. The aim in this research is to (1) establish both mid-to-far-IR emissivity and NIR reflectance spectral libraries for identification of possible dehydrated/or dehydroxylated phyllosilicates on Mars, and (2) compare the spectral changes in the mid-to-far-IR region with those in the NIR region to characterize the different trends that could lead to the apparent disconnect between mid-to-far-IR and NIR detection of phyllosilicates on Mars.

3.2. Methods

3.2.1 Sample description, preparation, and characterization

In this study we collected the mid-to-far-IR emissivity spectra and NIR reflectance spectra of the same suite of phyllosilicates and natural zeolites from Che *et al.* (2011) (**Table 3.1**). All samples were purchased from the Clay Mineral Society (CMS) Source Clay Repository unless otherwise stated. Chemical compositions for these samples are summarized in **Table 3.2**. To facilitate precise characterization of all samples, the phyllosilicates and natural zeolites were prepared to <2 μ m size fractions prior to heat treatments. The phyllosilicates and natural zeolites were then heated for 24 hours to 100, 200, 300, 400, 500, 600, 700, 800, and 900 °C. To minimize the effects of rehydration processes, all heated products were stored in a desiccator before the spectral measurements and a purge gas system was used to remove CO₂ and water vapor from the spectrometer. Details of the preparation and X-ray diffraction (XRD) characterization of phyllosilicates and natural zeolites used for this work were reported in Che *et al.* (2011).

Table 3.1 Summary of phyllosilicates and zeolites for this study*

1.

Structural Group	Mineral	Sample Number	Source	Size Fraction
Smectite group				
	“Cheto” montmorillonite	SAz-1	CMS	<2 μm
	Texas montmorillonite	STx-1	CMS	<2 μm
	Na-montmorillonite (Wyoming)	SWy-2	CMS	<2 μm
	Montmorillonite (Otay)	SCa-3	CMS	<2 μm
	Mica-montmorillonite	Syn-1	CMS	<2 μm
	Beidellite	SBCa-1	CMS	<2 μm
	Hectorite	SHCa-1	CMS	<2 μm
	Saponite	SapCa-2	CMS	<2 μm
	Nontronite	NAu-1	CMS	<2 μm
	Nontronite	NAu-2	CMS	<2 μm
Kaolinite-serpentine group				
	Kaolinite	KGa-1b	CMS	<2 μm
Sepiolite-palygorskite group				
	Sepiolite	SepSp-1	CMS	<2 μm
	Palygorskite (Attapulgit)	PFl-1	CMS	<2 μm
Chlorite group				
	Clinochlore	Clinochlore	Mineral Unlimited	<2 μm
Zeolite group				
	Mordenite	27133	Mineral Research	<2 μm
	Clinoptilolite	27031	Mineral Research	<2 μm

* Table adopted from Che *et al.* 2011

Table 3.2 Summary of major elemental composition*

Sample number	SiO ₂	Al ₂ O ₃	Fe ₂ O ₃	FeO	TiO ₂	MgO	CaO	Na ₂ O	K ₂ O	P ₂ O ₅	OH/H ₂ O ¹
SAz-1 ²	51.36	17.20	1.54	n.a.	0.22	5.80	2.71	0.05	0.16	0.01	20.96
STx-1 ²	63.36	16.17	1.09	n.a.	0.24	3.43	1.57	0.28	0.06	0.01	13.78
SWy-2 ²	56.08	20.12	3.99	n.a.	0.08	2.68	1.08	1.34	0.18	0	14.45
SCa-3 ³	55.78	12.47	1.53	n.a.	n.a.	8.55	0.04	2.84	n.a.	n.a.	18.78
Syn-1 ²	47.70	36.75	0.11	n.a.	0.03	0.17	0.05	0.08	0	0	14.91
SBCa-1 ⁴	51.03	30.71	2.34	0.11	0.57	1.03	1.11	<0.01	0.79	0.12	12.17
SHCa-1 ²	46.11	0.85	0.32	n.a.	0.04	19.77	13.84	1.33	0.14	0	17.60
NAu-1 ⁵	41.55	6.59	29.07	n.a.	0.02	0.15	2.89	0.02	0.01	n.a.	19.70
NAu-2 ⁵	49.52	2.74	33.36	n.a.	0.02	0.23	2.06	0.12	0.01	n.a.	11.94
SapCa-2 ⁶	53.33	4.60	1.19	n.a.	0.09	24.49	1.30	1.19	0.19	n.a.	13.63
KGa-1b ⁷	43.98	38.22	0.20	n.a.	1.62	0.06	0.03	0.03	0.02	n.a.	15.84
SepSp-1 ⁸	55.00	1.40	0.40	0.02	0.04	22.38	1.07	<0.15	0.20	<0.05	19.29
PFI-1 ²	54.33	10.02	3.37	n.a.	0.43	9.52	1.70	0.05	0.78	0.83	18.97
Clinochlore ⁹	26.38	29.24	1.64	5.05	n.a.	25.36	n.a.	n.a.	n.a.	n.a.	12.34
27133 ¹⁰	67.06	15.51	n.a.	n.a.	n.a.	0.37	3.10	3.92	0.51	n.a.	12.58
27031 ¹¹	61.94	11.97	2.12	n.a.	0.23	1.61	0.91	4.02	1.54	n.a.	15.55

*Table adopted from Che *et al.* 2011;

¹ OH/H₂O takes as total weight loss on ignition (after heating sample to 1000 °C);

² Mermur & Faz Cano [2001];

³ Van olphen & Fripiat [1979];

⁴ Unofficially reported by CMS: <http://www.clays.org/SOURCE%20CLAYS/SCdata.html>;

⁵ Keeling *et al.* [2000];

⁶ Post [1984];

⁷ Pruett & Webb [1993];

⁸ USGS Digital Spectral Library: <http://speclab.cr.usgs.gov/spectral.lib04/DESCRIPT/sepiolite.SepSp-1.html>;

⁹ Ballet *et al.* [1985];

¹⁰ <http://www.handbookofmineralogy.org/pdfs/mordenite.pdf>;

¹¹ Bish [1984];

n.a.=not analysed

3.2.2 Differential scanning calorimetry measurements (DSC)

DSC measures the difference in heat required to maintain isothermal conditions between the sample and an inert reference at the same temperature (e.g., Hedley *et al.* 2007). DSC can be used to study the thermal reactions (e.g. endothermic and exothermic reactions) of phyllosilicates and natural zeolites during dehydration and/or dehydroxylation processes. In this study, DSC analyses of all phyllosilicates and natural zeolites were carried out in order to record thermal activity of each sample. We collected DSC curves of all size-separated samples by heating them from 25 °C to 1000 °C at 10 °C • min⁻¹ using a Netzsch Simultaneous TG-DTA/DSC Apparatus Model STA 449C analyser. All DSC curves were recorded in a N₂-protected environment. We relate the thermal behaviors of the phyllosilicates and zeolites with their IR spectral properties using DSC curves in Section 4.

3.2.3 Infrared spectroscopic measurements

The NIR diffuse reflectance and mid-to-far-IR emissivity spectra were acquired at Stony Brook University in the Vibrational Spectroscopy Laboratory (VSL) using a Nicolet 6700 FTIR spectrometer produced by Thermo Fisher. Each sample was pressed in a Carver hydraulic press at ~18,000 PSI to create a pellet, 13mm in diameter and about 3mm in thickness. This method has been used previously to prepare phyllosilicate samples for analysis by emission and specular reflectance spectroscopy (e.g., Michalski *et al.* 2005; Glotch *et al.* 2007). The purpose of pressing the samples into pellets with smooth surfaces is to minimize the spectral effects caused by physical properties, such as surface roughness and particle size (Michalski *et al.* 2005).

Therefore the spectral measurements of pressed samples could allow us to focus on the spectral differences among the phyllosilicates induced by their mineralogical properties. Although spectral laboratory studies of pelletized phyllosilicates may not be applied to the analysis of finely particulate phyllosilicates on Mars, previous work showed that the spectral features of pellet samples could be used for remote sensing of phyllosilicates occurring as coarse particles or indurated materials (Michalski *et al.* 2005).

3.2.3.1 NIR diffuse reflectance spectra The NIR reflectance spectra (1.2 – 2.5 μm) were collected for all samples and their heated products using a Thermo Fisher diffuse reflectance accessory. Spectra were ratioed to a gold mirror standard. For these measurements, the spectrometer was equipped with a CaF_2 beamsplitter and an InGaAs detector. For each sample, 2048 scans in the NIR spectral range were recorded with a resolution of 4 cm^{-1} .

3.2.3.2 Emissivity spectra Emissivity spectra in the mid-to-far-IR (100-2000 cm^{-1} , 100-5 μm) range were acquired by switching off the Global IR source and measuring the radiation from the heated samples directly. The samples were heated and maintained at 80 $^\circ\text{C}$ to provide adequate signal for the measurements. A blackbody heated to 70 $^\circ\text{C}$ and 100 $^\circ\text{C}$ was used to calibrate the emissivity spectra in the manner of Ruff *et al.* (1997). Spectra from 400 to 2000 cm^{-1} were acquired at 4 cm^{-1} resolution using a KBr beamsplitter and a DLaTGS detector with a KBr window. A total of 512 scans were averaged to produce each spectrum. Far-IR spectra were collected from 100 to 600 cm^{-1} using a Thermo Fisher Solid Substrate beamsplitter and a DLaTGS detector. A total of 2048 scans and 4 cm^{-1} resolution were used for this spectral range. The emissivity spectra were obtained for all samples and their heated products.

3.3. Results

3.3.1 Differential thermal investigation: DSC

DSC results for phyllosilicates and natural zeolites studied here are illustrated in **Fig. 3.1**. The endothermic or exothermic peaks shown in DSC curves are important features associated with physical or chemical transformation with a thermal effect. In **Fig. 3.1** the endothermic and exothermic activities of each sample are identified as absorption features and peak features, respectively.

In general, kaolinite (**Fig. 3.1a**) and clinocllore (**Fig. 3.1n**) both show two strong endothermic effects at ~600 °C and ~800 °C. The other 14 samples all exhibit an endothermic feature near 100 °C and distinct thermal activity features in the higher temperature range (200-1000 °C). The DSC curves of minerals from the same structural group resemble each other in shape but not in details. For example, DSC curves of PFI-1 palygorskite (**Fig. 3.1l**) and SepSp-1 sepiolite (**Fig. 3.1m**) are both characterized by a multistep endothermic process at temperatures lower than 600 °C and an endothermic-exothermic inversion feature near 850 °C. The temperature and extent of each reaction, however, are different for these two samples. This is also found to be the case for nontronites NAu-1 and NAu-2 (**Figs. 3.1f and 3.1g**), samples SBCa-1 and Syn-1 (**Figs. 3.1j and 3.1k**) with a beidellite composition (Kloprogge et al. 1999a), and natural zeolites 27031 and 27133 (**Figs. 3.1o and 3.1p**). In the case of montmorillonites, STx-1 sample (**Fig. 3.1d**) gives a DCS curve similar to the SWy-2 sample (**Fig. 3.1e**) while DSC patterns for SAz-1 and SCa-3 montmorillonites differ from the previous two montmorillonite samples.

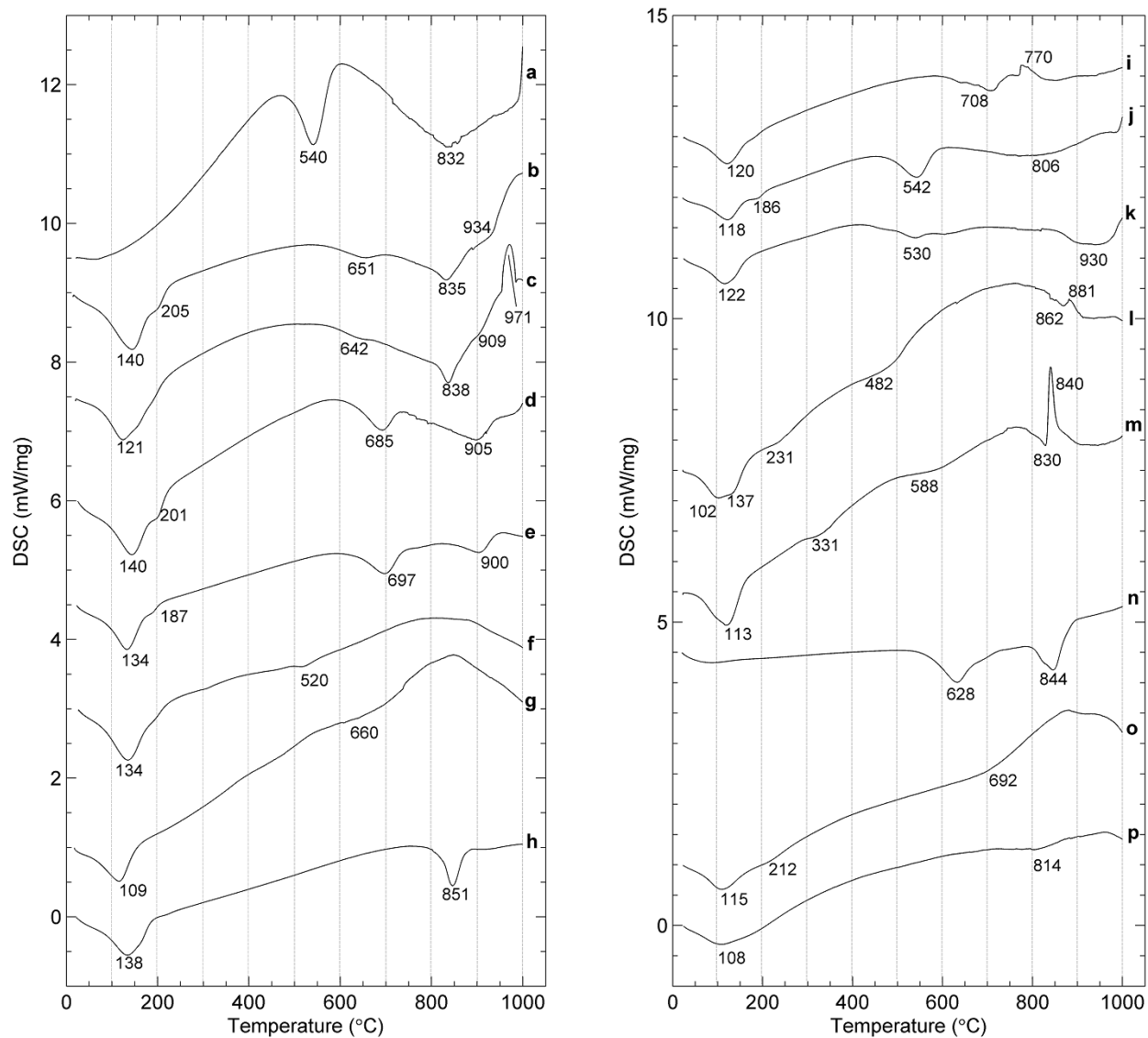


Figure 3.1 DSC curves (offset) of (a) KGa-1b kaolinite, (b) SAz-1 "Cheto" montmorillonite, (c) SCa-3 montmorillonite (Otay), (d) STx-1 Texas montmorillonite, (e) SWy-2 Na-montmorillonite (Wyoming), (f) NAu-1 nontronite, (g) NAu-2 nontronite, (h) SapCa-2 saponite, (i) SHCa-1 hectorite, (j) SBa-1 beidellite, (k) Syn-1 mica-montmorillonite, (l) PFI-1 palygorskite, (m) SepSp-1 sepiolite, (n) Clinochlore, (o) 27031 clinoptilolite, and (p) 27133 mordenite.

3.3.2 Mid-to-far-IR emissivity spectra

Spectral features in the mid-to-far-IR region are dominated by fundamental molecular vibration bands and are a particularly important indicator of mineralogy and chemical composition for the major rock-forming minerals (e.g., Salisbury 1993). Spectral features of phyllosilicates in this region and their interpretations have been studied comprehensively by numerous authors (e.g., Farmer 1974; Van der Marel and Beutelspacher 1976; Klopogge *et al.* 1998; Klopogge *et al.* 1999a, 1999b; Klopogge *et al.* 2000; Frost and Klopogge 2000; Frost *et al.* 2002; Madajova and Komadel 2001; Michalski *et al.* 2005; Bishop *et al.* 2008; Che *et al.* 2011). In general, absorption bands near 1200-1000 cm^{-1} are due to Si-O stretching motions in the tetrahedral sheets, spectral features near 550-400 cm^{-1} are associated with Si-O-Si bending vibrations in the tetrahedral sheets and M-O-Si (M=Al³⁺, Fe³⁺, Fe²⁺, or Mg²⁺ in the octahedral sheets) deformation modes, and spectral bands observed in the 950-590 cm^{-1} range are related to M-OH or M-M-OH bending vibrations in octahedral sheets. Spectral features in the far-IR region (<400 cm^{-1}) are assigned to the interlayer cations and mixed vibrations that include the Si-O network, octahedral cations, and hydroxyl groups. It is noteworthy that the ~1600 cm^{-1} spectral feature due to H-O-H bending vibration is extremely weak, due to the use of pelletized samples (e.g., Salisbury 1993). As a result, the 1400-2000 cm^{-1} region of the spectrum appears featureless. Therefore the subsequent figures only show the 100-1400 cm^{-1} region of the spectrum.

3.3.2.1 Kaolinite group

For kaolinite (**Fig. 3.2**), the multiple spectral bands occurring near 1200-1000 cm^{-1} and 550-400 cm^{-1} change significantly upon heating. At 400 $^{\circ}\text{C}$ they are replaced by new bands near 1067 cm^{-1} and 440 cm^{-1} , respectively. These two new absorption features shift gradually to higher wavenumbers with increasingly higher temperatures. These two bands also become narrower at 800 $^{\circ}\text{C}$. As with the spectral features in the mid-IR region (1400-400 cm^{-1}), spectral bands in the far-IR region disappear at 400 $^{\circ}\text{C}$. No new bands are observed at higher temperatures in this region.

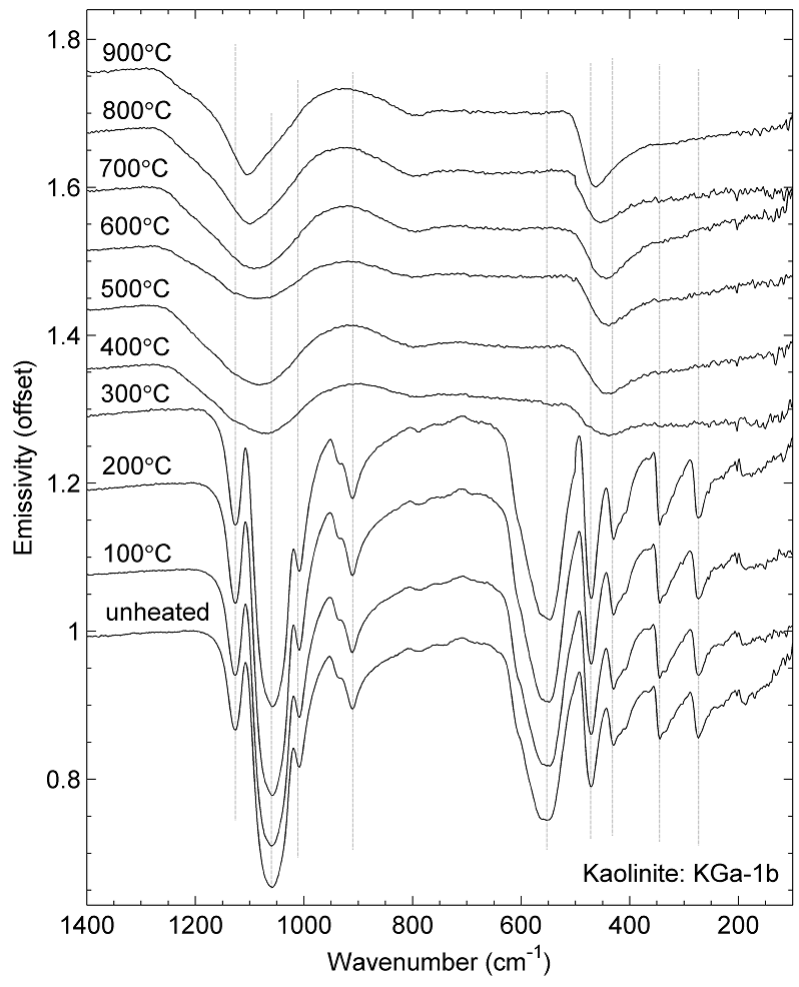


Figure 3.2 100-1400 cm⁻¹ emissivity spectra of kaolinite (KGa-1b) calcined at various temperatures. Linear vertical offset is applied to the spectra for clarity.

3.3.2.2 Smectite group

Fig. 3.3 shows mid-to-far-IR emissivity spectra for four montmorillonite samples (a fifth sample, Syn-1 mica-montmorillonite is discussed later with the beidellite sample SB_{Ca}-1, because a previous study (Kloprogge et al. 1999a) indicates that both its chemical composition and spectral features are close to those for beidellite.) and their Si-O stretching bands are all composed of a strong absorption feature near 1065 cm⁻¹ and a weak shoulder absorption feature near 1130 cm⁻¹. The shoulder absorption feature becomes stronger as temperature is increased and at 600 °C, it develops into an absorption feature with a detectable intensity. However, this feature becomes weak again at 700 °C for SAz-1 and S_{Ca}-3 montmorillonites, then disappears completely at 800 °C for all four montmorillonites. The strong Si-O stretching band of the four montmorillonites disappears and is replaced by a new strong band at ~1100 cm⁻¹ at 800 °C. At 900 °C, this 1100 cm⁻¹ feature displays a distinct shift towards high wavenumbers for the SAz-1 and S_{Ca}-3 samples while showing no change for STx-1 and SWy-2. In the Si-O bending region, all montmorillonite samples exhibit a doublet feature at ~470 and ~530 cm⁻¹, which is completely lost and replaced by a strong band (~490 cm⁻¹) with two weak shoulders (~570 and ~420 cm⁻¹) at 500 °C (600 °C for SWy-2). At 800 °C, these shoulder spectral bands disappear and the new strong feature shifts to lower wavenumbers. Therefore, the Si-O bending region of all four montmorillonites has a strong absorption near 460 cm⁻¹ at 800 °C. No additional changes occur to this strong feature for STx-1 and SWy-2 at 900 °C. However, this 460 cm⁻¹ spectral feature becomes significantly stronger and shifts to lower wavenumbers (~425 cm⁻¹) for SAz-1 and S_{Ca}-3. A weak spectral band at ~330 cm⁻¹ is observed for all montmorillonites. This feature shifts to lower wavenumbers (~300 cm⁻¹) at 500 °C (600 °C for SWy-2 montmorillonite) and disappears completely at 800 °C.

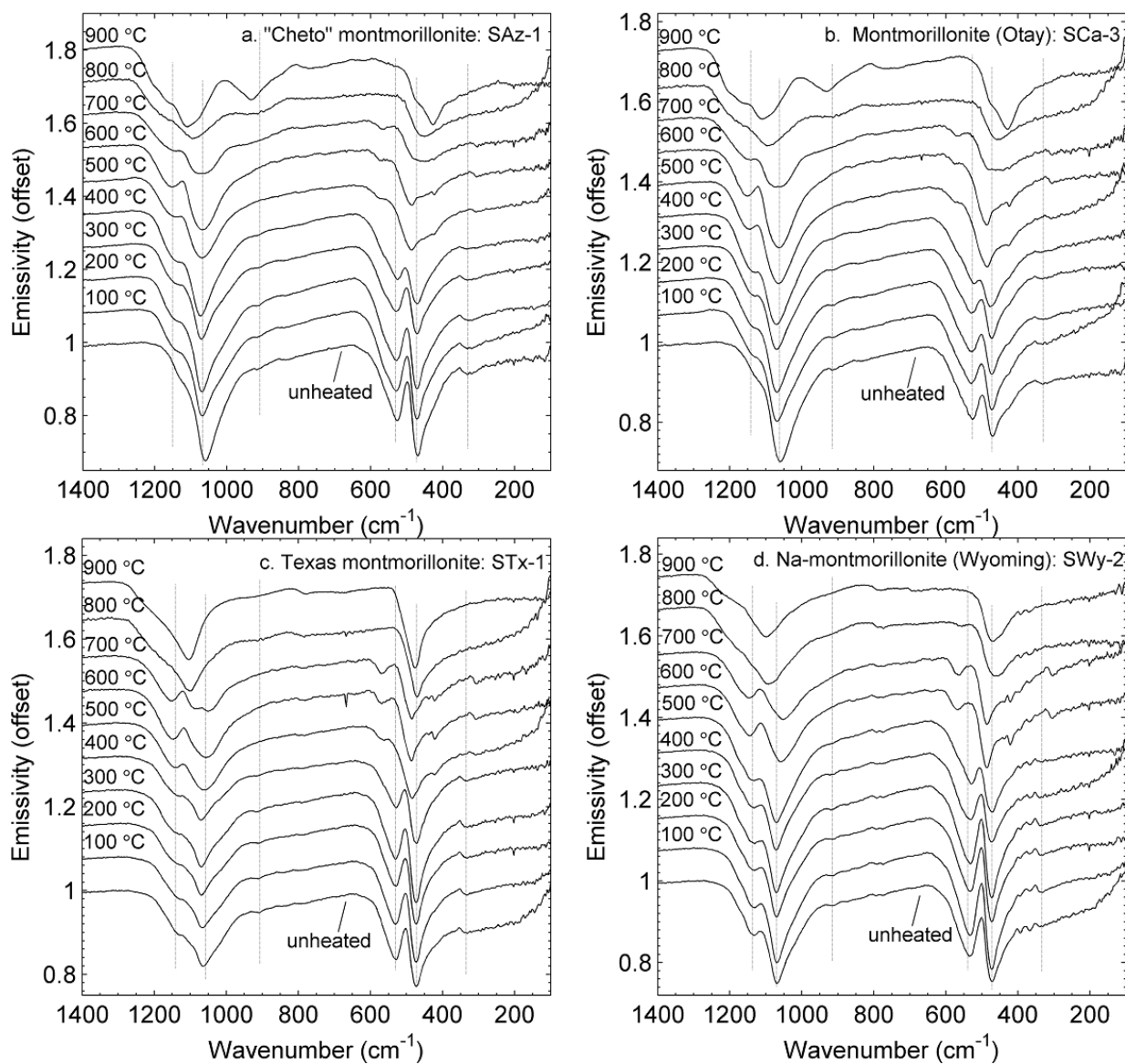


Figure 3.3 (a) 100-1400 cm^{-1} emissivity spectra of “Cheto” montmorillonite (SAz-1) calcined at various temperatures. (b) 100-1400 cm^{-1} emissivity spectra of montmorillonite (Otay) (SCa-3) calcined at various temperatures. (c) 100-1400 cm^{-1} emissivity spectra of Texas montmorillonite (STx-1) calcined at various temperatures. (d) 100-1400 cm^{-1} emissivity spectra of Na-montmorillonite (Wyoming) (SWy-2) calcined at various temperatures. Linear vertical offset is applied to the spectra for clarity.

For the two nontronite samples (**Fig. 3.4a**: N Au-1 and **Fig. 3.4b**: N Au-2) in this study, the multiple Si-O stretching features near 1100 cm^{-1} are replaced by a strong absorption band at $\sim 1080\text{ cm}^{-1}$ upon heating to $400\text{ }^{\circ}\text{C}$. This new feature continually shifts towards higher wavenumbers with increasing temperature. It is also important to note that a new shoulder feature develops near 1200 cm^{-1} at $800\text{ }^{\circ}\text{C}$ for both nontronite samples. The Si-O bending bands of the nontronite samples disappear and forming a single new feature near 450 cm^{-1} . At $800\text{ }^{\circ}\text{C}$ this new band becomes narrower and shows a slight shift to higher wavenumbers ($\sim 470\text{ cm}^{-1}$). Two nontronite samples both display multiple weak features in the $400\text{-}200\text{ cm}^{-1}$ range. At $400\text{ }^{\circ}\text{C}$ these bands are lost and replaced by a weak band near 310 cm^{-1} . This weak feature then disappears at $800\text{ }^{\circ}\text{C}$.

Only one main spectral change is observed for SapCa-2 saponite (**Fig. 3.5**) during the heating treatment. Upon heating to $700\text{ }^{\circ}\text{C}$, the spectrum of saponite exhibits completely different features from those at $600\text{ }^{\circ}\text{C}$. These new bands become stronger as temperature is increased. SHCa-1 hectorite (**Fig. 3.6**) has a similar spectral behavior to saponite, which includes the disappearance of the original spectral bands and appearance of multiple spectral features in Si-O stretching, Si-O bending and far-IR regions at $700\text{ }^{\circ}\text{C}$. These new features become stronger upon heating to $900\text{ }^{\circ}\text{C}$.

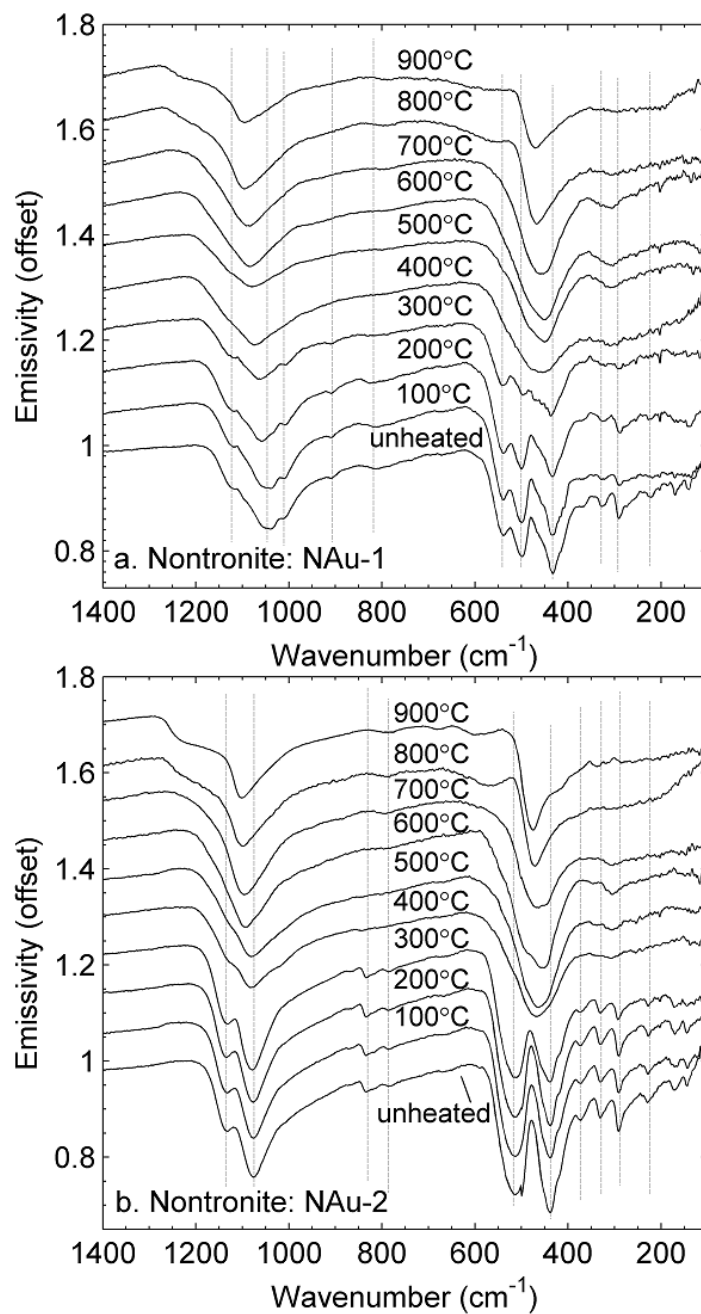


Figure 3.4 (a) 100-1400 cm^{-1} emissivity spectra of nontronite (NAu-1) calcined at various temperatures. (b) 100-1400 cm^{-1} emissivity spectra of nontronite (NAu-2) calcined at various temperatures. Linear vertical offset is applied to the spectra for clarity.

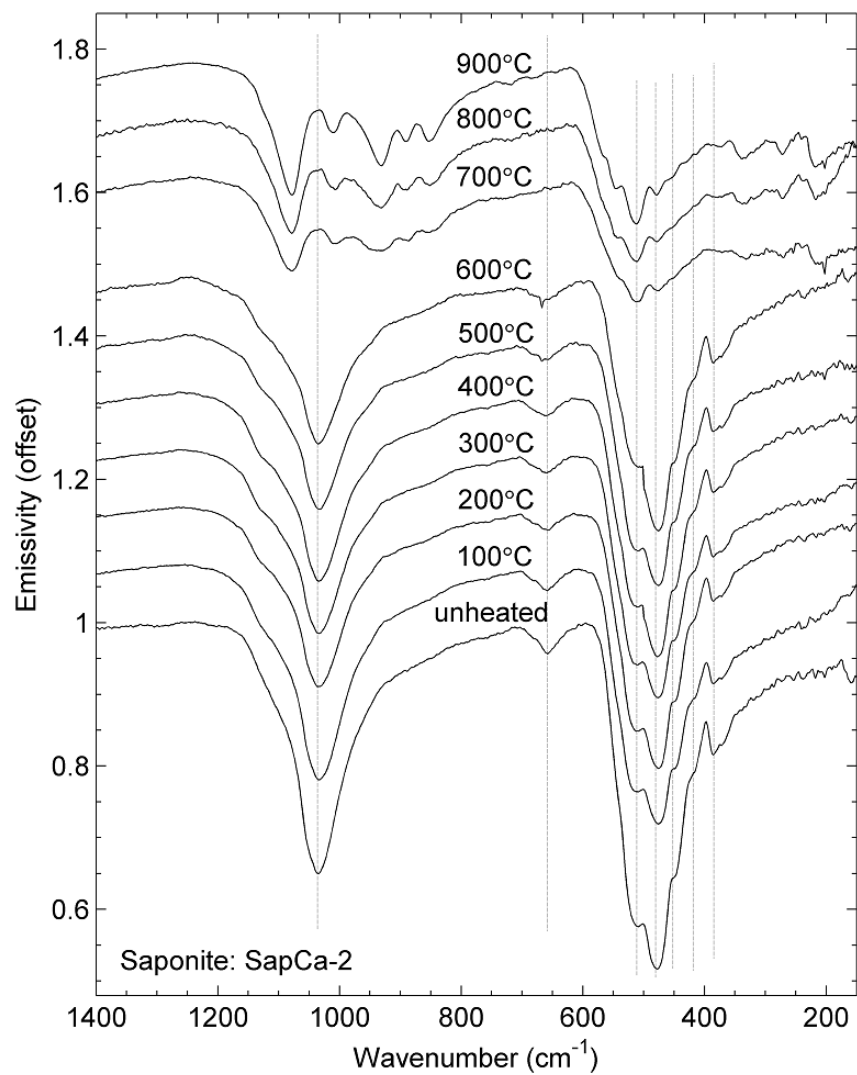


Figure 3.5 150-1400 cm^{-1} emissivity spectra of Saponite (SapCa-2) calcined at various temperatures. Linear vertical offset is applied to the spectra for clarity.

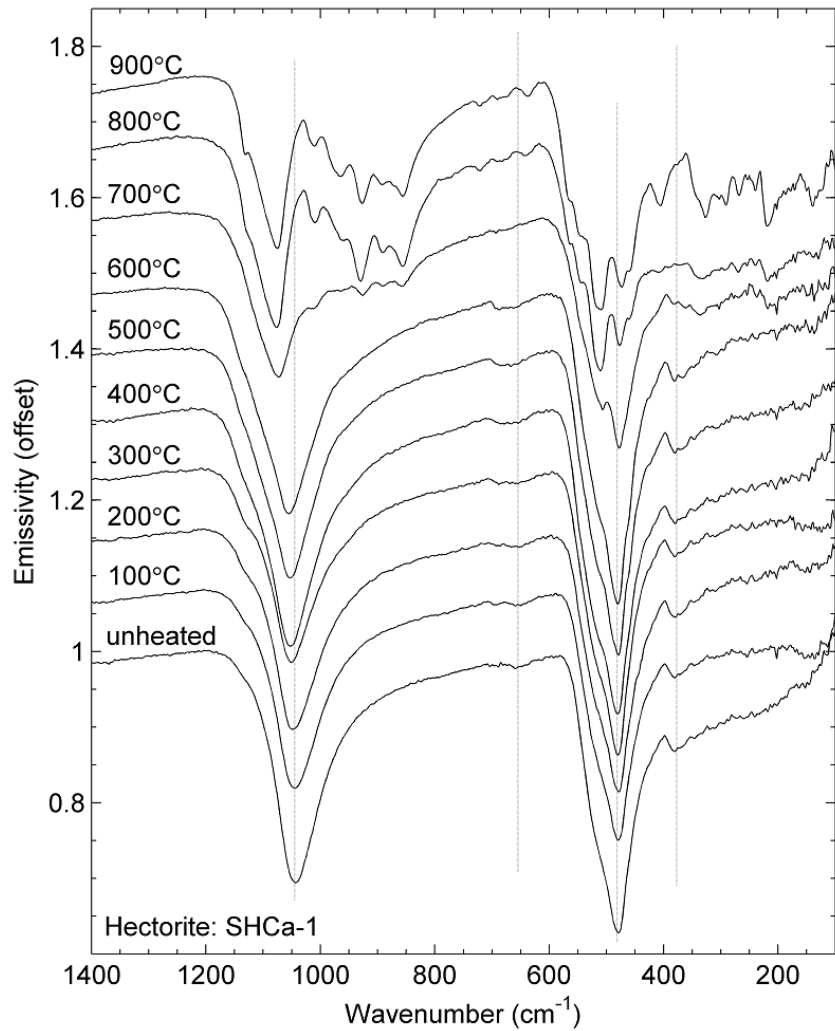


Figure 3.6 100-1400 cm^{-1} emissivity spectra of Hectorite (SHCa-1) calcined at various temperatures. Linear vertical offset is applied to the spectra for clarity.

For SBCa-1 beidellite (**Fig. 3.7a**), two spectral bands in the Si-O stretching region continuously shift away from each other with an increase in temperature. At 900 °C these two bands are replaced by single strong absorption near 1100 cm⁻¹. In the Si-O bending region, SBCa-1 shows only a minor change upon heating to 800 °C; the 546 cm⁻¹ band becomes weak at 400 °C and then gradually shifts to high wavenumbers. At 900 °C, the original spectral band disappears and the spectrum exhibits a strong feature at ~463 cm⁻¹ with a weak feature at ~555 cm⁻¹ in the Si-O bending region. The 338 and 255 cm⁻¹ bands of beidellite are lost at 400 °C. A new feature at ~307 cm⁻¹ then forms at 500 °C and eventually disappears at 900 °C. In the case of Syn-1 montmorillonite (**Fig. 3.7b**), the spectral features all show slight changes in intensities and positions upon heating. Besides these, the spectral bands of Syn-1 remain stable to 900 °C.

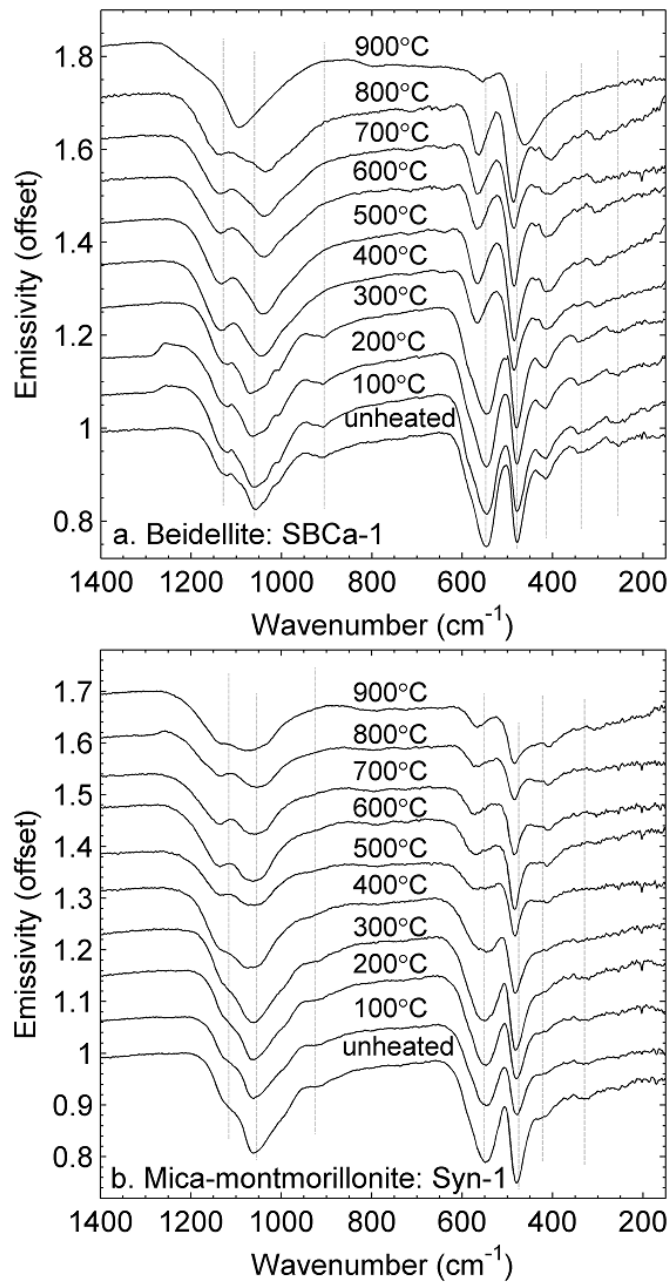


Figure 3.7 (a) 150-1400 cm⁻¹ emissivity spectra of Beidellite (SBCa-1) calcined at various temperatures. (b) 150-1400 cm⁻¹ emissivity spectra of Mica-montmorillonite (Syn-1) calcined at various temperatures. Linear vertical offset is applied to the spectra for clarity.

3.3.2.3 Sepiolite-palygorskite group

Two distinct spectral changes are observed for palygorskite (**Fig. 3.8a**) in the Si-O stretching region upon heating. At 300 °C the spectral features near 1200-1000 cm^{-1} combine together to form a new band centered at $\sim 1050 \text{ cm}^{-1}$. At 800 °C this new feature shifts significantly toward high wavenumbers and ending up near 1103 cm^{-1} at 900 °C. The three spectral bands of sepiolite (**Fig. 3.8b**) in the Si-O stretching region behave differently with heating, then at 700 °C they are replaced by a single absorption feature at $\sim 1035 \text{ cm}^{-1}$. Upon heating to 800 °C, the single absorption feature shows a dramatic change, being replaced by several bands over the range 900-1200 cm^{-1} . The Si-O bending bands of palygorskite are lost at 400 °C and are replaced by a broad 450 cm^{-1} feature plus a weak shoulder feature at $\sim 550 \text{ cm}^{-1}$. Upon heating to 800 °C, palygorskite loses the spectral features developed at 400 °C and exhibits a strong new feature at $\sim 465 \text{ cm}^{-1}$. The intensities and band positions of sepiolite spectral features in the Si-O bending region show several steps of changes upon heating (at 300, 700, 800 °C, respectively), the most distinct spectral change occurring at 800 °C. At temperatures lower than 800 °C, the complex spectral bands of sepiolite in the Si-O bending region are centered at $\sim 480 \text{ cm}^{-1}$. At 800 °C new spectral bands are developed at higher wavenumbers (centered at $\sim 520 \text{ cm}^{-1}$). The spectral change in far-IR region for palygorskite is difficult to observe due to water vapor present in the spectrum, but no major bands appear to be present in this region. In the case of sepiolite, the band at $\sim 365 \text{ cm}^{-1}$ disappears and several bands are observed to develop from 400-200 cm^{-1} at 800 °C.

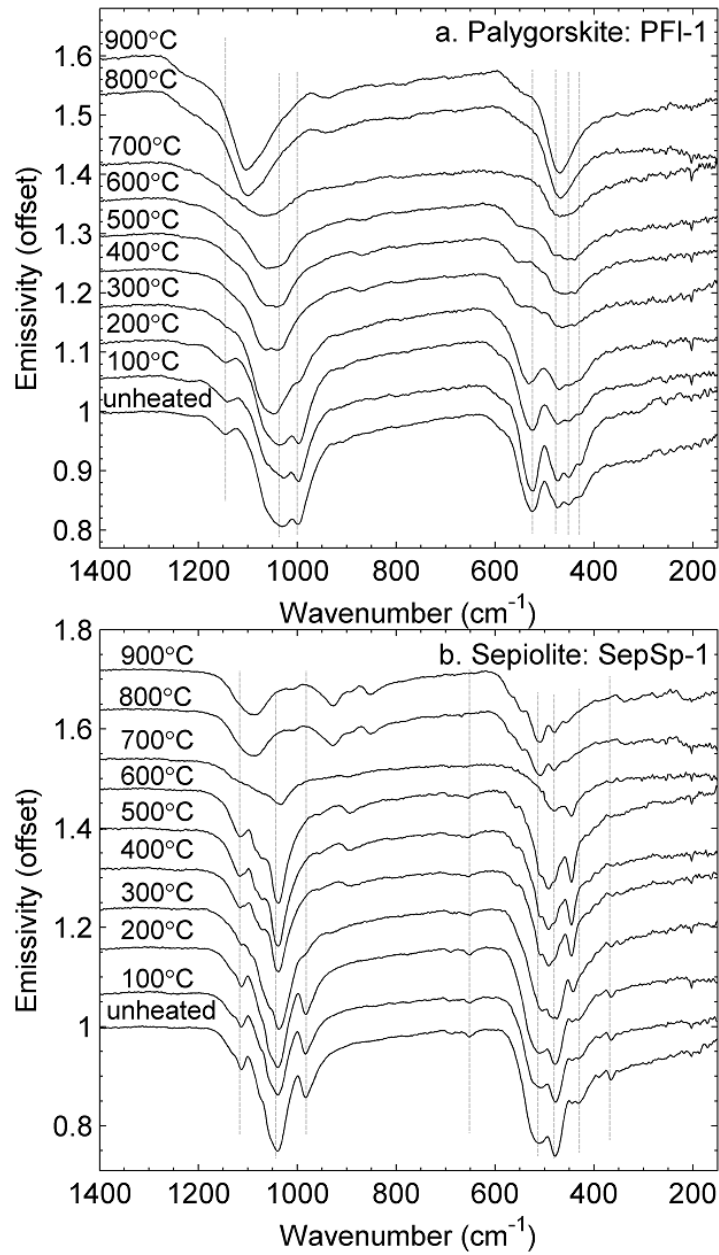


Figure 3.8 (a) 150-1400 cm^{-1} emissivity spectra of Palygorskite (PFI-1) calcined at various temperatures. (b) 150-1400 cm^{-1} emissivity spectra of Sepiolite (SepSp-1) calcined at various temperatures. Linear vertical offset is applied to the spectra for clarity.

3.3.2.4 Chlorite group

Spectra of clinochlore (**Fig. 3.9**) and its heating products show two steps of spectral changes occurring at 500 °C and 800 °C. At 500 °C, the original Si-O stretching bands combine together to form a single feature at $\sim 1080\text{ cm}^{-1}$, which disappears completely at 800 °C. In the Si-O bending region, at 500 °C all original features disappear and are replaced by a strong band at 476 cm^{-1} . At 800 °C this new band splits into multiple spectral features that develop and become stronger at 900 °C. In the far-IR region, a spectral feature at $\sim 370\text{ cm}^{-1}$ becomes very weak at 500 °C and disappears at 800 °C. New multiple spectral features in the $400\text{-}200\text{ cm}^{-1}$ region start to develop upon heating to 800 °C.

3.3.2.5 Zeolite group

The IR spectral properties of zeolites were summarized by previous studies (e.g., Breck 1974a). The tetrahedral stretching band ($\sim 1082\text{ cm}^{-1}$) of 27031 clinoptilolite (**Fig. 3.10a**) shows no major changes upon heating, although it shifts slightly to higher wavenumbers (1094 cm^{-1}) at 800 °C. In the case of 27133 mordenite (**Fig. 3.10b**), its tetrahedral stretching bands near 1086 cm^{-1} shifts to 1097 cm^{-1} at 800 °C while the shoulder Si (Al)-O stretching band ($\sim 1230\text{ cm}^{-1}$) remains unchanged to 900 °C. The Si (Al)-O bending bands of clinoptilolite (471 cm^{-1}) and mordenite (469 cm^{-1}) are both stable and do not show any distinct spectral change upon heating. In the far-IR region, these two samples display no major spectral features and no new spectral features are observed to form upon heating.

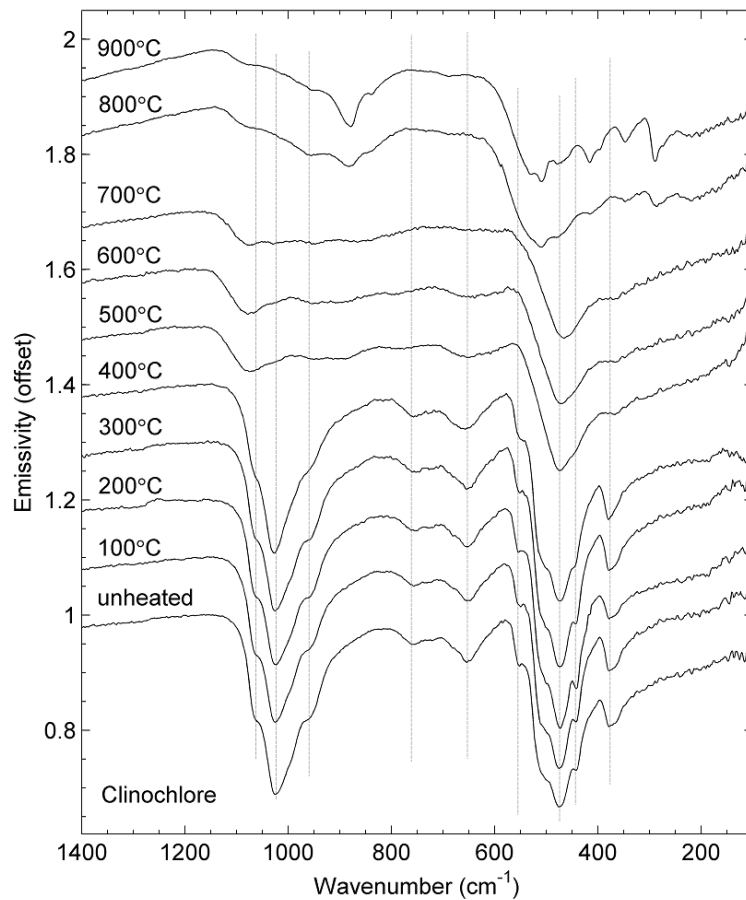


Figure 3.9 100-1400 cm^{-1} emissivity spectra of Clinochlore calcined at various temperatures.

Linear vertical offset is applied to the spectra for clarity.

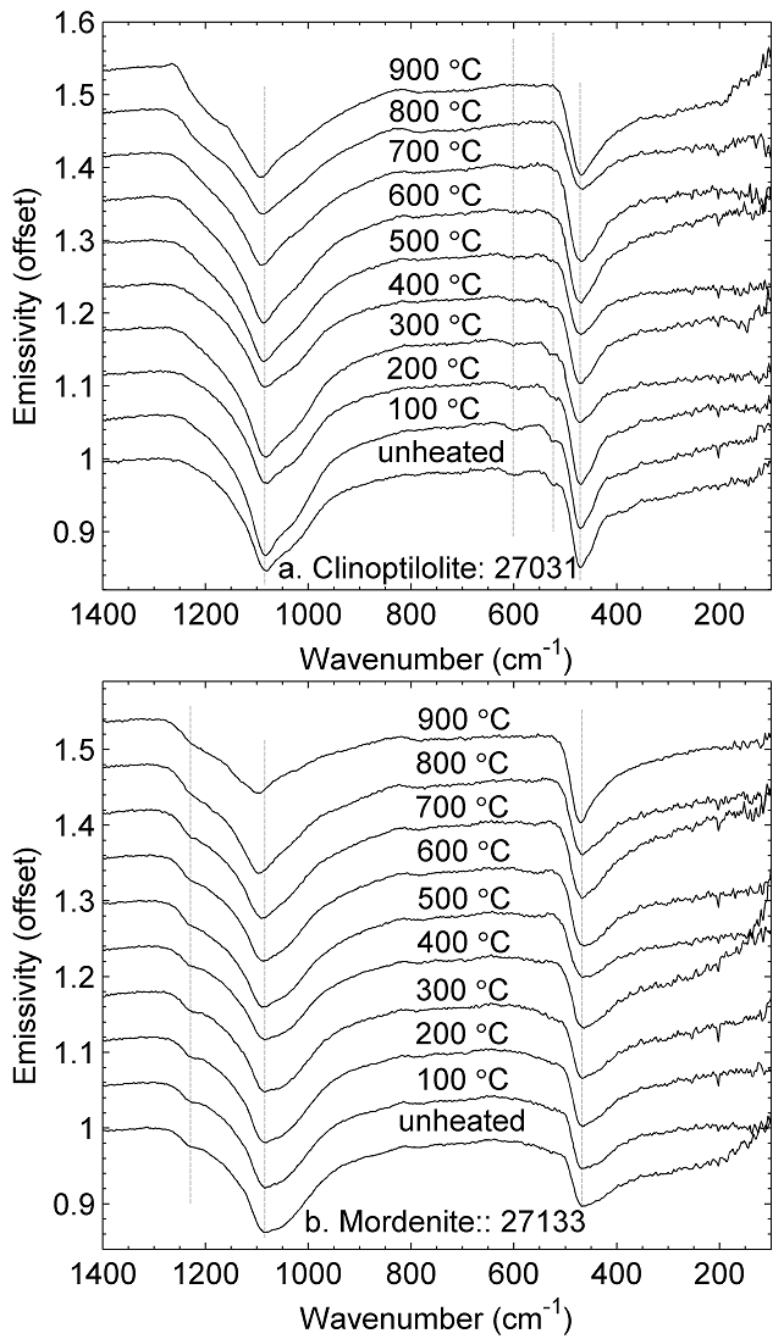


Figure 3.10 (a) 100-1400 cm⁻¹ emissivity spectra of Clinoptilolite (27031) calcined at various temperatures. (b) 150-1400 cm⁻¹ emissivity spectra of Mordenite (27133) calcined at various temperatures. Linear vertical offset is applied to the spectra for clarity.

3.3.2.6 Other observations

The 950-590 cm^{-1} region of phyllosilicates exhibit absorption bands attributable to bending vibration of hydroxyls groups bound to octahedral cations. Overall, the spectra of all sample studied here show that absorption features in this region disappear or become too weak to be identified after the samples are heated to a certain high temperature. For some of the phyllosilicates, however, distinct spectral features appear in this region when samples are heated to 700 $^{\circ}\text{C}$. Saponite (**Fig. 3.5**), hecorite (**Fig. 3.6**), and sepiolite (**Fig. 3.8b**) exhibit multiple spectral bands near 900 cm^{-1} upon heating to 700 $^{\circ}\text{C}$ (800 $^{\circ}\text{C}$ for sepiolite). For montmorillonites SAz-1 (**Fig. 3.3a**), SCa-3 (**Fig. 3.3b**), palygorskite (**Fig. 3.8a**), and clinochlore (**Fig. 3.9**), a single spectral band begins to develop near 900 cm^{-1} at 800 $^{\circ}\text{C}$, becoming a strong absorption band at 900 $^{\circ}\text{C}$.

3.3.3 NIR diffuse reflectance spectra

The NIR (1.2-2.5 μm in this study) is very useful for remote sensing analysis of hydrous minerals, because it is in this region that the minerals have spectral bands due to overtones and combinations of OH and H_2O vibrations. In general, the overtone of the OH stretching modes occurs in the 1.4 μm region, combination modes of H_2O molecules produce the absorptions in the 1.9 μm region, and spectral features near 2.2-2.4 μm regions are due to a combination of the OH stretching and M-OH bending modes (e.g., Gaffey *et al.* 1993; Bishop *et al.* 1994).

3.3.3.1 Kaolinite group

Kaolinite (**Fig. 3.11**) exhibits strong OH overtones in the 1.4 μm region. These spectral features become weak at 400 $^{\circ}\text{C}$ and then disappear at 700 $^{\circ}\text{C}$. Upon heating, a very weak spectral band at 1.367 μm appears at 400 $^{\circ}\text{C}$ and it is present in the spectrum until 900 $^{\circ}\text{C}$. Kaolinite does not have structural H_2O . However, weak spectral features are observed near 1.9 μm , which is probably due to adsorbed water or H_2O associated with impurities in the sample (Bishop et al. 2008). These features are replaced by one weak band at ~ 1.9 μm upon heating to 400 $^{\circ}\text{C}$. This weak new feature is present until kaolinite is heated to 900 $^{\circ}\text{C}$. Kaolinite exhibits 2.16 and 2.21 μm bands due to the AlAlOH combination modes. These two features are replaced by a broad absorption centered at 2.19 μm upon heating to 400 $^{\circ}\text{C}$. This 2.19 μm band is present in the spectrum until 900 $^{\circ}\text{C}$.

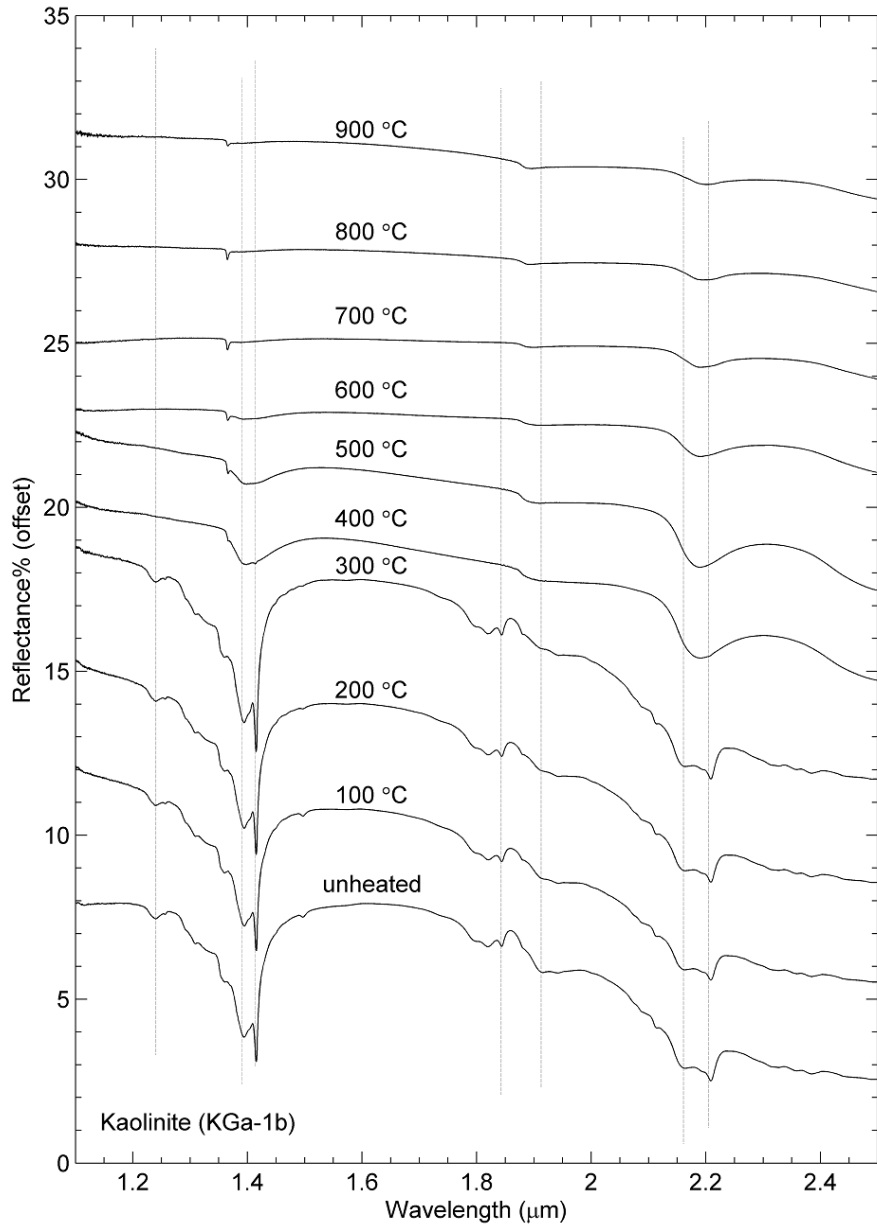


Figure 3.11 1.1-2.5 μm diffuse reflectance spectra of kaolinite (KGa-1b) calcined at various temperatures. Linear vertical offset is applied to the spectra for clarity.

3.3.3.2 Smectite group

The 1.410 μm feature of montmorillonites SAz-1 (**Fig. 3.12a**) and SCa-3 (**Fig. 3.12b**) does not show obvious changes upon heating to 400 $^{\circ}\text{C}$. At 500 $^{\circ}\text{C}$, the original band is replaced by two weak absorptions at ~ 1.365 and ~ 1.399 μm which both disappear completely at 800 $^{\circ}\text{C}$. STx-1 (**Fig. 3.12c**) displays similar spectral behaviors to SAz-1 and SCa-3. However, the 1.410 μm feature shifts to 1.400 μm at 600 $^{\circ}\text{C}$ and the new 1.366 μm feature of STx-1 is present in the spectrum from 400-800 $^{\circ}\text{C}$. Swy-2 (**Fig. 3.12d**) keeps its 1.410 μm feature stable upon heating to 500 $^{\circ}\text{C}$. In the 600 and 700 $^{\circ}\text{C}$ spectra of SWy-2, two extremely weak absorptions occur at ~ 1.366 and ~ 1.396 μm . At 800 $^{\circ}\text{C}$ no major spectral feature is observed in the 1.4 μm region for SWy-2. The 1.9 μm band of SAz-1, SCa-3, STx-1, and Swy-2 montmorillonites each displays slight shifts to shorter wavelengths at 400 $^{\circ}\text{C}$ and decreases in intensity at 700 $^{\circ}\text{C}$, before disappearing completely upon heating to 800 $^{\circ}\text{C}$. For the four montmorillonites analyzed here, there are two obvious spectral changes observed in the 2.2 μm region upon heating: the 2.21 μm feature disappears and new bands at ~ 2.19 , ~ 2.3 , and ~ 2.4 μm begin to develop at 500 $^{\circ}\text{C}$ (600 $^{\circ}\text{C}$ for SWy-2). At 800 $^{\circ}\text{C}$ their spectra only exhibit extremely weak 2.2 μm band and at 900 $^{\circ}\text{C}$ montmorillonites lose all spectral features in the 2.2-2.4 μm region.

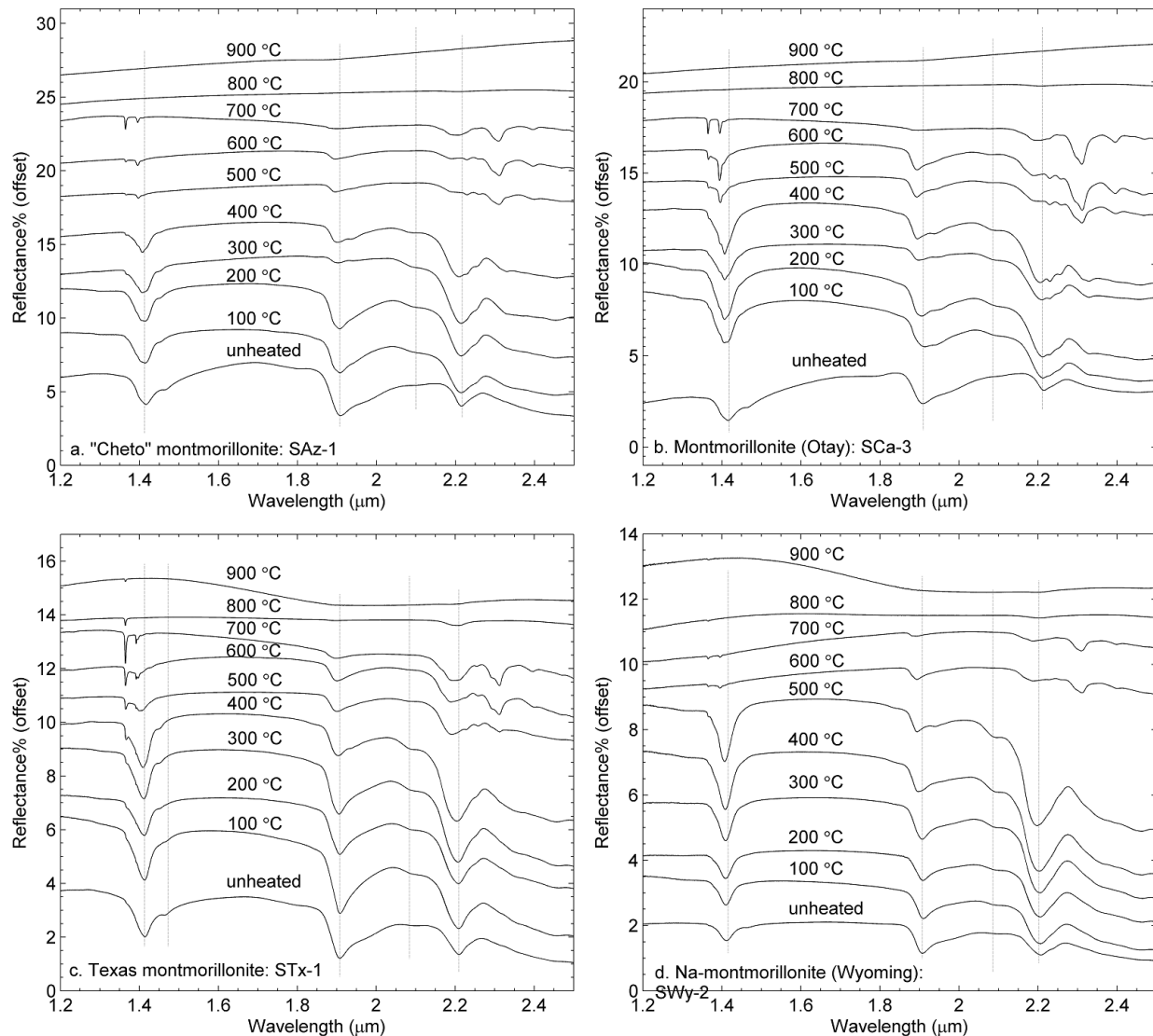


Figure 3.12 (a) 1.2-2.5 μm diffuse reflectance spectra of “Cheto” montmorillonite (SAz-1) calcined at various temperatures. (b) 1.2-2.5 μm diffuse reflectance spectra of montmorillonite (Otay) (SCa-3) calcined at various temperatures. (c) 1.2-2.5 μm diffuse reflectance spectra of Texas montmorillonite (STx-1) calcined at various temperatures. (d) 1.2-2.5 μm diffuse reflectance spectra of Na-montmorillonite (Wyoming) (SWy-2) calcined at various temperatures. Linear vertical offset is applied to the spectra for clarity.

For both nontronite samples (**Fig. 3.13a**: N Au-1; **Fig. 3.13b**: N Au-2) in this study, the bands in 1.4 μm region disappear completely upon heating to 400 $^{\circ}\text{C}$ and no new spectral features appear in the following heating treatments. A strong feature near 1.91 μm is observed for both nontronites in this study. At 400 $^{\circ}\text{C}$ this band is split into two weak absorptions at ~ 1.91 and ~ 1.95 μm which then disappear upon heating to 700 $^{\circ}\text{C}$. The 2.2, 2.3, and 2.4 μm features of the nontronites become very weak and shift slightly away from their original spectral positions at 400 $^{\circ}\text{C}$, then disappear completely at 700 $^{\circ}\text{C}$.

The 1.41 μm feature of SapCa-2 saponite (**Fig. 3.14**) becomes weak at 100 $^{\circ}\text{C}$ and completely disappears at 200 $^{\circ}\text{C}$. Saponite also displays a sharp absorption at 1.392 μm , which is observed to be present in the spectrum until 800 $^{\circ}\text{C}$. During the heating treatment, very weak bands in the 1.38-1.36 μm range accompany the 1.392 μm features. All bands then disappear at 900 $^{\circ}\text{C}$. For SHCa-1 hectorite (**Fig. 3.15**), the 1.41 μm feature disappears at 400 $^{\circ}\text{C}$, and the 1.391 μm band is lost at 800 $^{\circ}\text{C}$. A new band at 1.365 μm is present in the spectrum of hectorite from 700-800 $^{\circ}\text{C}$. Upon heating to 900 $^{\circ}\text{C}$ all features are lost completely. Saponite and hectorite both exhibit a strong absorption band near 1.91 μm , which gradually becomes weaker with heating. Both saponite and hectorite still have extremely weak 1.91 μm bands upon heating to 900 $^{\circ}\text{C}$. No major spectral changes are observed for the 2.3 and 2.4 μm bands of saponite and hectorite before these two samples lose these features completely at 800 $^{\circ}\text{C}$ (for hectorite) or 900 $^{\circ}\text{C}$ (for saponite).

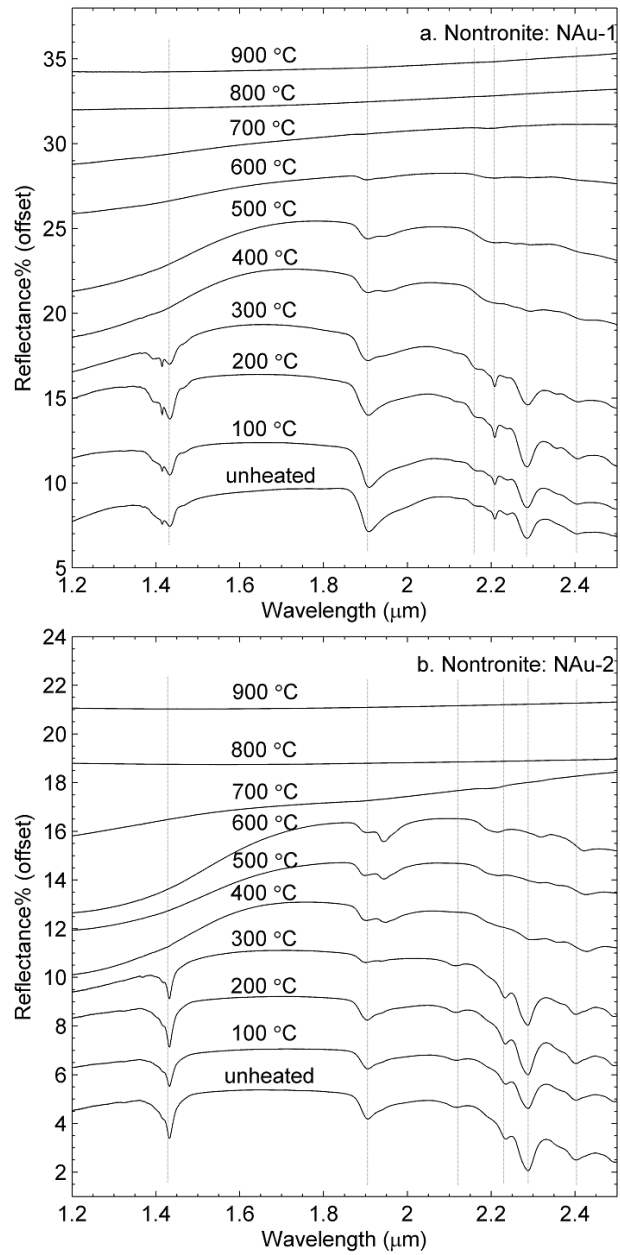


Figure 3.13 (a) 1.2-2.5 μm diffuse reflectance spectra of nontronite (NAu-1) calcined at various temperatures. (b) 1.2-2.5 μm diffuse reflectance spectra of nontronite (NAu-2) calcined at various temperatures. Linear vertical offset is applied to the spectra for clarity.

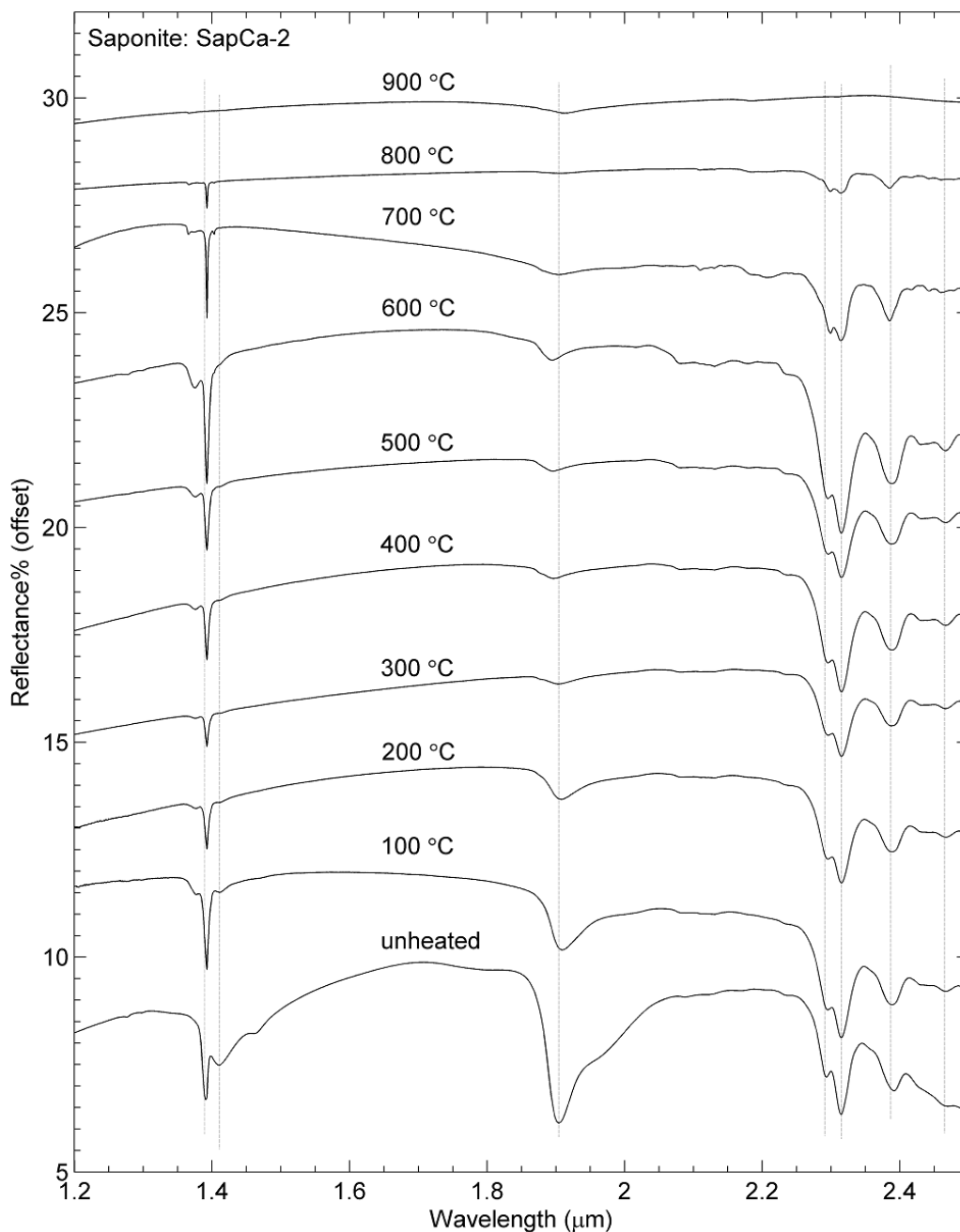


Figure 3.14 1.2-2.5 μm diffuse reflectance spectra of Saponite (SapCa-2) calcined at various temperatures. Linear vertical offset is applied to the spectra for clarity.

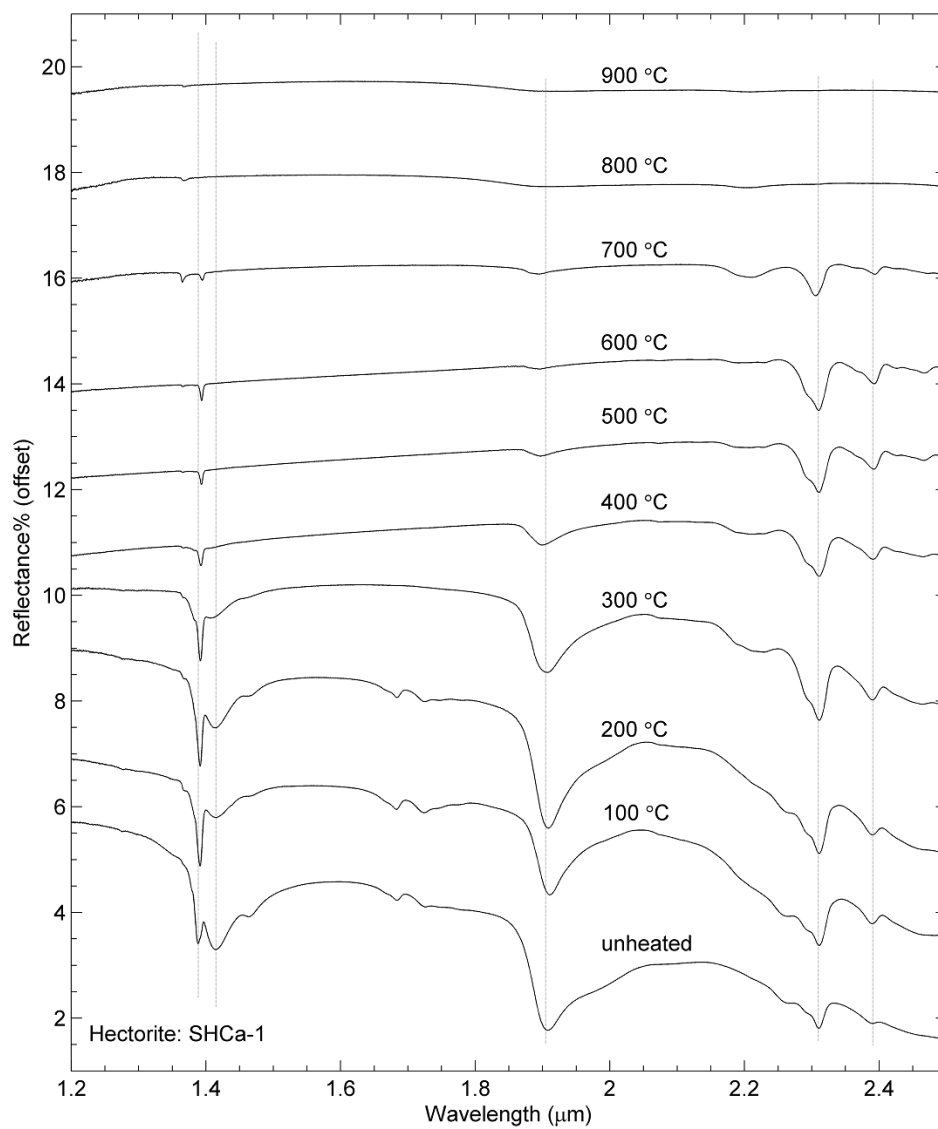


Figure 3.15 1.2-2.5 μm diffuse reflectance spectra of Hectorite (SHCa-1) calcined at various temperatures. Linear vertical offset is applied to the spectra for clarity.

The sharp 1.41 μm feature of SBCa-1 beidellite disappears at 400 $^{\circ}\text{C}$ while the 1.399 μm band (**Fig. 3.16a**) does not show distinct changes from 100-700 $^{\circ}\text{C}$. At 800 $^{\circ}\text{C}$, the 1.399 μm band becomes extremely weak and disappears at 900 $^{\circ}\text{C}$. A new weak band at $\sim 1.366 \mu\text{m}$ begins to develop for beidellite at 600 $^{\circ}\text{C}$ and is lost at 900 $^{\circ}\text{C}$. For Syn-1 montmorillonite (**Fig. 3.16b**), the 1.407 μm band begins to shift gradually to shorter wavelengths ($\sim 1.396 \mu\text{m}$ at 900 $^{\circ}\text{C}$) at 400 $^{\circ}\text{C}$ and this shifted feature exists in the spectrum until 900 $^{\circ}\text{C}$. In addition, a new spectral feature at 1.365 μm is observed to be present in the spectrum from 400-900 $^{\circ}\text{C}$. In the 1.9 μm region, a similar trend to saponite and hectorite is observed for beidellite and Syn-1 montmorillonite, although the 1.9 μm feature of Syn-1 montmorillonite remains strong at 900 $^{\circ}\text{C}$. Beidellite and Syn-1 montmorillonite both have their 2.2 μm features shifted slightly toward shorter wavelengths with heating. Beidellite loses its M-OH combination feature at 900 $^{\circ}\text{C}$ while Syn-1 montmorillonite still displays a strong absorption band at $\sim 2.17 \mu\text{m}$ at the same temperature.

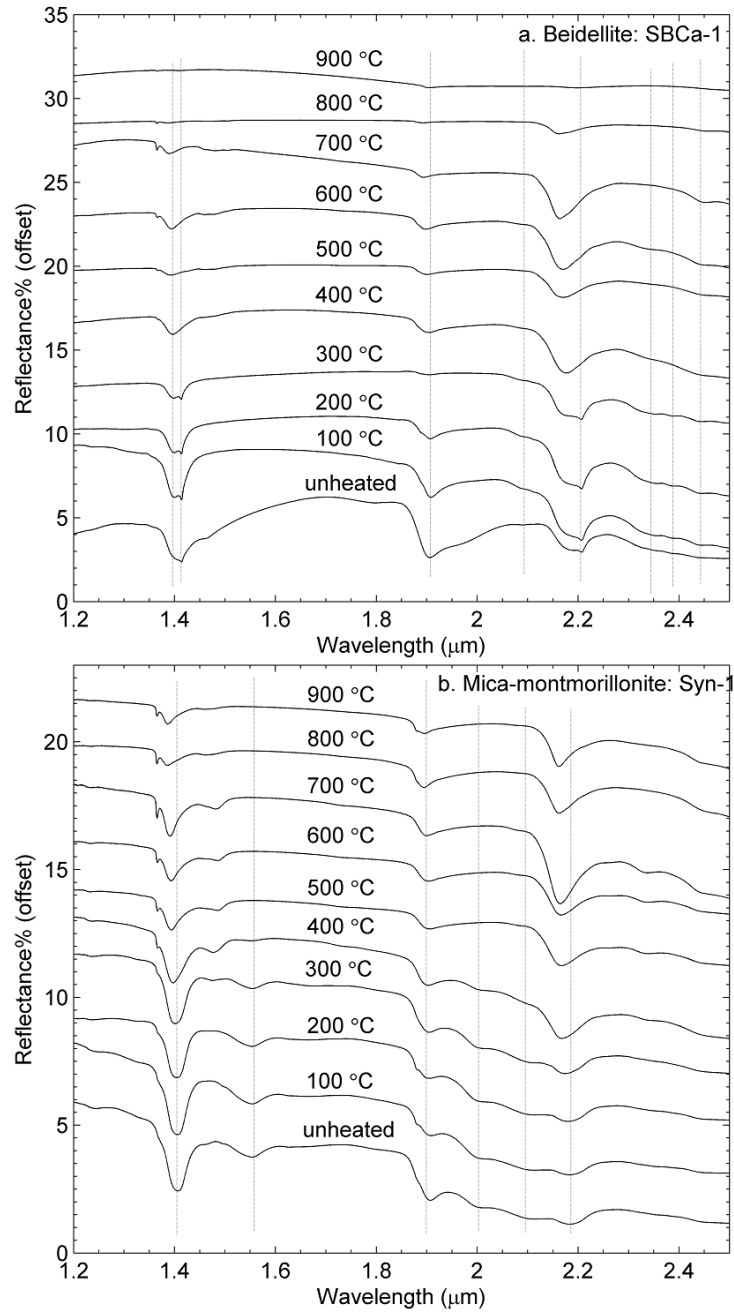


Figure 3.16 (a) 1.2-2.5 μm diffuse reflectance spectra of Beidellite (SBCa-1) calcined at various temperatures. (b) 1.2-2.5 μm diffuse reflectance spectra of Mica-montmorillonite (Syn-1) calcined at various temperatures. Linear vertical offset is applied to the spectra for clarity.

3.3.3.3 Sepiolite-palygorskite group

PFI-1 palygorskite's spectral bands (**Fig. 3.17a**) occurring at 1.38 and 1.41 μm change significantly at 500 $^{\circ}\text{C}$; the 1.41 μm feature is lost and two new spectral features appear at 1.366 and 1.370 μm . The 1.366 μm band is still present in the 900 $^{\circ}\text{C}$ spectrum while the 1.370 μm feature disappears upon heating to 700 $^{\circ}\text{C}$. SepSp-1 sepiolite (**Fig. 3.17b**) displays three spectral features at 1.38, 1.39, and 1.42 μm . They show different behaviors upon heating: the 1.42 μm band becomes broad and weak at 400 $^{\circ}\text{C}$ and disappears at 700 $^{\circ}\text{C}$; the 1.39 μm feature is present as a strong absorption in the 700 $^{\circ}\text{C}$ spectrum and disappears completely at 800 $^{\circ}\text{C}$; the 1.38 μm feature disappears at 700 $^{\circ}\text{C}$. In addition, a new band at 1.364 μm starts to develop at 600 $^{\circ}\text{C}$ and becomes a strong absorption band at 900 $^{\circ}\text{C}$. The 1.92 μm bands of palygorskite and sepiolite decrease gradually in intensity and shift slightly to shorter wavelengths with heating, but these features are still detectable at 900 $^{\circ}\text{C}$. Palygorskite's original spectral features near 2.2 μm are replaced by 2.19 and 2.31 μm bands at 400 $^{\circ}\text{C}$. Upon heating to 800 $^{\circ}\text{C}$ and 900 $^{\circ}\text{C}$, only a broad spectral absorption centered at ~ 2.21 μm is observed for palygorskite. In the case of sepiolite, there are multiple spectral features in the range 2.2-2.4 μm . These bands are not strongly affected by temperatures as high as 700 $^{\circ}\text{C}$. At 800 and 900 $^{\circ}\text{C}$, only one broad band at 2.21 μm is present in the sepiolite spectrum.

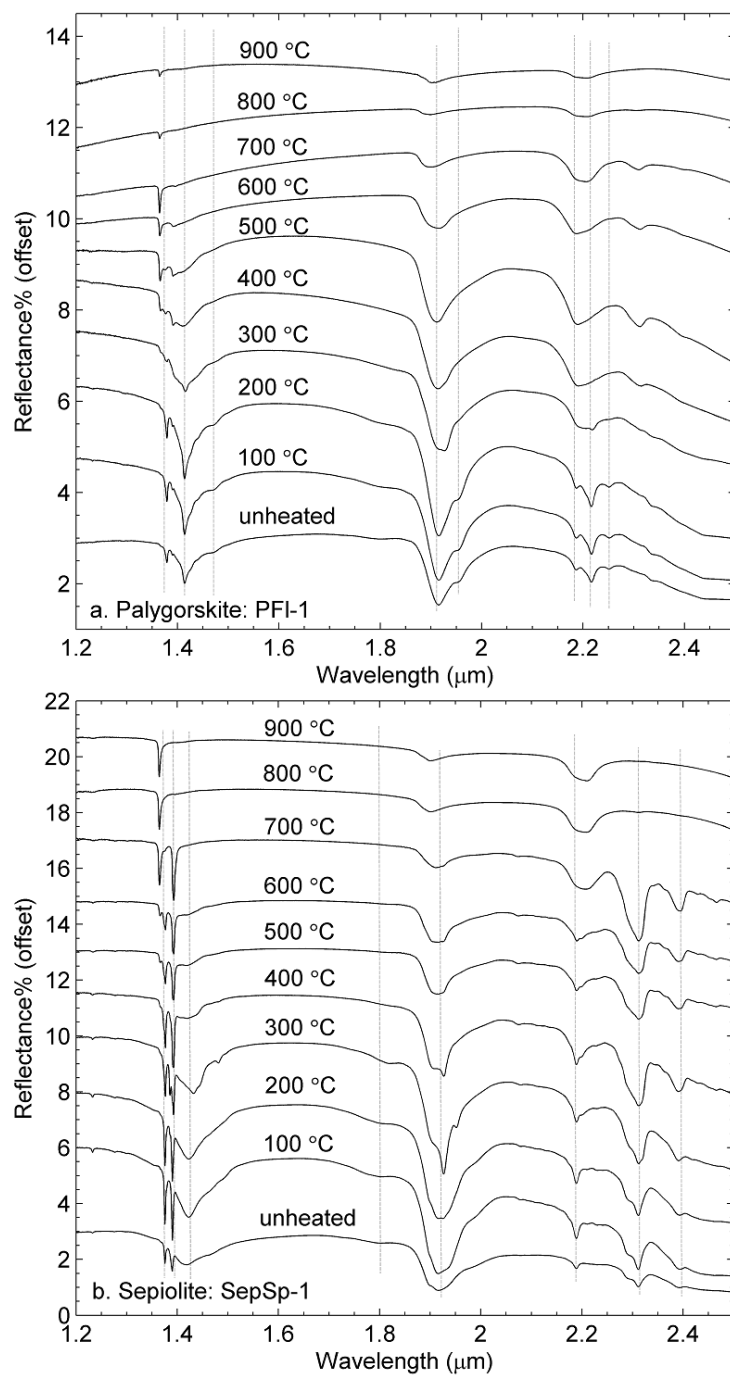


Figure 3.17 (a) 1.2-2.5 μm diffuse reflectance spectra of Palygorskite (PFI-1) calcined at various temperatures. (b) 1.2-2.5 μm diffuse reflectance spectra of Sepiolite (SepSp-1) calcined at various temperatures. Linear vertical offset is applied to the spectra for clarity.

3.3.3.4 Chlorite group

Clinochlore's 1.39 μm feature is not affected by heating until 800 $^{\circ}\text{C}$ (**Fig. 3.18**), at which point this feature disappears completely. The 1.45 μm band, however, is affected significantly by heating, disappearing completely at 500 $^{\circ}\text{C}$. Two absorption features due to combination modes of H_2O occur in the 1.9-2.0 μm range. These two bands become weak at 500 $^{\circ}\text{C}$, and then completely disappear at 800 $^{\circ}\text{C}$. Clinochlore also has multiple features present in the 2.2-2.4 μm range. Although these spectral bands shift slightly away from their original positions with heating, they do not show major changes before their complete disappearance at 800 $^{\circ}\text{C}$.

3.3.3.5 Zeolite group

Two natural zeolites in this study exhibit weak absorption bands in the 2.2-2.4 μm region (**Figs. 3.19a** and **3.19b**). Given that zeolites do not have OH in their structures, the spectral features in this region may be due to the occurrence of M-OH combination modes occurring when a small amount of H_2O hydrogen atoms bond to extraframework (K^+ , Ca^{2+} , and Na^+) and tetrahedral (Si^{4+} , Al^{3+}) cations (Cloutis et al. 2002). These features are very weak, but they remain in the spectra when heated to 800 $^{\circ}\text{C}$ (clinoptilolite) or 900 $^{\circ}\text{C}$ (mordenite). No distinct changes in the 1.9 region of mordenite and clinoptilolite occur before a significant decrease in intensity of the 1.91 μm band at 800 $^{\circ}\text{C}$ (for clinoptilolite) or 900 $^{\circ}\text{C}$ (for mordenite). Clinoptilolite and mordenite both exhibit strong absorption bands near 1.42 μm . The shape and position of this feature is not affected by heating before the complete disappearance of this band at 800 $^{\circ}\text{C}$ for clinoptilolite and 900 $^{\circ}\text{C}$ for mordenite. The extremely weak spectral feature near 1.365 μm of both natural zeolites is present in their spectra until 800 $^{\circ}\text{C}$.

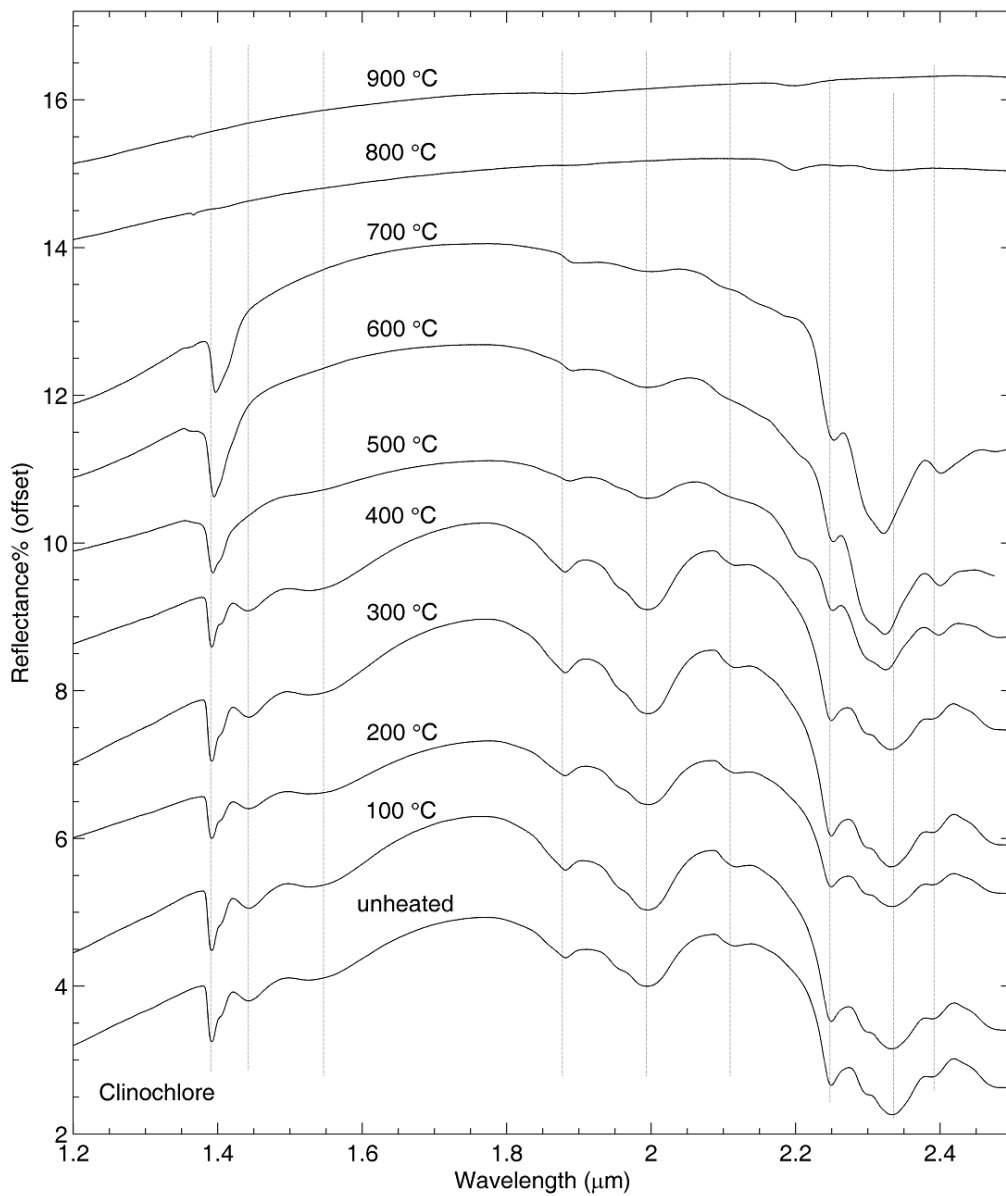


Figure 3.18 1.2-2.5 μm diffuse reflectance spectra of Clinochlore calcined at various temperatures. Linear vertical offset is applied to the spectra for clarity.

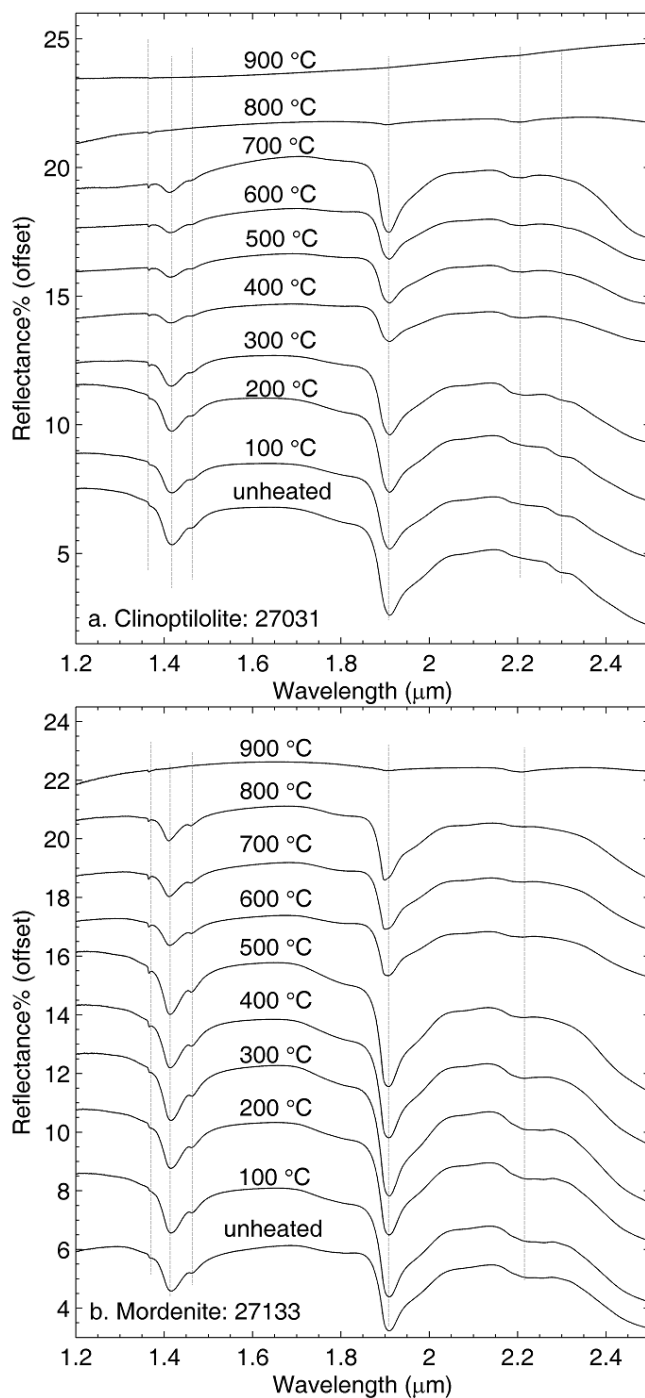


Figure 3.19 (a) 1.2-2.5 μm diffuse reflectance spectra of Clinoptilolite (27031) calcined at various temperatures. (b) 1.2-2.5 μm diffuse reflectance spectra of Mordenite (27133) calcined at various temperatures. Linear vertical offset is applied to the spectra for clarity.

3.3.3.6 Other observations

Fourteen of the samples studied here exhibit an absorption feature near 1.365 μm when samples are heated to temperatures between 400 and 900 $^{\circ}\text{C}$. The temperature range over which this non-diagnostic feature occurs as well as its intensity are different for each sample. Kaolinite (**Fig. 3.11**) exhibits a very weak 1.367 μm band from 400 $^{\circ}\text{C}$ to 900 $^{\circ}\text{C}$. Among the montmorillonites, SAz-1 (**Fig. 3.12a**) and SCa-3 (**Fig. 3.12b**) have new 1.366 μm features with comparable intensities from 500-700 $^{\circ}\text{C}$, and 1.366 μm bands appear from 400-800 $^{\circ}\text{C}$ and 600-800 $^{\circ}\text{C}$ for STx-1 (**Fig. 3.12c**) and SWy-2 (**Fig. 3.12d**), respectively. Saponite (**Fig. 3.14**) and hectorite (**Fig. 3.15**) exhibit recognizable 1.365 μm bands only at 700 $^{\circ}\text{C}$. An extremely weak 1.366 μm feature is observed for beidellite (**Fig. 3.16a**) from 600-800 $^{\circ}\text{C}$. For Syn-1 montmorillonite (**Fig. 3.16b**), a 1.365 μm band appears at 500 $^{\circ}\text{C}$ and develops as an absorption band with detectable intensity at 900 $^{\circ}\text{C}$. Palygorskite (**Fig. 3.17a**) and sepiolite (**Fig. 3.17b**) both exhibit this new feature from 500-900 $^{\circ}\text{C}$. The 1.364 μm band of sepiolite develops as a very strong feature at 900 $^{\circ}\text{C}$. In the case of clinochlore (**Fig. 3.18**), an extremely weak 1.364 μm band is present from 600-800 $^{\circ}\text{C}$. In the case of two natural zeolites (**Figs. 3.19a** and **3.19b**), the untreated samples already exhibit weak 1.365 bands and their bands are still present in the spectra upon heating to 900 $^{\circ}\text{C}$. However, for Fe-rich nontronites (**Figs. 3.13a** and **3.13b**), such spectral features do not appear at all. Nontronites lose their 1.4 μm features completely at 400 $^{\circ}\text{C}$ and no new spectral bands form during following heating treatment.

3.4. Discussion

3.4.1 Effects of thermal behaviors of phyllosilicates and natural zeolites

The integration of mid-to-far-IR emissivity and NIR reflectance spectral results along with DSC results of phyllosilicates and natural zeolites allow us to conclude that, in general, the diverse spectral changes observed in this study are significantly affected by samples' thermal behaviors.

Kaolinite group. There is no endothermic peak observed in DSC curve of kaolinite associated with the loss of adsorbed and interlayer H₂O, because kaolinite contains no structural H₂O (e.g., Farmer 1974; Bailey 1980). Kaolinite's first endothermic reaction, which is caused by removal of structural OH (Holdridge and Vaughan 1957), occurs in the temperature range 460-600 °C (**Fig. 3.1a**). Correspondingly, all spectral features observed for kaolinite change significantly at 400 °C and new bands related to heating products remain up to 900 °C (**Figs. 3.2 and 3.11**). This consistency suggests the dehydroxylation process of kaolinite is the reason leading to its major spectral change. Kaolinite displays a second strong endothermic effect centered at ~830 °C, which has been previously interpreted as being caused by transition from a more-ordered structure to a less-ordered amorphous alumina (Holdridge and Vaughan 1957). This transition may contribute to the distinct narrowing of kaolinite's major spectral features observed at 800 °C in the mid-to-far-IR region (**Fig. 3.2**). This reaction, however, does not affect kaolinite's spectral properties in the NIR region (**Fig. 3.11**).

Smectite group. In this study, we analyzed 10 samples from the smectite structural group. Minerals of the smectite group are characterized by 2:1 (one octahedral sheet is linked to a tetrahedral sheet on each side) layers with OH associated with octahedral cations and H₂O

molecules in their interlayer region (e.g., Farmer 1974; Bailey 1980). Our results exhibit a large variety of spectral changes among the smectite samples.

In general, all montmorillonite samples (SAz-1, SCA-3, STx-1, and SWy-2) display two notable changes in both NIR reflectance and mid-to-far-IR emissivity spectra (**Figs. 3.3 and 3.12**). Based on the investigation of the thermal behaviors by DSC analysis (**Figs. 3.1b-3.1e**), the IR properties of montmorillonites are largely affected by their dehydroxylation processes. All montmorillonites show their first endothermic peak in the range 120-140 °C, due to the loss of H₂O (Greene-Kelly 1957). However, neither their NIR nor the mid-to-far-IR major spectral bands display distinct changes upon heating to this temperature. At ~550 °C a second endothermic reaction commences and ends at ~750 °C, which is followed immediately by a third endothermic effect centered at ~850-900 °C. These two endothermic peaks are interpreted as being due to the loss of structural OH groups and breakdown of the anhydrous montmorillonite to an “amorphous” phase (Greene-Kelly 1957), respectively. By comparing the IR spectra of montmorillonites upon heating to their DSC results, we account for the two distinct spectral changes occurring at 500-600 °C and 800 °C associated with dehydroxylation of the montmorillonites and collapse of montmorillonites’ layer structure, respectively. Upon further heating to ~1000 °C, an exothermic peak is observed for both SAz-1 and SCA-3 montmorillonites (**Figs. 3.1b and 3.1c**). This reaction was interpreted as formation of new high temperature phases, which may include cristobalite, sillimanite, enstatite, and some amorphous phases (e.g., Greene-Kelly 1957; Gavin and Chevier, 2010). Correspondingly, the mid-to-far-IR spectra of SAz-1 and SCA-3 samples show notable changes at 900 °C (**Figs. 3.3a and 3.3b**), probably due to the formation of a new crystal structure. The STx-1 and SWy-2 montmorillonites behave differently from the previous two montmorillonites. Neither the DSC

(**Figs. 3.1d and 3.1e**) nor the IR results (**Figs. 3.3c and 3.3d**) show the formation of new phases at 900 °C. High Mg²⁺ concentration (**Table 3.2**) might be the reason leading to the significant spectral change at 900 °C for SAz-1 and SCa-3; previous studies (e.g., Earley et al. 1953; Greene-Kelly 1957; Gavin and Chevier, 2010) have concluded that a minor enstatite (MgSiO₃) structure begins to form at ~900 °C for Mg²⁺-rich smectites while other high temperature phases appear upon heating to 1000 °C.

Both nontronite samples (NAu-1 and NAu-2) display a dehydration peak in the 110-135 °C range and a less-pronounced dehydroxylation endothermic peak in the ~500-700 °C region (**Figs. 3.1f and 3.1g**). Similar to montmorillonite, loss of H₂O does not lead to distinct IR spectral changes. Given the results that all spectral features of nontronites show significant change at 400 °C (**Figs. 3.4 and 3.13**), dehydroxylation may be the major factor affecting nontronite's IR properties.

The first endothermic peak (**Figs. 3.1h and 3.1i**) of both saponite and hectorite is centered at ~135 °C, due to the removal of H₂O (Greene-Kelly 1957; Vicente *et al.* 2001). Similar to all of the smectite samples discussed above, the IR spectral features (Saponite: **Figs. 3.5 and 3.14**; Hectorite: **Figs. 3.6 and 3.15**) of both samples are not substantially affected by dehydration reactions. However, the 1.41 μm and 1.9 μm features of saponite and hectorite show a decrease in intensity at 100 °C, and the weak 1.95 μm shoulder band of both samples disappears at 100 °C. At higher temperatures (~800-950 °C for saponite, ~600-850 °C for hectorite), an endothermic-exothermic inversion occurs for these two samples, indicating the removal of structural hydroxyl groups followed by a phase change (Greene-Kelly 1957; Vicente *et al.* 2001). This high temperature phase of saponite and hectorite has been determined by previous investigators (e.g., Kulbicki 1959; Green et al. 1970; Kloprogge et al. 2000; Kloprogge and Frost

2000) and confirmed in our previous XRD studies (Che et al., 2011) to be enstatite (MgSiO_3). The mid-to-far-IR emissivity spectral results of both samples are in good agreement: saponite and hectorite display completely different spectral features from their original bands at temperatures higher than 700 °C. In addition, NIR spectra of both samples reveal more detailed information of their thermal behaviors. Saponite keeps its hydration spectral features at 800 °C while the 800 °C hectorite spectrum has already become featureless. This behavior is in agreement with the fact that saponite shows an endothermic-exothermic inversion at a higher temperature range than hectorite does in their DSC curves. Therefore, the IR properties of these two samples are significantly affected by dehydroxylation and recrystallization reactions.

Similar to the montmorillonites, beidellite and Syn-1 montmorillonite both exhibit three main endothermic peaks (**Figs. 3.1j and 3.1k**) near 120 °C, 540 °C, and 800-900 °C, which are attributed to the loss of H_2O , loss of structural hydroxyl groups, and collapse of the layer structure, respectively (Greene-Kelly 1957). Spectral bands of beidellite and Syn-1 montmorillonite do show a slight shift from their original positions with increasingly higher temperature (**Figs. 3.7 and 3.16**). However, these two minerals' major spectral bands are resistant to changes at temperatures as high as 800 °C for beidellite and 900 °C for Syn-1 montmorillonite. The dehydration process occurring in the temperature range 100-200 °C, as observed in the DSC analysis, does not affect the IR spectral properties of these two samples distinctly. The dehydroxylation reaction begins at 400-500 °C, which may be responsible for the minor change of IR spectra of beidellite and Syn-1; a few of their spectral features shift slightly away from the original positions in this temperature range. Neither of these last two effects, however, strongly alters their IR spectra. Finally, the third endothermic reaction near 810 °C is correlated with a major change in beidellite's IR spectrum, as beidellite loses all of its original

spectral features at 900 °C. For Syn-1, the third endothermic effect occurs at ~930 °C, therefore, neither the mid-to-far-IR nor NIR spectrum changes distinctly at 900 °C.

Of all the smectites studied here, the major differences among them are compositions of the octahedral cations. Montmorillonite and nontronites are Al³⁺-, and Fe³⁺-rich dioctahedral smectites; beidellite and Syn-1 montmorillonite are significantly rich in Al³⁺; hectorite and saponite are Mg²⁺-rich trioctahedral smectites. These differences may yield the variable spectral behaviors we have observed among the smectite minerals, and further discussion appears in the next section.

Sepiolite-Palygorskite group The structure represented by palygorskite and sepiolite is composed of octahedral and tetrahedral sheets that are divided into ribbons by inversion. The tetrahedral sheets are still linked and alternating channels are formed by this ribbon-like morphology, while the alternating channels between ribbon strips are occupied by H₂O molecules and exchangeable cations (e.g., Farmer 1974; Bailey 1980). Palygorskite and sepiolite both have several forms of H₂O present inside their structure. For palygorskite, there are H₂O molecules attached to octahedral cations, a small amount of zeolitic H₂O (that is coordinated with a cation on the exchange sites in the interlayers of phyllosilicates and within the cages of zeolites (e.g., Ming *et al.* 2008)) in channels, and H₂O groups situated laterally along the channels. Sepiolite has a similar structure except most H₂O exists in its channels as zeolitic H₂O (e.g., Bailey 1980). Consequently, both DSC (**Figs. 3.1l and 3.1m**) and IR results (**Figs. 3.8 and 3.17**) show that palygorskite and sepiolite have more complicated thermal behaviors compared to the other samples in this study. In the temperature range of 50-550 °C, palygorskite displays several weak endothermic peaks (~100 °C, ~140 °C, ~230 °C, and ~480 °C) reflecting the dehydration and dehydroxylation reactions (Caillere and Henin 1957a). IR spectra of

palygorskite agree well with the DSC curve by showing spectral changes at 300, 400, and 500 °C. Upon heating to ~880 °C, an endothermic-exothermic inversion appears in the DSC curve of palygorskite, reflecting a recrystallization into enstatite (e.g., Kulbicki, 1959; Caillere and Henin 1957a). Correspondingly, IR spectra of palygorskite in both mid-to-far-IR and NIR regions show major changes at 800 °C. However, no characterized enstatite spectral features (compared to the enstatite emissivity spectrum in Hamilton et al. 1997) are observed in palygorskite's 900 °C emissivity spectrum. It is possible that only minor enstatite structure forms at the temperature of 900 °C. Similar to palygorskite, the DSC curve of sepiolite is also composed of several endothermic peaks in the low temperature range (~110 °C, 330 °C, and 590 °C) associated with dehydration and dehydroxylation reactions, and an endothermic-exothermic inversion near 840 °C due to the crystallization of enstatite (e.g., Kulbicki, 1959; Caillere and Henin 1957a). The exothermic peak of sepiolite, however, is significantly stronger than that of palygorskite. The IR spectra of sepiolite are in good agreement with the sample's thermal behaviors showed by DSC analysis. The spectral features, especially sepiolite's hydration spectral bands, display several distinct changes in the temperature range 25-500 °C. The mid-to-far-IR spectra reveal the formation of enstatite at 800 °C for sepiolite by displaying completely different spectral features from those of unheated sepiolite. The major features of 800 and 900 °C emissivity spectra match well with the spectral bands of enstatite recorded in Arizona State University Spectral Library (spectrum ID: 537).

Chlorite group Clinochlore only has hydroxyls in its structure. However, there are two types of OH present: one is coordinated to octahedral cations and the other is associated with the $(R^{2+}, R^{3+})_3(OH)_6$ (R is an octahedral cation such as Fe^{2+} , Mg^{2+} , Zn^{2+} , or Al^{3+}) octahedral sheet in the interlayers (e.g., Farmer 1974; Bailey 1980). The DSC curve of clinochlore (**Fig. 3.1n**) shows

corresponding results by giving two strong endothermic peaks. The first endothermic peak in the ~500-650 °C region represents the decomposition of the brucite-like layer in its interlayer and the second one in the ~800-900 °C range is due to the dehydroxylation of sample's layer structure (Caillere and Henin 1957b). Previous studies (Villieras et al. 1994) have concluded that clinocllore transforms to "modified chlorite" termed by Villieras et al. (1994) at 500 °C, then at 800 °C new phases olivine and spinel start to form (e.g., Brindley and Ali 1950). The IR spectra of clinocllore (**Figs. 3.9 and 3.18**) agree well with the thermal behavior determined by DSC measurement: two distinct changes occurring at 500 °C and 800 °C are observed in both the NIR and mid-to-far-IR spectral results. Therefore, as each phase of dehydroxylation is taking place, the IR properties of clinocllore show major changes.

Zeolite group Phyllosilicates exhibit a wide variety of significant spectral changes as temperature is increased. However, the mid-to-far-IR emissivity spectra of clinoptilolite and mordenite show no obvious change upon heating (**Figs. 3.10 and 3.19**). The shapes and locations of the NIR spectral bands are not affected by thermal treatment before the completion of dehydration. These spectral results are consistent with the fact that zeolites all have three-dimensionally linked and rigid crystal structures (e.g., Breck 1974b; Barrer 1978, 1982; Newsam 1986; Armbruster and Gunter 2001), that are more stable than the layer structures of phyllosilicates. DSC curves of both zeolites (**Figs. 3.10 and 3.1p**) reveal more detailed information of their thermal properties. The first endothermic peak of clinoptilolite and mordenite occurred near 110 °C, corresponding to the loss of large amount H₂O from their crystal structures (Földesová *et al.* 1999; Alver *et al.* 2010). However, neither the mid-to-far-IR nor the NIR spectral features are affected by this dehydration reaction. The endothermic peaks occurring at higher temperatures (~690 °C for clinoptilolite and ~810 °C for mordenite) may

reflect the collapse of the zeolite structure (Földesová *et al.* 1999; Alver *et al.* 2010). NIR spectra of the two zeolites are in good agreement with this high temperature reaction: clinoptilolite tends to lose all its hydration features at 800 °C and the spectrum of mordenite becomes featureless at 900 °C. However, corresponding changes are not observed in zeolites' mid-to-far-IR spectra.

3.4.2 Effects of octahedral cations

The IR spectral features of phyllosilicates are affected by their octahedral cations because different cations need different energies to pull charge away from hydroxyls (e.g., Bishop *et al.* 2008). Previous investigators also observed that the position of the M-O-Si absorption appears to be linearly related to the average ionic radius of the cations in phyllosilicates' octahedral sites. The wavenumber position decreases in the order $\text{Al}^{3+} > \text{Al}^{3+}/\text{Fe}^{3+} > \text{Fe}^{3+} > \text{Mg}^{2+}$ (e.g., Michalski *et al.* 2005). Our results indicate that this order is also suitable to describe the IR spectral stability of phyllosilicates. Spectral bands of Al^{3+} -rich smectites are less affected by high temperatures than those of Fe^{3+} -smectites. The stability of Al^{3+} -rich smectites decreases as their Al^{3+} abundance decreases. Montmorillonites SAz-1 ($\text{Al}/\text{Si}=0.33$), SCa-3 ($\text{Al}/\text{Si}=0.22$), and STx-1 ($\text{Al}/\text{Si}=0.25$) display their first distinct spectral changes in both NIR reflectance and mid-to-far-IR emissivity spectra at 500 °C (**Figs. 3.3a-3.3c, 3.12a-3.12c**). SWy-2 ($\text{Al}/\text{Si}=0.36$), however, shows its first obvious change at 600 °C (**Figs. 3.3d and 3.12d**). In the case of beidellite ($\text{Al}/\text{Si}=0.6$), its original mid-to-far-IR emissivity and NIR reflectance spectra are changed significantly only at 900 °C (**Figs. 3.7a and 3.16a**). Before 900 °C, the major spectral change in beidellite is related to a slight shifting of original spectral bands (to both longer and shorter

wavelengths). Syn-1 montmorillonite (Al/Si=0.77) exhibits the strongest resistance to high temperature by maintaining the OH/H₂O overtone and combination bands at temperature as high as 900 °C (Figs. 3.7b and 3.16b). In addition, Syn-1's emissivity spectra do not show a conspicuous change upon heating to 900 °C. Nontronites with a high Fe³⁺ abundance, however, lose all original spectral features in the mid-to-far-IR and NIR regions at 400 °C (Figs. 3.4 and 3.13). In addition, no NIR spectral band is observed for nontronite at 700 °C while the other smectite minerals all retain distinct spectral bands upon heating to 700 °C.

The spectral features of phyllosilicates with a certain amount (Mg/Si=~0.11-0.96) of Mg²⁺ show unique behavior during thermal treatments. For the trioctahedral phyllosilicates hectorite (Mg/Si=0.43), saponite (Mg/Si=0.46), clinochlore (Mg/Si=0.96), and sepiolite (Mg/Si=0.41), mid-to-far-IR emissivity spectra at 700 °C display evidence for the formation of new phases (Figs. 3.5, 3.6, 3.8b and 3.9), which were determined to be enstatite (olivine+spinel for clinochlore) by previous studies (e.g., Brindley and Ali 1950; Kulbicki 1959). The same transformation occurred for clinochlore and sepiolite at 800 °C. These new spectral features are completely different from the familiar phyllosilicate features that dominate Si-O stretching and bending bands. For montmorillonites SAz-1 (Mg/Si=0.11), SCa-3 (Mg/Si=0.15), and palygorskite (Mg/Si=0.18), the presence of a small amount of Mg²⁺ in their octahedral sites also affect the high temperature spectral behaviors. At 800 °C, a unique spectral band at ~920 cm⁻¹ appears and becomes strong and dominant at 900 °C (Figs. 3.3a, 3.3b, and 3.8a). Given the fact that Mg²⁺-rich phyllosilicates tend to form new crystal structures at high temperatures, this new band could be due to newly-formed bonds associated with Mg²⁺ and could be a diagnostic spectral feature of high temperature Mg²⁺-rich dioctahedral phyllosilicates.

3.4.3 Inconsistency between spectral behaviors in the mid-to-far-IR and NIR regions and geologic implications

One of the important objectives of this study is to determine if thermal treatment could affect the TIR (400-1400 cm^{-1}) and NIR regions in different ways, which could partially be responsible for the difficulty in detecting phyllosilicates on Mars using TIR emission spectroscopy. Results from this study have shown that phyllosilicates can lose all original spectral features in the TIR region while maintaining their characteristic hydration bands in NIR region in the same temperature range.

Nontronite: Michalski et al. (2010) analyzed the nontronite deposits in the Nili Fossae region using TES data. They did not detect the spectral features showing the occurrences of nontronite in long-wavelength region. Instead, TES data consistently exhibit a spectral absorption located near $\sim 450 \text{ cm}^{-1}$ on the same surfaces where OMEGA and CRISM data display the diagnostic NIR spectral bands (1.4, 1.9, 2.3, and 2.4 μm) for nontronite. Our laboratory results (**Figs. 3.4 and 3.13**) show that the doublet or triplet spectral feature in the Si-O bending region of nontronites disappear at 400 $^{\circ}\text{C}$ and is replaced by one single absorption centered at $\sim 450 \text{ cm}^{-1}$. In the NIR region, both nontronite samples display the 1.9 μm band and extremely weak 2.3 and 2.42 μm features when heated to 400 $^{\circ}\text{C}$. We also observe that both nontronites lose the 1.4 μm feature completely at the 400 $^{\circ}\text{C}$. Based on the observation from Nili Fossae and spectral results from this study, we suggest that the nontronite deposits in Nili Fossae have been partially altered at temperatures up to 400 $^{\circ}\text{C}$. This thermally altered nontronite may occur within an assemblage that is composed of both unaltered and thermally altered nontronite along with a variety of other silicate minerals. The NIR spectrum of this assemblage could have a weak 1.4 μm feature, a strong 1.9 μm feature, and the diagnostic 2.3 μm band, while the far-IR region is dominated by a

strong 450 cm^{-1} absorption band. This hypothesis will be investigated by detailed future remote sensing study.

Trioctahedral phyllosilicates: As discussed in previous sections, the octahedral sites of trioctahedral phyllosilicates are occupied with Mg^{2+} , and they tend to form the enstatite structure upon heating to $700\text{ }^{\circ}\text{C}$. In this study, hectorite (**Figs. 3.6 and 3.15**), saponite (**Figs. 3.5 and 3.14**), and sepiolite (**Figs. 3.8b and 3.17b**) all still maintained diagnostic NIR spectral bands of phyllosilicates at high temperatures (e.g. 1.9, 2.3 and 2.4 μm features at $700\text{ }^{\circ}\text{C}$ for hectorite and saponite; 1.9, 2.2 μm bands at $900\text{ }^{\circ}\text{C}$ for sepiolite), while their mid-to-far-IR spectra at temperatures of $700\text{ }^{\circ}\text{C}$ or higher were already dominated by spectral bands of enstatite, which are completely different from those of phyllosilicates.

3.5. Summary and conclusions

In order to complement mid-to-far-IR studies of dehydrated and/or dehydroxylated phyllosilicates and zeolites (Che *et al.* 2011) and supplement the spectral library (available at <http://aram.ess.sunysb.edu/tglotch/spectra.html>) at the Stony Brook University Vibrational Spectroscopy Laboratory, we reported NIR diffuse reflectance and mid-to-far-IR emissivity spectra of 14 phyllosilicates and 2 natural zeolites at various temperatures. DSC measurements were also performed on each sample in order to clarify their thermal activities. We conclude that:

- (1) Spectral features in both the NIR and mid-to-far-IR regions of phyllosilicates and natural zeolites are significantly affected by heating. The spectral behavior of each sample is unique and thermal behaviors of phyllosilicates and zeolites showed a great influence on the IR spectra upon heating. In general, the effect of dehydration on the IR properties of

all phyllosilicates and zeolites in this study is very small. The major spectral changes to phyllosilicate spectra are associated with dehydroxylation reactions, collapse of layer structures, and/or recrystallization to new phases. The two natural zeolites studied here showed minor spectral changes, corresponding to deformation of the zeolite structure at ~700-900 °C.

- (2) The composition of octahedral sites strongly influences the spectral behaviors of phyllosilicates: IR spectra of Al³⁺-rich smectites are more stable than those of Fe³⁺-rich smectites; stability of Al³⁺-rich smectites decreases as the Al³⁺ abundance decreases; spectral behaviors of Mg²⁺-rich phyllosilicates are distinctly affected by the formation of new crystalline phases near 700 °C; phyllosilicates with a small amount of Mg²⁺ in their octahedral sites all displayed a new spectral band at ~920 cm⁻¹ upon heating to 700 °C or higher temperatures.
- (3) For future remote sensing of phyllosilicate bearing regions on Mars, both NIR reflectance and mid-to-far-IR emissivity spectral results from this study may contribute towards detecting possible dehydrated and/or dehydroxylated phyllosilicates present on the Martian surface.

Acknowledgments

This work was supported by the Mars Fundamental Research Program award # NNX08AN62G made to TDG. Detailed reviews by Dr. Steve Ruff and an anonymous reviewer are greatly appreciated and improved the manuscript.

References

- Abramov, O., Kring, D. A. 2005. Impact-induced hydrothermal activity on early Mars, *J. Geophys. Res.* 110, E12S09. doi:10.1029/2005JE002453.
- Alver, B. E., Sakizci, M., Yorukogullari, E. 2010. Investigation of clinoptilolite rich natural zeolites from Turkey: a combined XRF, TG/DTG, DTA and DSC study. *J. Therm. Anal. Calorim.* 100, 19-26.
- Armbruster, T., Gunter, M. E. 2001. Crystal structure of natural zeolites. In: Bish, D. L., Ming, D. W. (Eds.), *Natural zeolites: Occurrence, properties, application. Reviews in Mineralogy and Geochemistry*, vol. 45, Mineralogical Society of America and Geochemical Society, Washington, D. C., pp, 1-57.
- Bailey, S. W. 1980. Structures of layer silicates. In: Brindley, G. W., Brown, G. (Eds.), *Crystal Structures of Clay Minerals and Their X-ray Identification*. Mineral. Soc., London, pp. 1-124.

- Ballet, O., Coey, J. M. D., Burke, K. J. 1985. Magnetic properties of sheet silicates: 2:1:1 layer minerals. *Phys. Chem. Minerals* 12, 370-378.
- Bandfield, J. L. 2002. Global minerals distributions on Mars. *J. Geophys. Res.* 107(E6), 5042. doi:10.1029/2001JE001510.
- Bandfield, J. L., Hamilton, V. E., Christensen, P. R. 2000. A global view of Martian surface compositions from MGS-TES. *Science* 287, 1626--1630.
- Barrer, R. M. 1978. Zeolite frameworks, cations and water molecules. In: Barrer, R. M. (Eds.), *Zeolites and Clay Minerals as Sorbents and Molecular Sieves*. Academic Press, London, pp. 32-102.
- Barrer, R. M. 1982. Occurrence, classification and some properties of zeolites, In: Barrer, R. M. (Eds.), *Hydrothermal Chemistry of Zeolites*. Academic Press, London, pp. 1-42.
- Bibring, J. -P., et al. 2006, Global mineralogical and aqueous Mars history derived from OMEGA/Mars Express data. *Science* 312, 400--404.
- Bish, D. L. 1984. Effects of exchangeable cation composition on the thermal expansion/contraction of clinoptilolite. *Clays Clay Miner.* 32, 444-452.
- Bishop, J. L., Pieters, C. M., Edwards, J. O. 1994. Infrared spectroscopic analyses on the nature of water in montmorillonite. *Clays Clay Miner.* 42, 701-715.
- Bishop, J. L., Lane, M. D., Dyar, M. D., Brown, A. J. 2008. Reflectance and emission spectroscopy study of four groups of phyllosilicates: smectites, kaolinite-serpentines, chlorites and micas, *Clay Miner.* 43, 35-54.

- Breck, D. W. 1974a. Chemical properties and reactions of zeolites, In: Breck, D. W. (Eds.), Zeolite Molecular Sieves: Structure, Chemistry, and Use. John Wiley and Sons, London, pp. 441-528.
- Breck, D. W. 1974b. Structure of zeolites. In: Breck, D. W. (Eds.), Zeolite Molecular Sieves: Structure, Chemistry, and Use. John Wiley and Sons, London, pp. 29-185.
- Brindley, G. W., Ali, S. Z. 1950. X-ray study of thermal transformations in some magnesian chlorite minerals. *Acta Cryst.* 3, 25-30.
- Caillere, S., Henin, S. 1957a. The sepiolite and palygorskite minerals. In: Mackenzie, R. C. (Eds.), The Differential Thermal Investigations of Clays. Mineralogical Society, London, pp. 231-247.
- Caillere, S., Henin, S. 1957b. The chlorite and serpentine minerals, In: Mackenzie, R. C. (Eds.), The Differential Thermal Investigations of Clays. Mineralogical Society, London, pp. 207-230.
- Che, C., Glotch, T. D., Bish, D. L., Michalski, J. R., Xu, W. 2011. Spectroscopic study of the dehydration and/or dehydroxylation of phyllosilicate and zeolite minerals. *J. Geophys. Res.* 116, E05007. doi:10.1029/2010JE003740.
- Cloutis, E. A., Asher, P. M., Mertzman, S. A. 2002. Spectral reflectance properties of zeolites and remote sensing implications. *J. Geophys. Res.* 107(E9), 5067. doi: 10.1029/2000JE001467.
- Earley, J. W., Milne, I. H., and McVeagh, W. J. 1953. Dehydration of montmorillonite. *Amer. Min.* 38, 770-783.
- Ehlmann, B. L., et al. 2009. Identification of hydrated silicate minerals on Mars using MRO-CRISM: Geologic context near Nili Fossae and implications for aqueous alteration. *J. Geophys. Res.* 114, E00D08. doi:10.1029/2009JE003339.

- Fairén, A. G., et al. 2010. Noachian and more recent phyllosilicates in impact craters on Mars. *Proc. Natl. Acad. Sci.* 107, 12095-12100. doi:10.1073/pnas.1002889107.
- Farmer, V. C. 1974. The layer silicates, In: Farmer, V. C. (Eds.), *The Infrared Spectra of Minerals*. Mineral. Soc., London, pp. 331-363.
- Földesová, M., Lukáč, P., Dillinger, P., Balek, V., Svetík, S. 1999. Thermochemical properties of chemically modified zeolite. *J. Therm. Anal. Calorim.* 58, 671-675.
- Frost, R. L., Kloprogge, J. T. 2000. Vibrational spectroscopy of ferruginous smectite and nontronite. *Spectrochimica Acta Part A* 56, 2177-2189.
- Frost, R. L., Kloprogge, J. T., Zhe, D. 2002. The Garfield and Uley nontronites-an infrared spectroscopic comparison. *Spectrochimica Acta Part A* 58, 1881-1894.
- Gaffey, S. J., McFadden, L. A., Nash, D., Pieters, C. M. 1993. Ultraviolet, Visible, and Near-infrared Reflectance Spectroscopy: Laboratory spectra of Geologic Materials, In: Pieters, C. M., Englert, P. A. J. (Eds.), *Remote Geochemical Analysis: Elemental and Mineralogical Composition*. Cambridge University Press, Cambridge, pp. 43-78.
- Gavin, P., Chevrier, V. 2010. Thermal alteration of nontronite and montmorillonite: Implications for the martian surface. *Icarus* 208, 721-734. doi:10.1016/j.icarus.2010.02.027.
- Glotch, T. D., Rossman, G. R., Aharonson, O. 2007. Mid-infrared (5-100 μm) reflectance spectra and optical constants of ten phyllosilicate minerals. *Icarus* 192, 604-622. Doi: 10.1016/j.icarus.2007.07.002.
- Green, J. M., Mackenzie, K. J. D., Sharp, J. H. 1970. Thermal reactions of synthetic hectorite. *Clays Clay Miner.* 18, 339-346. doi: 10.1346/CCMN.1970.0180606.

- Greene-Kelly, R. 1957. The montmorillonite minerals (smectites), In: Mackenzie, R. C. (Eds.), The Differential Thermal Investigations of Clays. Mineralogical Society, London, pp. 140–164.
- Hamilton, V. E., Christensen, P. R., McSween Jr., H. Y. 1997. Determination of Martian meteorite lithologies and mineralogies using vibrational spectroscopy. *J. Geophys. Res.* 102, 25,593-26603.
- Hedley, C. B., Yuan, G., Theng, B. K. G. 2007. Thermal analysis of montmorillonites modified with quaternary phosphonium and ammonium surfactants. *Appl. Clay Sci.* 35, 180-188.
- Holdridge, D. A., Vaughan, F. 1957. The kaolin minerals (kaolinites), In: Mackenzie, R. C. (Eds.), The Differential Thermal Investigations of Clays. Mineralogical Society, London, pp. 98–139.
- Keeling, J. L., Raven, M. D., Gates, W. P. 2000. Geology and characterization of two hydrothermal nontronites from weathered metamorphic rock at the Uley graphite mine, South Australia. *Clays Clay Miner.* 48, 537-548.
- Kloprogge, J. T., Komarneni, S., Yanagisawa, K., Frost, R. L., Fry, R. 1998. Infrared study of some synthetic and natural beidellites. *J. Mater. Sci. Lett.* 17, 1853-1855.
- Kloprogge, J. T., Frost, R. L., Hickey, L. 1999a. Infrared absorption and emission study of synthetic mica-montmorillonite in comparison to rectorite, beidellite and paragonite. *J. Mater. Sci. Lett.* 18, 1921-1923.
- Kloprogge, J. T., Fry, R., Frost, R. L. 1999b. An infrared emission spectroscopic study of the thermal transformation mechanisms in Al₁₃-pillared clay catalysts with and without tetrahedral substitutions. *J. Catal.* 184, 157-171.

- Kloprogge, J. T., Frost, R. L., Hickey, L. 2000. Infrared emission spectroscopic study of the dehydroxylation of some hectorites. *Thermochim. Acta* 345, 145-156.
- Kloprogge, J. T., Frost, R. L. 2000. The effect of synthesis temperature on the FT-Raman and FT-IR spectra of saponites. *Vib. Spectrosc.* 23, 119-127.
- Kulbicki, G. 1959. High temperature phases in sepiolite, attapulgite and saponite, *Am. Mineral.* 44, 752-764.
- Loizeau, D., et al. 2007. Phyllosilicates in the Mawrth Vallis region of Mars, *J. Geophys. Res.* 112, E08S08. doi:10.1029/2006JE002877.
- Madajová J., Komadel, P. 2001. Baseline studies of the clay minerals society source clays: Infrared methods. *Clays Clay Miner.* 49, 410-432.
- Mangold, N., et al. 2007. Mineralogy of the Nili Fossae region with OMEGA/Mars Express data; 2. Aqueous alteration of the crust. *J. Geophys. Res.* 112, E08S04. doi:10.1029/2006JE002835.
- McDowell, M. L., Hamilton, V. E. 2007a. Phyllosilicate detection and uncertainty from thermal infrared data in the vicinity of the Nili Fossae. *Lunar Planet. Sci.* XXXVIII, 1872 (abstract).
- McDowell, M. L., Hamilton, V. E. 2007b. Examination of phyllosilicate-bearing materials in the vicinity of the Nili Fossae using thermal infrared data. *Intl. Conf. Mars* 7, 3095 (abstract).
- Mermut, A. R., Faz Cano, A. 2001. Baseline studies of the clay minerals society source clays: Chemical analyses of major elements. *Clays Clay Miner.* 49, 381-386.
- Michalski, J. R., Fergason, R. L. 2009. Composition and thermal inertia of the Mawrth Vallis region of Mars and THEMIS data. *Icarus* 199, 25-48. doi: 10.1016/j.icarus.2008.08.016.

- Michalski, J. R., Noe Dobrea, E. Z. 2007. Evidence for a sedimentary origin of clay minerals in the Mawrth Vallis region, Mars. *Geology*35, 951-954.
- Michalski, J. R., Kraft, M. D., Sharp, T. G., Williams, L. B., Christensen, P. R. 2005. Mineralogical constraints on the high-silica martian surface component observed by TES. *Icarus*174, 161-177.
- Michalski, J. R., Kraft, M. D., Sharp, T. G., Williams, L. B., Christensen, P. R. 2006. Emission spectroscopy of clay minerals and evidence for poorly crystalline aluminosilicates on Mars from Thermal Emission Spectrometer data. *J. Geophys. Res.*111, E03004.doi:10.1029/2005JE002438.
- Michalski, J. R., Poulet, F., Bibring, J. -P., Mangold, N. 2010. Analysis of phyllosilicate deposits in Nili Fossae region of Mars: Comparison of TES and OMEGA data. *Icarus* 206 (1), 269-289. doi:10.1016/j.icarus.2009.09.006.
- Milliken, R. E., Mustard, J. F. 2005. Quantifying absolute water content of minerals using near-infrared reflectance spectroscopy. *J. Geophys. Res.*110, E12001.doi:10.1029/2005JE002534.
- Ming, D. W., Morris, R. V., Clark, B. C. 2008. Aqueous alteration on Mars, In: Bell, J. (Eds.), *The Martian Surface - composition, Mineralogy, and Physical Properties*. Cambridge University Press, Cambridge, pp. 519-540.
- Newsam, J. M. 1986. The zeolite cage structure. *Science*231, 1093--1099.
- Post, J. L. 1984. Saponite from near Ballarat, California. *Clays Clay Miner.* 32, 147-153.
- Poulet, F., et al. 2005. Phyllosilicates on Mars and implications for early martian climate. *Nature*438, 623--627.

- Pruett, R. J., Webb, H. L. 1993. Sampling and analysis of KGa-1b well-crystallized kaolin source clay. *Clays Clay Miner.* 41, 514-519.
- Ruff, S. W. 2003. Basaltic andesite or weathered basalt: A new assessment. *Intl. Conf. Mars* 6, 3258 (abstract).
- Ruff, S. W. 2004. Spectral evidence for zeolite in the dust on Mars. *Icarus* 168, 131-143. doi:10.1016/j.icarus.2003.11.003.
- Ruff, S. W., Christensen, P. R. 2007. Basaltic andesite, altered basalt, and a TES-based search for smectite clay minerals on Mars. *Geophys. Res. Lett.* 34, L10204. doi:10.1029/2007GL029602.
- Ruff, S. W., Christensen, P. R., Barbera, P. W., Anderson, D. L. 1997. Quantitative thermal emission spectroscopy of minerals: A technique for measurement and calibration. *J. Geophys. Res.* 102, 14899-14913.
- Salisbury, J. W. (1993), Mid-infrared spectroscopy: laboratory data, In: Pieters, C. M., Englert, P. A. J. (Eds.), *Remote Geochemical Analysis: Elemental and Mineralogical Composition*. Cambridge University Press, Cambridge, pp. 79-98.
- Salisbury, F. B., Wald, A., D'Aria, D. M. 1994. Thermal-infrared remote sensing and Kirchhoff's law 1. Laboratory measurements. *J. Geophys. Res.* 99 (B6), 11897-11911.
- Schwenzer, S. P., Kring, D. A. 2009. Impact-generated hydrothermal systems capable of forming phyllosilicates on Noachian Mars. *Geology* 37, 1091-1094.
- Van der Marel, H. W., Beutelspacher, H. 1976. *Atlas of infrared spectroscopy of clay minerals and their admixtures*. Elsevier Scientific Pub.Co., Amsterdam, New York.

- Van Olphen, H., Fripiat, J. J. 1979. Data handbook for Clay Materials and other Non-Metallic Minerals. Pergamon, Oxford.
- Vicente, M. A., Bañares-Muñoz, M. A., Gandía, L. M., Gil, A. 2001. On the structural changes of a saponite intercalated with various polycations upon thermal treatments, *Appl. Catal., A*. 217, 191-204.
- Villieras, F., Yvon, J., Cases, J. M., De Donato, P., Lhote, F., Baeza, R. 1994. Development of microporosity in clinocllore upon heating. *Clays Clay Miner.* 42(6), 679-688. doi: 10.1346/CCMN.1994.0420604.
- Viviano, C. E., Moersch, J. E. 2011. Using THEMIS to address discrepancies between OMEGA/CRISM and TES detections of phyllosilicates. *Lunar Planet. Sci.* XLII, 2251 (abstract).

Chapter 4: Characterizing thermally altered nontronites in Nili Fossae, Mars using thermal and near IR spectroscopy

This chapter has been presented at the 43rd Lunar and Planetary Science Conference. This part manuscript will undergo minor additions and be submitted to a peer-reviewed scientific journal as well.

Che, C. and T. D. Glotch (2012), Characterizing dehydrated nontronites in Nili Fossae, Mars using thermal and near IR spectroscopy. 43rd Lunar Planet. Sci., abstract #1377 (oral presentation).

Phyllosilicates in the Nili Fossae region on Mars have been studied in great detail due to the diversity and complex geomorphologic and geologic contexts with which they are associated. Detailed analyses of phyllosilicates in the ancient Nili Fossae region give insights into the complicated sedimentary and aqueous alteration history of Mars. In this study, analysis of remote sensing data including both thermal and near IR data sets suggests that thermally altered (at 400 °C) nontronite may be present in Nili Fossae and mixed with unaltered nontronite. The presence of dehydrated nontronite suggests that previously formed phyllosilicates may have been significantly modified by post-depositional heating. Post-depositional thermal alteration of sedimentary deposits has important implications for understanding hydration processes during the Noachian.

4.1 Introduction

The composition, geologic setting, and assemblages of phyllosilicate minerals on Mars are important for understanding Martian environmental and climatic history. Previous studies of visible and near infrared (VNIR) spectra from the Mars Express Observatoire pour la Minéralogie, l'Eau, les Glaces, et l'Activité (MEx/OMEGA) and the Mars Reconnaissance Orbiter Compact Reconnaissance Imaging Spectrometer for Mars (MRO/CRISM) have shown that most phyllosilicates are associated with ancient, heavily cratered terrains [e.g., *Poulet et al. 2005; Bibring et al. 2006; Mangold et al. 2007; Michalski and Noe Dobrea 2007*], suggesting that they may have been exposed to post-depositional thermal alteration [e.g., *Fair én et al. 2010*]. Sources of high temperatures could include impact processes, volcanic events, or deep burial. Models [*Abramov and Kring, 2005*] have shown that meteoric impacts could lead to long term heating of the target rocks and post-shock temperatures could reach as high as 1200 °C. Preexisting phyllosilicates could be significantly modified by the impact crater excavation process. Most phyllosilicates start to lose H₂O at temperatures of ~100 °C and lose their hydroxyl groups completely at ~1000 °C [e.g., *Milliken and Mustard, 2005; Fair én et al. 2010; Gavin and Chevrier, 2010; Che et al., 2011; Che and Glotch, 2012*]. Hence, we propose that dehydration and/or dehydroxylation of phyllosilicates subjected to post-depositional thermal alteration may have been a widespread process on early Mars, and that dehydrated and/or dehydroxylated phyllosilicates may be still abundant on the Martian surface.

We present here a detailed study of the nontronite deposits that numerous authors have identified in the Nili Fossae region [e.g., *Poulet et al., 2005; Mangold et al., 2007; Ehlmann et al., 2009; Michalski et al., 2010*]. Nili Fossae is located west of the large Isidis Basin and the Noachian crust is well exposed. Previous studies revealed that Nili Fossae has been heavily modified by normal faulting, impact, and erosion and infilling by Hesperian lava flows [*Greeley*

and Guest, 1987; Wichman and Schultz, 1989]. Therefore this region holds important information about complicated Martian geologic history. Interpretation of both OMEGA and CRISM spectra shows that Nili Fossae contains one of the most significant phyllosilicate exposures on Mars, and that phyllosilicates detected in this region are predominantly Fe/Mg-rich smectite minerals. Michalski *et al.* [2010] analyzed the nontronite deposits in the Nili Fossae area using data from both OMEGA and the Mars Global Surveyor Thermal Emission Spectrometer (MGS/TES). The VNIR spectrum of the area displays an Fe-OH feature at 2.28 μm and associated hydration bands (1.4 and 1.9 μm), suggesting the presence of nontronite or a nontronite-like Fe-rich smectite mineral. However, thermal IR (TIR) spectra from TES consistently exhibit an absorption near 450 cm^{-1} , that does not match any particular Fe-rich smectite. Using CRISM spectra, Ehlmann *et al.* [2009] analyzed the Nili Fossae region nearby the study area of Michalski *et al.* [2010]. CRISM results revealed a spectral absorption feature near 2.3 μm , suggesting the presence of Fe/Mg smectite mineral solid solution. Therefore, the 450 cm^{-1} spectral feature in the TES spectra [Michalski *et al.* 2010] could be explained by the presence of Fe/Mg-bearing smectites, which exhibit a strong spectral feature from 500-450 cm^{-1} . However, the strong absorption band of Mg-rich smectites such as saponite and hectorite occur at 470-480 cm^{-1} [e.g., Che and Glotch, 2012] (**Figure 4.1**), which makes this explanation less likely. We obtained laboratory spectra [Che and Glotch, 2012] of heated nontronite and found that the doublet or triplet spectral feature in the Si-O bending region disappears at 400 $^{\circ}\text{C}$ and is replaced by a single absorption at $\sim 450 \text{ cm}^{-1}$ while the nontronite sample keeps weak 1.9, 2.29, and 2.4 μm spectral bands in the VNIR region (**Figure 4.2**). This leads us to suggest that the Fe/Mg smectite deposits in the Nili Fossae region may be partly composed of nontronite heated to temperatures around 400 $^{\circ}\text{C}$.

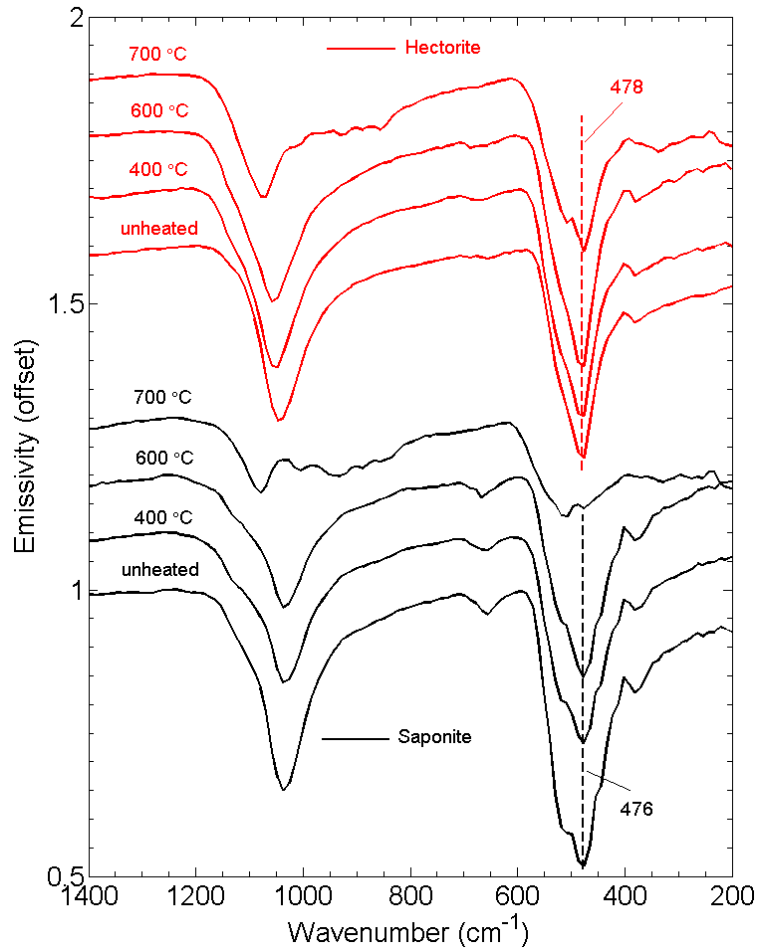


Figure 4.1 Laboratory emissivity spectral results of hectorite, saponite, and their heating products [Che and Glotch, 2012]. All emissivity spectral were resampled to TES spectral resolution (143 bands). The spectral features in the lower wavenumber range of both samples are dominated by a single strong band at $\sim 477 \text{ cm}^{-1}$ until $600 \text{ }^\circ\text{C}$ heating.

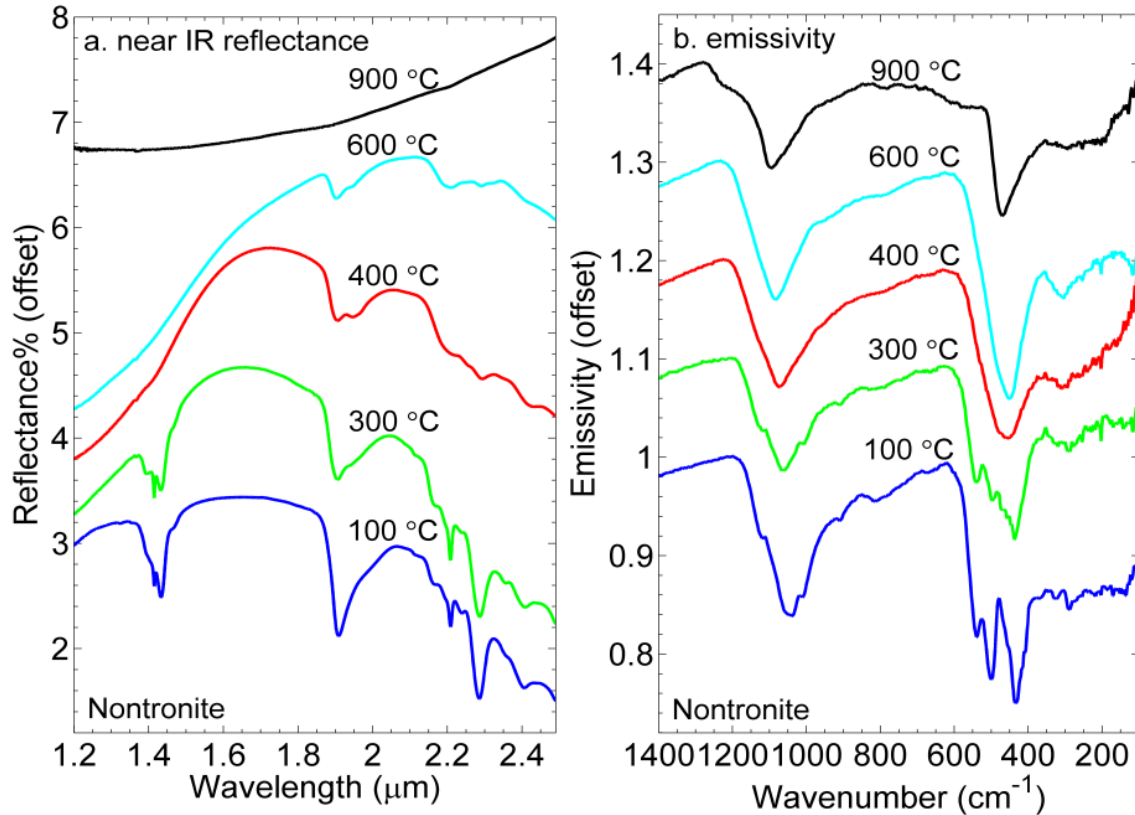


Figure 4.2 (a) Near IR reflectance and (b) emissivity spectra of nontronite heated for 24 hours to 100 °C, 300 °C, 400 °C, 600 °C, and 900 °C. At 300 °C, the spectral features in the range 400-600 cm⁻¹ display significant change, while no obvious changes are observed for nontronite's NIR spectral features. At 400 °C, the triplet spectral feature in the Si-O bending region is replaced by one single absorption centered at ~450 cm⁻¹, while nontronite sample keeps the weak 1.9, 2.3, and 2.4 μm spectral bands in NIR region (spectra adopted from *Che and Glotch, 2012*).

4.2 Data and methods

To search for possible thermally altered nontronites in Nili Fossae, we used a variety of spectroscopic methods, covering VNIR to TIR wavelengths. (1) We used the non-negative least squares (NNLS) deconvolution algorithm of *Rogers and Aharonson* [2008], with an enhanced spectral library (**Table 4.1**) that includes thermally altered (at 400 °C) nontronite, to deconvolve an averaged TES spectrum of a surface in the Nili Fossae region that was determined to be Fe/Mg smectite and nontronite-bearing based on CRISM [*Ehlmann et al.*, 2009] and OMEGA data [*Michalski et al.*, 2010], respectively. For comparison, we also deconvolved an average TES spectrum of a nearby surface that appears spectrally neutral in OMEGA data. For this method, 30 and 23 high quality (low water ice opacity, low dust opacity, and high surface temperature) TES spectra from OCK 3245 were selected and averaged for the nontronite-bearing surface and the nearby surface, respectively. (2) We also used spectral ratios of TES data to help us determine the long-wavelength spectral character of the nontronite-bearing deposits. An average of 30 un-atmospherically corrected high quality TES spectra covering a deposit of interest was divided by an spectrum averaged from 23 un-atmospherically corrected TES spectra from an adjacent, relatively “spectrally neutral” surface. TES spectra from the same orbit were used to avoid errors brought by different atmospheric conditions between orbits [*Rogers and Bandfield*, 2009; *Michalski et al.*, 2010]. (3) We used local-scale spectral index mapping of thermally altered nontronite, based on the unique TIR spectral properties of this phase. This index was developed to map the $\sim 450 \text{ cm}^{-1}$ absorption feature of 400 °C nontronite. This index was created according to the formula $(\epsilon_{508} + \epsilon_{371})/(\epsilon_{444} + \epsilon_{466})$. (4) We also used factor analysis and target transformation (FATT) [*Malinowski*, 1991] to determine the independently variable spectral components in regions of interest. We gathered 5616 individual TES spectra from the Nili

Fossae region and applied R-mode factor analysis and target transformation, using a linear deconvolution algorithm, with spectra of atmospheric components, basaltic TES Surface Type 1 (ST1), TES Surface Type 2 (ST2), Martian surface dust, 400 °C heated and unheated nontronite as “targets”. (5) Using CRISM data, we performed local-scale index mapping of thermally altered nontronites using the ratio of band depths of the 1.4 and 1.9 µm spectral features. *Che and Glotch* [2012] showed that the 1.4 µm feature reduces in intensity at a faster rate than the 1.9 µm band as nontronite is heated. At 400 °C, the 1.4 µm feature of nontronite disappears completely while the 1.9 µm feature is still strong. Therefore mapping the ratio of 1.4 and 1.9 µm could provide insight about the degree of thermal alteration of nontronite in Nili Fossae. To map this ratio, we created a 1.4 µm band depth index according to $(1 - R_{1430} / (0.4 * R_{1370} + 0.6 * R_{1470}))$ and a 1.9 µm band depth index according to $(1 - R_{1915} / (0.77 * R_{1857} + 0.23 * R_{2112}))$.

Table 4.1 Spectral library used in the deconvolution of TES data and FATT-derived spectrum*

Mineral Group	End-Member
Quartz	Quartz BUR-4120
Feldspar	Microcline BUR-3460 Albite WAR-0244 Oligoclase WAR-5804 Andesine BUR-240 Labradorite WAR-4524 Bytownite WAR-1384 Anorthite BUR-340
Orthopyroxene	Bronzite NMNH-93527 Enstatite HS-9.4B Bronzite BUR-1920
Clinopyroxene	Diopside NMNH-R15161 Diopside WAR-6474 Augite DSM-AUG01 Augite BUR-620 Hedenbergite manganooan DSM-HED01
Olivine	Forsterite BUR-3720A Olivine Fo ₆₈ KI-3115 (a) Olivine Fo ₆₀ KI-3362 (a) Olivine Fo ₃₅ KI-3373 (a) Olivine Fo ₁₀ KI-3008 (a)
Zeolite	Heulandite (b) Stilbite(b)
Phyllosilicates	Biotite BUR-840 Muscovite WAR-5474 Serpentine HS-8.4B Antigorite NMNH-47108 Illite IMt-2 Saponite Montmorillonite Swy-2 Nontronite WAR-5108 Kaolinite KGa-1b
Amorphous silica	K-rich Glass (c) Opal-A (d)
Amphibole	Magnesiohastingsite HS-115.4B Actinolite HS-116.4 B
Hematite	Average Martian Hematite (e)
Carbonate	Calcite C40 Dolomite C20

Sulfate	Anhydrite ML-S9 Gypsum ML-S5 Gypsum (selenite) ML-S8
Atmosphere	Dust Low CO2 (f) Dust High CO2 (f) Water Ice Cloud (High Latitude) (f) Water Ice Cloud (Low Latitude) (f) CO2 Gas (g) H2O Gas (g)
Thermally altered nontronite	400 °C heated nontronite (h)

*Mineral spectra are from the ASU spectral library [Christensen *et al.*, 2000] (available online at spelib.asu.edu), unless otherwise stated.

(a) *Hamilton*, [2010]; (b) *Ruff*, [2004]; (c) *Wyatt et al.*, [2001]; (d) *Michalski et al.*, [2003]; (e) *Glotch et al.*, [2004]; (f) *Smith et al.*, [2000]; (g) *Bandfield et al.*, [2000a]; (h) *Che and Glotch*, [2012].

4.3 Results

This study is focused on the NE-SW striking grabens shown in **Figure 4.3**. The “on deposit” surface contains phyllosilicate signatures (Fe/Mg smectite) based on analysis of OMEGA and CRISM data [Ehlmann *et al.*, 2009; Michalski *et al.*, 2010]. The “off deposit” surface is located within the graben, eroded and flooded by Syrtis Major basaltic lavas; a mineralogical map based on OMEGA data shows that phyllosilicate minerals are rare in this region [Michalski *et al.*, 2010].

The results of the deconvolution models of TES data (OCK 3245) are shown in **Figure 4.4** and **Table 4.2**. TES spectra both on and off the “deposit” are matched well with relatively similar abundances of pyroxene, olivine, and minor sulfate and carbonate. The averaged TES spectrum covering the “on deposit” surface is modeled with a substantial fraction ($24\pm 5\%$) of thermally altered nontronite (400 °C) and a relative minor amount ($8\pm 6\%$) of unaltered phyllosilicates and zeolites. By contrast, the “off deposit” spectrum is modeled with a smaller fraction ($15\pm 6\%$) of altered nontronite, $9\pm 6\%$ phyllosilicates and zeolites, and a substantial amount ($28\pm 4\%$) of plagioclase feldspar. The mineralogical differences between these two deposits are also expressed in the measured and modeled spectra from these regions, which are shown in **Figure 4.4**. In general, the spectra from both on and off the deposit look similar. However, as noted by Michalski *et al.* [2010], there are important differences at long wavelengths. The gray area in **Figure 4.4** highlights the region of the main long-wavelength absorption band ($\sim 450\text{ cm}^{-1}$) seen in the 400 °C heated nontronite. In this spectral region, the emissivity maximum is muted for the spectrum on the deposit, with a lower overall emissivity, and a shallower slope towards longer wavelengths as compared to the spectrum collected off the deposit. We suggest that this is a direct consequence of the long-wavelength spectral nature of

the thermally altered nontronite (**Figure 4.2b**) and the contribution of this component to the TES spectrum on the deposit.

The spectral ratio approach can help eliminate the errors due to atmospheric conditions and gain a better understanding of the spectral character of regions of interest [*Rogers and Bandfield, 2009; Michalski et al., 2010*]. *Michalski et al.* [2010] used this method to show that regions in Nili Fossae identified as nontronite-bearing by OMEGA display a unique long wavelength spectral feature centered at $\sim 450 \text{ cm}^{-1}$. *Michalski et al.* [2010] were not able to uniquely identify this feature at the time, but noted that it was a poor match to laboratory emissivity spectra of nontronite. In this work, we created ratio spectra from two TES orbits covering “nontronite” deposits identified by OMEGA and CRISM (on and off deposits shown in **Figure 4.3**). These ratio spectra, shown in **Figure 4.5**, are poor matches to the long-wavelength spectral features of nontronite, but are very good matches to the long wavelength features of nontronite thermally altered at $400 \text{ }^\circ\text{C}$. The match between the laboratory and ratio spectra is relatively poor at shorter wavelengths ($800\text{-}1300 \text{ cm}^{-1}$), but this is likely due to the strong influence of atmospheric dust in this region. Atmospheric dust is spectrally neutral at longer wavelengths ($\sim 200\text{-}600 \text{ cm}^{-1}$), providing for a cleaner ratio in this region.

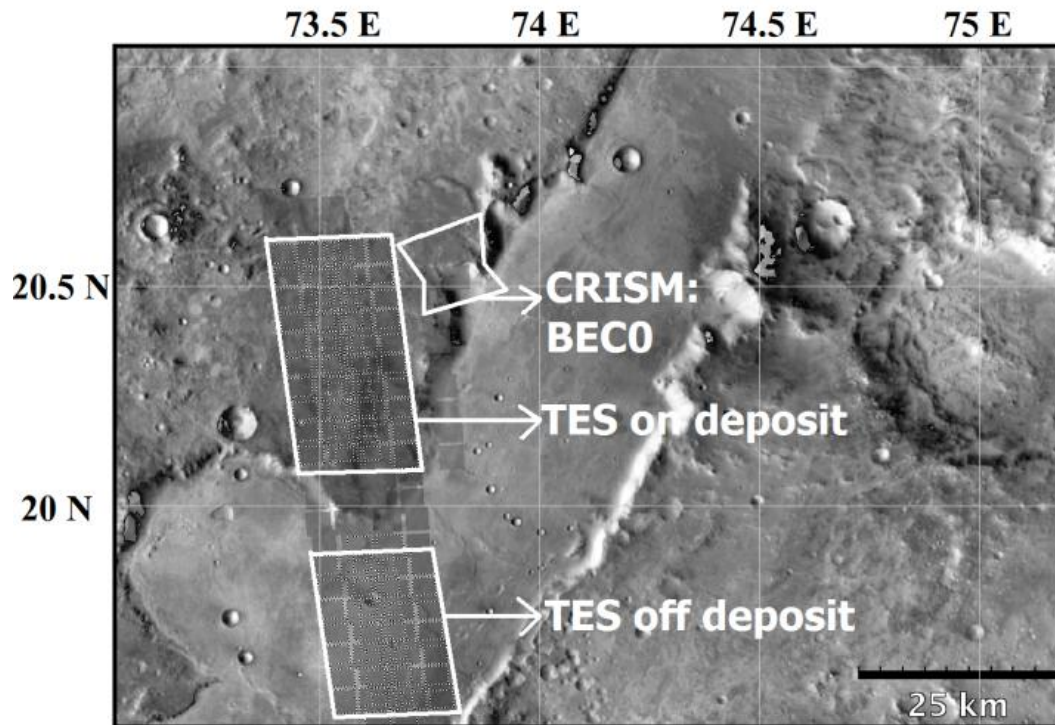


Figure 4.3 Context image of the Nili Fossae region showing positions of TES and CRISM data discussed below and shown in Figures 4.4, 4.5, and 4.10.

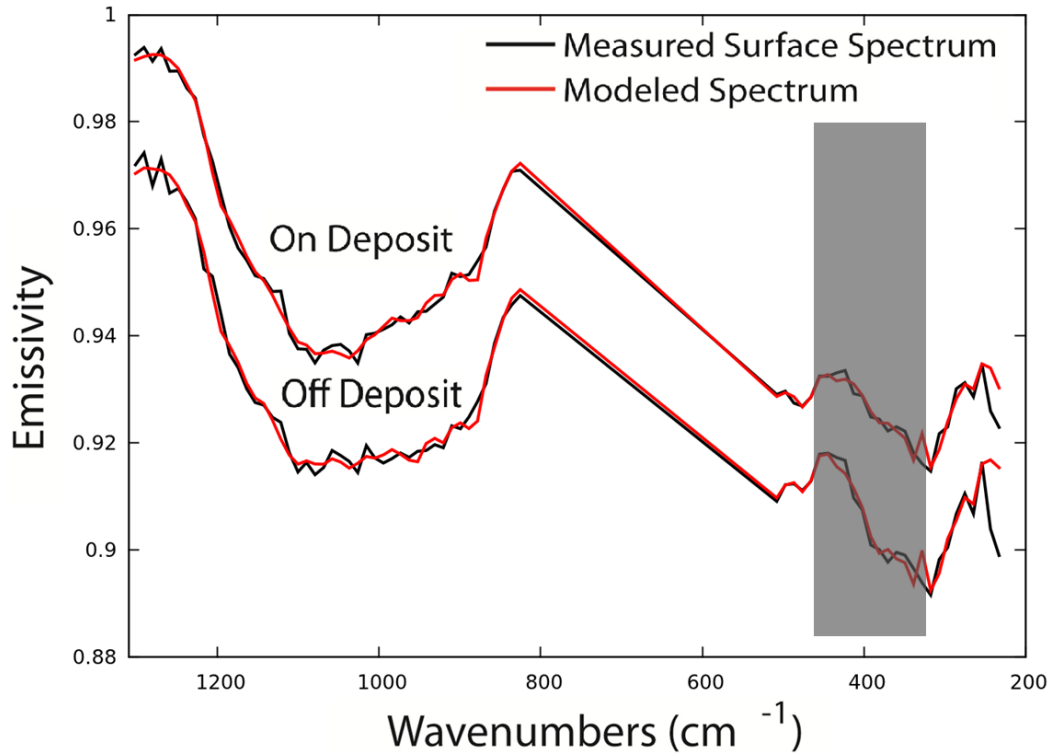


Figure 4.4 Measured surface and modeled TES spectra occurring on and off the nontronite deposit identified by OMEGA [Michalski *et al.*, 2010] and CRISM [Ehlmann *et al.*, 2009]. The gray box indicates a long wavelength region where the spectra differ due to the presence of thermally altered nontronite in the deposit.

Table 4.2 Modeled mineral abundances of TES spectra occurring on and off a “nontronite” deposit identified by OMEGA and CRISM.

Mineral Group	On Deposit	Off Deposit
Altered Nontronite	24 ±5	15 ±6
Pyroxene	25 ±9	26 ±9
Plagioclase	24 ±4	28 ±4
Sulfate	5 ±1	6 ±2
Carbonate	5 ±1	6 ±1
Olivine	8 ±3	9 ±3
Phyllosilicates/zeolites	8 ±6	9 ±6
RMS Error (%)	0.1488	0.1784

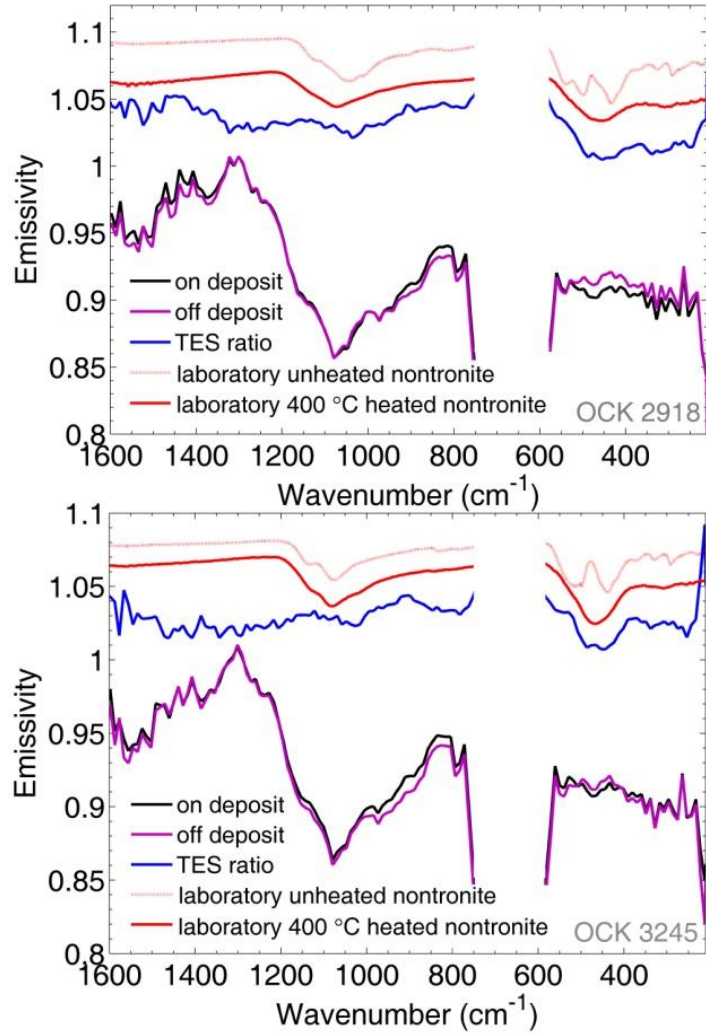


Figure 4.5 Ratios of TES spectra occurring on and off deposits identified in Nili Fossae as nontronite-bearing by CRISM. The long-wavelength (low-wavenumber) portion of each ratio spectrum is a good match to a laboratory spectrum of nontronite [Che and Glotch, 2012] heated to 400 °C. It is a poor match to spectra of unaltered nontronite. TES OCK 2918 ratio spectrum is compared with nontronite NAu-1. B) TES OCK 3245 ratio spectrum is compared with nontronite NAu-2.

Figure 4.6 shows the band depth index map created to highlight regions in Nili Fossae region displaying a spectral band at $\sim 450\text{ cm}^{-1}$, which is the position of the main long wavelength spectral feature of nontronite thermally altered at $400\text{ }^{\circ}\text{C}$. Investigation of the regional map (**Figure 4.6**) shows that while most of the Nili Fossae region appears to have low index values, several smaller regions do indeed have high index values (arrows). The black arrow in this index map points to a high 450 cm^{-1} index value that corresponds to the TES spectra outlined in **Figure 4.3**. Linear deconvolution and ratio spectra confirm that the index is making a positive detection of thermally altered nontronite in this region. The spectral indexing, deconvolution, and spectral ratio methods all suggest the presence of this spectrally unique material in the Nili Fossae region.

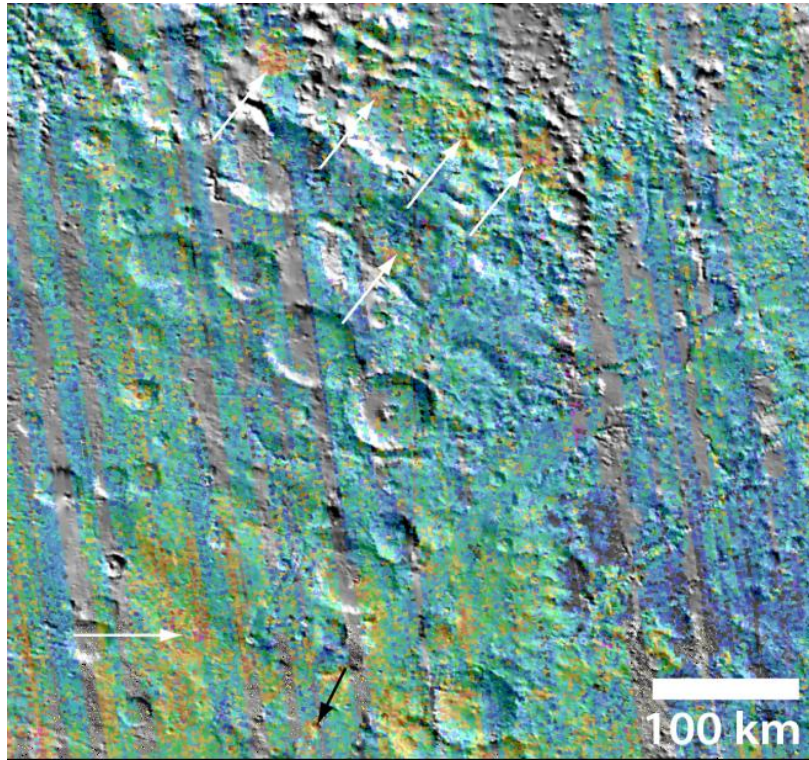


Figure 4.6 Regional-scale map of the 450 cm^{-1} index in the Nili Fossae region. The white and black arrows point to areas having high index values. Several smaller regions do indeed have high index values (white and black arrows). The black arrow in this index map points to a high 450 cm^{-1} index value that corresponds to the TES spectra outlined in **Figure 4.3**.

FATT-derived spectra are shown in **Figures 4.7, 4.8, and 4.9**.

Atmospheric endmembers As would be expected, Martian atmospheric components were recovered by the FATT algorithm (**Figure 4.7**). The target spectra of atmospheric components used for this recovery were spectral shapes of atmospheric dust (both high and low dust to CO₂ concentration), water ice (both high and low latitude clouds), synthetic CO₂ and H₂O vapor derived from *Smith et al.*, [2000] and *Bandfield* [2002]. Dust, water ice (high latitude), and synthetic CO₂ spectral shapes were recovered from the study area. Of these, spectral shapes of atmospheric dust (with high and low dust to CO₂ concentration) and water ice (high latitude) are well constrained, and the overall fit of the recovered spectrum to the synthetic Martian CO₂ is good, with the exception of the region between 950 and 1100 cm⁻¹. In this region, the main spectral features are shallower and broader than the synthetic Martian CO₂. Therefore, the recovered spectral shapes from the Martian atmospheric components indicate that the atmospheric dust, water ice clouds, and CO₂ are likely the main atmospheric endmembers of the study area.

Surface endmembers We also attempted to recover three Martian surface components in this study: surface dust, basalt, and 400 °C heated nontronite. **Figure 4.8** shows the spectral shapes recovered from FATT method using TES ST1 (basalt), TES ST2 (basaltic andesite), and TES average high albedo surface dust [*Bandfield et al.*, 2000; *Bandfield and Smith*, 2003] as target spectra. There is good overall agreement between the target spectrum TES ST1 and recovered spectrum, indicating that basalt is a likely component of the study area. At long wavelengths, a poor match between the TES ST2 spectrum and FATT-derived spectrum is observed, suggesting that basaltic andesite is not a component of the study area in the Nili Fossae region. For Martian surface dust, a good overall agreement between the target and FATT-derived spectra is observed,

particularly at the higher wavenumbers ($>400\text{ cm}^{-1}$), suggesting that the surface dust is likely to be another component of the study area. The distinct drop-off to lower emissivity at lower wavenumbers ($<400\text{ cm}^{-1}$) is likely due to the lower signal-noise-ratio for this wavenumber range [Glotch and Bandfield, 2006]. In **Figure 9**, neither FATT-derived spectrum is a perfect match to the laboratory target spectra, but the match to the thermally altered nontronite spectrum is clearly better. It is not surprising that a perfect fit cannot be made to a single mineral target spectrum [e.g., Glotch and Bandfield, 2006]. The most likely scenario on the Martian surface is that the thermally altered nontronite occurs within an *assemblage*, and it is the spectrum of this assemblage that varies independently with other components in the scene. To determine the composition of this assemblage, we deconvolved the FATT spectrum (using the spectral library shown in **Table 4.1**) derived from the thermally altered nontronite spectrum. The results are shown in **Table 4.3** and **Figure 4.9b**. The spectrum is modeled as 35% thermally altered nontronite, 22% other (unaltered) phyllosilicates and zeolites, and $<15\%$ of every other phase.

Therefore, four Martian atmospheric components and three surface components were recovered using FATT methods. For the study area, atmospheric dust, water ice, and synthetic CO_2 are likely the main components for the regional atmospheric condition. The surface components include basalt, dust, and a mineral assemblage including thermally altered nontronite.

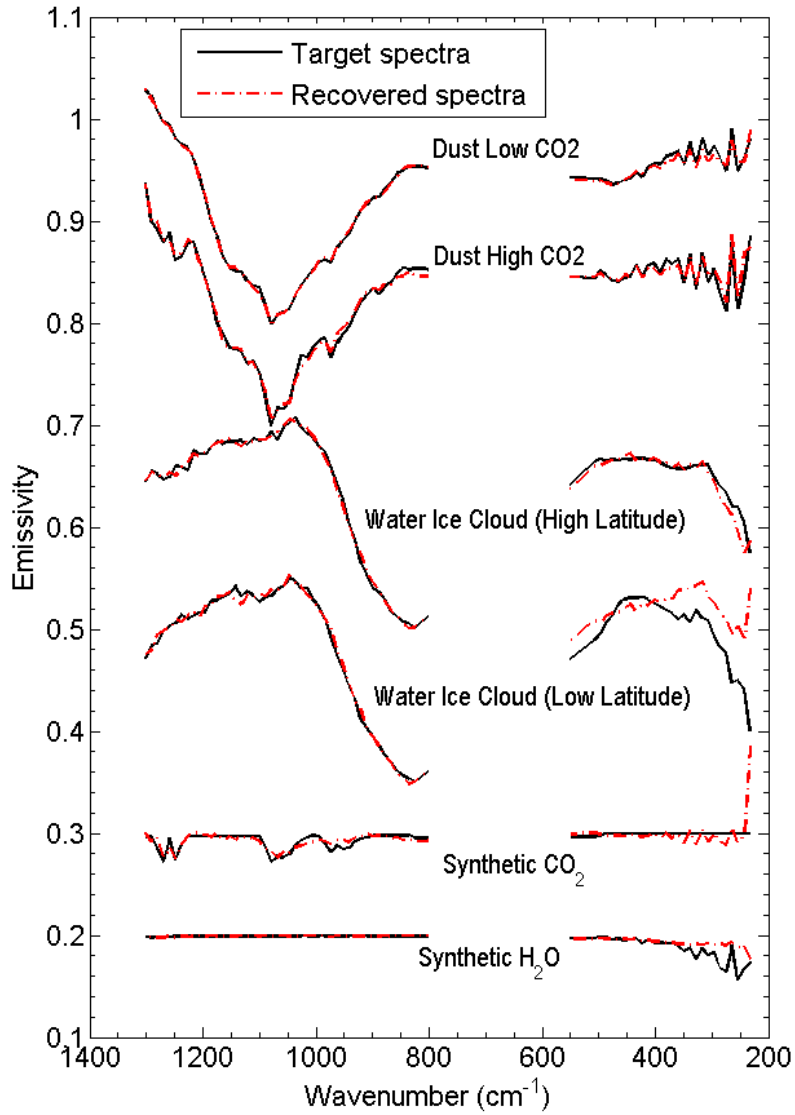


Figure 4.7 Target and recovered spectra of atmospheric components (atmospheric dust, water ice cloud, synthetic atmospheric CO₂, and synthetic H₂O vapor) derived from *Smith et al.*, [2000] and *Bandfield et al.*, [2000a].

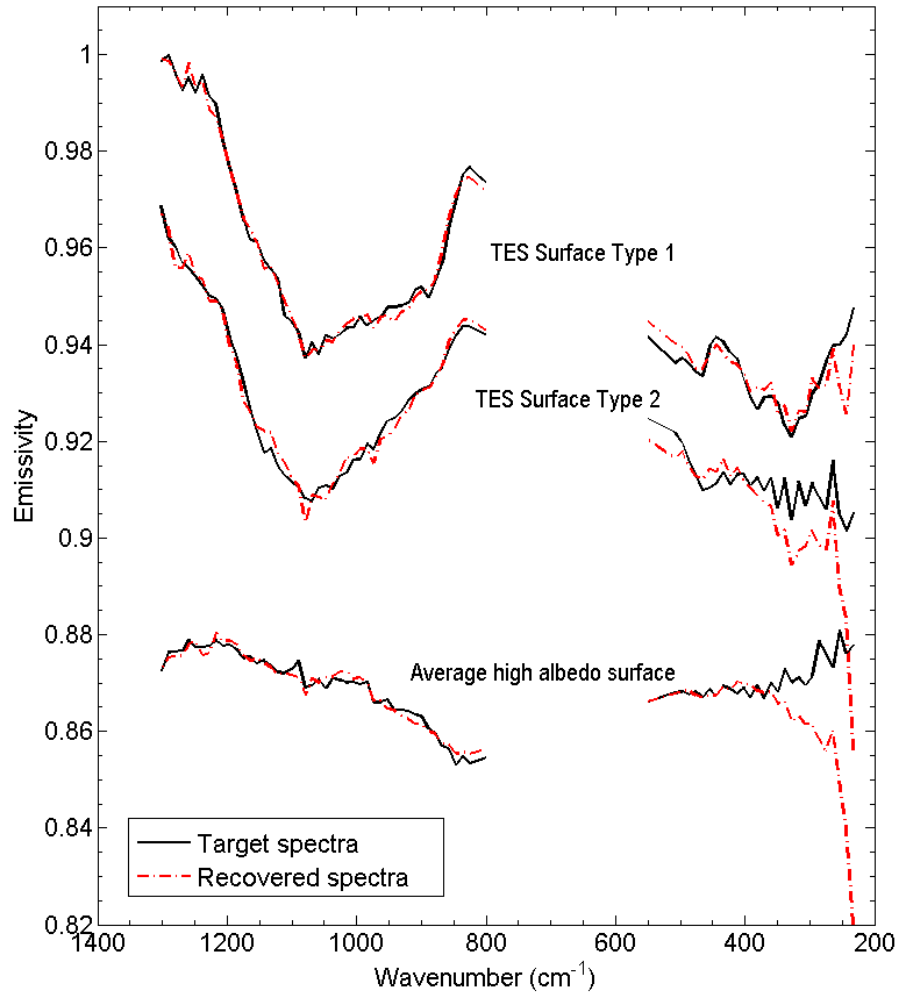


Figure 4.8 Spectral shapes recovered from FATT method using TES ST1 (basalt), TES ST2 (basaltic andesite), and Martian average surface dust [Bandfield *et al.*, 2000b; Bandfield and Smith, 2003] as target spectra.

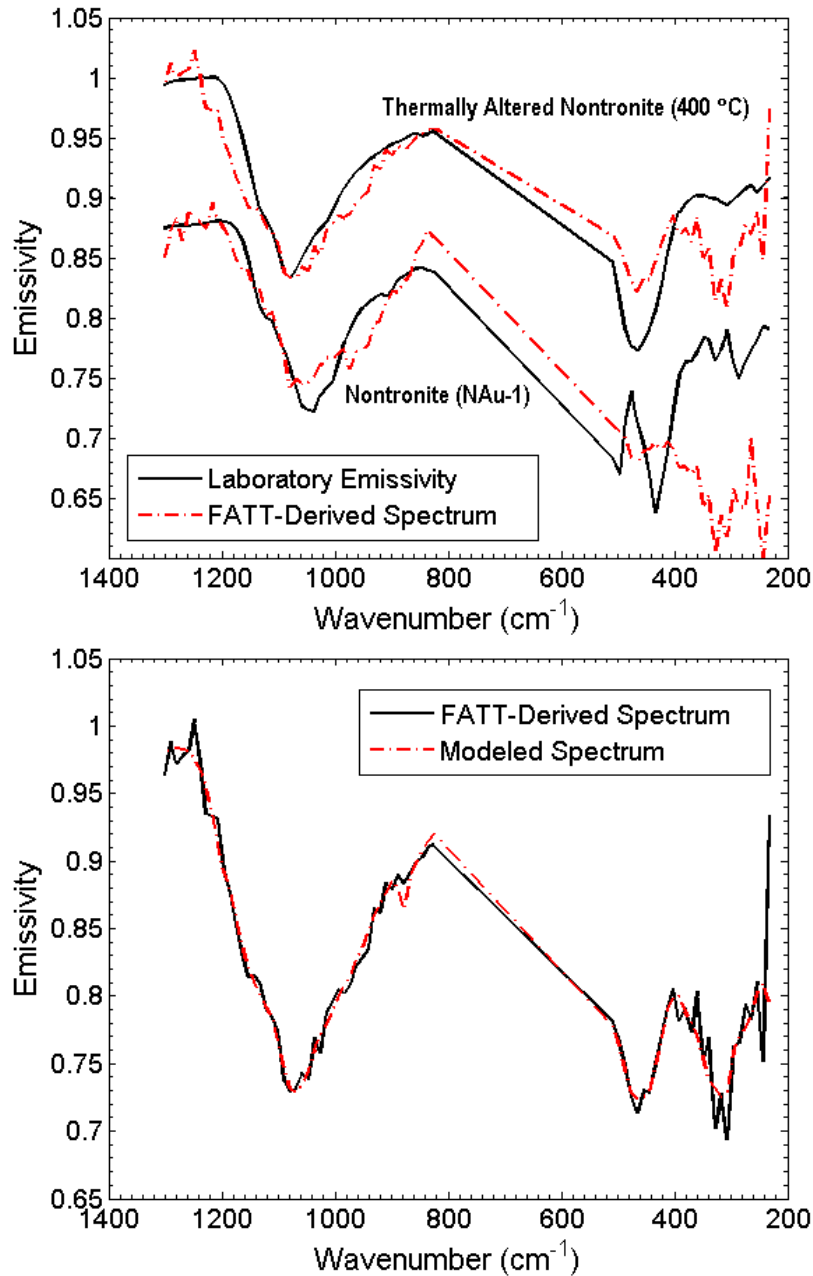


Figure 4.9 a) FATT-derived spectra of thermally altered nontronite and pure nontronite. The TES data provide a much better fit to the thermally altered nontronite. b) Linear deconvolution of our FATT-derived spectrum results in a good model fit using 35% altered nontronite.

Table 4.3 Mineral group abundances associated with the thermally altered nontronite FATT-derived spectrum.

Mineral Group	Abundance
Altered Nontronite	35±11
Phyllosilicates/zeolites	22±11
Plagioclase	13±14
Pyroxene	15±20
Sulfate	7±3
Carbonate	4±1
Other	4±13
RMS Error (%)	1.5

Figure 4.10 shows a 1.4 to 1.9 μm ratio index map created from CRISM image FRT0000BEC0_07 (location shown in **Figure 4.3**) and two characteristic ratio spectra of phyllosilicates. The strong nontronite signature in the image is indicated by the band absorptions near 1.428 and 2.296 μm [e.g., *Bishop et al.*, 2002; *Ehlmann et al.*, 2009; *Che and Glotch*, 2012], therefore the smectites of the study area are likely dominated by Fe-rich smectite instead of Fe/Mg smectite solid solution. Detailed inspection of the index map reveals that the spectrum of spot A displays a relatively higher 1.4/1.9 μm index value than spot B. Spot A matches relatively well to a mixed spectrum of unaltered and thermally altered nontronite. The CRISM spectrum of spot B exhibits a weaker 1.4 μm feature. One interpretation of this observation is that spot B has more thermally altered nontronite than spot A. This result suggests that 1.4/1.9 μm index mapping could provide useful information for detection of thermally altered phyllosilicates (the relationship between the 1.4 and 1.9 μm band depths shown in this study holds for several other phyllosilicates, such as montmorillonite, palygorskite, sepiolite, hectorite and saponite [*Che and Glotch*, 2012]), and it agrees well with the TES deconvolution and FATT results (**Tables 4.2 and 4.3**), that a shared existence of thermally altered and unaltered nontronite minerals may occur in the Nili Fossae region.

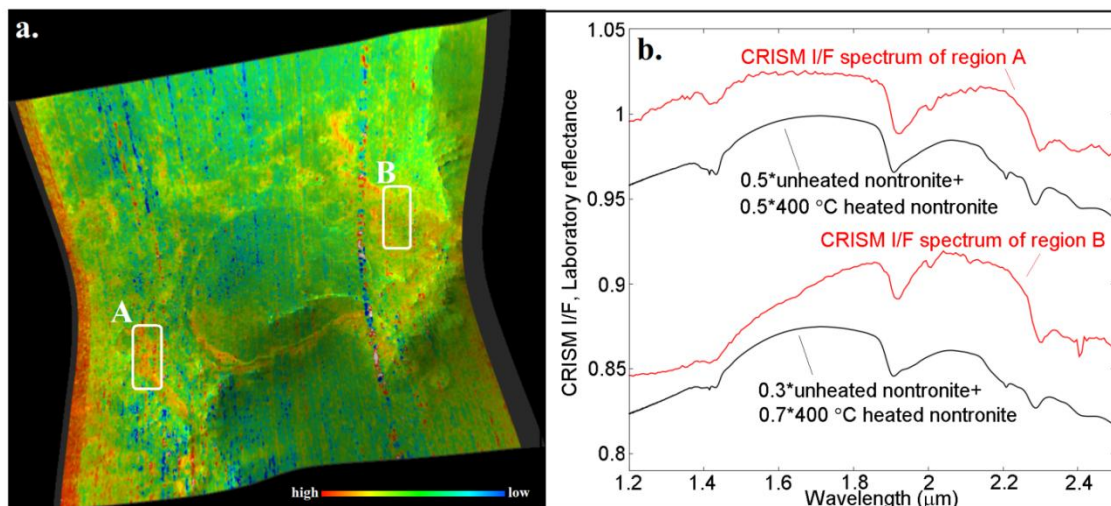


Figure 4.10 a) Ratio of 1.4 and 1.9 μm indices from CRISM image FRT0000BEC0 overlaid on 1.3 μm reflectance. b) CRISM I/F spectra shown for each of the regions of interest and compared to spectra of mixtures of pure and thermally altered nontronite.

4.4 Discussion

The close relationship between phyllosilicates and impact craters on Mars has been modeled and discussed in detail previously [Fairén *et al.* 2010]. The authors concluded that preexisting phyllosilicates have not been altered by post-shock temperatures as long as they were located outside of the cratering center because the shock temperature is not sufficiently high, and that a hydrothermal circulation might be triggered in the center area of an impact event, evidenced by the recently identification of hydrothermal products in central areas of impact craters on Mars [e.g., Ehlmann *et al.*, 2009, 2011]. However, results from this study, together with the potentially limited accessibility to the early hydrothermal systems on ancient Mars, lead us to propose another scenario that preexisting phyllosilicate sediments were excavated through impact processes, and subsequently modified by high temperatures in the crater centers. Low water availability on early Mars would make it difficult for these phyllosilicates to be altered by hydrothermal processes.

It is also important to note that our results imply mixing is occurring and that thermally altered nontronite may not exist as a pure phase in Nili Fossae. The co-existence of heated and unheated nontronite is likely the reason for the inconsistency between TIR and VNIR detections of nontronite in Nili Fossae revealed by *Michalski et al.* [2010]. We suggest that the unaltered and thermally altered nontronite are mixed together that the VNIR spectrum displays characteristic 1.4, 1.9, 2.3, and 2.4 μm features while the long wavelength range is dominated by a strong 450 cm^{-1} feature. This result is possible because mixing of VNIR spectra is highly non-linear [e.g., *Nash and Conel*, 1974; *Singer*, 1981; *Mustard and pieters*, 1989] and the spatial resolutions of TES and CRISM are very different ($\sim 3 \times 8\text{ km/pixel}$ vs. 18m/pixel).

Further, the identification of dehydrated or dehydroxylated phyllosilicates on the Martian surface would allow us to assess the role of post-depositional thermal alteration of sediments and, consequently the potential for preservation of biosignatures in these regions. If life was ever present on Mars and was in close association with phyllosilicate deposits [e.g., *Summons et al.* 2011], thermal alteration processes suggested by this study would be destructive to such putative Martian organics, due to the fact that the dehydration and dehydroxylation of phyllosilicates commonly require significantly higher temperatures than the hospitable temperatures (e.g. <100 °C [*Summons et al.* 2011]) even extreme thermophilic these organics have adapted to (e.g. 150 °C [Stetter et al. 1990]). Therefore, the occurrence of thermally altered phyllosilicate deposits would make preservation of biosignatures less likely.

4.5 Conclusion

This study has shown that thermally altered nontronite (400 °C) is likely present in the Nili Fossae region of Mars. Nontronite in the Nili Fossae region is not present as a pure phase, suggesting that it was partially affected by post-depositional thermal alteration. The mixing of altered and unaltered phyllosilicates is the likely cause for the apparent disconnect between previous VNIR and TIR observations of nontronite-bearing surfaces in Nili Fossae. The presence of thermally altered nontronite may also help understand the potential effects of post-depositional thermal alteration on Martian sediments as a key component of understanding past Martian habitability and biosignature preservation.

References:

Abramov, O., and D. A. Kring (2005), Impact-induced hydrothermal activity on early Mars, *J. Geophys. Res.*, *110*, E12S09, doi:10.1029/2005JE002453.

Bandfield, J. L., and M. D. Smith (2003), Multiple emission angle surface-atmosphere separations of Thermal Emission Spectrometer data, *Icarus*, *161*, 47-65.

Bandfield, J. L., P. R. Christensen, and M. D. Smith (2000a), Spectral data set factor analysis and end-member recovery: Application to analysis of Martian atmospheric particulates, *Journal of Geophysical Research*, *105*, 9573-9587.

Bandfield, J. L., V. E. Hamilton, and P. R. Christensen (2000b), A global view of Martian Surface Compositions from MGS-TES, *Science*, *287*, 1626.

Bibring, J. -P., Y. Langevin, J. F. Mustard, F. Poulet, R. Arvidson, A. Gendrin, B. Gondet, N. Mangold, P. Pinet, F. Forget, and the OMEGA team (2006), Global mineralogical and aqueous Mars history derived from OMEGA/Mars Express data, *Science*, *312*, 400-404.

Bishop J. L., Madejova J., Komadel P., and Froeschl H. (2002) The Influence of Structural Fe, Al and Mg on the Infrared OH Bands in Spectra of Dioctahedral Smectites. *Clay Miner.* *37* , 607-616.

Che, C., and T. D. Glotch (2012), The effect of high temperatures on the mid-to-far-infrared emission and near-infrared reflectance spectra of phyllosilicates and natural zeolites: Implications for Martian exploration, *Icarus*, *218*, 585-601.

Che, C., T. D. Glotch, D. L. Bish, J. R. Michalski, and W. Xu (2011), Spectroscopic study of the dehydration and/or dehydroxylation of phyllosilicate and zeolite minerals, *J. Geophys. Res.*, *116*, E05007, doi:10.1029/2010JE003740.

Christensen, P. R., J. L. Bandfield, V. E. Hamilton, D. A. Howard, M. D. Lane, J. L. Piatek, S. W. Ruff, and W. L. Stefanov (2000c), A thermal emission spectral library of rock-forming minerals, *J. Geophys. Res.*, *105(E4)*, 9735–9739.

Deer, W. A., R. A. Howie, and J. Zussman (1997), *An Introduction to the Rock-Forming Minerals*, Addison Wesley Longman Ltd.

Ehlmann, B. L., J. F. Mustard, R. N. Clark, G. A. Swayze, and S. L. Murchie (2011), Evidence for low-grade metamorphism, hydrothermal alteration, and diagenesis on Mars from phyllosilicates minerals assemblages, *Clay. Clay Min.*, *59*, 359-377.

Ehlmann, B. L., J. F. Mustard, G. A. Swayze, R. N. Clark, J. L. Bishop, F. Poulet, D. J. Des Marais, L. H. Roach, R. E. Milliken, J. J. Wray, O. Barnouin-Jha, and S. L. Murchie (2009), Identification of hydrated silicate minerals on Mars using MRO-CRISM: Geologic context near Nili Fossae and implications for aqueous alteration, *J. Geophys. Res.*, *114*, E00D08, doi:10.1029/2009JE003339.

Fairén, A. G. et al. (2010), Noachian and more recent phyllosilicates in impact craters on Mars, *Proceedings of the National Academy of Sciences*, *107*, 12095-12100, doi:10.1073/pnas.1002889107.

Gavin, P., V. Chevrier (2010), Thermal alteration of nontronite and montmorillonite: Implications for the martian surface, *Icarus*, *208*, 721-734, doi:10.1016/j.icarus.2010.02.027.

Glotch, T. D., and J. L. Bandfield (2006), Determination and interpretation of surface and atmospheric Miniature Thermal Emission Spectrometer spectral end-members at the Meridiani Planum landing site, *J. Geophys. Res.*, *111*, E12S06, doi:10.1029/2005JE002671.

Glotch, T. D., R. V. Morris, P. R. Christensen, and T. G. Sharp (2004), Effect of precursor mineralogy on the thermal infrared emission spectra of hematite: Application to Martian hematite mineralization, *J. Geophys. Res.*, *109*, E07003, doi:10.1029/2003JE002224.

Greeley, R., and J. E. Guest (1987), Geologic map of the eastern equatorial region of Mars, *U. S. Geol. Surv. Misc. Invest. Ser. Map I-1802-B*.

Hamilton, V.E. (2010), Thermal infrared (vibrational) spectroscopy of Mg-Fe olivines: A review and applications to determining the composition of planetary surfaces, *Chemie der Erde*, *70*, doi:10.1016/j.chemer.2009.12.005.

Malinowski, E. R. (1991), *Factor Analysis in Chemistry*, 2nd ed., John Wiley, Hoboken, N. J.

Mangold, N., et al. (2007), Mineralogy of the Nili Fossae region with OMEGA/Mars Express data; 2. Aqueous alteration of the crust, *J. Geophys. Res.*, *112*, E08S04, doi:10.1029/2006JE002835.

Michalski, J. R., M. D. Kraft, T. Diedrich, T. G. Sharp, and P. R. Christensen (2003), Thermal emission spectroscopy of the silica polymorphs and considerations for remote sensing of Mars, *Geophys. Res. Lett.*, *30*(19), 2008, doi:10.1029/2003GL018354.

Michalski, J. R., and E. Z. Noe Dobrea (2007), Evidence for a sedimentary origin of clay minerals in the Mawrth Vallis region, Mars, *Geology*, *35*, 951-954.

Michalski, J. R., F. Poulet, J. -P. Bibring, and N. Mangold (2010), Analysis of phyllosilicate deposits in Nili Fossae region of Mars: Comparison of TES and OMEGA data, *Icarus*, doi:10.1016/j.icarus.2009.09.006.

Milliken, R. E., and J. F. Mustard (2005), Quantifying absolute water content of minerals using near-infrared reflectance spectroscopy, *J. Geophys. Res.*, *110*, E12001, doi:10.1029/2005JE002534.

Mustard, J.F., C.M. Pieters (1989), Photometric phase functions of common geologic minerals and applications to quantitative analysis of mineral mixture reflectance spectra. *J. Geophys. Res.* *94*, 13619–13634.

Nash, D.B., J.E. Conel (1974), Spectral reflectance systematics for mixtures of powdered hypersthene, labradorite, and ilmenite. *J. Geophys. Res.* *79*, 1615–1621.

Poulet, F., J. -P. Bibring, J. F. Mustard, A. Gendrin, N. Mangold, Y. Langevin, R. E. Arvidson, B. Gondet, and the OMEGA team (2005), Phyllosilicates on Mars and implications for early martian climate, *Nature*, *438*, 623-627.

Rogers, A. D., and O. Aharonson (2008), Mineralogical composition of sands in Meridiani Planum from MER data and comparison to orbital measurements, *J. Geophys. Res.*, *113*, E06S14, doi:10.1029/2007JE002995.

Rogers, A. D. and J. L. Bandfield, Mineralogical Characterization of Mars Science Laboratory Candidate Landing Sites from THEMIS and TES Data, *Icarus*, doi:10.1016/j.icarus.2009.04.020, 2009.

Ruff, S. W. (2004), Spectral evidence for zeolite in the dust on Mars, *Icarus*, *168*(1), 131–143.

Singer, R.B. (1981), Near-Infrared spectral reflectance of mineral mixtures: Systematic combinations of pyroxenes, olivine, and iron oxides. *J. Geophys. Res.* *86*, 7967–7982.

Smith, M. D., J. L. Bandfield, and P. R. Christensen (2000), Separation of atmospheric and surface spectral features in Mars Global Surveyor Thermal Emission Spectrometer (TES) spectra, *Journal of Geophysical Research*, *105*, 9589-9607.

Stetter, K., G. Fiala, G. Huber, R. Huber, and A. Seegerer (1990), Hyperthermophilic microorganisms. *FEMS Microbiology Letters*, *75*: 117–124. doi: 10.1111/j.1574-6968.1990.tb04089.x

Summons, R. E., J. P. Amend, D. Bish, R. Buick, G. D. Cody, D. J. Des Marais, G. Dromart, J. L. Eigenbrode, A. H. Knoll, and D. Y. Sumner (2011), Preservation of Martian organic and environmental records: Final report of the Mars biosignature working group, *Astrobiology*, *11*, 157-181.

Wichman, R. W., and P. H. Schultz (1989), Sequence and mechanisms of deformation around the Hellas and Isidis impact basins on Mars, *J. Geophys. Res.*, *94*, 17,333-17357, doi: 10.1029/JB094iB12p17333.

Wyatt, M. B., V. E. Hamilton, H. Y. McSween, P. R. Christensen, and L. A. Taylor (2001), Analysis of terrestrial and Martian volcanic compositions using thermal emission spectroscopy: 1. Determination of mineralogy, chemistry, and classification strategies, *J. Geophys. Res.*, *106*(E7), 14,711– 14,732.

References

Chapter 1

Abramov, O., and D. A. Kring (2005), Impact-induced hydrothermal activity on early Mars, *J. Geophys. Res.*, *110*, E12S09, doi:10.1029/2005JE002453.

Aceman, S., N. Lahav, and S. Yariv (1997), XRD study of the dehydration and rehydration of Al-pillared smectites differing in source of charge, *J. Therm. Anal.*, *50*, 241--256.

Bailey, S. W. (1980), Structures of layer silicates, In *Crystal Structures of Clay Minerals and Their X-ray Identification*, edited by G. W. Brindley and G. Brown, pp. 1-124, Mineral. Soc., London.

Bandfield, J. L. (2002), Global minerals distributions on Mars, *J. Geophys. Res.*, *107*(E6), 5042, doi:10.1029/2001JE001510.

Bandfield, J. L., V. E. Hamilton, P. R. Christensen (2000), A global view of Martian surface compositions from MGS-TES, *Science*, *287*, 1626-1630.

Barrer, R. M. (1978), Zeolite frameworks, cations and water molecules, In *Zeolites and Clay Minerals as Sorbents and Molecular Sieves*, pp. 32-102, Academic Press, London.

Bibring, J. -P., Y. Langevin, J. F. Mustard, F. Poulet, R. Arvidson, A. Gendrin, B. Gondet, N. Mangold, P. Pinet, F. Forget, and the OMEGA team (2006), Global mineralogical and aqueous Mars history derived from OMEGA/Mars Express data, *Science*, *312*, 400-404.

Bishop, J. L., W. P. Gates, H. D. Makarewicz, N. K. McKeown, and T. Hiroi (2011), Reflectance spectroscopy of beidellites and their importance for Mars, , *Clays Clay Miner.*, *59*, 378-399.

Bishop, J. L., C. M. Pieters, J. O. Edwards (1994). Infrared spectroscopic analyses on the nature of water in montmorillonite. *Clays Clay Miner.* *42*, 701-715.

Bruckenthal, E. A., and R. B. Singer (1987), Spectral effects of dehydration on phyllosilicates, *Proc. Lunar Planet. Sci. Conf. 18th*, 135.

Chemtob, S. M., and T. D. Glotch (2007), Linear deconvolution of attenuated total reflectance infrared spectra of fine-grained mineral mixtures, *Lunar Planet. Sci.*, *38th*, abstract 1097.

Ehlmann, B. L., J. F. Mustard, G. A. Swayze, R. N. Clark, J. L. Bishop, F. Poulet, D. J. Des Marais, L. H. Roach, R. E. Milliken, J. J. Wray, O. Barnouin-Jha, and S. L. Murchie (2009), Identification of hydrated silicate minerals on Mars using MRO-CRISM: Geologic context near Nili Fossae and implications for aqueous alteration, *J. Geophys. Res.*, *114*, E00D08, doi:10.1029/2009JE003339.

Fairén, A. G. et al. (2010), Noachian and more recent phyllosilicates in impact craters on Mars, *Proceedings of the National Academy of Sciences*, *107*, 12095-12100, doi:10.1073/pnas.1002889107.

Farmer, V. C. (1974), The layer silicates, In *The Infrared Spectra of Minerals*, edited by V. C. Farmer, pp. 331-363, Mineral. Soc., London.

Fitzgerald, J. J., S. F. Dec, and A. I. Hamza (1989), Observation of 5-coordinated Al in pyrophyllite dehydroxylate by solid-state ^{27}Al NMR spectroscopy at 14 T, *Am. Mineral.*, *74*, 1405-1408.

Fitzgerald, J. J., A. I. Hamza, S. F. Dec, and C. E. Bronnimann (1996), Solid-state ^{27}Al and ^{29}Si NMR and ^1H CRAMPS studies of the thermal transformations of the 2:1 phyllosilicate pyrophyllite, *J. Phys. Chem.*, *100*, 17351-17360.

Frost, R. L., and P. F. Barron (1984), Solid-state silicon-29 and aluminum-27 nuclear magnetic resonance investigation of the dehydroxylation of pyrophyllite, *J. Phys. Chem.*, *88*, 6206-6209.

Gaffey, S. J., L. A. McFadden, D. Nash, C. M. Pieters (1993), Ultraviolet, Visible, and Near-infrared Reflectance Spectroscopy: Laboratory spectra of Geologic Materials, In: Pieters, C. M., Englert, P. A. J. (Eds.), *Remote Geochemical Analysis: Elemental and Mineralogical Composition*. Cambridge University Press, Cambridge, pp. 43-78.

Gavin, P., V. Chevrier (2010), Thermal alteration of nontronite and montmorillonite: Implications for the martian surface, *Icarus*, *208*, 721-734, doi:10.1016/j.icarus.2010.02.027.

Guggenheim, S. and A. F. Koster van Groos (2001), Baseline studies of the clay minerals society source clays: Thermal analysis, *Clays Clay Miner.*, *49*, 433-443.

Harris, W. G., K. A. Hollien, S. R. Bates, and W. A. Acree (1992), Dehydration of hydroxyl-interlayered vermiculite as a function of time and temperature, *Clay. Clay Min.*, *40*, 335-340.

Loizeau, D., N. Mangold, F. Poulet, J. -P. Bibring, A. Gendrin, V. Ansan, C. Gomez, B. Gondet, Y. Langevin, P. Masson, and G. Neukum (2007), Phyllosilicates in the Mawrth Vallis region of Mars, *J. Geophys. Res.*, *112*, E08S08, doi:10.1029/2006JE002877.

Madejov *a'*, J. (2003), FTIR techniques in clay mineral studies, *Vib. Spectrosc.*, *31*, 1-10.

Mangold, N., et al. (2007), Mineralogy of the Nili Fossae region with OMEGA/Mars Express data; 2. Aqueous alteration of the crust, *J. Geophys. Res.*, *112*, E08S04, doi:10.1029/2006JE002835.

McDowell, M. L., and V. E. Hamilton (2007a), Phyllosilicate detection and uncertainty from thermal infrared data in the vicinity of the Nili Fossae, *Lunar Planet. Sci.*, *XXXVIII*, abstract 1872.

McDowell, M. L., and V. E. Hamilton (2007b), Examination of phyllosilicate-bearing materials in the vicinity of the Nili Fossae using thermal infrared data, *Seventh Intl. Conf. Mars*, abstract 3095.

Michalski, J. R., and R. L. Fergason (2009), Composition and thermal inertia of the Mawrth Vallis region of Mars and THEMIS data, *Icarus*, *199*, 25-48, doi: 10.1016/j.icarus.2008.08.016.

Michalski, J. R., and E. Z. Noe Dobrea (2007), Evidence for a sedimentary origin of clay minerals in the Mawrth Vallis region, Mars, *Geology*, *35*, 951-954.

Michalski, J. R., F. Poulet, J. -P. Bibring, and N. Mangold (2010), Analysis of phyllosilicate deposits in Nili Fossae region of Mars: Comparison of TES and OMEGA data, *Icarus*, doi:10.1016/j.icarus.2009.09.006.

Michalski, J. R., M. D. Kraft, T. G. Sharp, L. B. Williams, and P. R. Christensen (2005), Mineralogical constraints on the high-silica martian surface component observed by TES, *Icarus*, *174*, 161-177.

Michalski, J. R., M. D. Kraft, T. G. Sharp, L. B. Williams, and P. R. Christensen (2006), Emission spectroscopy of clay minerals and evidence for poorly crystalline aluminosilicates on Mars from Thermal Emission Spectrometer data, *J. Geophys. Res.*, *111*, E03004, doi:10.1029/2005JE002438.

Milliken, R. E., and J. F. Mustard (2005), Quantifying absolute water content of minerals using near-infrared reflectance spectroscopy, *J. Geophys. Res.*, *110*, E12001, doi:10.1029/2005JE002534.

Poulet, F., J. -P. Bibring, J. F. Mustard, A. Gendrin, N. Mangold, Y. Langevin, R. E. Arvidson, B. Gondet, and the OMEGA team (2005), Phyllosilicates on Mars and implications for early martian climate, *Nature*, *438*, 623-627.

Ruff, S. W. (2003), Basaltic andesite or weathered basalt: A new assessment, *Sixth Intl. Conf. Mars*, abstract 3258.

Ruff, S. W., and P. R. Christensen (2007), Basaltic andesite, altered basalt, and a TES-based search for smectite clay minerals on Mars, *Geophys. Res. Lett.*, *34*, L10204, doi:10.1029/2007GL029602.

Ruff, S. W., P. R. Christensen, P. W. Barbera, D. L. Anderson (1997), Quantitative thermal emission spectroscopy of minerals: A technique for measurement and calibration. *J. Geophys. Res.* *102*, 14899-14913.

Salisbury, J. W. (1993), Mid-infrared spectroscopy: laboratory data, In *Remote Geochemical Analysis: Elemental and Mineralogical Composition*, edited by C. M. Pieters and P. A. J. Englert, pp. 79-98, Cambridge Univ. Press, New York.

Salisbury, F. B., A. Wald, D. M. D'Aria (1994), Thermal-infrared remote sensing and Kirchhoff's law 1. Laboratory measurements. *J. Geophys. Res.* 99 (B6), 11897-11911.

Sanchez-Soto, P. J., I. Sobrados, J. Sanz, and J. L. Perez-Rodriguez (1993), ^{29}Si and ^{27}Al magic-angle-spinning nuclear magnetic resonance study of the thermal transformations of pyrophyllite, *J. Am. Ceram. Soc.*, 76, 3024-3028.

Schwenzer, S. P., and D. A. Kring (2009), Impact-generated hydrothermal systems capable of forming phyllosilicates on Noachian Mars, *Geology*, 37, 1091-1094.

Viviano, C. E., J. E. Moersch (2011), Using THEMIS to address discrepancies between OMEGA/CRISM and TES detections of phyllosilicates. *Lunar Planet. Sci. XLII*, 2251 (abstract).

Chapter 2

Abramov, O., and D. A. Kring (2005), Impact-induced hydrothermal activity on early Mars, *J. Geophys. Res.*, 110, E12S09, doi:10.1029/2005JE002453.

Aceman, S., N. Lahav, and S. Yariv (1997), XRD study of the dehydration and rehydration of Al-pillared smectites differing in source of charge, *J. Therm. Anal.*, 50, 241--256.

Armbruster, T. and Gunter, M. E. (2001), Crystal structure of natural zeolites. In D. L. Bish and D. W. Ming, Eds., *Natural zeolites: Occurrence, properties, application*. Reviews in *Mineralogy and Geochemistry*, 45, 1-57. Mineralogical Society of America and Geochemical Society, Washington, U. S. A.

Bailey, S. W. (1980), Structures of layer silicates, In *Crystal Structures of Clay Minerals and Their X-ray Identification*, edited by G. W. Brindley and G. Brown, pp. 1-124, Mineral. Soc., London.

Ballet, O., J.M.D. Coey, and K. J. Burke (1985), Magnetic properties of sheet silicates; 2:1:1 layer minerals, *Phys. Chem. Minerals*, 12, 370-378.

Bandfield, J. L., V. E. Hamilton, P. R. Christensen (2000), A global view of Martian surface compositions from MGS-TES, *Science*, 287, 1626--1630.

Bandfield, J. L. (2002), Global minerals distributions on Mars, *J. Geophys. Res.*, 107(E6), 5042, doi:10.1029/2001JE001510.

Barrer, R. M. (1978), Zeolite frameworks, cations and water molecules, In *Zeolites and Clay Minerals as Sorbents and Molecular Sieves*, pp. 32-102, Academic Press, London.

Barrer, R. M. (1982), Occurrence, classification and some properties of zeolites, In *Hydrothermal Chemistry of Zeolites*, pp. 1-42, Academic Press, London.

Bibring, J. -P., Y. Langevin, A. Gendrin, B. Gondet, F. Poulet, M. Berthé A. Soufflot, R. Arvidson, N. Mangold, J. Mustard, P. Drossart, and the OMEGA team (2005), Mars surface diversity as revealed by the OMEGA/Mars Express observations, *Science*, 307, 1576--1581

Bibring, J. -P., Y. Langevin, J. F. Mustard, F. Poulet, R. Arvidson, A. Gendrin, B. Gondet, N. Mangold, P. Pinet, F. Forget, and the OMEGA team (2006), Global mineralogical and aqueous Mars history derived from OMEGA/Mars Express data, *Science*,312, 400--404.

Bish, D. L. (1984), Effects of exchangeable cation composition on the thermal expansion/contraction of clinoptilolite, *Clays and Clay Minerals*, 32 (6), 444-452.

Bish, D. L. (1988), Effects of composition on the dehydration behavior of clinoptilolite and heulandite, in *Occurrence, Properties and Utilization of Natural Zeolites*, D. Kallo and H.S. Sherry, eds., pp565, Akadémiai Kiadó, Budapest.

Bish, D. L. and J.W. Carey (2001), Thermal properties of natural zeolites, in *Natural Zeolites: occurrence, properties, applications*, D.L. Bish and D.W. Ming, eds., pp403, Mineralogical Society of America, Washington.

Bish, D. L., J. W. Carey, D. T. Vaniman, and S. J. Chipera (2003), Stability of hydrous minerals on the martian surface, *Icarus*,164, 96-103.

Bishop, J. L., E. Z. Noe Dobrea, N. K. McKeown, M. Parente, B. L. Ehlmann, J. R. Michalski, R. E. Milliken, F. Poulet, G. A. Swayze, J. F. Mustard, S. L. Murchie, and J. -P. Bibring (2008a), Phyllosilicate diversity and past aqueous activity revealed at Mawrth Vallis, Mars, *Science*,321, 830-833.

Bishop, J. L., M. D. Lane, M. D. Dyar, and A. J. Brown (2008b), Reflectance and emission spectroscopy study of four groups of phyllosilicates: smectites, kaolinite-serpentines, chlorites and micas, *Clay Minerals*,43, 35-54.

Bishop, J. L., N. K. McKeown, D. J. DesMarais, E. Z. Noe Dobrea, M. Parente, F. Seelos, S. L. Murchie, and J. F. Mustard (2009), The ancient phyllosilicates at Mawrth Vallis and what they can tell us about possible habitable environments on early Mars, *Lunar Planet. Sci.*, 40th, abstract 2239.

Boslough, M. B., R. J. Weldon, and T. J. Ahrens (1980), Impact-induced water loss from serpentine, nontronite and kernite, *Proc. Lunar Planet. Sci. Conf. 11th*, 2145-2158.

Breck, D. W. (1974a), Structure of zeolites, In *Zeolite Molecular Sieves: Structure, Chemistry, and Use*, pp. 29-185, John Wiley and Sons, London.

Breck, D. W. (1974b), Chemical properties and reactions of zeolites, In *Zeolite Molecular Sieves: Structure, Chemistry, and Use*, pp. 441-528, John Wiley and Sons, London.

Brindley, G. W., S. Z. Ali (1950), X-ray study of thermal transformations in some magnesian chlorite minerals. *Acta Cryst.* 3, 25-30.

Bruckenthal, E. A., and R. B. Singer (1987), Spectral effects of dehydration on phyllosilicates, *Proc. Lunar Planet. Sci. Conf. 18th*, 135.

Carroll, D. L., T. F. Kemp, T. J. Bastow, and M. E. Smith (2005), Solid-state NMR characterisation of the thermal transformation of a Hungarian white illite, *Solid State Nucl. Magn. Reson.*, 28, 31-43.

Che, C. and T. D. Glotch (2010), The effect of high temperatures on the emission and VNIR reflectance spectra of phyllosilicates and zeolites, *Lunar Planet. Sci.*, 41st, abstract 1513.

Chemtob, S. M., and T. D. Glotch (2007), Linear deconvolution of attenuated total reflectance infrared spectra of fine-grained mineral mixtures, *Lunar Planet. Sci.*, 38th, abstract 1097.

Cruciani, G. (2006), Zeolites upon heating: Factors governing their thermal stability and structural changes, *Journal of Physics and Chemistry of Solids*, 67, 1973-1994.

Dogan, A. U., M. Dogan, M. Onal, Y. Sarikaya, A. Aburub and D. E. Wurster (2006), Baseline studies of the Clay Minerals Society source clays: specific surface area by the Brunauer Emmett Teller (BET) method, *Clays and Clay Minerals*, 54, 62-66.

Drachman, S. R., G. E. Roch, and M. E. Smith (1997), Solid state NMR characterisation of the thermal transformation of Fuller's Earth, *Solid State Nucl. Magn. Reson.*, 9, 257-267.

Ehlmann, B. L., J. F. Mustard, G. A. Swayze, R. N. Clark, J. L. Bishop, F. Poulet, D. J. Des Marais, L. H. Roach, R. E. Milliken, J. J. Wray, O. Barnouin-Jha, and S. L. Murchie (2009), Identification of hydrated silicate minerals on Mars using MRO-CRISM: Geologic context near Nili Fossae and implications for aqueous alteration, *J. Geophys. Res.*, 114, E00D08, doi:10.1029/2009JE003339.

Fairén, A. G. et al. (2010), Noachian and more recent phyllosilicates in impact craters on Mars, *Proceedings of the National Academy of Sciences*, 107, 12095-12100, doi:10.1073/pnas.1002889107.

Farmer, V. C. (1974), The layer silicates, In *The Infrared Spectra of Minerals*, edited by V. C. Farmer, pp. 331-363, Mineral. Soc., London.

Farrand, W. H., T. D. Glotch, J. W. Rice Jr, J. A. Hurowitz, and G. A. Swayze (2009), Discovery of jarosite within the Mawrth Vallis region of Mars: Implications for the geologic history of the region, *Icarus*, 204, 478-488, doi: 10.1016/j.icarus.2009.07.014.

Fitzgerald, J. J., S. F. Dec, and A. I. Hamza (1989), Observation of 5-coordinated Al in pyrophyllite dehydroxylate by solid-state ^{27}Al NMR spectroscopy at 14 T, *Am. Mineral.*, *74*, 1405-1408.

Fitzgerald, J. J., A. I. Hamza, S. F. Dec, and C. E. Bronnimann (1996), Solid-state ^{27}Al and ^{29}Si NMR and ^1H CRAMPS studies of the thermal transformations of the 2:1 phyllosilicate pyrophyllite, *J. Phys. Chem.*, *100*, 17351-17360.

Frost, R. L., and P. F. Barron (1984), Solid-state silicon-29 and aluminum-27 nuclear magnetic resonance investigation of the dehydroxylation of pyrophyllite, *J. Phys. Chem.*, *88*, 6206-6209.

Frost, R. L., J. T. Kloprogge (2000), Vibrational spectroscopy of ferruginous smectite and nontronite, *Spectrochimica Acta Part A*, *56*, 2177-2189.

Frost, R. L., J. T. Kloprogge, D. Zhe (2002), The Garfield and Uley nontronites-an infrared spectroscopic comparison, *Spectrochimica Acta Part A*, *58*, 1881-1894.

Frost, R. L., O. B. Locos, H. Ruan, J. T. Kloprogge (2001), Near-infrared and mid-infrared spectroscopic study of sepiolites and palygorskites, *Vib. Spectrosc.*, *27*, 1-13.

Gavin, P., V. Chevrier, and K. Ninagawa (2008), Effect of impact and heating on the spectral properties of clays on Mars, *Lunar Planet. Sci.*, *39th*, abstract 2033.

Gavin, P., V. Chevrier (2010), Thermal alteration of nontronite and montmorillonite: Implications for the martian surface, *Icarus*, *208*, 721-734, doi:10.1016/j.icarus.2010.02.027.

Green, J. M., K. J. D. Mackenzie, and J. H. Sharp (1970), Thermal reactions of synthetic hectorite, *Clays Clay Miner.*, *18*, 339-346.

Grim, R. E., and G. Kulbicki (1961), Montmorillonite: high temperature reactions and classification, *Amer. Mineral.*,*46*, 1329-1369.

Guggenheim, S. and A. F. Koster van Groos (2001), Baseline studies of the clay minerals society source clays: Thermal analysis, *Clays Clay Miner.*,*49*, 433-443.

Harris, W. G., K. A. Hollien, S. R. Bates, and W. A. Acree (1992), Dehydration of hydroxyl-interlayered vermiculite as a function of time and temperature, *Clay. Clay Min.*,*40*, 335-340.

He, H. P., J. G. Guo, J. X. Zhu, and C. Hu (2003), ²⁹Si and ²⁷Al MAS NMR study of the thermal transformations of kaolinite from North China, *Clay Min.*,*38*, 551-559.

Keeling, J. L., M. D. Raven, and W. P. Gates (2000), Geology and characterization of two hydrothermal nontronites from weathered metamorphic rocks at the Uley graphite mine, South Australia, *Clay. Clay Min.*,*48*, 537-548.

Kloprogge, J. T., S. Komarneni, K. Yanagisawa, R. L. Frost, R. Fry (1998), Infrared study of some synthetic and natural beidellites, *J. Mater. Sci. Lett.*,*17*, 1853-1855.

Kloprogge, J. T., R. L. Frost, and L. Hickey (1999a), Infrared absorption and emission study of synthetic mica-montmorillonite in comparison to rectorite, beidellite and paragonite, *J. Mater. Sci. Lett.*,*18*, 1921-1923.

Kloprogge, J. T., R. Fry, and R. L. Frost (1999b), An infrared emission spectroscopic study of the thermal transformation mechanisms in Al₁₃-pillared clay catalysts with and without tetrahedral substitutions, *J. Catal.*,*184*, 157-171.

Kloprogge, J. T., R. L. Frost, and L. Hickey (2000a), Infrared emission spectroscopic study of the dehydroxylation of some hectorites, *Thermochim. Acta*,*345*, 145-156.

Kloprogge, J. T., and R. L. Frost (2000b), The effect of synthesis temperature on the FT-Raman and FT-IR spectra of saponites, *Vib. Spectrosc.*,23, 119-127.

Kloprogge, J. T., and R. L. Frost (2005), Infrared emission spectroscopy of clay minerals: In *The application of vibrational spectroscopy to clay minerals and layered double hydroxides*, CMS Workshop Lectures, Vol. 13, J. Theo Kloprogge ed., The Clay Mineral Society, Aurora, CO, 99-124.

Kulbicki, G. (1959), High temperature phases in sepiolite, attapulgite and saponite, *The American Mineralogist*, 44, 752-764.

Lambert, J. F., W. S. Millman, and J. J. Fripiat (1989), Revisiting kaolinite dehydroxylation: A ^{29}Si and ^{27}Al MAS NMR study, *J. Am. Chem. Soc.*,111, 3517-3522.

Lange, M. A., and T. J. Ahrens (1982), Impact induced dehydration of serpentine and the evolution of planetary atmosphere. *Proc. 13th Lunar Planet. Sci. Conf.*, A451-A456.

Loizeau, D., N. Mangold, F. Poulet, J. -P. Bibring, A. Gendrin, V. Ansan, C. Gomez, B. Gondet, Y. Langevin, P. Masson, and G. Neukum (2007), Phyllosilicates in the Mawrth Vallis region of Mars, *J. Geophys. Res.*,112, E08S08, doi:10.1029/2006JE002877.

Madejov *a'*, J., and P. Komadel (2001), Baseline studies of the clay minerals society source clays: Infrared methods, *Clay. Clay Min.*,49, 410-432.

Mangold, N., et al. (2007), Mineralogy of the Nili Fossae region with OMEGA/Mars Express data; 2.Aqueous alteration of the crust, *J. Geophys. Res.*, 112, E08S04, doi:10.1029/2006JE002835.

Massiot, D., P. Dion, J. F. Alcover, and F. Bergaya (1995), ^{27}Al and ^{29}Si MAS NMR study of kaolinite thermal decomposition by controlled rate thermal analysis, *J. Am. Ceram. Soc.*, *78*, 2940-2944.

McManus, J., S. E. Ashbrook, K. J. D. MacKenzie, and S. Wimperis (2001), ^{27}Al multiple-quantum MAS and $^{27}\text{Al}\{^1\text{H}\}$ CPMAS NMR study of amorphous aluminosilicates, *J. Non-Cryst. Solids*, *282*, 278-290.

Mermut, A. R., and A. Faz Cano (2001), Baseline studies of the clay minerals society source clays: Chemical analyses of major elements, *Clay. Clay Min.*, *49*, 381-386.

Michalski, J. R., and R. L. Fergason (2009), Composition and thermal inertia of the Mawrth Vallis region of Mars and THEMIS data, *Icarus*, *199*, 25-48, doi: 10.1016/j.icarus.2008.08.016.

Michalski, J. R., and E. Z. Noe Dobrea (2007), Evidence for a sedimentary origin of clay minerals in the Mawrth Vallis region, Mars, *Geology*, *35*, 951-954.

Michalski, J. R., M. D. Kraft, T. G. Sharp, L. B. Williams, and P. R. Christensen (2005), Mineralogical constraints on the high-silica martian surface component observed by TES, *Icarus*, *174*, 161-177.

Michalski, J. R., M. D. Kraft, T. G. Sharp, L. B. Williams, and P. R. Christensen (2006), Emission spectroscopy of clay minerals and evidence for poorly crystalline aluminosilicates on Mars from Thermal Emission Spectrometer data, *J. Geophys. Res.*, *111*, E03004, doi:10.1029/2005JE002438.

Michalski, J. R., F. Poulet, J. -P. Bibring, and N. Mangold (2010), Analysis of phyllosilicate deposits in Nili Fossae region of Mars: Comparison of TES and OMEGA data, *Icarus*, doi:10.1016/j.icarus.2009.09.006.

Milliken, R. E., and J. F. Mustard (2005), Quantifying absolute water content of minerals using near-infrared reflectance spectroscopy, *J. Geophys. Res.*, 110, E12001, doi:10.1029/2005JE002534.

Milliken, R. E., J. F. Mustard, F. Poulet, D. Jouglet, J.-P Bibring, B. Gondet, and Y. Langevin (2007), Hydration state of the Martian surface as seen by Mars Express OMEGA: 2. H₂O content of the surface, *J. Geophys. Res.*, 112, E08S07, doi:10.1029/2006JE002853.

Moore, D. M. and R. C. Reynolds Jr. (1989a), Structure and properties of clay minerals, In *X-Ray Diffraction and the Identification and Analysis of Clay Minerals*, pp. 102-178, Oxford University Press, Oxford.

Moore, D. M. and R. C. Reynolds Jr. (1989b), *X-Ray Diffraction and the Identification and Analysis of Clay Minerals*, pp. 187-190, Oxford University Press, Oxford.

Murchie, S. L., et al. (2009), Compact Reconnaissance Imaging Spectrometer for Mars investigation and data set from the Mars Reconnaissance Orbiter's primary science phase, *J. Geophys. Res.*, 114, E00D07, doi: 10.1029/2009JE003344.

Mustard, J. F., S. L. Murchie, B. L. Ehlmann, S. M. Pelkey, L. A. Roach, F. Seelos, F. Poulet, J. -P. Bibring, N. Mangold, J. A. Grant, R. E. Milliken and the CRISM team (2007), CRISM-OMEGA observations of phyllosilicate-olivine stratigraphy in Nili Fossae, Mars, *Lunar Planet. Sci.*, 38th, abstract 2071.

Mustard, J. F., S. L. Murchie, S. M. Pelkey, B. L. Ehlmann, R. E. Milliken, J. A. Grant, J.-P. Bibring, F. Poulet, J. L. Bishop, E. Z. Noe Dobrea, L. H. Roach, F. P. Seelos, R. E. Arvidson, S. Wiseman, R. Green, C. Hash, D. Humm, E. Malaret, J. A. McGovern, Y. Langevin, T. Martin, P. McGuire, R. Morris, M. S. Robinson, T. Roush, M. Smith, G. Swayze, H. Taylor, and M. Wolf (2008), Hydrated silicate minerals on Mars observed by the Mars Reconnaissance Orbiter CRISM instrument, *Nature*, 454, 305-309, doi:10.1038/nature07097.

Newsam, J. M. (1986), The zeolite cage structure, *Science*, 231, 1093--1099.

Ohnishi, I., and K. Tomeoka (2002), Dark inclusions in the Mokoia CV3 chondrite: Evidence for aqueous alteration and subsequent thermal and shock metamorphism, *Met. Planet.Sci.*, 37, 1843--1856.

Post, J. L. (1984), Saponite from near Ballarat, California, *Clay. Clay Min.*, 32, 147--153.

Poulet, F., J. -P. Bibring, J. F. Mustard, A. Gendrin, N. Mangold, Y. Langevin, R. E. Arvidson, B. Gondet, and the OMEGA team (2005), Phyllosilicates on Mars and implications for early martian climate, *Nature*, 438, 623--627.

Poulet, F., C. Gomez, J.-P. Bibring, Y. Langevin, B. Gondet, P. Pinet, G. Belluci, and J. Mustard (2007), Martian surface mineralogy from Observatoire pour la Minéralogie, l'Eau, les Glaces et l'Activité on board the Mars Express spacecraft (OMEGA/MEx): Global mineral maps, *J. Geophys. Res.*, 112, E08S02, doi:10.1029/2006JE002840.

Prasad, P. S. R., K. S. Prasad, and S. R. Murthy (2005), Dehydration of natural stilbite: An in situ FTIR study, *American Mineralogist*, 90, 1630-1640.

Prasad, P. S. R., and K. S. Prasad (2007), Dehydration and rehydration of mesolite: An *in situ* FTIR study, *Microporous and Mesoporous Materials*, *100*, 287-294.

Pruett, R. J., and H. L. Webb (1993), Sampling and analysis of KGa-1b well-crystallized kaolin source clay, *Clay. Clay Min.*, *41*, 514--519.

Roch, G. E., M. E. Smith, and S. R. Drachman (1998), Solid state NMR characterization of the thermal transformation of an illite-rich clay, *Clays Clay Min.*, *46*, 694-704.

Rocha, J. (1999), Single- and triple-quantum ^{27}Al MAS NMR study of the thermal transformation of kaolinite, *J. Phys. Chem. B*, *103*, 9801-9804.

Rocha, J., and J. Klinowski (1990), ^{29}Si and ^{27}Al magic-angle-spinning NMR studies of the thermal transformation of kaolinite, *Phys. Chem. Mineral.*, *17*, 179-186.

Rodriguez-Fuentes, G., A. R. Ruiz-Salvador, M. Mir, O. Picazo, G. Quintana, and M. Delgado (1998), Thermal and cation influence on IR vibrations of modified natural clinoptilolite, *Microporous and Mesoporous Materials*, *20*, 269-281.

Rogers, A. D., and P. R. Christensen (2007), Surface mineralogy of Martian low-albedo regions from MGS-TES data: Implications for upper crustal evolution and surface alteration, *J. Geophys. Res.*, *112*, E01003, doi:10.1029/2006JE002727.

Ruff, S. W. (2003), Basaltic andesite or weathered basalt: A new assessment, *Sixth Intl. Conf. Mars*, abstract 3258.

Ruff, S. W. (2004), Spectral evidence for zeolite in the dust on Mars, *Icarus*, *168*, 131-143, doi:10.1016/j.icarus.2003.11.003.

Ruff, S. W., and P. R. Christensen (2007), Basaltic andesite, altered basalt, and a TES-based search for smectite clay minerals on Mars, *Geophys. Res. Lett.*,*34*, L10204, doi:10.1029/2007GL029602.

Salisbury, J. W. (1993), Mid-infrared spectroscopy: laboratory data, In *Remote Geochemical Analysis: Elemental and Mineralogical Composition*, edited by C. M. Pieters and P. A. J. Englert, pp. 79-98, Cambridge Univ. Press, New York.

Sanchez-Soto, P. J., I. Sobrados, J. Sanz, and J. L. Perez-Rodriguez (1993), ^{29}Si and ^{27}Al magic-angle-spinning nuclear magnetic resonance study of the thermal transformations of pyrophyllite, *J. Am. Ceram. Soc.*,*76*, 3024-3028.

Sanz, J., A. Madani, J. M. Serratosa, J. S. Moya, and S. Aza (1988), ^{27}Al and ^{29}Si magic-angle spinning nuclear magnetic resonance study of the kaolinite-mullite transformation, *J. Am. Ceram.Soc.*,*71*, C418-C421.

Sarikaya, Y., M. Onal, B. Baran, and T. Alemdaroglu (2000), The effect of thermal treatment on some of the physiochemical properties of a bentonite, *Clay. Clay Min.*,*48*, 557-562.

Slade, R. C. T., and T. W. Davies (1991), Evolution of structural changes during flash calcination of kaolinite: A ^{29}Si and ^{27}Al nuclear magnetic resonance spectroscopy study, *J. Mater. Chem.*,*1*, 361-364.

Tomioka, N., K. Tomeoka, K. Nakamura-Messenger, and T. Sekine (2007), Heating effects of the matrix of experimentally shocked Murchison CM chondrite: Comparison with micrometeorites, *Met. Planet. Sci.*,*42*, 19-30.

Tonui, E. K., M. E. Zolensky, M. E. Lipschutz, M. S. Wang, and T. Nakamura (2003), Yamato 86029: Aqueously altered and thermally metamorphosed CI-like chondrite with unusual textures, *Met. Planet. Sci.*, 38, 269-292.

Tyburczy, J. A., and T. J. Ahrens (1988), Dehydration kinetics of shocked serpentine, *Proc. Lunar Planet. Sci. Conf. 18th*, 435-441.

Van der Marel, H. W., and H. Beutelspacher (1976), in: *Atlas of infrared spectroscopy of clay minerals and their admixtures*, Elsevier, Amsterdam, pp191.

Van Olphen, H., and J. J. Fripiat (1979), *Data Handbook for Clay Materials and other Non-Metallic Minerals*, Pergamon, Oxford.

Villieras, F., J. Yvon, J. M. Cases, P. De Donato, F. Lhote, and R. Baeza (1994), Development of microporosity in clinocllore upon heating, *Clays and Clay Minerals*, 42 (6), 679-688.

Wyatt, M. B., and H. Y. McSween Jr (2002), Spectral evidence for weathered basalt as an alternative to andesite in the northern lowlands of Mars, *Nature*, 417, 263—266.

Chapter 3

Abramov, O., Kring, D. A. 2005. Impact-induced hydrothermal activity on early Mars, *J. Geophys. Res.* 110, E12S09. doi:10.1029/2005JE002453.

Alver, B. E., Sakizci, M., Yorukogullari, E. 2010. Investigation of clinoptilolite rich natural zeolites from Turkey: a combined XRF, TG/DTG, DTA and DSC study. *J. Therm. Anal. Calorim.* 100, 19-26.

- Armbruster, T., Gunter, M. E. 2001. Crystal structure of natural zeolites. In: Bish, D. L., Ming, D. W. (Eds.), Natural zeolites: Occurrence, properties, application. Reviews in Mineralogy and Geochemistry, vol. 45, Mineralogical Society of America and Geochemical Society, Washington, D. C., pp, 1-57.
- Bailey, S. W. 1980. Structures of layer silicates. In: Brindley, G. W., Brown, G. (Eds.), Crystal Structures of Clay Minerals and Their X-ray Identification. Mineral. Soc., London, pp. 1-124.
- Ballet, O., Coey, J. M. D., Burke, K. J. 1985. Magnetic properties of sheet silicates: 2:1:1 layer minerals. Phys. Chem. Minerals 12, 370-378.
- Bandfield, J. L. 2002. Global minerals distributions on Mars. J. Geophys. Res. 107(E6), 5042. doi:10.1029/2001JE001510.
- Bandfield, J. L., Hamilton, V. E., Christensen, P. R. 2000. A global view of Martian surface compositions from MGS-TES. Science 287, 1626--1630.
- Barrer, R. M. 1978. Zeolite frameworks, cations and water molecules. In: Barrer, R. M. (Eds.), Zeolites and Clay Minerals as Sorbents and Molecular Sieves. Academic Press, London, pp. 32-102.
- Barrer, R. M. 1982. Occurrence, classification and some properties of zeolites, In: Barrer, R. M. (Eds.), Hydrothermal Chemistry of Zeolites. Academic Press, London, pp. 1-42.
- Bibring, J. -P., et al. 2006, Global mineralogical and aqueous Mars history derived from OMEGA/Mars Express data. Science 312, 400--404.
- Bish, D. L. 1984. Effects of exchangeable cation composition on the thermal expansion/contraction of clinoptilolite. Clays Clay Miner. 32, 444-452.

- Bishop, J. L., Pieters, C. M., Edwards, J. O. 1994. Infrared spectroscopic analyses on the nature of water in montmorillonite. *Clays Clay Miner.* 42, 701-715.
- Bishop, J. L., Lane, M. D., Dyar, M. D., Brown, A. J. 2008. Reflectance and emission spectroscopy study of four groups of phyllosilicates: smectites, kaolinite-serpentines, chlorites and micas, *Clay Miner.* 43, 35-54.
- Breck, D. W. 1974a. Chemical properties and reactions of zeolites, In: Breck, D. W. (Eds.), *Zeolite Molecular Sieves: Structure, Chemistry, and Use*. John Wiley and Sons, London, pp. 441-528.
- Breck, D. W. 1974b. Structure of zeolites. In: Breck, D. W. (Eds.), *Zeolite Molecular Sieves: Structure, Chemistry, and Use*. John Wiley and Sons, London, pp. 29-185.
- Brindley, G. W., Ali, S. Z. 1950. X-ray study of thermal transformations in some magnesian chlorite minerals. *Acta Cryst.* 3, 25-30.
- Caillere, S., Henin, S. 1957a. The sepiolite and palygorskite minerals. In: Mackenzie, R. C. (Eds.), *The Differential Thermal Investigations of Clays*. Mineralogical Society, London, pp. 231-247.
- Caillere, S., Henin, S. 1957b. The chlorite and serpentine minerals, In: Mackenzie, R. C. (Eds.), *The Differential Thermal Investigations of Clays*. Mineralogical Society, London, pp. 207-230.
- Che, C., Glotch, T. D., Bish, D. L., Michalski, J. R., Xu, W. 2011. Spectroscopic study of the dehydration and/or dehydroxylation of phyllosilicate and zeolite minerals. *J. Geophys. Res.* 116, E05007. doi:10.1029/2010JE003740.
- Cloutis, E. A., Asher, P. M., Mertzman, S. A. 2002. Spectral reflectance properties of zeolites and remote sensing implications. *J. Geophys. Res.* 107(E9), 5067. doi: 10.1029/2000JE001467.

- Earley, J. W., Milne, I. H., and McVeagh, W. J. 1953. Dehydration of montmorillonite. *Amer. Min.* 38, 770-783.
- Ehlmann, B. L., et al. 2009. Identification of hydrated silicate minerals on Mars using MRO-CRISM: Geologic context near Nili Fossae and implications for aqueous alteration. *J. Geophys. Res.* 114, E00D08. doi:10.1029/2009JE003339.
- Fairén, A. G., et al. 2010. Noachian and more recent phyllosilicates in impact craters on Mars. *Proc. Natl. Acad. Sci.* 107, 12095-12100. doi:10.1073/pnas.1002889107.
- Farmer, V. C. 1974. The layer silicates, In: Farmer, V. C. (Eds.), *The Infrared Spectra of Minerals*. Mineral. Soc., London, pp. 331-363.
- Földesová, M., Lukáč, P., Dillinger, P., Balek, V., Svetík, S. 1999. Thermochemical properties of chemically modified zeolite. *J. Therm. Anal. Calorim.* 58, 671-675.
- Frost, R. L., Kloprogge, J. T. 2000. Vibrational spectroscopy of ferruginous smectite and nontronite. *Spectrochimica Acta Part A* 56, 2177-2189.
- Frost, R. L., Kloprogge, J. T., Zhe, D. 2002. The Garfield and Uley nontronites-an infrared spectroscopic comparison. *Spectrochimica Acta Part A* 58, 1881-1894.
- Gaffey, S. J., McFadden, L. A., Nash, D., Pieters, C. M. 1993. Ultraviolet, Visible, and Near-infrared Reflectance Spectroscopy: Laboratory spectra of Geologic Materials, In: Pieters, C. M., Englert, P. A. J. (Eds.), *Remote Geochemical Analysis: Elemental and Mineralogical Composition*. Cambridge University Press, Cambridge, pp. 43-78.
- Gavin, P., Chevrier, V. 2010. Thermal alteration of nontronite and montmorillonite: Implications for the martian surface. *Icarus* 208, 721-734. doi:10.1016/j.icarus.2010.02.027.

- Glotch, T. D., Rossman, G. R., Aharonson, O. 2007. Mid-infrared (5-100 μm) reflectance spectra and optical constants of ten phyllosilicate minerals. *Icarus* 192, 604-622. Doi: 10.1016/j.icarus.2007.07.002.
- Green, J. M., Mackenzie, K. J. D., Sharp, J. H. 1970. Thermal reactions of synthetic hectorite. *Clays Clay Miner.* 18, 339-346. doi: 10.1346/CCMN.1970.0180606.
- Greene-Kelly, R. 1957. The montmorillonite minerals (smectites), In: Mackenzie, R. C. (Eds.), *The Differential Thermal Investigations of Clays*. Mineralogical Society, London, pp. 140–164.
- Hamilton, V. E., Christensen, P. R., McSween Jr., H. Y. 1997. Determination of Martian meteorite lithologies and mineralogies using vibrational spectroscopy. *J. Geophys. Res.* 102, 25,593-26603.
- Hedley, C. B., Yuan, G., Theng, B. K. G. 2007. Thermal analysis of montmorillonites modified with quaternary phosphonium and ammonium surfactants. *Appl. Clay Sci.* 35, 180-188.
- Holdridge, D. A., Vaughan, F. 1957. The kaolin minerals (kandites), In: Mackenzie, R. C. (Eds.), *The Differential Thermal Investigations of Clays*. Mineralogical Society, London, pp. 98–139.
- Keeling, J. L., Raven, M. D., Gates, W. P. 2000. Geology and characterization of two hydrothermal nontronites from weathered metamorphic rock at the Uley graphite mine, South Australia. *Clays Clay Miner.* 48, 537-548.
- Kloprogge, J. T., Komarneni, S., Yanagisawa, K., Frost, R. L., Fry, R. 1998. Infrared study of some synthetic and natural beidellites. *J. Mater. Sci. Lett.* 17, 1853-1855.

- Kloprogge, J. T., Frost, R. L., Hickey, L. 1999a. Infrared absorption and emission study of synthetic mica-montmorillonite in comparison to rectorite, beidellite and paragonite. *J. Mater. Sci. Lett.*18, 1921-1923.
- Kloprogge, J. T., Fry, R., Frost, R. L. 1999b. An infrared emission spectroscopic study of the thermal transformation mechanisms in Al₁₃-pillared clay catalysts with and without tetrahedral substitutions.*J. Catal.*184, 157-171.
- Kloprogge, J. T., Frost, R. L., Hickey, L. 2000. Infrared emission spectroscopic study of the dehydroxylation of some hectorites.*Thermochim. Acta*345, 145-156.
- Kloprogge, J. T., Frost, R. L. 2000. The effect of synthesis temperature on the FT-Raman and FT-IR spectra of saponites.*Vib.Spectrosc.*23, 119-127.
- Kulbicki, G. 1959. High temperature phases in sepiolite, attapulgite and saponite, *Am. Mineral.* 44, 752-764.
- Loizeau, D., et al. 2007. Phyllosilicates in the Mawrth Vallis region of Mars, *J. Geophys.Res.*112, E08S08.doi:10.1029/2006JE002877.
- Madajová J., Komadel, P. 2001. Baseline studies of the clay minerals society source clays: Infrared methods. *Clays Clay Miner.*49, 410-432.
- Mangold, N., et al. 2007. Mineralogy of the Nili Fossae region with OMEGA/Mars Express data; 2.Aqueous alteration of the crust. *J. Geophys. Res.* 112, E08S04.doi:10.1029/2006JE002835.
- McDowell, M. L., Hamilton, V. E. 2007a. Phyllosilicate detection and uncertainty from thermal infrared data in the vicinity of the Nili Fossae.*Lunar Planet. Sci.*XXXVIII, 1872 (abstract).

- McDowell, M. L., Hamilton, V. E. 2007b. Examination of phyllosilicate-bearing materials in the vicinity of the Nili Fossae using thermal infrared data. *Intl. Conf. Mars* 7, 3095 (abstract).
- Mermut, A. R., Faz Cano, A. 2001. Baseline studies of the clay minerals society source clays: Chemical analyses of major elements. *Clays Clay Miner.* 49, 381-386.
- Michalski, J. R., Fergason, R. L. 2009. Composition and thermal inertia of the Mawrth Vallis region of Mars and THEMIS data. *Icarus* 199, 25-48. doi: 10.1016/j.icarus.2008.08.016.
- Michalski, J. R., Noe Dobrea, E. Z. 2007. Evidence for a sedimentary origin of clay minerals in the Mawrth Vallis region, Mars. *Geology* 35, 951-954.
- Michalski, J. R., Kraft, M. D., Sharp, T. G., Williams, L. B., Christensen, P. R. 2005. Mineralogical constraints on the high-silica martian surface component observed by TES. *Icarus* 174, 161-177.
- Michalski, J. R., Kraft, M. D., Sharp, T. G., Williams, L. B., Christensen, P. R. 2006. Emission spectroscopy of clay minerals and evidence for poorly crystalline aluminosilicates on Mars from Thermal Emission Spectrometer data. *J. Geophys. Res.* 111, E03004. doi:10.1029/2005JE002438.
- Michalski, J. R., Poulet, F., Bibring, J. -P., Mangold, N. 2010. Analysis of phyllosilicate deposits in Nili Fossae region of Mars: Comparison of TES and OMEGA data. *Icarus* 206 (1), 269-289. doi:10.1016/j.icarus.2009.09.006.
- Milliken, R. E., Mustard, J. F. 2005. Quantifying absolute water content of minerals using near-infrared reflectance spectroscopy. *J. Geophys. Res.* 110, E12001. doi:10.1029/2005JE002534.

- Ming, D. W., Morris, R. V., Clark, B. C. 2008. Aqueous alteration on Mars, In: Bell, J. (Eds.), The Martian Surface - composition, Mineralogy, and Physical Properties. Cambridge University Press, Cambridge, pp. 519-540.
- Newsam, J. M. 1986. The zeolite cage structure. *Science* 231, 1093--1099.
- Post, J. L. 1984. Saponite from near Ballarat, California. *Clays Clay Miner.* 32, 147-153.
- Poulet, F., et al. 2005. Phyllosilicates on Mars and implications for early martian climate. *Nature* 438, 623--627.
- Pruett, R. J., Webb, H. L. 1993. Sampling and analysis of KGa-1b well-crystallized kaolin source clay. *Clays Clay Miner.* 41, 514-519.
- Ruff, S. W. 2003. Basaltic andesite or weathered basalt: A new assessment. *Intl. Conf. Mars* 6, 3258 (abstract).
- Ruff, S. W. 2004. Spectral evidence for zeolite in the dust on Mars. *Icarus* 168, 131-143. doi:10.1016/j.icarus.2003.11.003.
- Ruff, S. W., Christensen, P. R. 2007. Basaltic andesite, altered basalt, and a TES-based search for smectite clay minerals on Mars. *Geophys. Res. Lett.* 34, L10204. doi:10.1029/2007GL029602.
- Ruff, S. W., Christensen, P. R., Barbera, P. W., Anderson, D. L. 1997. Quantitative thermal emission spectroscopy of minerals: A technique for measurement and calibration. *J. Geophys. Res.* 102, 14899-14913.

- Salisbury, J. W. (1993), Mid-infrared spectroscopy: laboratory data, In: Pieters, C. M., Englert, P. A. J. (Eds.), *Remote Geochemical Analysis: Elemental and Mineralogical Composition*. Cambridge University Press, Cambridge, pp. 79-98.
- Salisbury, F. B., Wald, A., D'Aria, D. M. 1994. Thermal-infrared remote sensing and Kirchhoff's law 1. Laboratory measurements. *J. Geophys. Res.* 99 (B6), 11897-11911.
- Schwenzer, S. P., Kring, D. A. 2009. Impact-generated hydrothermal systems capable of forming phyllosilicates on Noachian Mars. *Geology* 37, 1091-1094.
- Van der Marel, H. W., Beutelspacher, H. 1976. *Atlas of infrared spectroscopy of clay minerals and their admixtures*. Elsevier Scientific Pub.Co., Amsterdam, New York.
- Van Olphen, H., Fripiat, J. J. 1979. *Data handbook for Clay Materials and other Non-Metallic Minerals*. Pergamon, Oxford.
- Vicente, M. A., Bañares-Muñoz, M. A., Gandía, L. M., Gil, A. 2001. On the structural changes of a saponite intercalated with various polycations upon thermal treatments, *Appl. Catal., A* 217, 191-204.
- Villieras, F., Yvon, J., Cases, J. M., De Donato, P., Lhote, F., Baeza, R. 1994. Development of microporosity in clinocllore upon heating. *Clays Clay Miner.* 42(6), 679-688. doi: 10.1346/CCMN.1994.0420604.
- Viviano, C. E., Moersch, J. E. 2011. Using THEMIS to address discrepancies between OMEGA/CRISM and TES detections of phyllosilicates. *Lunar Planet. Sci.* XLII, 2251 (abstract).

Chapter 4

Abramov, O., and D. A. Kring (2005), Impact-induced hydrothermal activity on early Mars, *J. Geophys. Res.*, *110*, E12S09, doi:10.1029/2005JE002453.

Bandfield, J. L., and M. D. Smith (2003), Multiple emission angle surface-atmosphere separations of Thermal Emission Spectrometer data, *Icarus*, *161*, 47-65.

Bandfield, J. L., P. R. Christensen, and M. D. Smith (2000a), Spectral data set factor analysis and end-member recovery: Application to analysis of Martian atmospheric particulates, *Journal of Geophysical Research*, *105*, 9573-9587.

Bandfield, J. L., V. E. Hamilton, and P. R. Christensen (2000b), A global view of Martian Surface Compositions from MGS-TES, *Science*, *287*, 1626.

Bibring, J. -P., Y. Langevin, J. F. Mustard, F. Poulet, R. Arvidson, A. Gendrin, B. Gondet, N. Mangold, P. Pinet, F. Forget, and the OMEGA team (2006), Global mineralogical and aqueous Mars history derived from OMEGA/Mars Express data, *Science*, *312*, 400-404.

Bishop J. L., Madejova J., Komadel P., and Froeschl H. (2002) The Influence of Structural Fe, Al and Mg on the Infrared OH Bands in Spectra of Dioctahedral Smectites. *Clay Miner.* *37*, 607-616.

Che, C., and T. D. Glotch (2012), The effect of high temperatures on the mid-to-far-infrared emission and near-infrared reflectance spectra of phyllosilicates and natural zeolites: Implications for Martian exploration, *Icarus*, *218*, 585-601.

Che, C., T. D. Glotch, D. L. Bish, J. R. Michalski, and W. Xu (2011), Spectroscopic study of the dehydration and/or dehydroxylation of phyllosilicate and zeolite minerals, *J. Geophys. Res.*, *116*, E05007, doi:10.1029/2010JE003740.

Christensen, P. R., J. L. Bandfield, V. E. Hamilton, D. A. Howard, M. D. Lane, J. L. Piatek, S. W. Ruff, and W. L. Stefanov (2000c), A thermal emission spectral library of rock-forming minerals, *J. Geophys. Res.*, *105(E4)*, 9735–9739.

Deer, W. A., R. A. Howie, and J. Zussman (1997), *An Introduction to the Rock-Forming Minerals*, Addison Wesley Longman Ltd.

Ehlmann, B. L., J. F. Mustard, R. N. Clark, G. A. Swayze, and S. L. Murchie (2011), Evidence for low-grade metamorphism, hydrothermal alteration, and diagenesis on Mars from phyllosilicates minerals assemblages, *Clay. Clay Min.*, *59*, 359-377.

Ehlmann, B. L., J. F. Mustard, G. A. Swayze, R. N. Clark, J. L. Bishop, F. Poulet, D. J. Des Marais, L. H. Roach, R. E. Milliken, J. J. Wray, O. Barnouin-Jha, and S. L. Murchie (2009), Identification of hydrated silicate minerals on Mars using MRO-CRISM: Geologic context near Nili Fossae and implications for aqueous alteration, *J. Geophys. Res.*, *114*, E00D08, doi:10.1029/2009JE003339.

Fairén, A. G. et al. (2010), Noachian and more recent phyllosilicates in impact craters on Mars, *Proceedings of the National Academy of Sciences*, *107*, 12095-12100, doi:10.1073/pnas.1002889107.

Gavin, P., V. Chevrier (2010), Thermal alteration of nontronite and montmorillonite: Implications for the martian surface, *Icarus*, *208*, 721-734, doi:10.1016/j.icarus.2010.02.027.

Glotch, T. D., and J. L. Bandfield (2006), Determination and interpretation of surface and atmospheric Miniature Thermal Emission Spectrometer spectral end-members at the Meridiani Planum landing site, *J. Geophys. Res.*, *111*, E12S06, doi:10.1029/2005JE002671.

Glotch, T. D., R. V. Morris, P. R. Christensen, and T. G. Sharp (2004), Effect of precursor mineralogy on the thermal infrared emission spectra of hematite: Application to Martian hematite mineralization, *J. Geophys. Res.*, *109*, E07003, doi:10.1029/2003JE002224.

Greeley, R., and J. E. Guest (1987), Geologic map of the eastern equatorial region of Mars, *U. S. Geol. Surv. Misc. Invest. Ser. Map I-1802-B*.

Hamilton, V.E. (2010), Thermal infrared (vibrational) spectroscopy of Mg-Fe olivines: A review and applications to determining the composition of planetary surfaces, *Chemie der Erde*, *70*, doi:10.1016/j.chemer.2009.12.005.

Malinowski, E. R. (1991), *Factor Analysis in Chemistry*, 2nd ed., John Wiley, Hoboken, N. J.

Mangold, N., et al. (2007), Mineralogy of the Nili Fossae region with OMEGA/Mars Express data; 2. Aqueous alteration of the crust, *J. Geophys. Res.*, *112*, E08S04, doi:10.1029/2006JE002835.

Michalski, J. R., M. D. Kraft, T. Diedrich, T. G. Sharp, and P. R. Christensen (2003), Thermal emission spectroscopy of the silica polymorphs and considerations for remote sensing of Mars, *Geophys. Res. Lett.*, *30*(19), 2008, doi:10.1029/2003GL018354.

Michalski, J. R., and E. Z. Noe Dobrea (2007), Evidence for a sedimentary origin of clay minerals in the Mawrth Vallis region, Mars, *Geology*, *35*, 951-954.

Michalski, J. R., F. Poulet, J. -P. Bibring, and N. Mangold (2010), Analysis of phyllosilicate deposits in Nili Fossae region of Mars: Comparison of TES and OMEGA data, *Icarus*, doi:10.1016/j.icarus.2009.09.006.

Milliken, R. E., and J. F. Mustard (2005), Quantifying absolute water content of minerals using near-infrared reflectance spectroscopy, *J. Geophys. Res.*, *110*, E12001, doi:10.1029/2005JE002534.

Mustard, J.F., C.M. Pieters (1989), Photometric phase functions of common geologic minerals and applications to quantitative analysis of mineral mixture reflectance spectra. *J. Geophys. Res.* *94*, 13619–13634.

Nash, D.B., J.E. Conel (1974), Spectral reflectance systematics for mixtures of powdered hypersthene, labradorite, and ilmenite. *J. Geophys. Res.* *79*, 1615–1621.

Poulet, F., J. -P. Bibring, J. F. Mustard, A. Gendrin, N. Mangold, Y. Langevin, R. E. Arvidson, B. Gondet, and the OMEGA team (2005), Phyllosilicates on Mars and implications for early martian climate, *Nature*, *438*, 623-627.

Rogers, A. D., and O. Aharonson (2008), Mineralogical composition of sands in Meridiani Planum from MER data and comparison to orbital measurements, *J. Geophys. Res.*, *113*, E06S14, doi:10.1029/2007JE002995.

Rogers, A. D. and J. L. Bandfield, Mineralogical Characterization of Mars Science Laboratory Candidate Landing Sites from THEMIS and TES Data, *Icarus*, doi:10.1016/j.icarus.2009.04.020, 2009.

Ruff, S. W. (2004), Spectral evidence for zeolite in the dust on Mars, *Icarus*, *168*(1), 131–143.

Singer, R.B. (1981), Near-Infrared spectral reflectance of mineral mixtures: Systematic combinations of pyroxenes, olivine, and iron oxides. *J. Geophys. Res.* *86*, 7967–7982.

Smith, M. D., J. L. Bandfield, and P. R. Christensen (2000), Separation of atmospheric and surface spectral features in Mars Global Surveyor Thermal Emission Spectrometer (TES) spectra, *Journal of Geophysical Research*, *105*, 9589-9607.

Stetter, K., G. Fiala, G. Huber, R. Huber, and A. Seeger (1990), Hyperthermophilic microorganisms. *FEMS Microbiology Letters*, *75*: 117–124. doi: 10.1111/j.1574-6968.1990.tb04089.x

Summons, R. E., J. P. Amend, D. Bish, R. Buick, G. D. Cody, D. J. Des Marais, G. Dromart, J. L. Eigenbrode, A. H. Knoll, and D. Y. Sumner (2011), Preservation of Martian organic and environmental records: Final report of the Mars biosignature working group, *Astrobiology*, *11*, 157-181.

Wichman, R. W., and P. H. Schultz (1989), Sequence and mechanisms of deformation around the Hellas and Isidis impact basins on Mars, *J. Geophys. Res.*, *94*, 17,333-17357, doi: 10.1029/JB094iB12p17333.

Wyatt, M. B., V. E. Hamilton, H. Y. McSween, P. R. Christensen, and L. A. Taylor (2001), Analysis of terrestrial and Martian volcanic compositions using thermal emission spectroscopy: 1. Determination of mineralogy, chemistry, and classification strategies, *J. Geophys. Res.*, *106*(E7), 14,711– 14,732.